Investigation of the electrochemical electrolyte decomposition in lithium-ion pouch cells by liquid chromatography and gas chromatography

Zur Erlangung des akademischen Grades eines
DOKTORS DER INGENIEURWISSENSCHAFTEN (Dr.-Ing.)

von der KIT-Fakultät für Maschinenbau des
Karlsruher Instituts für Technologie (KIT)
angenommene

DISSERTATION

von

Herrn M.Sc. Jan Richard Stockhausen

Tag der mündlichen Prüfung: 28.02.2023

Hauptreferent: Prof. Dr. Michael J. Hoffmann

Korreferent: Prof. Dr. Helmut Ehrenberg

Korreferent: Prof. Dr. Thomas Hanemann

Abstract

For a further, systematic optimization of lithium-ion batteries, it is crucial to understand electrochemical processes in the battery cells during their operation. Nevertheless, the processes leading to capacity decay and cell aging are not yet fully understood. Cell aging and capacity decay are accompanied by electrolyte decomposition to gaseous products and solid products that form surface layers on the electrodes. As a result, the electrolyte amount diminishes in the battery cell during formation and subsequent cycling. Thus, the conventional determination of quantity ratios or concentrations of electrolyte components does not provide reliable insight into the actual consumptions of the electrolyte components by the electrochemical decompositions. For this purpose, the absolute, consumed amounts of the electrolyte components need to be determined directly. Indeed, only the concentrations and not the absolute, consumed amounts of the electrolyte components can be determined using the conventional methods for electrolyte extraction (simple electrolyte extraction). Within the scope of this thesis, a new method for electrolyte extraction from pouch cells by injection of the diluent diethyl carbonate (DEC) is presented that allows the determination of these absolute consumptions of the electrolyte components. The compositions of the analyzed electrolytes are determined by high-performance liquid chromatography (HPLC) coupled to an electrospray ionization mass spectrometer (ESI/MS) and an ultraviolet/visible light (UV/Vis) detector. First, HPLC methods are developed to determine the concentrations of the electrolyte components in non-extracted, fresh electrolytes as accurately as possible. Subsequently, electrolytes are extracted from electrochemically untreated, fresh $LiNi_{1/3}Co_{1/3}Mn_{1/3}O_2$ (NCM111)/graphite lithium-ion pouch cells containing 1 M $LiPF_6$ in ethylene carbonate (EC)/dimethyl carbonate (DMC) 1:1 by weight with 3 wt% vinylene carbonate (VC) using the new extraction method and centrifugation (a standard extraction method). The determined compositions of the electrolytes extracted from the electrochemically untreated cells by both methods are similar confirming the suitability of the new extraction method. Furthermore, electrolytes are extracted from equal NCM111/graphite pouch cells after formation, after 25 cycles, and after 2000 cycles by means of the new extraction method. The extracted electrolytes are quantitatively analyzed by HPLC-UV/Vis and HPLC-ESI/MS using the developed HPLC methods. Based on the obtained measurement data, the concentrations of the electrolyte components in these electrolytes, as well as the consumed amounts of the electrolyte components during formation plus the following about 2000 cycles are determined. The consumed amounts or consumptions of the components reveal a dominant EC decomposition during formation and the 2000 cycles, beside a simultaneous, moderate VC and salt degradation. In contrast, the usually determined concentrations reveal solely VC decomposition during formation and long-term cycling.

This example confirms that only the absolute consumptions and not the concentrations reveal the actual decompositions in battery electrolytes. Further, the electrochemical decompositions in the electrolyte during formation and long-term cycling in $LiNi_{0.6}Co_{0.2}Mn_{0.2}O_2$ (NCM622)/graphite lithium-ion pouch cells containing 1 M $LiPF_6$ in EC/DMC 1:1 by weight with 3 wt% VC are investigated by HPLC-UV/Vis, and HPLC-ESI/MS. For this purpose, the electrolyte is extracted from these cells by the developed extraction method at selected aging steps, namely before formation, after formation, after 25 cycles, as well as after cycling until a remaining capacity of 95%, 90%, and 80%. X-ray photoelectron spectroscopy (XPS), gas chromatography coupled to a thermal conductivity detector (GC-TCD), scanning electron microscopy (SEM), energy-dispersive X-ray spectroscopy (EDX), and inductively coupled plasma optical emission spectrometry (ICP-OES) are applied as complementary analysis methods to gain deeper insight into the mechanisms responsible for electrolyte consumption, solid electrolyte interphase (SEI) growth, and capacity decay. Two phases of electrochemical aging (phase I, and phase II) can be identified: In phase I during formation and the subsequent, first 25 cycles, an exclusive decomposition of EC and VC each to similar extents is observed leading to the buildup of a thin SEI especially at the graphite particle edges. An incomplete anode passivation due to a thin and unfinished SEI is the identified, crucial trigger for the electrolyte decomposition, the associated SEI buildup, and the capacity loss in phase I. In phase II, from the 26^{th} cycle until the about 800^{th} cycle, a non-preferential decomposition of each electrolyte component is found, meaning each component is decomposed according to its abundance. Simultaneously, the growth of a thick SEI is observed at edges and basal planes of the graphite particles. Besides, a linear increase of the manganese amounts in the anodes with the number of cycles is detected. From the obtained results, it is concluded that the electrolyte consumption, the associated SEI growth, and the capacity loss are induced by two triggers in phase II: Firstly, there is the ongoing accumulation of manganese in the SEI, which deteriorates the anode passivation, so that electrolyte decomposition, SEI growth, and capacity loss are accelerated. Secondly, crack formation in the graphite particles by volume changes during de-/lithiation leads to the creation of new, electrochemically active surface, which leads to buildup of new SEI, electrolyte reduction, and capacity loss. Finally, the electrochemical decomposition processes in NCM622/silicon-graphite lithium-ion pouch cells containing either 1 M $LiPF_6$ in VC/DMC 1:1 by weight or 1 M $LiPF_6$ in fluoroethylene carbonate (FEC)/DMC 1:1 by weight during formation and subsequent cycling are investigated. The investigated electrolytes are extracted by the newly developed extraction method from these cells before formation, after formation, after 15 cycles, and 40 cycles. HPLC-UV/Vis, HPLC-ESI/MS, and gas chromatography coupled to a flame ionization detector (GC-FID) are applied for the quantification of the electrolyte components. To gain comprehensive insight into the mechanisms responsible for the capacity decay, GC-TCD, XPS, SEM, EDX, and ICP-OES are applied. Compared to the cells with the FEC-containing electrolyte, the cells with the VC-containing electrolyte have lower, initial

discharge capacities due to more pronounced capacity losses during formation. Indeed, the capacity fade of the cells with the VC-containing electrolyte during subsequent cycling is slower, so that the discharge capacities of the cells with the VC-containing electrolyte are higher than those of the cells with the FEC-containing electrolyte after 20 to 30 cycles. From the obtained results, it can be concluded that the capacity losses of the NCM622/silicon-graphite pouch cells with the VC-containing electrolyte and the FEC-containing electrolyte are (almost) exclusively triggered by trapping of cycleable lithium in the SEI and trapping of cycleable lithium in irreversibly lithiated silicon and silicon oxide under the SEI during the first cycle of the formation program. The capacity losses of the NCM622/silicon-graphite pouch cells with the VC-containing electrolyte and the FEC-containing electrolyte after the first cycle of the formation program during the subsequent cycles are (almost) exclusively induced by trapping of cycleable lithium in the SEI. VC is preferentially decomposed in the investigated cells with the VC-containing electrolyte during formation and the following 40 cycles. Simultaneously, a slight DMC decomposition can be observed in the cells with the VC-containing electrolyte. The results from the analyses indicate that reductive decomposition of one VC molecule at the anode leads to the consumption of one lithium-ion and one electron. As a result, lithium-containing, polymerized VC (poly(VC)) is deposited on the anodes, which is the main SEI component after formation and following cycling in the cells with the VC-containing electrolyte. This proposed mechanism for the reductive decomposition of VC is almost exclusively responsible for the capacity loss of the examined NCM622/silicon-graphite pouch cells with the VC-containing electrolyte after formation during following cycling. FEC is exclusively decomposed during formation and the subsequent 40 cycles in the examined cells with the FEC-containing electrolyte. The results from the investigations suggest that the reductive decomposition of one FEC molecule at the anode leads to the consumption of three lithium-ions and three electrons. The reductive decomposition of FEC eventually yields the SEI components LiF, a cross-linked polyethylene oxide (PEO)-type polymer, as well as possibly a mixture of lithium formate, lithium oxalate, and lithium carbonate. This proposed mechanism for the reductive decomposition of FEC is mainly responsible for the capacity loss of the investigated NCM622/silicon-graphite pouch cells with the FEC-containing electrolyte after formation during following cycling.

Zusammenfassung

Für eine weitere, systematische Optimierung von Lithium-Ionen-Batterien, ist es entscheidend die elektrochemischen Prozesse in den Batteriezellen während ihres Betriebes zu verstehen. Allerdings sind die Prozesse, die zu Kapazitätsverlust und Zellalterung führen, noch nicht vollständig aufgeklärt. Zellalterung und Kapazitätsverlust gehen einher mit einer Zersetzung des Elektrolyten zu gasförmigen Produkten und festen Produkten, die Oberflächenschichten auf den Elektroden bilden. Infolgedessen nimmt die Elektrolytmenge in Batteriezellen während Formierung und anschließender Zyklierung ab. Somit gewährt die konventionelle Bestimmung von Mengenverhältnissen oder Konzentrationen von Elektrolytbestandteilen keinen zuverlässigen Einblick in die tatsächlichen Verbräuche der Elektrolytkomponenten durch die elektrochemischen Zersetzungen. Zu diesem Zweck müssen die absoluten, verbrauchten Mengen der Elektrolytkomponenten direkt bestimmt werden. Allerdings können nur die Konzentrationen und nicht die absoluten, verbrauchten Mengen der Elektrolytkomponenten bestimmt werden bei Verwendung konventioneller Methoden zur Elektrolytextraktion (einfache Elektrolytextraktion). Im Rahmen dieser Doktorarbeit wird eine neue Methode zur Elektrolytextraktion aus Pouchzellen durch Injektion des Verdünnungsmittels Diethylcarbonat (DEC) vorgestellt, welche die Bestimmung dieser absoluten Verbräuche der Elektrolytkomponenten ermöglicht. Die Zusammensetzungen der analysierten Elektrolyte werden bestimmt durch Hochleistungsflüssigkeitschromatographie (HPLC), welche an ein Massenspektrometer mit Elektrosprayionisation (ESI/MS) und ein UV/Vis-Detektor gekoppelt ist. Zunächst werden HPLC-Methoden entwickelt, um die Konzentrationen der Elektrolytbestandteile in nicht extrahierten, frischen Elektrolyten so genau wie möglich zu bestimmen. Anschließend wird Elektrolyt extrahiert aus elektrochemisch unbehandelten, frischen $LiNi_{1/3}Co_{1/3}Mn_{1/3}O_2$ (NCM111)/Graphit-Lithium-Ionen-Pouchzellen, die 1 M $LiPF_6$ in Ethylencarbonat (EC)/ Dimethylcarbonat (DMC) (im Verhältnis 1:1 nach Gewicht) mit 3 wt% Vinylencarbonat (VC) enthalten, wobei die neue Extraktionsmethode und die Zentrifugation (eine Standardmethode zur Elektrolytextraktion) verwendet werden. Die ermittelten Zusammensetzungen der Elektrolyte, die aus den elektrochemisch unbehandelten Zellen durch beide Methoden extrahiert werden, sind ähnlich, was die Eignung der neuen Extraktionsmethode bestätigt. Außerdem werden Elektrolyte extrahiert aus gleichartigen NCM111/Graphit-Pouchzellen nach Formierung, nach 25 Zyklen und nach 2000 Zyklen mittels der neuen Extraktionsmethode. Die extrahierten Elektrolyte werden quantitativ analysiert durch HPLC-UV/Vis und HPLC-ESI/MS unter Verwendung der entwickelten HPLC-Methoden. Anhand der gewonnenen Messdaten werden die Konzentrationen der Elektrolytkomponenten in diesen Elektrolyten bestimmt, genauso wie die Mengen der Elektrolytkomponenten, die während

Formierung und den darauffolgenden ungefähr 2000 Zyklen verbraucht wurden. Die verbrauchten Mengen oder Verbräuche der Komponenten offenbaren eine dominante EC-Zersetzung während Formierung und den 2000 Zyklen, neben einer gleichzeitigen, moderaten VC- und Salz-Zersetzung. Im Gegensatz dazu offenbaren die üblicherweise bestimmten Konzentrationen lediglich die VC-Zersetzung während Formierung und Langzeit-Zyklierung. Dieses Beispiel bestätigt, dass nur die absoluten Verbräuche und nicht die Konzentrationen die tatsächlichen Zersetzungen in Batterie-Elektrolyten offenbaren. Darüber hinaus werden die elektrochemischen Zersetzungen im Elektrolyten während Formierung und langfristiger Zyklierung in $LiNi_{0.6}Co_{0.2}Mn_{0.2}O_2$ (NCM622)/Graphit-Lithium-Ionen-Pouchzellen, die 1 M $LiPF_6$ in EC/DMC (im Verhältnis 1:1 nach Gewicht) mit 3 wt% VC enthalten, durch HPLC-UV/Vis und HPLC-ESI/MS untersucht. Zu diesem Zweck wird der Elektrolyt aus diesen Zellen extrahiert durch die entwickelte Extraktionsmethode bei ausgewählten Alterungsstufen, und zwar vor Formierung, nach Formierung, nach 25 Zyklen, sowie nach Zyklierung bis zu einer Restkapazität von 95%, 90% und 80%. Röntgenphotoelektronenspektroskopie (XPS), Gaschromatographie gekoppelt mit einem Wärmeleitfähigkeitsdetektor (GC-TCD), Rasterelektronenmikroskopie (SEM), energiedispersive Röntgenspektroskopie (EDX) und optische Emissionsspektrometrie mit induktiv gekoppeltem Plasma (ICP-OES) werden als komplementäre Analysemethoden angewandt, um tieferen Einblick in die Mechanismen zu gewinnen, die verantwortlich sind für Elektrolytverbrauch, SEI (solid electrolyte interphase) Wachstum und Kapazitätsverlust. Zwei Phasen der elektrochemischen Alterung (Phase I und Phase II) können identifiziert werden: In Phase I, während Formierung und den darauffolgenden, ersten 25 Zyklen, wird eine ausschließliche Zersetzung von EC und VC jeweils in ähnlichem Ausmaß beobachtet, was zum Aufbau einer dünnen SEI insbesondere an den Graphit-Partikel-Kanten führt. Eine unvollständige Anoden-Passivierung aufgrund einer dünnen und unfertigen SEI ist der identifizierte, entscheidende Auslöser für die Elektrolytzersetzung, den damit verbundenen SEI-Aufbau und den Kapazitätsverlust in Phase I. In Phase II, vom 26. Zyklus bis zum ungefähr 800. Zyklus, wird eine nicht bevorzugte Zersetzung aller Elektrolytbestandteile festgestellt, das heißt jede Komponente wird gemäß ihrer Häufigkeit zersetzt. Gleichzeitig wird das Wachstum einer dicken SEI an Kanten und Basalflächen der Graphit-Partikel beobachtet. Außerdem wird ein linearer Anstieg der Mangan-Mengen in den Anoden mit der Zyklenzahl nachgewiesen. Aus den erzielten Ergebnissen wird geschlussfolgert, dass der Elektrolytverbrauch, das damit verbundene SEI-Wachstum und der Kapazitätsverlust hervorgerufen werden durch zwei Auslöser in Phase II: Zum Ersten, gibt es die kontinuierliche Ansammlung von Mangan in der SEI, was die Anoden-Passivierung verschlechtert, sodass Elektrolytzersetzung, SEI-Wachstum und Kapazitätsverlust beschleunigt werden. Zum Zweiten, führt Rissbildung in den Graphit-Partikeln durch Volumenänderungen während Delithiierung/Lithiierung zur Erzeugung neuer, elektrochemisch aktiver Oberfläche, was zu Aufbau neuer SEI, Elektrolytreduktion und

Kapazitätsverlust führt. Schließlich werden die elektrochemischen Zersetzungsprozesse in NCM622/Silizium-Graphit-Lithium-Ionen-Pouchzellen, die entweder 1 M $LiPF_6$ in VC/DMC (im Verhältnis 1:1 nach Gewicht) oder 1 M $LiPF_6$ in Fluorethylencarbonat (FEC)/DMC (im Verhältnis 1:1 nach Gewicht) enthalten, während Formierung und anschließender Zyklierung untersucht. Die untersuchten Elektrolyte werden mithilfe der neu entwickelten Extraktionsmethode aus diesen Zellen vor Formierung, nach Formierung, nach 15 Zyklen und nach 40 Zyklen extrahiert. HPLC-UV/Vis, HPLC-ESI/MS und Gaschromatographie gekoppelt mit einem Flammenionisationsdetektor (GC-FID) werden eingesetzt für die Quantifizierung der Elektrolytbestandteile. Um umfassenden Einblick in die Mechanismen zu gewinnen, die verantwortlich sind für den Kapazitätsverlust, werden zusätzlich GC-TCD, XPS, SEM, EDX und ICP-OES eingesetzt. Im Vergleich zu den Zellen mit dem FEC-haltigen Elektrolyten, haben die Zellen mit dem VC-haltigen Elektrolyten niedrigere, anfängliche Entladekapazitäten aufgrund von ausgeprägteren Kapazitätsverlusten während Formierung. Allerdings ist der Kapazitätsverlust der Zellen mit dem VC-haltigen Elektrolyten langsamer während anschließender Zyklierung, sodass die Entladekapazitäten der Zellen mit dem VC-haltigen Elektrolyten höher sind als jene der Zellen mit dem FEC-haltigen Elektrolyten nach 20 bis 30 Zyklen. Aus den erzielten Ergebnissen kann geschlussfolgert werden, dass die Kapazitätsverluste der NCM622/Silizium-Graphit-Pouchzellen mit dem VC-haltigen Elektrolyten und dem FEC-haltigen Elektrolyten (fast) ausschließlich ausgelöst werden durch irreversible Bindung von zyklierbarem Lithium in der SEI und irreversible Bindung von zyklierbarem Lithium in irreversibel lithiiertem Silizium und Siliziumoxid unter der SEI während des ersten Zyklus‘ des Formierungsprogramms. Die Kapazitätsverluste der NCM622/Silizium-Graphit-Pouchzellen mit dem VC-haltigen Elektrolyten und dem FEC-haltigen Elektrolyten nach dem ersten Zyklus des Formierungsprogramms während den nachfolgenden Zyklen werden (fast) ausschließlich verursacht durch irreversible Bindung von zyklierbarem Lithium in der SEI. VC wird bevorzugt zersetzt in den untersuchten Zellen mit dem VC-haltigen Elektrolyten während Formierung und den darauffolgenden 40 Zyklen. Gleichzeitig kann eine leichte DMC-Zersetzung in den Zellen mit dem VC-haltigen Elektrolyten beobachtet werden. Die Ergebnisse der Analysen deuten darauf hin, dass die reduktive Zersetzung eines VC-Moleküls an der Anode zum Verbrauch eines Lithium-Ions und eines Elektrons führt. Infolgedessen lagert sich lithiumhaltiges, polymerisiertes VC (poly(VC)) auf den Anoden ab, welches der Hauptbestandteil der SEI nach Formierung und anschließender Zyklierung in den Zellen mit dem VC-haltigen Elektrolyten ist. Dieser vorgeschlagene Mechanismus für die reduktive Zersetzung von VC ist fast ausschließlich verantwortlich für den Kapazitätsverlust der untersuchten NCM622/Silizium-Graphit-Pouchzellen mit dem VC-haltigen Elektrolyten nach Formierung während anschließender Zyklierung. FEC wird exklusiv zersetzt während Formierung und den anschließenden 40 Zyklen in den untersuchten Zellen mit dem FEC-haltigen Elektrolyten. Die Ergebnisse der Untersuchungen deuten darauf hin, dass die reduktive Zersetzung

eines FEC-Moleküls an der Anode zum Verbrauch von drei Lithium-Ionen und drei Elektronen führt. Die reduktive Zersetzung von FEC bringt schließlich die SEI-Komponenten LiF, einen vernetzten Polyethylenoxid (PEO)-artigen Polymer, sowie möglicherweise eine Mischung aus Lithiumformiat, Lithiumoxalat und Lithiumcarbonat hervor. Der vorgeschlagene Mechanismus für die reduktive Zersetzung von FEC ist größtenteils verantwortlich für den Kapazitätsverlust der untersuchten NCM622/Silizium-Graphit-Pouchzellen mit dem FEC-haltigen Elektrolyten nach Formierung während anschließender Zyklierung.

Content

1 Introduction

1.1 Motivation

In 2021, 82.3% of the consumed primary energy was produced by the combustion of oil, natural gas, and coal [1], which is associated with the release of CO_2. The accumulation of CO_2 in the atmosphere leads to global warming, one of the most existential problems of our times. Renewables are a key to solve this problem. To ensure the supply with energy from renewables, suitable energy storages are necessary. Electrochemical energy storages, like lithium-ion batteries (LIBs), can fulfill the requirements due to their high energy and power density [2]. Besides, LIBs are applied in portable devices and electric vehicles [2]. Especially for the application in electric vehicles, the lithium-ion battery cells need to be further optimized with respect to energy density, power density, production costs, safety, and environmental sustainability. For a systematic optimization of LIBs, a comprehensive understanding of the electrochemical processes in the lithium-ion battery cells during operation is of crucial importance. Nowadays, a typical, commercially used lithium-ion cell is comprised of a graphitic carbon anode, a layered transition metal oxide cathode, a separator, and a liquid electrolyte [3]. The electrolyte is a key component of the cell, as it is in contact with all cell components. It is generally known that surface layers on the electrodes especially the solid electrolyte interphase (SEI) on the anode are formed during cycling accompanied by electrolyte consumption. The resulting, continuous reduction of the electrolyte amount is one reason, why the usual determination of concentrations of the electrolyte components do not enable a reliable identification of the dominating decompositions in the electrolyte. Quantitative analyses of battery electrolytes are usually limited to the determination of concentrations of the electrolyte components. Indeed, concentrations are quantity ratios that do not contain information about the absolute magnitude of the decompositions in the electrolyte from battery cells. Instead, the absolute, consumed amounts of the electrolyte components during cell aging need to be determined. These consumptions indicate the absolute magnitudes of the different decompositions in the electrolyte from battery cells. The electrochemical decompositions in the electrolyte are accompanied by SEI buildup on the anodes and capacity loss of the cell. The consumptions of the electrolyte components reveal thus not only the magnitude of the decompositions in the electrolyte, but also important information about the decomposition mechanism that are responsible for the capacity loss of the cell. The motivation of this thesis is to

develop a method for the determination of the absolute consumptions of the electrolyte components in battery cells during cell aging. Another motivation of this work is to investigate the electrochemical decomposition of electrolytes in different pouch cells by determining the consumptions of the electrolyte components during formation and subsequent cycling. Complementary analysis methods are used to further support the findings of the electrolyte analyses and clarify the processes that are eventually responsible for the capacity losses of the investigated pouch cells.

1.2 Scope of work

The investigation of the electrochemical decomposition of electrolytes in lithium-ion pouch cells with different cell chemistries is the primary aim of the present thesis. Besides, the electrochemical aging of the electrodes and the electrochemically formed gases from the examined pouch cells are analyzed. Thereby, the mechanisms responsible for the capacity losses of the examined pouch cells during formation and subsequent cycling are eventually clarified. The different tasks of the present thesis are listed in the following.

In the first part of this thesis, high-performance liquid chromatography (HPLC) methods are developed to determine the concentrations of the electrolyte components in non-extracted, fresh electrolytes as accurately as possible. Subsequently, a new method for electrolyte extraction from battery cells by injection of a diluent is developed. The new extraction method and the subsequent analyses of the extracted electrolytes eventually allow for a determination of the absolute consumptions of the electrolyte components during cell aging. Electrolytes are extracted from electrochemically untreated, fresh $LiNi_{1/3}Co_{1/3}Mn_{1/3}O_2$ (NCM111)/graphite lithium-ion pouch cells containing 1 M $LiPF_6$ in ethylene carbonate (EC)/dimethyl carbonate (DMC) 1:1 by weight with 3 wt% vinylene carbonate (VC) using the new electrolyte extraction method by injection and the electrolyte extraction by centrifugation (a standard method). The extracted electrolytes are quantitatively analyzed using the developed HPLC methods. Thereby, the suitability of the new extraction method is confirmed. Subsequently, the electrolytes are extracted from equal NCM111/graphite lithium-ion pouch cells after formation, after 25 cycles, and after about 2000 cycles by means of the new electrolyte extraction method. These extracted electrolytes are also quantitatively analyzed using the developed HPLC methods. Based on the results from these electrolyte analyses, the concentrations of the electrolyte components and the consumptions of the electrolyte components during formation and the subsequent about 2000 cycles in the NCM111/graphite pouch cells are determined. The results from this investigation highlight the necessity of the consideration of the absolute consumptions for an enlightenment of the electrochemical decomposition processes in the cell.

In the second part of this thesis, the method for the determination of the absolute consumptions is applied for the investigation of the electrochemical decomposition of the electrolyte in $LiNi_{0.6}Co_{0.2}Mn_{0.2}O_2$ (NCM622)/graphite lithium-ion pouch cells containing 1 M $LiPF_6$ in EC/DMC 1:1 by weight with 3 wt% vinylene carbonate (VC). These electrolyte analyses are supplemented with analyses of the electrodes by X-ray photoelectron spectroscopy (XPS), scanning electron microscopy (SEM), energy-dispersive X-ray spectroscopy (EDX), and inductively coupled plasma optical emission spectrometry (ICP-OES), as well as analyses of the evolved gases by gas chromatography (GC). The electrolyte, the evolved gases, and the electrodes are investigated in different stages of electrochemical aging, namely before formation, after formation, after 25 cycles, as well as after cycling until a remaining capacity of 95%, 90%, and 80%. The results from these investigations reveal that the electrolyte decomposition during formation and short-term cycling is completely different from the electrolyte decomposition during long-term cycling. Additionally, the main triggers for the capacity losses during formation plus short-term cycling on the one hand and long-term cycling on the other hand are identified.

In the third part of this thesis, the method for the determination of the absolute consumptions is used for the investigation of the electrochemical decomposition of the electrolyte in NCM622/silicon-graphite lithium-ion pouch cells. For these investigations suitable electrolytes need to be found that enable optimal cycle-life of these cells first. The electrolytes 1 M $LiPF_6$ in VC/DMC 1:1 by weight and 1 M $LiPF_6$ in fluoroethylene carbonate (FEC)/DMC 1:1 by weight allow the best capacity retention during cycling. Hence, these two electrolytes are selected as the initial electrolytes of the examined NCM622/silicon-graphite pouch cells. To gain deeper insight into the decomposition mechanisms in these cells, the evolved gases are quantitatively analyzed by GC, while the electrodes are investigated by XPS, SEM, EDX, and ICP-OES. The electrolyte, the evolved gases, and the electrodes are examined before formation, after formation, after 15 cycles, and after 40 cycles. Based on the results from these investigations, mechanisms for the reductive decomposition of VC and FEC in lithium-ion batteries can be proposed. The reductive decomposition of VC and FEC, and the associated consumption of cycleable lithium-ions is the main trigger for the capacity losses of the examined NCM622/silicon-graphite pouch cells.

2 Basics

2.1 Lithium-ion battery cells

Rechargeable batteries are energy storages that can reversibly convert electrical energy into chemical energy during charging and reconvert chemical energy into electrical energy during discharging. Especially for the application in portable electronics and electric vehicles, batteries with high energy and power densities are needed. Lithium-based batteries offer high energy and power densities due to the following reasons: Firstly, lithium has the lowest reduction potential among all elements, so that lithium-based batteries have the highest possible cell potential [2]. Secondly, lithium is the third lightest element and has one of the smallest ionic radii of any single charged ion [2]. A lithium-based battery consists of lithium-based battery cells that are composed of several components. A schematic illustration of a rechargeable, lithium-based battery cell, in this case a $LiCoO_2$/graphite lithium-ion cell, can be seen in Figure 2.1.

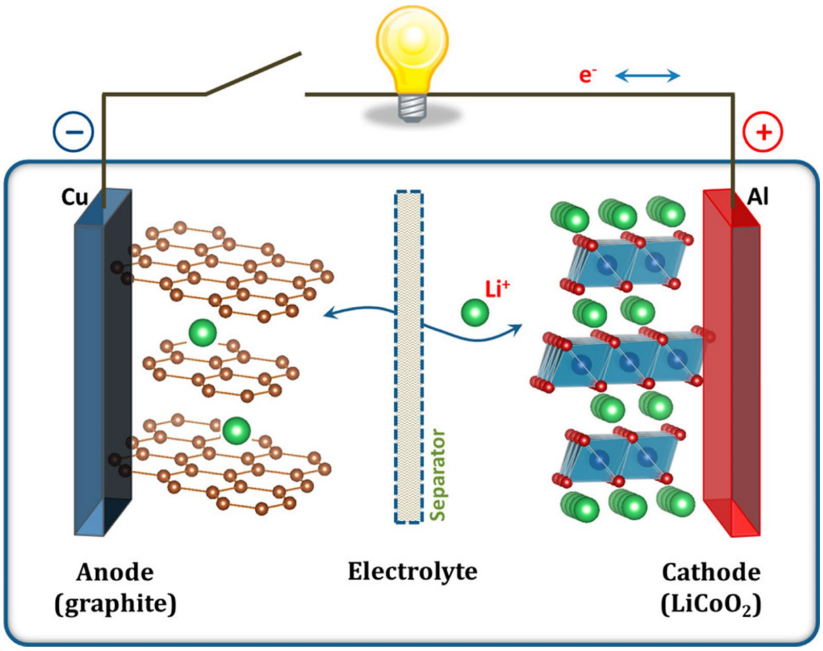

Figure 2.1: Schematic illustration of a rechargeable, lithium-ion battery cell. In this case, the anode active material is graphite, while the cathode active material is $LiCoO_2$. In addition, the current collector consists of copper (Cu) on the anode side and aluminum (Al) on the cathode side. Reprinted with permission from [4]. Copyright (2013) American Chemical Society.

The usual lithium-based battery cell consists of two electrodes, namely the anode and the cathode, which are soaked with liquid electrolyte. These electrodes each consist of a current collector and a coating that contains the active material. The anode and the cathode have different potentials. The difference between the anode potential and the cathode potential is the cell voltage. Cathode and anode are electronically isolated from each other by a separator that is placed between both electrodes in the cell. The separator is also soaked with the liquid electrolyte. The liquid electrolyte serves as a lithium-ion conductor, and the separator is permeable for the ions in the electrolyte. As a result, charge transport by lithium-ions, but not by electrons is possible between both electrodes. The electrons can only reach the opposite electrode via the current collectors through an external circuit. The electrodes, the separator, and the electrolyte are located inside the tight casing of the cell. In common, rechargeable lithium-ion battery cells, lithium-ions are deintercalated from the cathode active material and intercalated into the anode active material during charging [5]. For each transferred lithium-ion during charging, one electron is transferred from the cathode to the anode via the external circuit. Electrical energy needs to be invested for this electron transfer, as the anode and the cathode have different potentials. Accordingly, lithium-ions are deintercalated from the anode active material and intercalated into the cathode active material during discharging [5]. For each transferred lithium-ion during discharging, one electron is transferred from the anode to the cathode via the external circuit. Due to the different potentials of anode and cathode, electrical energy is released by this electron transfer during discharging, which can be used for the energy supply of a consumer. These processes are highly reversible, so that a rechargeable, lithium-based battery cell can be charged and discharged for thousands of cycles. The first commercially available, rechargeable, lithium-ion battery with the cathode active material $LiCoO_2$ (LCO) and the anode active material carbon was launched by Sony Corporation in 1991 [6,7]. The anode materials, the cathode materials, and the electrolytes from the lithium-ion cells that are investigated in this thesis are described in the following subsections. Furthermore, the SEI and the most important aging mechanisms in lithium-ion cells are described.

2.1.1 Electrodes

An electrode from a common, rechargeable lithium-ion battery cell consists of a current collector and its coating. The current collector of the anode is usually a copper foil, while the current collector of the cathode is typically an aluminum foil. The electrode coating consists of the active material, the conductive additive, and a binder. Active materials reversibly store the lithium-ions in the electrode. Conductive additives, such as carbon black, ensure the electronic contact between the active material and the current collector. Binders, such as polyvinylidene fluoride (PVDF) or sodium carboxymethylcellulose (NaCMC) in combination with styrene-butadiene rubber (SBR), enable the

adhesion of the electrode coating on the current collector, as well as the cohesion within the electrode coating.

To develop lithium-based battery cells with maximum energy density, anode active materials should have a low potential versus metallic lithium (vs. Li/Li^+), so that a high cell voltage and thus a high energy density of the cell is achieved. Apart from that, anode active materials should also have a high specific capacity to allow a high cell capacity and thus also a high energy density of the cell. Lithium metal would be an optimal anode material in terms of energy density of the cell since it has a high specific capacity of about 3860 $mAh \cdot g^{-1}$ [8,9] and a low potential vs. Li/Li^+ of 0 V. Indeed, rechargeable batteries with lithium metal anodes have not yet been commercialized, as lithium forms needle-like deposits called dendrites on the anode [8]. These dendrites can create short circuits in the battery cell, which eventually is a safety hazard [8–10]. These problems are mainly eliminated by the use of intercalation materials as anode active materials, such as carbon or graphite, instead of lithium metal. Nowadays, graphite is a commonly used anode active material in commercial lithium-ion battery cells. The lithium-ions can be reversibly intercalated between the graphene planes of graphite [2]. Up to one lithium-ion per 6 carbon atoms can be stored in this way [2]. Graphite has several advantages, such as low cost, abundant availability, high lithium-ion diffusivity, and high electrical conductivity [2]. Furthermore, graphite enables a high cycle-life of the cells [2]. Additionally, graphite has low delithiation potentials at about 0.1 V-0.23 V vs. Li/Li^+ [2], which allows a high cell voltage and thus a high energy density of the cell. Nevertheless, the theoretical, specific capacity of graphite is only 372 $mAh \cdot g^{-1}$ [2,11,12]. Graphite is used as anode active material in pouch cells that are investigated in the present thesis, because it is still the anode material of choice for commercial lithium-ion battery cells [2]. Silicon is an anode active material that offers a very high, theoretical, specific capacity of about 3600 $mAh \cdot g^{-1}$ (regarding the phase $Li_{15}Si_4$ [13–15]). In addition, silicon has low delithiation potentials of about 0.31 V vs. Li/Li^+ and 0.47 V vs. Li/Li^+ [2]. Furthermore, silicon is very abundant and therefore rather inexpensive [2]. Hence, silicon as anode active material is a promising anode active material especially in terms of energy density of the cell. Silicon can electrochemically alloy and form compound phases with lithium [2], such as $Li_{15}Si_4$. Indeed, the lithiation of silicon is accompanied by a massive volume increase of up to 320%, which leads to severe volume changes of the silicon particles during cycling [16]. Consequently, new, electrochemically active surface is continuously created during cycling, which leads to rapid, irreversible capacity loss, continuous SEI formation, and enhanced electrolyte decomposition [17]. To overcome this problem, silicon combined with graphite is used as anode active material in lithium-ion cells. Thereby, the energy density of the cell is enhanced, while the cycle-life of the cell is still sufficient. The use of silicon combined with graphite as anode active material is an attractive possibility to boost the energy density of future, commercial lithium-ion battery cells. For

this reason, silicon combined with graphite is used as anode active material in pouch cells that are examined in the present thesis.

For the development of lithium-based battery cells with maximum energy density, cathode active materials should have a high potential versus metallic lithium (vs. Li/Li^+) to eventually enable a high cell voltage and thus a high energy density of the cell. Additionally, cathode active materials should have a high specific capacity to allow a high cell capacity and thus also a high energy density of the cell. Layered transition metal oxides, such as LCO or $LiNi_xCo_yMn_zO_2$ (NCM), are commonly used as cathode active material in commercial lithium-ion battery cells. LCO is the most commercially successful type of layered transition metal oxide cathodes [2] and was used as cathode active material in the first commercially available, rechargeable, lithium-ion battery from Sony Corporation [6,7]. LCO has a specific capacity of 140 $mAh \cdot g^{-1}$ and enables a high average cell voltage of around 3.7 V [18]. However, LCO has several disadvantages, such as high costs, low thermal stability, and fast capacity fade at high currents [2]. Compared to LCO, NCM has similar or higher, achievable, specific capacities, similar operating voltages, and lower costs due to the lower cobalt content [2]. There are different types of NCM, like NCM111, NCM622, and $LiNi_{0.8}Co_{0.1}Mn_{0.1}O_2$ (NCM811). A higher nickel content in NCM enables a higher lithium extraction from the cathode during charging of the cell without structure deterioration leading to an enhanced specific capacity and thus to an enhanced energy density of the cell [2]. The specific capacity of NCM111 and NCM811 is 160 $mAh \cdot g^{-1}$ and 220 $mAh \cdot g^{-1}$, respectively [18]. Currently, NCM is a state-of-the-art cathode material for commercial applications [18]. For this reason, NCM111 and NCM622 are used as cathode active materials in the pouch cells that are investigated in the present thesis.

2.1.2 Electrolytes

In a lithium-ion battery cell, the electrolyte primarily serves as a lithium-ion conductor that enables the transport of lithium-ions from one electrode to the other. For this purpose, the electrolyte should have a high ionic conductivity, as well as a high chemical and electrochemical stability [19,20]. In addition, the electrolyte should allow for a wide operational temperature range and a safe operation of the battery cell [19–22]. Furthermore, the electrolyte should be nontoxic and economical [20–22]. Most of the liquid electrolytes in commercial lithium-ion cells are nonaqueous solutions, in which about 1 M $LiPF_6$ is dissolved in a mixture of cyclic carbonates, such as EC, and linear carbonates, such as DMC, ethyl methyl carbonate (EMC), or diethyl carbonate (DEC) [19]. The structural formulas of $LiPF_6$ and the mentioned carbonates are shown in Figure 2.2. The mentioned linear carbonates have low viscosities, so that a facile ion transport and thus a high ionic conductivity of the electrolyte is enabled [23]. The cyclic carbonate EC has a high dielectric constant (ε_r), so that a strong dissociation

of $LiPF_6$ is ensured, which is also beneficial for a high ionic conductivity of the electrolyte [23]. The conducting salt $LiPF_6$ is used almost exclusively in commercial lithium-ion battery cells since the electrolytes with dissolved $LiPF_6$ have exceptionally high ionic conductivities [19]. Furthermore, $LiPF_6$-based electrolytes react to form a stable interface with the aluminum current collector at high potentials [19] preventing the corrosion of the aluminum.

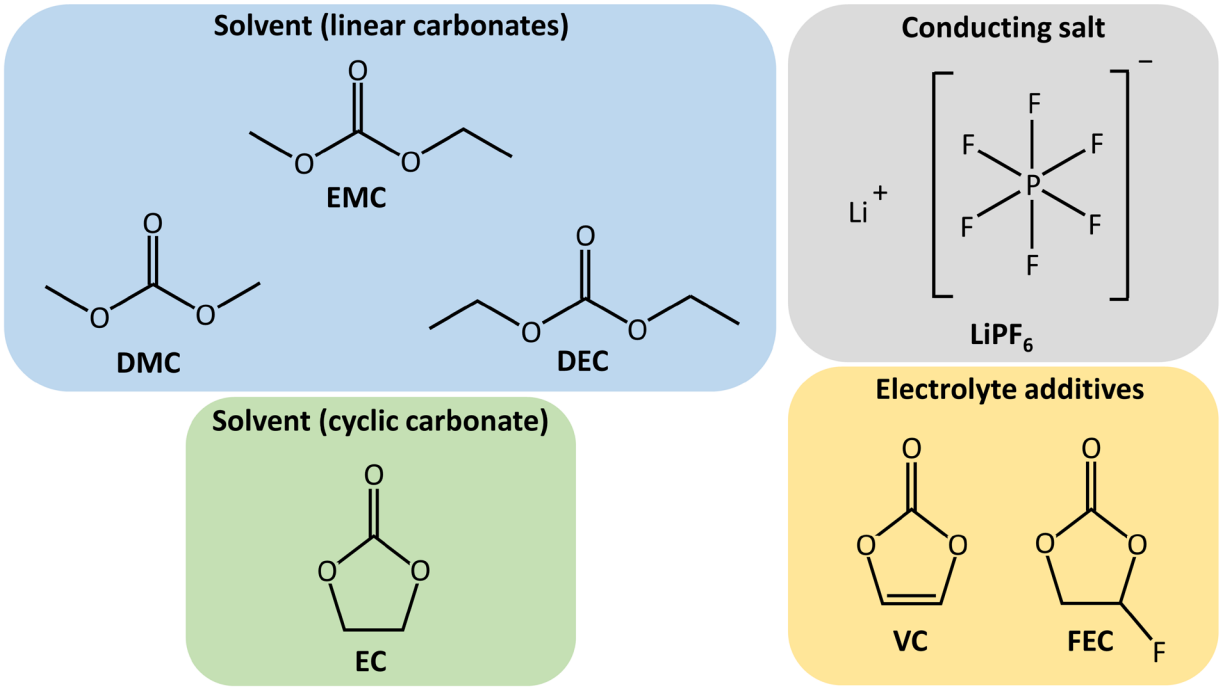

Figure 2.2: Structural formulas of commonly used electrolyte components for lithium-ion battery cells. Based on [19].

Apart from that, electrolyte additives are added to the electrolytes from lithium-ion cells to improve the properties of the SEI, the ionic conductivity of the electrolyte, or the safety of the battery cell among others [24]. In the following, only the electrolyte additives that are used for the investigations in the present thesis are described. The SEI-forming additive VC is one of the most used electrolyte additives for lithium-ion battery cells [3]. VC is preferentially reduced at the anode in lithium-ion cells during cycling [3]. The reductive decomposition of VC mainly leads to the formation of polymerized VC (poly(VC)) that contributes to the SEI growth [25]. The resulting, VC-derived SEI on the anode is more cohesive and flexible than the SEI formed in cells with VC-free electrolytes, so that a better anode passivation and thus a better performance of the battery cell is enabled [26]. Apart from VC, the SEI-forming additive FEC is the most commonly used additive in lithium-ion battery cells with silicon-containing anodes [24]. FEC is preferentially decomposed at the anode during cycling to SEI components, such as LiF [27] and poly(VC) [28]. The FEC-derived SEI has a high stability, which improves the capacity retention of lithium-ion cells with silicon-containing anodes [27]. Furthermore, the FEC-derived SEI offers a high conductivity for lithium-ions, which favors a low resistance of the lithium-ion

battery cell [29]. The structural formulas of VC and FEC can be seen in Figure 2.2. Formation and growth of the SEI is described in more detail in subsection 2.1.3.

2.1.3 Solid electrolyte interphase (SEI)

It is generally known that anodes from lithium-ion battery cells operate at potentials that are outside the electrochemical stability window of the electrolyte components [30]. As a result, the electrolyte components are reductively decomposed at low electrode potentials during charging or lithiation of the concerning electrode, which is associated with irreversible consumption of lithium-ions [30]. The decomposition products form a passivation layer on the concerning electrode (usually the anode), which is called the SEI [30]. In theory, the SEI is an electronically isolating and ionically conducting surface layer [31]. An ideal SEI is permeable for lithium-ions, but impermeable for electrons and other electrolyte components [30]. The SEI buildup occurs mainly at the beginning of cycling, especially during the first cycle [30]. The SEI inhibits further electrolyte reduction after its buildup [30]. Indeed, electrolyte decomposition is not completely prevented after the first cycle during subsequent cycling [30]. As a result, further, slight electrolyte decomposition and slight SEI growth continue after the first cycle throughout the entire life of the lithium-ion cell [30]. Thus, the SEI formation and growth admittedly consume cycleable lithium, which leads to capacity losses of the lithium-ion cells during cycling [32]. Indeed, the SEI restricts further reduction of the electrolyte, which is vital for the chemical and electrochemical stability of the lithium-ion cell [32]. The commonly used solvents in the electrolyte (see Figure 2.2) and $LiPF_6$ are decomposed at the anode to SEI components, such as lithium alkyl carbonates ($ROCO_2Li$) [33,34], lithium alkoxides (ROLi) [34,35], lithium carbonate (Li_2CO_3) [35], and LiF [33]. The reduction of these electrolyte components is also accompanied by the evolution of gases, such as ethylene (C_2H_4) [34,35], methane (CH_4) [34,35], or carbon monoxide (CO) [34,35]. The SEI-forming additive VC is preferentially reduced at the anode during cycling in lithium-ion cells, so that the SEI component poly(VC) is deposited on the anode [25]. The resulting, VC-derived SEI is more flexible and cohesive, so that it provides a better anode passivation than the SEI that is formed in cells without SEI-forming additives [26]. As a result, the irreversible capacity is reduced and the cycling behavior at elevated temperature is improved [26]. The SEI-forming additive FEC is preferentially reduced at the anode during cycling in lithium-ion cells yielding SEI components, such as LiF [27] and poly(VC) [28]. The FEC-derived SEI has a high stability, which enhances the capacity retention of lithium-ion cells with silicon-containing electrodes [27]. Additionally, the FEC-derived SEI has a high conductivity for lithium-ions, which is also a desirable property for an SEI [29]. The SEI continues to grow after its buildup during cycling since the de-/lithiation of the anode active material is associated with volume changes that lead to cracks in the SEI [17]. As a result, new, electrochemically active surface is created, which leads to further electrolyte reduction, buildup of new SEI material, and

irreversible capacity losses [17]. To minimize this SEI growth and the associated capacity losses during cycling, the SEI should also be flexible, so that it can adapt to the volume changes of the anode active material without cracking. The SEI flexibility is important especially for lithium-ion cells with silicon-containing electrodes because of the massive volume changes of silicon during de-/lithiation (see subsection 2.1.1). It is generally known that VC and FEC form a flexible SEI, which can adapt to the large volume changes of silicon during cycling [29]. For this reason, VC and FEC are the most commonly used additives in lithium-ion cells with silicon-containing electrodes [24]. Another trigger for SEI growth and associated capacity loss of lithium-ion cells with transition metal oxide cathodes is the contamination of the SEI with transition metals, especially manganese [36]. Transition metal ions from the cathode dissolve, migrate through the electrolyte to the anode, and deposit in the SEI [37]. The transition metals in the SEI deteriorate the passivating properties of the SEI [38]. As a result, electrolyte reduction, associated SEI growth, and irreversible capacity losses are accelerated [36,38].

2.2 High-performance liquid chromatography (HPLC)

In general, HPLC coupled with detectors is a suitable analysis method to separate, identify, and quantify components of a mixed liquid or a solution. HPLC is also valuable for the investigation of electrolytes from lithium-ion battery cells [39]. HPLC is coupled to detectors, such as an electrospray ionization mass spectrometer (ESI/MS) and an ultraviolet/visible light (UV/Vis) detector. HPLC-UV/Vis and HPLC-ESI/MS enable a quantification of commonly used electrolyte components for lithium-ion battery cells (see Figure 2.2) [40]. A schematic illustration of the HPLC system used for the investigations of the present thesis is shown in Figure 2.3. The used HPLC system includes the following, important components: Vessels with the two solvents, a solvent degasser, pumps, a sample injector, a column, a photodiode array (PDA) detector, an ESI/MS, and a computer.

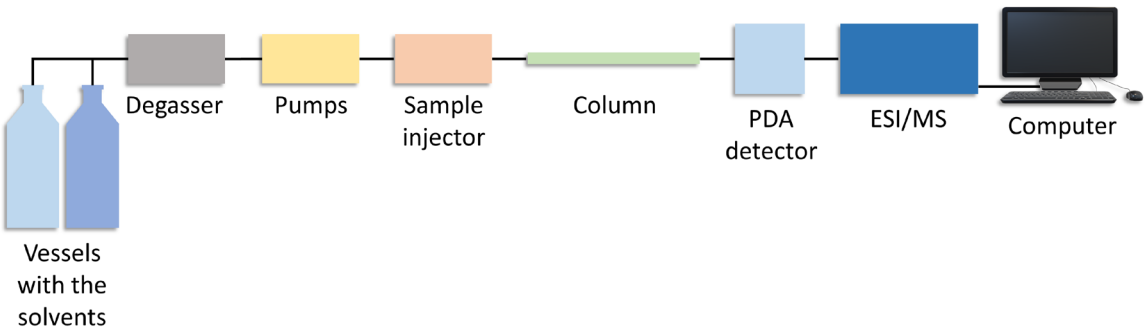

Figure 2.3: Schematic illustration of the HPLC system used for the analyses of the present thesis.

The two solvents (or eluents) are sucked out of the two vessels and pass through the degasser (see Figure 2.3), in which gas is removed from the solvents. For the HPLC analyses of the present thesis, pure water or water with added formic acid on the one hand and pure acetonitrile (ACN) on the other hand were used as solvents. The two degassed solvents are subsequently mixed in a given ratio and pumped through the column by the pumps with a given volumetric flow rate. The mixed solvents are also called the mobile phase. A given volume of the sample to be analyzed (the injection volume) is injected into the mobile phase by the sample injector. The injected sample moves through the column together with the mobile phase. In the column, the components of the sample (the analytes) are separated. The separation is based on the adsorption of the analytes on the column material [41]. The components of the column that interact with the analytes represent the so-called stationary phase. The intensity of the interaction of the analyte with the stationary phase depends on the analyte. As a result, the analytes need a specific time to pass through the column. An analyte with a weak affinity to the stationary phase reaches the column exit relatively fast. An analyte with a strong affinity to the stationary phase needs more time to pass through the column [41]. After the analytes have passed through the column, they are detected by the detectors. The detectors continuously measure the signal intensity and transmit the measurement data to the computer. The computer plots the acquired signal intensity against the time elapsed since sample injection. This plot is called the chromatogram. When a detectable analyte reaches the detector, the measured signal intensity reaches a maximum, so that a peak appears in the chromatogram at a retention time that is characteristic for the detected analyte. The retention time corresponds to the time that an analyte needs to pass through the column and reach the detector. The HPLC detectors used for analyses of the present thesis were a PDA detector (a type of UV/Vis detector) and an ESI/MS (see Figure 2.3). For this reason, only these detectors are described in more detail in the following. In the used HPLC system, the analytes first pass through the PDA detector and reach subsequently the ESI/MS (see Figure 2.3). The computer was used for the control of the HPLC system, the data acquisition, and the evaluation of the measurement data (see Figure 2.3).

The UV/Vis detector can detect analytes, which absorb visible light or ultraviolet light. The UV/Vis detector is suitable for the quantification of commonly used carbonates in electrolytes from lithium-ion battery cells (see Figure 2.2) [39,40]. The mobile phase with the analytes flow through the flow cell of the UV/Vis detector or PDA detector. Simultaneously, light in the visible and/or ultraviolet range pass through the flow cell, while the intensity of the transmitted light is determined by means of detectors. Based on the detected intensity of the transmitted light, the absorbance at one or several wavelengths of the light is determined. In the resulting chromatogram, the absorbance (or “absolute intensity”) at a specific wavelength is plotted against the time. If a conventional UV/Vis detector is used, the absorbance can only be recorded at a couple of given wavelengths at the same time. For the

present thesis, a PDA detector was used, which enables a determination of the absorbance over a wide wavelength range. Consequently, the absorbance spectrum can be measured at any point in time. As a result, the absorbance can be determined in dependence on the wavelength and the time. When a corresponding analyte exits the column and passes through the flow cell, the detector measures a short-term increase of the absorbance, so that the resulting chromatogram indicates an absorbance peak at the specific retention time. The area of this absorbance peak is approximately proportional to the concentration of the analyte in the sample for a certain concentration range. Hence, the concentration of the analyte in an electrolyte can eventually be determined based on peak areas. Chromatograms from a VC-containing, an EC-containing, a DMC-containing, and a DEC-containing sample can be seen in Figure 2.4. These chromatograms were recorded by means of HPLC coupled to a PDA detector at a selected wavelength of 190 nm. The peaks of VC, EC, DMC, and DEC appear at the different, specific retention times, as can be seen in Figure 2.4. In addition, the peak of ACN is visible in the chromatograms in Figure 2.4 since the analyzed samples also contained ACN. These shown chromatograms are measurement data that were acquired for the investigations described in section 4.1.

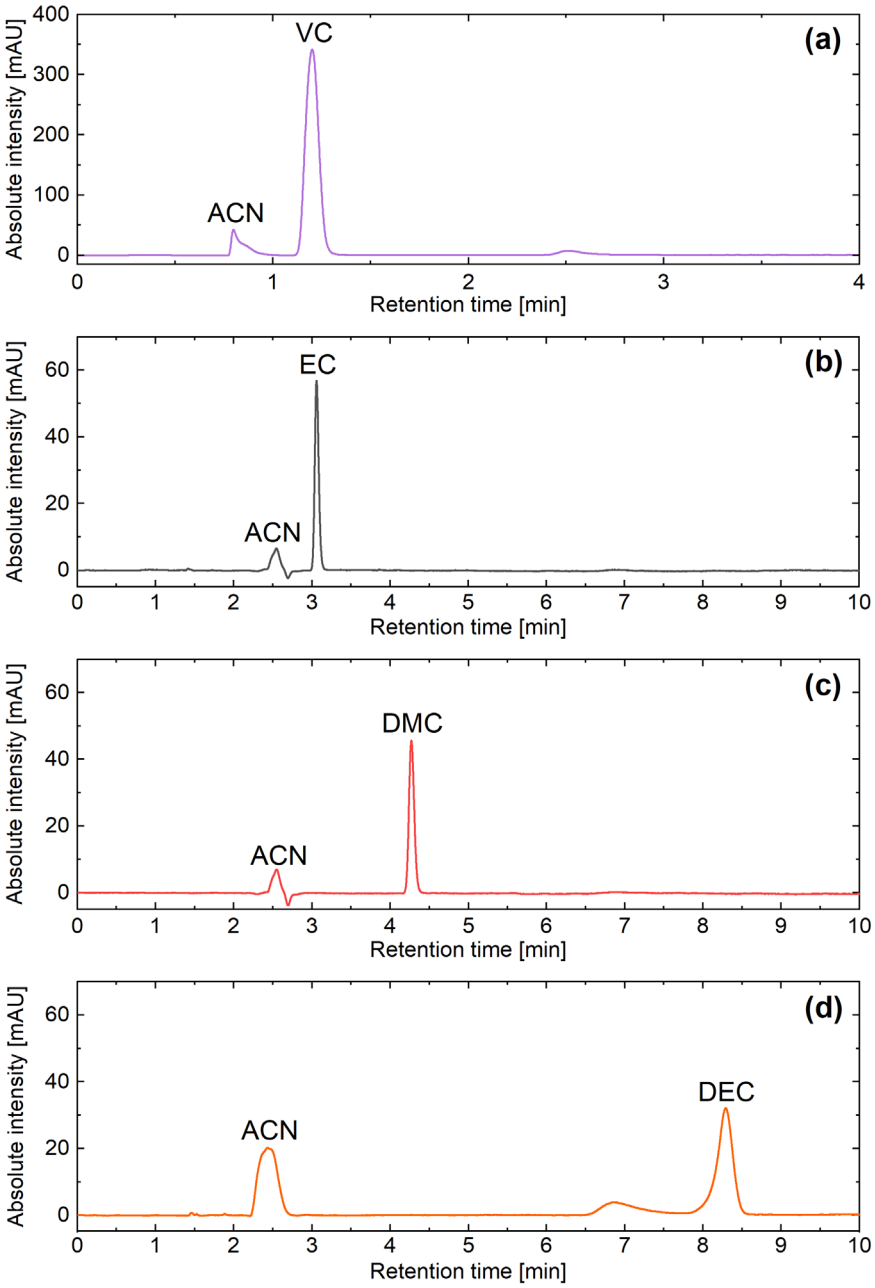

Figure 2.4: Chromatogram of a VC-containing sample (a), an EC-containing sample (b), a DMC-containing sample (c), and a DEC-containing sample (d) recorded by means of HPLC coupled to a PDA detector at a selected wavelength of 190 nm [40].

As the analytes are not destroyed by the PDA analyses, they can subsequently be analyzed by the ESI/MS (see Figure 2.3). The ESI/MS used for the analyses of the present thesis includes an electrospray ionization (ESI) source (as ion source), a desolvation line, a Qarray, an octopole, a quadrupole (as mass analyzer), and a detector. A schematic illustration of the used ESI/MS can be seen in Figure 2.5.

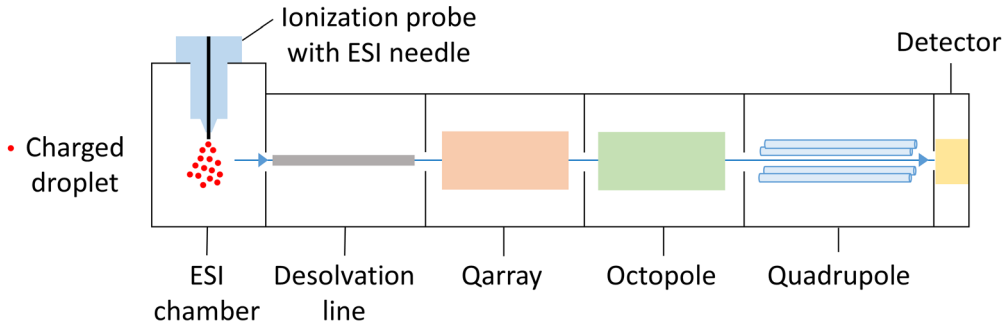

Figure 2.5: Schematic illustration of the ESI/MS used for the analyses of the present thesis.

The ESI/MS can detect analytes, which are ions or which are ionizable in an ESI source. The ESI/MS is suitable for the quantification of the ions from $LiPF_6$ [40], which is the common conducting salt in lithium-ion battery cells (see Figure 2.2). The mobile phase with the analytes is sprayed into the ESI chamber via a charged capillary needle (the ESI needle) by means of a nebulizing gas, as can be seen in Figure 2.5. The ESI needle is integrated into the ionization probe, as shown in Figure 2.5. A voltage of 2-3 kV is applied between the exit of the ESI chamber (counter electrode) and the tip of the ESI needle [42]. By the resulting electric field, a spray of charged droplets is formed at the tip of the ESI needle [42], as can be seen in Figure 2.5. These droplets are either positively or negatively charged depending on the sign of the applied voltage. Because of solvent evaporation, the volumes of these droplets decrease constantly, so that the charge density on its surfaces is continuously increased [43]. As a result, the repulsive, electrostatic force between the charge carriers in the droplet increase constantly. When the repulsive, electrostatic force exceeds the conservative force of surface tension, the droplet disintegrates into smaller subunits [43]. At the end of the ionization process, charged analyte ions are formed. Two mechanisms are currently discussed for the eventual formation of the gaseous analyte ions, namely the charged residue mechanism (CRM) and the ion evaporation mechanism (IEM) [42]. According to the CRM, the droplets are reduced until only one analyte molecule is present in the resulting microdroplets. Subsequently, one or more charges are added to the analyte molecule resulting in a charged analyte ion [42]. According to the IEM, the charged analyte ions are emitted from the droplets, when the radius of the droplets falls below a critical value [42]. To achieve a high ion yield and thus high signal intensities during the HPLC-ESI/MS measurements, charge carriers need to be added to the eluents [42]. For this reason, not pure water, but water with added formic acid was used as one of the two solvents for the HPLC-ESI/MS analyses of the present thesis. Note that an originally neutral analyte molecule is usually ionized in the ESI source by forming an adduct with an ion from the eluent, such as a hydrogen ion. The resulting, charged particles are accelerated by the electric field in the ESI chamber and can subsequently leave the ESI chamber, as can be seen in Figure 2.5. After exiting the ESI chamber, the charged particles pass through a desolvation line, a Qarray, and an octopole, as shown in Figure 2.5. In the desolvation line, remaining solvent molecules can be

removed from the charged particles. In the Qarray and the octopole, the beam of charged particles is subsequently focused. After the octopole, the charged particles pass through the mass analyzer, which is a single quadrupole (see Figure 2.5). Such a linear quadrupole mass analyzer is composed of four hyperbolically or cylindrically shaped rod electrodes that are mounted in a square configuration [43]. The pairs of opposite rods are each held at the same voltage that is composed of a direct current (DC) voltage and an alternating current (AC) voltage [43]. When an ion enters the quadrupole, an attractive force is exerted on this ion by one of the rods, whose charge is currently opposite to the charge of the ion [43]. As the voltage applied to the rods is periodic, the sign of the electric force also changes periodically in time, so that attraction and repulsion alternate in time [43]. For a given DC voltage, a given amplitude of the AC voltage, and a given frequency of the AC voltage, ions with a certain mass-to-charge ratio (m/z value) can fly along a stable trajectory, so that these ions can pass the quadrupole and reach the detector [43]. Ions with other m/z values do not fly along stable trajectories through the quadrupole, so that these ions cannot reach the detector. By the DC voltage, the amplitude of the AC voltage, and the frequency of the AC voltage, the m/z value of the ions that can reach the detector can be adjusted. After passing through the single quadrupole, the ions with the selected m/z value are detected by a detector, namely a secondary electron multiplier (see Figure 2.5). In a secondary electron multiplier, the ions first hit a conversion dynode, whereby secondary electrons are emitted from this conversion dynode [43]. These emitted electrons are accelerated towards a second dynode with a more positive potential, where they hit and cause the release of more secondary electrons [43]. These electrons are accelerated towards a third dynode with an even more positive potential, so that even more secondary electrons are emitted from this third dynode and so on. Thus, an electron avalanche is eventually created, which is associated with a current. This current can be detected by a preamplifier [43]. This current is converted into a voltage signal, which is translated into an intensity value by an analog-to-digital converter [43]. In the resulting chromatogram, the signal intensity (or “absolute intensity”) is plotted against the time for the ions with the selected m/z value. When a detectable analyte with a selected m/z value reaches the ESI/MS, the detector measures a short-term increase of the intensity, so that the resulting chromatogram indicates an intensity peak at the specific retention time. The area of this peak is approximately proportional to the concentration of the concerning analyte in the sample for a certain concentration range. Consequently, the concentration of the analyte in an electrolyte can eventually be determined based on peak areas. By periodically changing the DC voltage and AC voltage in the rods of the quadrupole, the m/z value of the detected ions can be changed periodically. Thereby, chromatograms for ions with different m/z values can be recorded simultaneously. Chromatograms from an EC-containing, a DMC-containing, a DEC-containing, and a $LiPF_6$-containing sample are shown in the diagrams in Figure 2.6. The chromatograms were recorded by means of HPLC-ESI/MS at the selected m/z values 89.1^+ u (in case of Figure 2.6(a)), 91.1^+ u (in case

of Figure 2.6(b)), 119.1^{+} u (in case of Figure 2.6(c)), 89.1^{+} u (in case of Figure 2.6(d)), and 145.0^{-} u (in case of Figure 2.6(e)). Note that the chromatograms in Figure 2.6(a), Figure 2.6(b), and Figure 2.6(c) do not show the peaks from EC, DMC, and DEC, but the peaks from the corresponding adducts each with one hydrogen-ion, namely the peaks from EC+H^{+}, DMC+H^{+}, and DEC+H^{+}. The chromatogram in Figure 2.6(d) also does not show the peak from lithium-ions, but the peak from adducts each consisting of one lithium-ion and two ACN molecules (Li^{+}+2 ACN) [40]. The chromatograms indicated in Figure 2.6 are measurement data that were acquired for the examinations described in section 4.1.

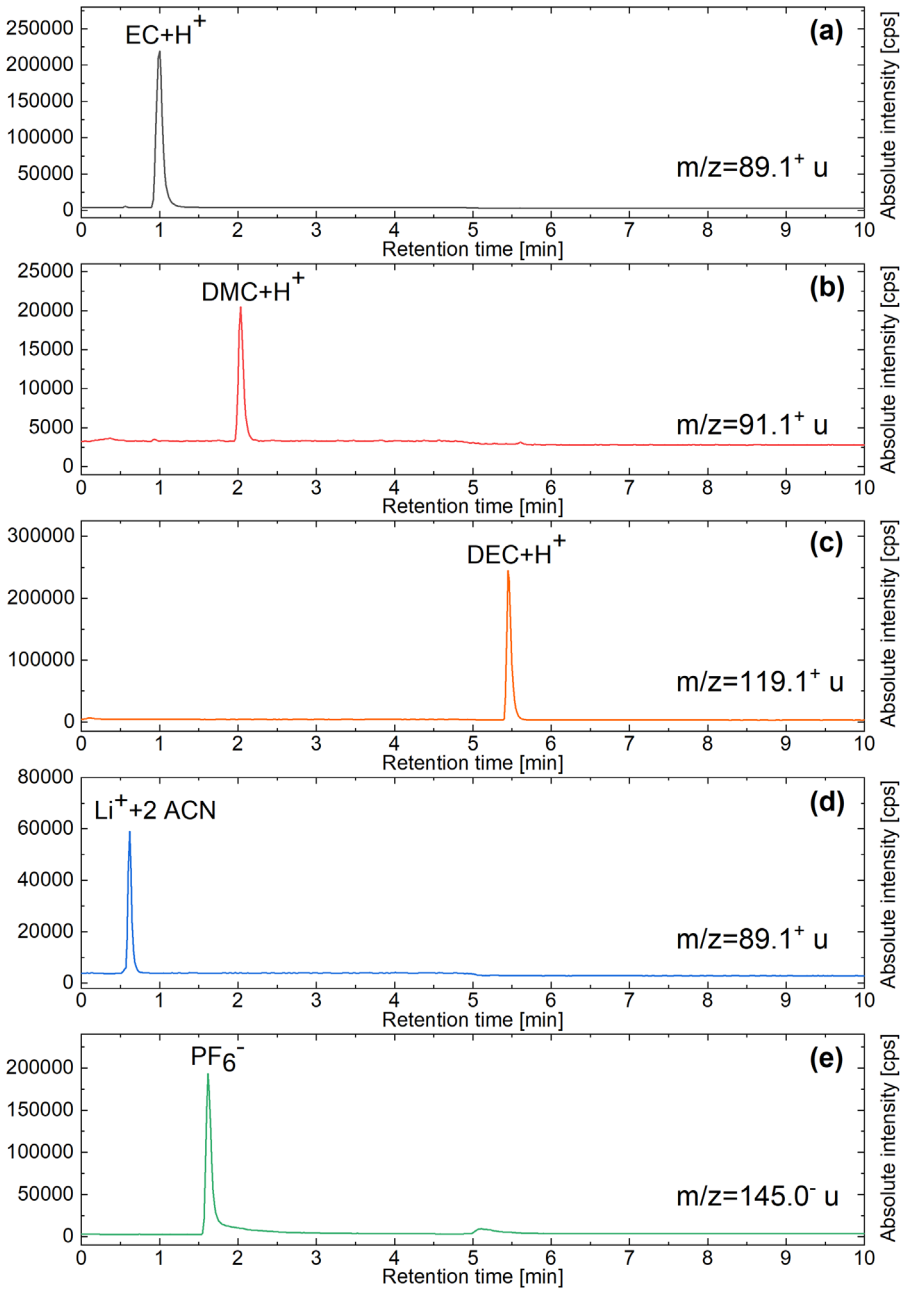

Figure 2.6: Chromatogram of an EC-containing sample (a), a DMC-containing sample (b), a DEC-containing sample (c), and a $LiPF_6$-containing sample (d/e) measured by means of HPLC-ESI/MS at different m/z values [40].

3 Experimental

3.1 Electrolytes

The electrolytes were mixed in an argon-filled glovebox with an oxygen and water content below 1 ppm. Each added electrolyte component was weighed to determine the precise, initial electrolyte compositions. The water contents of the electrolytes were lower than 20 ppm determined by Karl Fischer titration.

The electrolyte LP30+VC+LiTFSI was filled into the investigated NCM111/graphite pouch cells. The composition of this electrolyte is listed in Table 3.1.

Table 3.1: Composition of the electrolyte LP30+VC+LiTFSI filled into the NCM111/graphite pouch cells [40].

Component	Mass fraction [wt%]
EC (Sigma-Aldrich, anhydrous, 99%, USA)	42.7±0.1
DMC (Sigma-Aldrich, anhydrous, ≥99%, USA)	42.7±0.1
VC (Gotion, ≤200 ppm water, ≥99.5%, USA)	3.00±0.01
$LiPF_6$ (Gotion, ≤20 ppm water, ≥99.8%, USA)	11.5±0.1
LiTFSI (Sigma-Aldrich, 99.95% trace metals basis, USA)	0.100±0.001

The electrolyte LP30+VC was the initial electrolyte in the investigated NCM622/graphite pouch cells. The composition of this electrolyte is shown in Table 3.2.

Table 3.2: Composition of the electrolyte LP30+VC filled into the NCM622/graphite pouch cells [44].

Component	Mass fraction [wt%]
EC (Sigma-Aldrich, anhydrous, 99%, USA)	42.8±0.1
DMC (Sigma-Aldrich, anhydrous, ≥99%, USA)	42.8±0.1
VC (Gotion, ≤200 ppm water, ≥99.5%, USA)	3.00±0.01
$LiPF_6$ (Sigma-Aldrich, battery grade, ≥99.99%, USA)	11.4±0.1

The investigated NCM622/silicon-graphite pouch cells were filled either with the electrolyte 1 M $LiPF_6$ in VC:DMC or with the electrolyte 1 M $LiPF_6$ in FEC:DMC. The composition of 1 M $LiPF_6$ in VC:DMC can be seen in Table 3.3. The composition of 1 M $LiPF_6$ in FEC:DMC is listed in Table 3.4.

Table 3.3: Composition of the electrolyte 1 M $LiPF_6$ in VC:DMC filled into the NCM622/silicon-graphite pouch cells.

Component	Mass fraction [wt%]
DMC (Sigma-Aldrich, anhydrous, ≥99%, USA)	44.0±0.1
VC (Gotion, ≤200 ppm water, ≥99.5%, USA)	44.0±0.1
$LiPF_6$ (Sigma-Aldrich, battery grade, ≥99.99%, USA)	12.0±0.1

Table 3.4: Composition of the electrolyte 1 M $LiPF_6$ in FEC:DMC filled into the NCM622/silicon-graphite pouch cells.

Component	Mass fraction [wt%]
DMC (Sigma-Aldrich, anhydrous, ≥99%, USA)	44.2±0.1
FEC (Gotion, ≤20 ppm water, ≥99.5%, USA)	44.2±0.1
$LiPF_6$ (Sigma-Aldrich, battery grade, ≥99.99%, USA)	11.6±0.1

3.2 Electrodes and separators

For the NCM111/graphite pouch cells, commercially available electrodes were used. The double-sided coated anodes of these pouch cells had dimensions of 5.2 x 5.2 cm. The coating of these anodes consisted of about 90 wt% graphite as active material. The one-sided coated cathodes of the NCM111/graphite pouch cells had dimensions of 5.0 x 5.0 cm. The cathode coating was composed of about 90 wt% NCM111 as active material.

For the NCM622/graphite pouch cells, custom-made electrodes were utilized. The one-sided coated anodes from these pouch cells had dimensions of 5.2 x 5.2 cm. The coating of these anodes consisted of 93.5 wt% SMG-A5 graphite (Hitachi, Japan) as active material, 1.9 wt% Timcal C65 carbon black (Imerys, France), 1.75 wt% sodium carboxymethylcellulose (NaCMC) binder (DuPont, USA), and 2.85 wt% styrene-butadiene rubber (SBR) binder (JSR, Japan). The anode coating on copper foil had a mass loading of 7.7 $mg \cdot cm^{-2}$. The anodes of the NCM622/graphite pouch cells eventually had a theoretical areal capacity of 2.7 $mAh \cdot cm^{-2}$. The one-sided coated cathodes from the NCM622/graphite pouch cells had sizes of 5.0 x 5.0 cm. The coating of these cathodes was composed of 94 wt% NCM622 (Targray, Canada) as active material, 3 wt% polyvinylidene fluoride (PVDF) binder (Solvay, Belgium), 1 wt% Super C65 carbon black (Imerys, France), and 2 wt% Timcal SFG6L graphite (Imerys, France). The cathode coating on aluminum foil had a mass loading of 11.3 $mg \cdot cm^{-2}$. The theoretical areal capacity of the cathodes from the NCM622/graphite pouch cells was 1.9 $mAh \cdot cm^{-2}$. The theoretical areal capacity of the cathodes was distinctly lower than the theoretical areal capacity of the anodes to prevent lithium plating during cycling.

Custom-made electrodes were used also for the NCM622/silicon-graphite pouch cells. The dimensions of the one-sided coated anodes from these pouch cells were also 5.2 x 5.2 cm. The coating of the

silicon-graphite anodes was composed of 84.15 wt% SMG-A5 graphite (Hitachi, Japan) as active material, 9.35 wt% silicon nanopowder (Nanostructured & Amorphous Materials, average particle size: 30-50 nm, purity: >98%, USA) as active material, 1.9 wt% Timcal C65 carbon black (Imerys, France), 1.75 wt% NaCMC binder (DuPont, USA), and 2.85 wt% SBR binder (JSR, Japan). This anode coating on copper foil had a mass loading of 4.6 $mg \cdot cm^{-2}$. The resulting, theoretical areal capacity of the anodes from the NCM622/silicon-graphite pouch cells was 3.0 $mAh \cdot cm^{-2}$. The sizes of the one-sided coated cathodes from the NCM622/silicon-graphite pouch cells were 5.0 x 5.0 cm. The cathodes from the NCM622/silicon-graphite pouch cells basically had the same composition as the cathodes from the NCM622/graphite pouch cells. Indeed, the cathodes from the NCM622/silicon-graphite pouch cells had a mass loading of 10.8 $mg \cdot cm^{-2}$ and a theoretical areal capacity of 1.8 $mAh \cdot cm^{-2}$. For the NCM622/silicon-graphite pouch cells, the theoretical areal capacity of the anodes was also considerably higher than the theoretical areal capacity of the cathodes to avoid lithium plating during cycling.

For each of the investigated pouch cells, the same, PET-based, ceramically coated separators were used. These separators had dimensions of 5.5 x 5.5 cm.

Before the cell assembly, the electrodes were dried under reduced pressure at 130 °C for 12 hours. The separator drying was conducted under reduced pressure at 180 °C for 12 hours before the cell assembly.

3.3 Cell assembly

The pouch cell assembly was conducted in a dry room with a dew point of −68 °C.

In each NCM111/graphite pouch cell, one double-sided coated anode was placed in the middle, such that both anode sides each faced one one-sided coated cathode. In each NCM111/graphite pouch cell, two separators were integrated. In addition, 900 µl of the electrolyte LP30+VC+LiTFSI was filled into each of these pouch cells. Following this, the pouch cells were sealed under reduced pressure.

In each NCM622/graphite pouch cell and NCM622/silicon-graphite pouch cell, two one-sided coated anodes were placed back to back in the middle, such that both anodes each faced one one-sided coated cathode. Additionally, two separators were installed in each NCM622/graphite pouch cell and NCM622/silicon-graphite pouch cell. 900 µl of the electrolyte LP30+VC was filled into each NCM622/graphite pouch cell. Each NCM622/silicon-graphite pouch cell was filled either with 900 µl of the electrolyte 1 M $LiPF_6$ in VC:DMC or with 900 µl of the electrolyte 1 M $LiPF_6$ in FEC:DMC. The NCM622/graphite pouch cells and the NCM622/silicon-graphite pouch cells were sealed under reduced pressure after the electrolyte filling.

Each pouch cell was weighed before and after electrolyte filling and sealing of the cell for the determination of the initial electrolyte mass within the cell. The theoretical, initial capacities of the mentioned pouch cells were about 88 mAh.

3.4 Cell formation and cycling

A Basytec CTS LAB was used for the formation and the cycling of the pouch cells. The cells were placed in a climate chamber with a constant temperature of 25±0.1 °C for the formation and the cycling.

During formation, the pouch cells were first charged with 0.1 C until 4.2 V with constant current-constant voltage (CC-CV), until the current fell below 0.05 C. Following this, the cells were discharged until 3.0 V with constant current (CC) with 0.5 C (in case of the NCM111/graphite pouch cells) or with 0.1 C (in case of the NCM622/graphite pouch cells and the NCM622/silicon-graphite pouch cells). Subsequently, the cells were charged again until 4.2 V with 0.5 C (with CC-CV, until the current fell below 0.05 C) and discharged until 3.0 V with 0.5 C (with CC). Afterwards, the formation program was finished for each cell (in case of the NCM111/graphite pouch cells) and for the cells that were cycled following the formation (in case of the NCM622/graphite pouch cells and the NCM622/silicon-graphite pouch cells), respectively. The NCM622/graphite pouch cells and the NCM622/silicon-graphite pouch cells that were examined after their formation were held at 3.0 V for four hours after the discharge at 0.5 C before the analyses.

The continuous cycling following the formation was conducted in a voltage range of 3.0 V-4.2 V with charge at 2 C (with CC-CV, until the current fell below 0.05 C) and discharge at 3 C (with CC) for different numbers of cycles. Some of the NCM622/silicon-graphite pouch cells were cycled with 0.5 C charge (with CC-CV, until the current fell below 0.05 C) and 0.5 C discharge (with CC) in a voltage range of 3.0 V-4.2 V for various numbers of cycles after formation. In case of the NCM111/graphite pouch cells, the DC internal resistances were measured by means of discharge pulses with 1 C for 20 s at a SOC of 10%, 30%, 50%, 70%, and 90% at the beginning (right before the first cycle with 2 C charge and 3 C discharge) and after every 200 cycles. In case of the NCM622/graphite pouch cells, a checkup cycle was conducted, during which the cells were charged at 0.1 C (with CC-CV, until the current fell below 0.05 C) and discharged at 0.1 C (with CC) at the beginning (right before the first cycle with 2 C charge and 3 C discharge) and after every 100 cycles. In case of the NCM622/silicon-graphite pouch cells, the same checkup cycle was conducted only at the beginning (right before the first cycle with 2 C charge and 3 C discharge, or 0.5 C charge and 0.5 C discharge). Following each checkup cycle, the DC internal resistances were measured also by means of discharge pulses with 1 C for 20 s at a SOC of 10%, 30%, 50%, 70%, and 90%. For the determination of the DC internal resistances, the SOCs were set by charging using the Ah-counter method. The DC internal resistances were determined based on the

potential drop during the discharge pulses and the applied current of 1 C during the discharge pulses applying Ohm's law.

After cycling and before the analyses, the NCM111/graphite pouch cells were discharged until 3.0 V with 1 C. The NCM622/graphite pouch cells and the NCM622/silicon-graphite pouch cells, however, were charged until 4.2 V with 0.1 C (with CC-CV, until the current fell below 0.05 C), discharged to 3.0 V with 0.1 C (with CC), and held at 3.0 V for four hours after cycling and before the analyses.

The half-cells with the punched out silicon-graphite electrodes from the NCM622/silicon-graphite pouch cells were discharged to 0.005 V at 0.1 C (with CC-CV, until the current fell below 0.05 C) and charged to 1.0 V at 0.1 C (with CC) four times (four cycles at 0.1 C/0.1 C). Following this, these coin cells were discharged to 0.005 V at 0.5 C (with CC-CV, until the current fell below 0.05 C) and charged to 1.0 V at 0.5 C (with CC) four times (four cycles at 0.5 C/0.5 C). The half-cells with the punched out NCM622 electrodes from the NCM622/silicon-graphite pouch cells were charged to 4.3 V at 0.1 C (with CC-CV, until the current fell below 0.05 C) and discharged to 3.0 V at 0.1 C (with CC) four times (four cycles at 0.1 C/0.1 C). Subsequently, these coin cells were charged to 4.3 V at 0.5 C (with CC-CV, until the current fell below 0.05 C) and discharged to 3.0 V at 0.5 C (with CC) four times (four cycles at 0.5 C/0.5 C).

3.5 Electrolyte extraction

In this thesis, two methods for electrolyte extraction from pouch cells were applied: the extraction by centrifugation (centrifugation method) and the extraction by DEC injection (DEC extraction method). The DEC extraction method is the newly developed extraction method that was used for the investigation of the electrochemical decompositions in the electrolytes inside the pouch cells during formation and subsequent cycling. For comparison, the commonly used centrifugation method was used as reference method for electrolyte extraction [40]. In the following two subsections, the procedure of the electrolyte extraction by centrifugation and by DEC injection is specified.

3.5.1 Centrifugation method

The procedure of the electrolyte extraction by centrifugation is described in a publication [40]. The electrolyte extractions were carried out in a dry room with a dew point of −68 °C. A Hettich universal 320 R centrifuge was used for the centrifugation. In Figure 3.1, the important steps of the electrolyte extraction by centrifugation can be seen. First, the pouch cell was cut into four pieces using scissors [40], as shown in Figure 3.1(b). Following this, Piece 2 and Piece 3 (see Figure 3.1(b)) were inserted rolled-up into the filter inset of the centrifugal vessel with the open side facing downwards [40], as can be seen in Figure 3.1(c). Subsequently, the centrifugal vessel was screwed down and placed in the centrifuge. The used centrifugal vessels were 25 ml centrifugal filters (Thermo Fisher Scientific, USA).

The centrifugal vessel with the cell pieces was centrifuged for 20 min at 5000 RPM and at a temperature of 0 °C to reduce the solvent evaporation during the centrifugation [40]. After centrifugation, the extracted, filtered electrolyte with a yellowish color was located on the bottom of the centrifugal vessel, as shown in Figure 3.1(d).

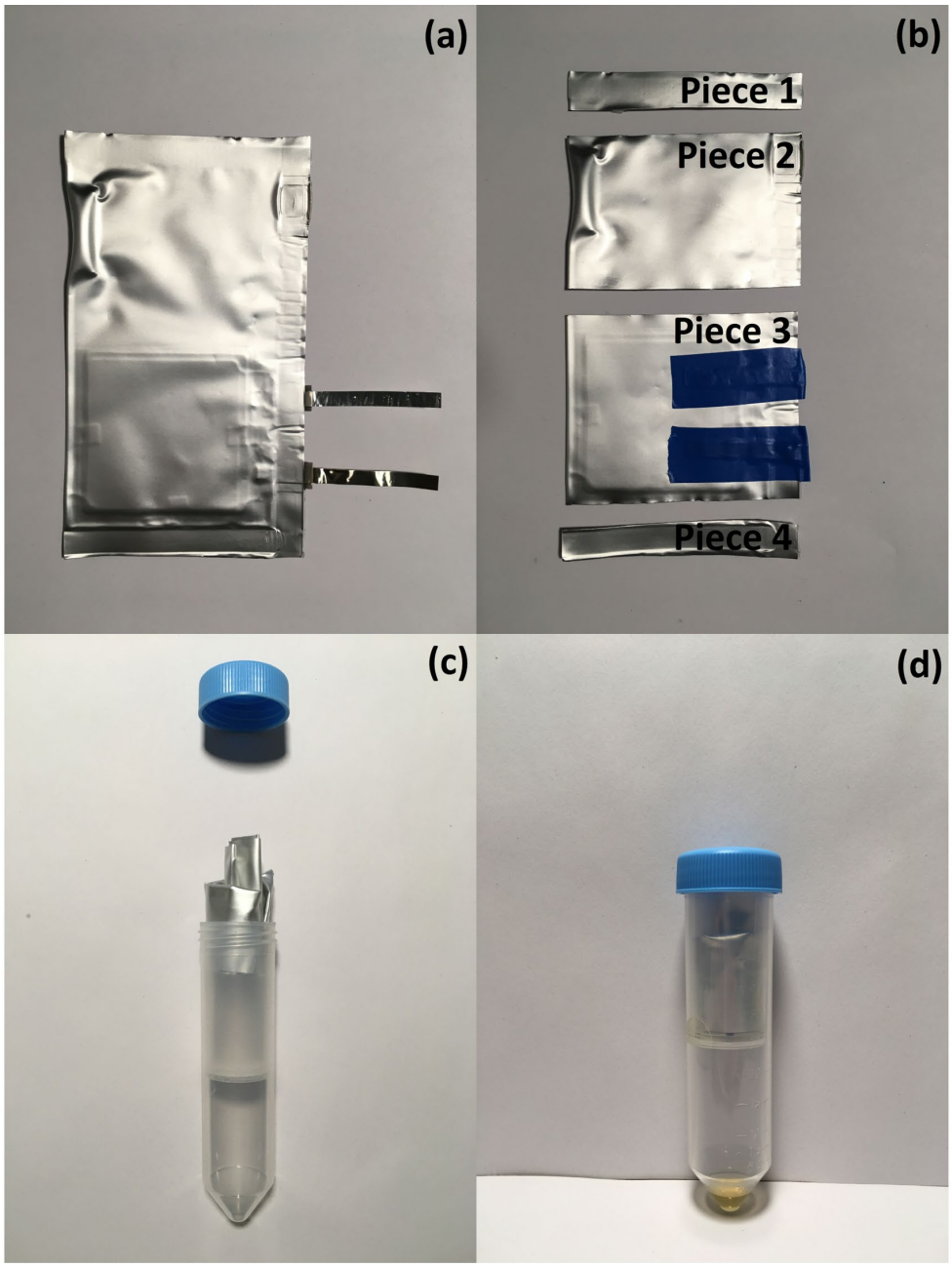

Figure 3.1: The steps of the electrolyte extraction by centrifugation: (a) Pouch cell in the initial state before electrolyte extraction. (b) Pouch cell cut into four pieces using scissors. (c) Centrifugal vessel with Piece 2 and 3 of the pouch cell rolled-up in the associated filter inset. (d) Centrifugal vessel with the extract on the bottom after 20 min of centrifugation [40].

3.5.2 DEC extraction method

The description of the electrolyte extraction by the DEC extraction method can be found in literature [40]. The electrolyte extractions from the pouch cells through the DEC extraction method were realized in a dry room with a dew point of −68 °C. The essential steps of the electrolyte extraction by this method are shown in Figure 3.2. First, a syringe was used to inject 500 µl DEC (in case of the NCM111/graphite pouch cells and the NCM622/graphite pouch cells) or 1000 µl DEC (in case of the NCM622/silicon-graphite pouch cells) into the pouch cell close to the sealed seam, as can be seen in Figure 3.2(b). Following this, the pouch cell was immediately sealed again under reduced pressure, directly next to the original sealed seam (see Figure 3.2(c)), such that the cell was completely tight again [40]. For the calculation of the mass of the injected DEC, the pouch cell weight was determined before and after the injection. The pouch cell was subsequently stored for 8 days (in case of the NCM111/graphite pouch cells) or 14 days (in case of the NCM622/graphite pouch cells and the NCM622/silicon-graphite pouch cells) to allow a complete mixing of the injected DEC with the original electrolyte in the pouch cell [40]. After the storage of the cell, a needle was used to make a puncture in one corner of the cell next to the electrodes without creating a short circuit for the actual electrolyte extraction. As a result, the extract dripped out of this puncture. This extracted electrolyte was collected in a vessel, as can be seen in Figure 3.2(d). The extracted electrolyte in Figure 3.2(d) was still unfiltered and thus colorless. After the actual electrolyte extraction, the extract was filtered by means of a syringe filter with a pore size of 0.45 µm (in case of the NCM111/graphite pouch cells and the NCM622/graphite pouch cells) and with a pore size of 0.1 µm (in case of the NCM622/silicon-graphite pouch cells), respectively.

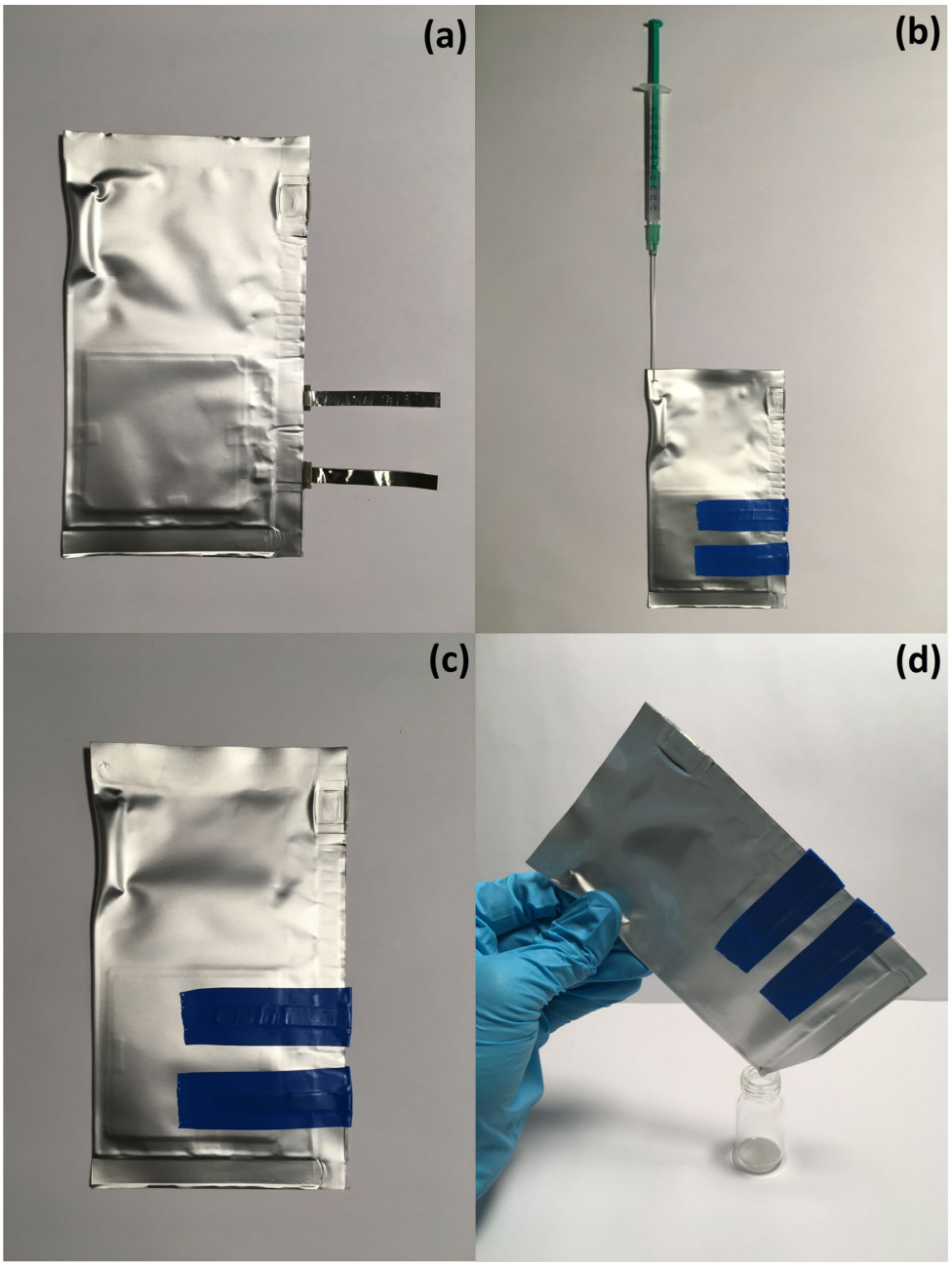

Figure 3.2: The steps of the electrolyte extraction by DEC injection: (a) Pouch cell in the initial state before electrolyte extraction. (b) DEC injection into pouch cell. (c) After sealing of the puncture, the pouch cell is tight. (d) After 8 days or 14 days of storage, the mixture of the injected DEC and the original electrolyte is extracted through a puncture. The unfiltered extract is collected in a vessel and filtered after that [40].

3.6 Calculation of the concentrations, absolute amounts, and consumptions

The calculation of the concentrations, the absolute amounts of substance, and the consumptions of the components in the electrolyte extracted by the DEC extraction method is specified in a publication [40]. In this section, the calculation of these values is explained.

The concentration of an electrolyte component in the original electrolyte (before the DEC injection) $c_{component}$ in mmol·g^{-1} was calculated according to Equation 3.1. The concentration of the component in the concerning, analyzed, electrolyte-containing sample $c_{component,sample}$ in mmol·g^{-1} was quantified by HPLC or GC. The weight of the sample is m_{sample} in g. The mass fraction of the original electrolyte (before the DEC injection) in the extract (original electrolyte plus DEC) is $w_{electrolyte,extract}$. The mass fraction of the extract (original electrolyte plus DEC) in the analyzed sample $w_{extract,sample}$ was calculated based on the weighed masses during sample preparation. The mass fraction of DEC in the extract (original electrolyte plus DEC) $w_{DEC,extract}$ was quantified by HPLC.

$$c_{component} = \frac{c_{component,sample} \cdot m_{sample}}{w_{electrolyte,extract} \cdot w_{extract,sample} \cdot m_{sample}} = \frac{c_{component,sample}}{(1 - w_{DEC,extract}) \cdot w_{extract,sample}} \tag{3.1}$$

For the determination of the absolute amounts of substance of the electrolyte components in the cell, the mass of the original electrolyte in the cell (before the DEC injection) needs to be determined first. The mass of the original electrolyte in the cell (before the DEC injection) $m_{electrolyte}$ in g was calculated by Equation 3.2. $m_{electrolyte}$ is also called the quantified, absolute electrolyte mass. The mass of the injected DEC m_{DEC} in g is the difference between the pouch cell weight before DEC injection and the pouch cell weight after DEC injection.

$$m_{electrolyte} = m_{DEC} \cdot \left(\frac{1}{w_{DEC,extract}} - 1 \right) \tag{3.2}$$

The absolute amount of substance of an electrolyte component in the cell $n_{component}$ in mmol is eventually given by Equation 3.3.

$$n_{component} = c_{component} \cdot m_{electrolyte} \tag{3.3}$$

The relative amount of substance of an electrolyte component in the cell $n_{component,relative}$ in % was calculated by Equation 3.4. The initial amount of substance of the component in the cell is $n_{component,0}$ in mmol. The initial concentration of the component in the original electrolyte (without DEC) $c_{component,0}$ in mmol·g^{-1} was calculated based on the weighed masses during mixing of the electrolyte. The initial mass of the original electrolyte (without DEC) in the cell $m_{electrolyte,0}$ in g corresponds to the weighed mass of the electrolyte filled into the cell during cell assembly.

$$n_{component,relative} = \left(\frac{n_{component}}{n_{component,o}} \right) \cdot 100 = \left(\frac{n_{component}}{c_{component,o} \cdot m_{electrolyte,0}} \right) \cdot 100 \tag{3.4}$$

To determine the absolute extent of the various electrolyte decompositions in the pouch cell during electrochemical aging, the absolute, consumed amounts of substance or consumptions need to be calculated. The consumption of an electrolyte component during a certain phase of electrochemical aging $\Delta n_{component}$ in mmol is given by Equation 3.5. The determined amount of substance of the concerning electrolyte component in the cell before the respective phase of electrochemical aging is

$n_{component,before}$ in mmol, which was determined according to Equation 3.3. The determined amount of substance of the concerning electrolyte component in the cell after the respective phase of electrochemical aging is $n_{component,afterwards}$ in mmol, which was also calculated according to Equation 3.3.

$$\Delta n_{component} = n_{component,before} - n_{component,afterwards} \quad (3.5)$$

If the consumption of an electrolyte component during the formation has to be calculated for example, $n_{component,before}$ is the determined amount of substance of the component in the electrochemically untreated, fresh cell, while $n_{component,afterwards}$ is the determined amount of substance of the component in the cell after formation. Accordingly, if the consumption of an electrolyte component after formation during the subsequent x cycles has to be calculated, $n_{component,before}$ is the determined amount of substance of the component in the cell after formation, while $n_{component,afterwards}$ is the determined amount of substance of the component in the cell after x cycles and so on. The cell before the respective phase of electrochemical aging and the cell after the respective phase of electrochemical aging were always from one set of cells analyzed together. The consumptions of the electrolyte components are always indicated in the unit µmol in this thesis.

3.7 HPLC analyses

For the quantification of DEC, EC, DMC, VC, Li^+, and PF_6^- in the electrolytes, HPLC coupled to an UV/Vis detector and an ESI/MS was used. In the following two subsections, the conditions of the conducted HPLC measurements and the preparation of the samples for the HPLC measurements are specified. The conditions of the HPLC measurements for the quantification of the components in the fresh electrolyte LP30+VC+LiTFSI and the electrolytes from the NCM111/graphite pouch cells, as well as the associated sample preparation are also described in literature [40]. Additionally, the conditions of the HPLC measurements for the quantification of the components in the electrolytes from the NCM622/graphite pouch cells, as well as the associated sample preparation are specified in literature [44]. For the control of the system and the evaluation of the data from the HPLC measurements, the software LabSolutions Version 5.97 was used.

3.7.1 HPLC coupled to UV/Vis detector (HPLC-UV/Vis)

DEC, EC, DMC, and VC were quantified in the electrolytes using a HPLC system of Nexera XR Ultra High Performance Liquid Chromatograph (Shimadzu, Japan) coupled to a type of UV/Vis detector, namely a PDA detector (SPD-M20A, Shimadzu, Japan). For the separation of the electrolyte components, the column Acclaim 120 C18 (Thermo Fisher Scientific, USA) was mostly used with the following characteristics: 250 mm length x 4.6 mm interior diameter, particle size of 5 µm, and pore size of 120 Å. Only for the VC quantification in the fresh electrolyte LP30+VC+LiTFSI and in the electrolytes from

the NCM111/graphite pouch cells, the column Acclaim 120 C18 (Thermo Fisher Scientific, USA) was utilized with the following characteristics: 100 mm length x 3.0 mm interior diameter, particle size of 2.2 µm, and pore size of 120 Å. During the measurements, the temperature of the column oven was always constantly 50 °C. Furthermore, the cell temperature of the PDA detector was always 50 °C. The slit width of the PDA detector was always set to 1.2 nm. The set wavelength of the PDA detector was 190 nm for all the analyses. The flow rate was always set to 1.00 ml·min^{-1} and the injection volume to 2.0 µl for the HPLC-UV/Vis analyses with two exceptions: In case of the analyses for the VC quantification in the fresh electrolyte LP30+VC+LiTFSI and in the electrolytes from the NCM111/graphite pouch cells, the flow rate was set to 0.75 ml·min^{-1} and the injection volume to 4.0 µl. In case of the measurements for the DEC quantification in the fresh electrolyte LP30+VC+LiTFSI and in the electrolytes from the NCM111/graphite pouch cells, the flow rate was 1.00 ml·min^{-1}, while the injection volume was 20.0 µl. The mobile phase consisted constantly of 60% water and 40% ACN (isocratic separation) during most of the analyses. Only in case of the analyses for the VC quantification in the fresh electrolyte LP30+VC+LiTFSI and in the electrolytes from the NCM111/graphite pouch cells, the composition of the mobile phase was changed during the measurements, as listed in Table 3.5.

Table 3.5: Composition of the mobile phase during the analyses for the VC quantification in the fresh electrolyte LP30+VC+LiTFSI and in the electrolytes from the NCM111/graphite pouch cells, respectively [40].

Time [min]	Water [%]	ACN [%]
0-3.5	95	5
3.5-4	95->40 (gradient)	5->60 (gradient)
4-10.5	40	60
10.5-11	40->95 (gradient)	60->5 (gradient)
11-14.5	95	5

To minimize the statistical errors, each analyzed sample was injected three times, and the average peak area from these three measurements was used for the eventual quantifications [40,44].

The preparation of the samples analyzed by HPLC-UV/Vis was conducted in a dry room with a dew point of −68 °C. For the quantification of EC, DMC, DEC, and VC by HPLC-UV/Vis, the electrolytes and the standard substances (in this case pure EC, DMC, DEC, and VC) were diluted with ACN. Each mass was weighed during sample preparation for the eventual quantifications of the analytes.

For the quantification of EC, DMC, DEC, and VC in the fresh electrolyte LP30+VC+LiTFSI and in the electrolytes from the NCM111/graphite pouch cells by HPLC-UV/Vis, the external standard method with a ten-point calibration was used. In Table 3.6, the ranges of the mass fractions of the quantified electrolyte components in the samples used for the analyses of the fresh electrolyte LP30+VC+LiTFSI and the electrolytes from the NCM111/graphite pouch cells by HPLC-UV/Vis are shown. The samples with the standard substances are called the standard samples, and the samples with the electrolytes

are the electrolyte samples. Additionally, the coefficients of determination R^2 of the associated calibration curves are indicated in Table 3.6.

Table 3.6: The ranges of the electrolyte component mass fractions in the samples used for the analyses of the electrolyte LP30+VC+LiTFSI and the electrolytes from the NCM111/graphite pouch cells by HPLC-UV/Vis, including the associated coefficients of determination R^2 [40].

Electrolyte component	Range of the electrolyte component mass fraction in the standard samples [wt%]	Range of the quantified electrolyte component mass fraction in the electrolyte samples [wt%]	R^2 [1]
EC	0.527-5.409	1.63-3.13	0.9999
DMC	0.516-5.396	1.59-2.79	0.9999
DEC	0.101-1.079	0.454-0.628	0.9999
VC	0.00181-0.01324	0.00577-0.01039	0.9999

To quantify EC, DMC, DEC, and VC in the electrolytes from the NCM622/graphite pouch cells by HPLC-UV/Vis, the external standard method with a seven-point calibration was used. The ranges of the mass fractions of the quantified electrolyte components in the standard samples and the electrolyte samples used for the HPLC-UV/Vis analyses of the electrolytes from the NCM622/graphite pouch cells are listed in Table 3.7. Besides, also the coefficients of determination R^2 of the associated calibration curves are shown in Table 3.7.

Table 3.7: The ranges of the electrolyte component mass fractions in the samples used for the analyses of the electrolytes from the NCM622/graphite pouch cells by HPLC-UV/Vis, including the associated coefficients of determination R^2 [44].

Electrolyte component	Range of the electrolyte component mass fraction in the standard samples [wt%]	Range of the quantified electrolyte component mass fraction in the electrolyte samples [wt%]	R^2 [1]
EC	0.961-4.735	1.740-2.675	0.9999
DMC	0.924-4.536	1.494-2.608	0.9999
DEC	1.093-5.368	1.956-3.188	0.9999
VC	0.00533-0.03051	0.01302-0.02110	0.9998

The external standard method with a seven-point calibration was also used for the quantification of DMC, DEC, and VC in the electrolytes from the NCM622/silicon-graphite pouch cells by HPLC-UV/Vis. The ranges of the mass fractions of the quantified electrolyte components in the samples used for the HPLC-UV/Vis analyses of the electrolytes from the NCM622/silicon-graphite pouch cells plus the associated coefficients of determination R^2 can be seen in Table 3.8.

Table 3.8: The ranges of the electrolyte component mass fractions in the samples used for the analyses of the electrolytes from the NCM622/silicon-graphite pouch cells by HPLC-UV/Vis, including the associated coefficients of determination R^2.

Electrolyte component	Range of the electrolyte component mass fraction in the standard samples [wt%]	Range of the quantified electrolyte component mass fraction in the electrolyte samples [wt%]	R^2 [1]
DMC	1.135-5.515	3.178-3.820	0.9999
DEC	2.386-11.648	6.619-7.806	0.9996
VC	0.00537-0.02758	0.01744-0.02153	0.9994

3.7.2 HPLC coupled to ESI/MS (HPLC-ESI/MS)

Concentrations of Li^+, PF_6^-, EC, DMC, and DEC were quantified in electrolytes using HPLC coupled to an ESI/MS (LCMS-2020, Shimadzu, Japan). The HPLC system was the same as for the HPLC-UV/Vis analyses (see subsection 3.7.1). The ESI/MS is composed of an ESI-source that ionizes the analytes and a single quadrupole MS for the detection of the ionized analytes. For the separation of the electrolyte components, the column Acclaim 120 C18 (Thermo Fisher Scientific, USA) was utilized with the following dimensions: 100 mm length x 3.0 mm interior diameter, particle size of 2.2 µm, and pore size of 120 Å. During the HPLC-ESI/MS measurements, the nebulizing gas flow was 1.5 $l \cdot min^{-1}$, while the drying gas flow was 20.0 $l \cdot min^{-1}$. Besides, the heat block temperature was at 400 °C, the desolvation line (DL) temperature at 300 °C, and the interface temperature at 350°C during the HPLC-ESI/MS analyses. In addition, the temperature of the column oven was set to 50 °C, the injection volume to 1.0 µl, and the flow rate to 0.75 $ml \cdot min^{-1}$ for each HPLC-ESI/MS measurement.

In Table 3.9, the composition of the mobile phase during the measurements for the quantification of EC, DEC, Li^+, and PF_6^- in the electrolyte LP30+VC+LiTFSI and the electrolytes from the NCM111/graphite pouch cells by HPLC-ESI/MS can be seen.

Table 3.9: Composition of the mobile phase during the analyses for the quantification of EC, DEC, Li^+, and PF_6^- by HPLC-ESI/MS in the electrolyte LP30+VC+LiTFSI and the electrolytes from the NCM111/graphite pouch cells, respectively [40].

Time [min]	Water+0.1% (per volume) formic acid [%]	ACN [%]
0-3.5	95	5
3.5-4	95->40 (gradient)	5->60 (gradient)
4-10.5	40	60
10.5-11	40->95 (gradient)	60->5 (gradient)
11-14.5	95	5

The composition of the mobile phase during the measurements for the DMC quantification in the electrolyte LP30+VC+LiTFSI by HPLC-ESI/MS is shown in Table 3.10.

Table 3.10: Composition of the mobile phase during the analyses for the DMC quantification in the electrolyte LP30+VC+LiTFSI by HPLC-ESI/MS [40].

Time [min]	Water+0.1% (per volume) formic acid [%]	ACN [%]
0-3.5	90	10
3.5-4	90->40 (gradient)	10->60 (gradient)
4-10.5	40	60
10.5-11	40->90 (gradient)	60->10 (gradient)
11-14.5	90	10

In Table 3.11, the composition of the mobile phase during the HPLC-ESI/MS measurements for the quantification of Li^+ and PF_6^- in the electrolytes from the NCM622/graphite pouch cells and the NCM622/silicon-graphite pouch cells are listed.

Table 3.11: Composition of the mobile phase during the analyses for the quantification of Li^+ and PF_6^- in the electrolytes from the NCM622/graphite pouch cells and the NCM622/silicon-graphite pouch cells by HPLC-ESI/MS [44].

Time [min]	Water+0.1% (per volume) formic acid [%]	ACN [%]
0-3.5	95	5
3.5-4	95->40 (gradient)	5->60 (gradient)
4-6.5	40	60
6.5-7	40->0 (gradient)	60->100 (gradient)
7-8	0	100
8-8.5	0->95 (gradient)	100->5 (gradient)
8.5-18	95	5

For a minimization of the statistical errors, each sample was analyzed three times (in case of the analyses of the electrolyte LP30+VC+LiTFSI and the electrolytes from the NCM111/graphite pouch cells) [40] or four times (in case of the analyses of the electrolytes from the NCM622/graphite pouch cells and the NCM622/silicon-graphite pouch cells) [44]. For the eventual quantifications, the average peak area from these three or four measurements was used [40,44]. The electrolyte components were quantified by HPLC-ESI/MS based on the peaks in traces of certain m/z values, namely EC ($[EC+H^+]$; m/z = 89.1$^+$ u), DMC ($[DMC+H^+]$; m/z = 91.1$^+$ u), DEC ($[DEC+H^+]$; m/z = 119.1$^+$ u), Li^+ ($[Li^+$+2 ACN]; m/z = 89.1$^+$ u), and PF_6^- ($[PF_6^-]$; m/z = 145.0$^-$ u) [40]. The samples for the HPLC-ESI/MS analyses were prepared in a dry room with a dew point of −68 °C. For the preparation of these samples, the electrolytes and the standard substances (pure EC, DMC, DEC, and $LiPF_6$) were each diluted with ACN. For the quantifications, each mass was weighed during sample preparation.

The external standard method with a ten-point calibration was used to determine the concentrations of EC, DEC, Li^+, and PF_6^- in the fresh electrolyte LP30+VC+LiTFSI and in the electrolytes from the NCM111/graphite pouch cells by HPLC-ESI/MS, respectively. In Table 3.12, the ranges of the mass fractions of these analytes in the samples used for the concerning quantifications in the fresh electrolyte LP30+VC+LiTFSI and in the electrolytes from the NCM111/graphite pouch cells by HPLC-

ESI/MS are shown. The standard samples are the samples with the standard substances (in this case pure EC, DEC, and $LiPF_6$), while the electrolyte samples are the samples with the electrolytes. Additionally, the coefficients of determination of the associated calibration curves R^2 can be seen in Table 3.12.

Table 3.12: The ranges of the electrolyte component mass fractions in the samples used for the quantification of EC, DEC, Li^+, and PF_6^- in the electrolyte LP30+VC+LiTFSI and in the electrolytes from the NCM111/graphite pouch cells by HPLC-ESI/MS with the associated coefficients of determination R^2 [40].

Electrolyte component	Range of the electrolyte component mass fraction in the standard samples [wt%]	Range of the quantified electrolyte component mass fraction in the electrolyte samples [wt%]	R^2 [1]
EC	0.0280-0.2904	0.141-0.155	0.9986
DEC	0.0245-0.2609	0.130-0.140	0.9999
$LiPF_6$	0.00142-0.01643	0.00700-0.00793 (quantified based on the PF_6^- peak)	0.9955 (Li^+) 0.9985 (PF_6^-)

For the quantification of DMC in the fresh electrolyte LP30+VC+LiTFSI by HPLC-ESI/MS, the standard addition method was applied, as it allowed a more accurate DMC quantification compared to the external standard method [40]. For this purpose, six different samples were prepared per analyzed electrolyte. Each one of these six samples contained the same amount of LP30+VC+LiTFSI [40]. Different amounts of DMC were added to five of these six samples, whereas no additional DMC was added to one of these six samples (the so-called “basic sample”) [40]. The range of the mass fraction of the added DMC in the analyzed samples, the range of the quantified DMC mass fraction in the basic samples, plus the associated coefficient of determination R^2 can be seen in Table 3.13.

Table 3.13: The ranges of the DMC mass fractions in the samples used for the DMC quantification in the electrolyte LP30+VC+LiTFSI by HPLC-ESI/MS with the associated coefficient of determination R^2 [40].

Electrolyte component	Range of the mass fraction of the added DMC in the samples [wt%]	Range of the quantified mass fraction of DMC in the basic samples [wt%]	R^2 [1]
DMC	0.0000-0.0546	0.0235-0.0310	0.9992

The concentrations of Li^+ and PF_6^- were determined in the electrolytes from the NCM622/graphite pouch cells and the NCM622/silicon-graphite pouch cells by HPLC-ESI/MS using the external standard method with seven-point calibrations. The ranges of the mass fractions of $LiPF_6$ in the standard samples and the electrolyte samples used for the quantification of Li^+ and PF_6^- in the electrolytes from the NCM622/graphite pouch cells and the NCM622/silicon-graphite pouch cells are listed in Table 3.14. Furthermore, the coefficients of determination of the associated calibration curves R^2 can be seen in Table 3.14.

Table 3.14: The ranges of the mass fractions of $LiPF_6$ in the samples used for the analyses of the electrolytes from the NCM622/graphite pouch cells and the NCM622/silicon-graphite pouch cells by HPLC-ESI/MS with the associated coefficients of determination R^2 [44].

Electrolyte component	Range of the mass fraction of $LiPF_6$ in the standard samples [wt%]	Range of the quantified mass fraction of $LiPF_6$ in the electrolyte samples [wt%]	R^2 [1]
$LiPF_6$	0.00220-0.01241	0.00670-0.00800 (quantified based on the PF_6^- peak)	0.9966 (Li^+) 0.9958 (PF_6^-)

3.8 GC analyses

Two different complementary analysis methods based on GC were applied: GC coupled to a flame ionization detector (FID) for complementary analyses of the electrolytes from the pouch cells and GC coupled to thermal conductivity detectors (TCDs) for analyses of the evolved gases in the pouch cells. In the following four subsections, the conditions of the performed GC analyses, the associated preparation of the samples, and the applied methods for gas extraction from the pouch cells are described. Turbomass 6.1.2 and TotalChrom 6.3.4 software packages were used to control the system and evaluate the data from the GC measurements. The gas extractions, the sample preparations for the GC analyses, the GC analyses, and the evaluation of the resulting measurement data were done by Dr. Andreas Hofmann from the “Institut für Angewandte Materialien-Werkstoffkunde” (IAM-WK) and Dr. Freya Janina Müller from the “Institute for Applied Materials-Energy Storage Systems” (IAM-ESS).

3.8.1 GC coupled to flame ionization detector (GC-FID)

DEC, EC, DMC, and VC were quantified in the electrolytes from the NCM111/graphite pouch cells using a Clarus 690 GC (PerkinElmer, USA) coupled to a FID. A precise description of the conditions of the GC-FID analyses for the quantification of DEC, EC, DMC, and VC in the electrolytes from the NCM111/graphite pouch cells plus the associated sample preparation can be found in literature [40]. In addition, the same GC-FID system was used to quantify FEC in the electrolytes from the NCM622/silicon-graphite pouch cells. For the separation of the electrolyte components, an OPTIMA 5MS column (Macherey-Nagel, Germany) was utilized with the following characteristics: 30 m length x 0.25 mm interior diameter and 0.5 µm film thickness. The injection volume was 0.5 µl and the injector temperature was 250 °C. Helium gas 6.0 was used as carrier gas at an initial pressure of 200 kPa (in case of the analyses of the electrolytes from the NCM111/graphite pouch cells) or 220 kPa (in case of the analyses of the electrolytes from the NCM622/silicon-graphite pouch cells). For the injections, the split flow was set to 10 $ml \cdot min^{-1}$ (in case of the analyses of the electrolytes from the NCM111/graphite pouch cells) or 20 $ml \cdot min^{-1}$ (in case of the analyses of the electrolytes from the NCM622/silicon-graphite pouch cells). The temperature of the column oven was changed during the

GC-FID analyses of the electrolytes from the NCM111/graphite pouch cells as follows: Constantly 40 °C during the first min, followed by a heating at 20 °C·min^{-1} until a maximum temperature of 250 °C. The temperature of the column oven was changed during the GC-FID analyses of the electrolytes from the NCM622/silicon-graphite pouch cells as follows: Constantly 40 °C during the first 1.5 min, heating at 20 °C·min^{-1} until a temperature of 220 °C, 5 min at a constant temperature of 220 °C, heating at 20 °C·min^{-1} until a maximum temperature of 280 °C, 1.5 min at a constant temperature of 280 °C. The gas flows in the FID were 450 ml·min^{-1} for synthetic air and 45 ml·min^{-1} for hydrogen. During the measurements, the temperature of these gases was 280 °C (in case of the analyses of the electrolytes from the NCM111/graphite pouch cells) or 250 °C (in case of the analyses of the electrolytes from the NCM622/silicon-graphite pouch cells). Each sample was analyzed three times. For the quantifications of DEC, EC, DMC, VC, and ACN in the samples with the electrolytes from the NCM111/graphite pouch cells by GC-FID, the external standard method with a seven-point calibration was used. For the quantifications of FEC in the electrolytes from the NCM622/silicon-graphite pouch cells by GC-FID, the external standard method with a nine-point calibration was used. Only electrolytes extracted from pouch cells by the DEC extraction method were analyzed by GC-FID.

The ACN concentrations were additionally quantified in the samples used for the analyses of the electrolytes from the NCM111/graphite pouch cells to correct the respective, quantified concentrations of DEC, EC, DMC, and VC in the electrolytes from these cells [40]. The concentrations of EC, DMC, and VC in the original electrolyte (before DEC injection) from the NCM111/graphite pouch cells were determined based on the corrected, quantified concentrations of DEC, EC, DMC, and VC in the extracts from these cells by GC-FID according to Equation 3.1. In Table 3.15, the ranges of the mass fractions of DEC, EC, DMC, VC, and ACN in the analyzed samples used for the quantifications in the electrolytes from the NCM111/graphite pouch cells by GC-FID can be seen. The samples with the pure standard substances (in this case pure DEC, EC, DMC, VC, and ACN) are the standard samples, whereas the electrolyte-containing samples are the electrolyte samples. The coefficients of determination of the associated calibration curves R^2 are also listed in Table 3.15.

Table 3.15: The ranges of the electrolyte component mass fractions in the samples used for the analyses of the electrolytes from the NCM111/graphite pouch cells by GC-FID with the associated coefficients of determination R^2 [40].

Electrolyte component	Range of the electrolyte component mass fraction in the standard samples [wt%]	Range of the quantified electrolyte component mass fraction in the electrolyte samples [wt%]	R^2 [1]
DEC	0.0040-0.0241	0.0122-0.0189	0.9998
EC	0.0040-0.0241	0.0089-0.0162	0.9997
DMC	0.0041-0.0246	0.0067-0.0132	0.9999
VC	0.00028-0.00170	0.00032-0.00114	0.9988
ACN	0.082-0.489	0.350-0.460	0.9999

The ranges of the FEC mass fractions in the analyzed samples that were used for the FEC quantification in the electrolytes from the NCM622/silicon-graphite pouch cells by GC-FID, including the associated coefficients of determination R^2 are shown in Table 3.16.

Table 3.16: The ranges of the FEC mass fractions in the samples used for the analyses of the electrolytes from the NCM622/silicon-graphite pouch cells by GC-FID, including the associated coefficients of determination R^2.

Electrolyte component	Range of the FEC mass fraction in the standard samples [wt%]	Range of the quantified FEC mass fraction in the electrolyte samples [wt%]	R^2 [1]
FEC	0.0082-0.6700	0.0841-0.1362	0.9984

3.8.2 GC coupled to thermal conductivity detector (GC-TCD)

A Clarus 690-Arnel GC system (PerkinElmer, USA) coupled to two TCDs were used for the quantification of the evolved amounts of the gases ethylene (C_2H_4) and methane (CH_4) in NCM622/graphite pouch cells. Additionally, the same GC-TCD system was used to quantify the evolved gases hydrogen (H_2), carbon dioxide (CO_2), ethylene, ethane (C_2H_6), methane, and carbon monoxide (CO) in NCM622/silicon-graphite pouch cells. The applied methods for gas extraction from the pouch cells are described in subsection 3.8.3 and subsection 3.8.4. The extracted gases from the pouch cells were injected into the gas injection system to fill all gas loops of the GC system with the gas from the pouch cells. For the GC-TCD measurements, either helium or nitrogen was used as carrier gas. The analyzed gases from the pouch cells were detected by the TCD-Arnel GC system. The conditions of the GC-TCD analyses for the quantification of ethylene and methane in the NCM622/graphite pouch cells plus the associated sample preparation is also described in literature [44].

3.8.3 Gas extraction by argon injection

The gases were extracted from the NCM622/graphite pouch cells by argon injection. The procedure of this gas extraction method is also described in literature [44]. First, a septum was fixed onto the pouch bag foil of the cell. Following this, 5 ml argon gas was injected into the pouch cell through the septum by a gas-tight syringe in an argon-filled glovebox (with a water and oxygen content below 1 ppm). Afterwards, 5 ml of the gas mixture consisting of the original gas of the pouch cell (before injection of argon) and the injected argon gas was extracted from the pouch cell using a gas-tight syringe. Subsequently, this gas-tight syringe was brought out of the glovebox, and the extracted gas was injected into the gas injection system to be analyzed by GC-TCD.

3.8.4 Gas extraction by the gas extraction valve

The gas extraction by a gas extraction valve was used to remove the gas from NCM622/silicon-graphite pouch cells. This gas extraction method is currently registered as patent [45]. The gas extraction method allows not only the determination of the concentrations of the evolved gases in the pouch cell, but also the determination of their absolute amounts. For this purpose, NCM622/silicon-graphite pouch cells were built each with an integrated gas extraction valve (a female double-end shutoff (DESO) Swagelok valve). For the gas extraction, the gas extraction valve of the cell was connected to an evacuated gas loop equipped with a male DESO Swagelok valve. After connection, the gas from the pouch cell expanded into the evacuated gas loop. The pressure in the gas loop was measured before and after connecting the cell. Afterwards, the gas from the pouch cell in the gas loop was injected into the gas injection system to be analyzed by GC-TCD.

Based on the determined pressure difference in the gas loop before and after connecting the cell Δp in Pa, the volume of the gas loop V in m^3, the measured room temperature T in K, and the molar gas constant R in $J \cdot K^{-1} \cdot mol^{-1}$, the total amount of the evolved gases in the pouch cell n_{gases} in mol was calculated by means of the ideal gas law according to Equation 3.6.

$$n_{gases} = \frac{\Delta p \cdot V}{R \cdot T} \tag{3.6}$$

The amounts of the individual gases n_{gas} in mol were determined by means of Equation 3.7 based on the total amount of the evolved gases in the pouch cell n_{gases} in mol and the mole fraction of the respective gas x_{gas} quantified by GC-TCD.

$$n_{gas} = n_{gases} \cdot x_{gas} \tag{3.7}$$

3.9 XPS analyses

The XPS analyses were performed by means of a K-Alpha spectrometer (Thermo Fisher Scientific, UK) using a microfocused, monochromated Al K_α X-ray source with a spot size of 400 µm and a pass energy of 50 eV. The Thermo Avantage software by Parry et al. [46] was used for data acquisition and handling. The spectra were fitted by one or more Voigt profiles. Scofield sensitivity factors were used for the quantifications. All spectra were referenced in binding energy to the hydrocarbon peak at 285 eV in the C1s spectrum. The signal intensities of each spectrum were normalized to the respective maximum intensity of the spectrum.

For sample preparation, the pouch cells were opened and electrode pieces were cut. Following this, the cut electrode pieces were briefly submerged in 1 ml DMC to remove electrolyte from the electrode pieces. The electrode pieces were subsequently mounted on a sample holder by means of conductive

copper tape. This sample preparation was done in an argon-filled glovebox with an oxygen and water content below 1 ppm. A transfer module was used for the transfer of the prepared samples to the spectrometer under inert gas conditions.

The conditions of the XPS measurements and the associated sample preparation are also described in literature [40,44]. The sample preparations for the XPS measurements, the XPS measurements, and the evaluation of the resulting measurement data were conducted by Lydia Gehrlein from the IAM-ESS and Dr. Julia Maibach from the IAM-ESS.

3.10 SEM/EDX analyses

The SEM images were acquired by means of a Supra 55 (Carl Zeiss AG, Germany). The EDX analyses were realized through an Ultim Extreme detector (Oxford Instruments, UK) with AZtec software (version 4.2). During the measurements, the SEM acceleration voltage was 4 kV.

For the sample preparation, the electrodes were removed from the opened pouch cell and immersed in DMC for one hour. Following this, pieces of around 0.5 cm^2 were cut out of the electrodes. These electrode pieces were subsequently mounted on sample holders by means of conductive tapes. Furthermore, no sputter-coating was applied. For the acquisition of cross-section images, the electrode pieces were cross-sectioned using an ion beam milling system (EM TIC 3X, Leica Microsystems GmbH, Germany) with argon ions, an accelerating voltage of 6 kV, and a gun current of 2.2 mA.

The conditions of the SEM and EDX analyses, as well as the associated sample preparation are also specified in literature [40,44]. The acquisition of the SEM images and the acquisition of the data from the EDX analyses were done by Dr. Marcus Müller from the IAM-ESS.

3.11 ICP-OES analyses

An iCAP 7600 ICP-OES Duo (Thermo Fisher Scientific, USA) was used for the quantitative analyses of the elements lithium, manganese, nickel, and cobalt in electrodes. The quantification of these elements was realized by means of four different matrix adapted standard samples and the internal standard scandium, which was added to each sample with a mass fraction of around $2.00 \cdot 10^{-4}$ wt%. For the quantification of lithium, manganese, nickel, and cobalt, the three major wavelengths of the respective element were used.

The ranges of the mass fractions of the quantified elements in the samples used for the quantifications in the anodes can be seen in Table 3.17. In addition, the wavelengths used for these quantifications are shown in Table 3.17.

Table 3.17: The ranges of the mass fractions of the analyzed elements in the standard samples and the anode-containing samples. Additionally, the wavelengths used for the quantifications are listed [44].

Element	Range of the element mass fraction in the standard samples [wt%]	Range of the quantified element mass fraction in the anode-containing samples [wt%]	Wavelength [nm]
Lithium	$5.70 \cdot 10^{-5}$-$5.67 \cdot 10^{-4}$	$2.38 \cdot 10^{-4}$-$4.88 \cdot 10^{-4}$	460.286/610.362/670.784
Manganese	$3.80 \cdot 10^{-7}$-$3.81 \cdot 10^{-6}$	$6.00 \cdot 10^{-7}$-$4.30 \cdot 10^{-6}$	257.610/259.373/260.569
Nickel	$7.60 \cdot 10^{-7}$-$7.59 \cdot 10^{-6}$	$1.00 \cdot 10^{-6}$-$4.50 \cdot 10^{-6}$	221.647/227.021/231.604
Cobalt	$3.80 \cdot 10^{-7}$-$3.81 \cdot 10^{-6}$	$1.00 \cdot 10^{-7}$-$8.00 \cdot 10^{-7}$	228.616/230.786/238.892

In Table 3.18, the ranges of the mass fractions of lithium in the samples used for the lithium quantifications in the cathodes are listed. Furthermore, the wavelengths used for these quantifications can be seen in Table 3.18.

Table 3.18: The ranges of the mass fractions of lithium in the standard samples and the cathode-containing samples. Besides, the wavelengths used for the lithium quantifications are shown [44].

Element	Range of the element mass fraction in the standard samples [wt%]	Range of the quantified element mass fraction in the cathode-containing samples [wt%]	Wavelength [nm]
Lithium	$6.0 \cdot 10^{-5}$-$2.36 \cdot 10^{-4}$	$1.16 \cdot 10^{-4}$-$1.85 \cdot 10^{-4}$	460.286/610.362/670.784

Before the ICP-OES analyses, the pouch cells were opened and the electrodes were removed. These electrodes were subsequently submerged in DMC for one hour. Afterwards, the electrodes were air dried at room temperature for half an hour. To calculate the absolute amounts of the quantified elements in the electrodes, the two anodes and the two cathodes from each investigated pouch cell were subsequently weighed. Following this, pieces were cut out of these electrodes. These pieces of the anodes and cathodes with a total weight of around 40-70 mg per cell were weighed and submerged in aqua regia (consisting of 6 ml hydrochloric acid subboiled and 2 ml nitric acid subboiled). The aqua regia with the electrode pieces was placed into a graphite oven at a temperature of 80 °C for four hours.

The absolute amount of substance of the respective, quantified element in the anodes or cathodes from a pouch cell $n_{element}$ in mol is given by Equation 3.8. The mass fraction of the concerning element in the anodes or cathodes from the pouch cell $w_{element}$ was quantified by ICP-OES. The weighed mass of the two anodes or the two cathodes from the investigated pouch cell is $m_{electrodes}$ in g, while the molar mass of the concerning element is $M_{element}$ in g/mol.

$$n_{element} = \frac{w_{element} \cdot m_{electrodes}}{M_{element}} \tag{3.8}$$

A description of the conditions of the ICP-OES measurements, as well as the associated sample preparation can also be found in literature [44]. The sample preparations for the ICP-OES measurements, the ICP-OES measurements, and the evaluation of the resulting measurement data were conducted by Dr. Thomas Bergfeldt from the “Institut für Angewandte Materialien-Angewandte Werkstoffphysik“ (IAM-AWP).

4 Investigations with the NCM111/graphite pouch cells

In this chapter the achieved accuracy and precision of the quantifications by HPLC-UV/Vis and HPLC-ESI/MS in the non-extracted, fresh electrolyte LP30+VC+LiTFSI are presented. Furthermore, the influence of the extraction from NCM111/graphite pouch cells filled with the electrolyte LP30+VC+LiTFSI on the electrolyte composition is investigated. For this purpose, the analyzed electrolytes are extracted from untreated, fresh NCM111/graphite pouch cells by centrifugation (a standard extraction method) and by the DEC extraction method. To check the plausibility of the determination of the absolute amounts in the electrolytes extracted by the DEC extraction method, the quantified amounts of the electrolyte components in the fresh cells are compared to the amounts of the electrolyte components calculated by the weighed masses. Eventually, electrolytes are extracted from NCM111/graphite pouch cells with LP30+VC+LiTFSI as initial electrolyte at different aging steps using the DEC extraction method. These extracted electrolytes are analyzed to investigate the influence of electrochemical aging on the electrolyte composition. Complementary analysis methods, namely GC-FID, XPS, and SEM, are applied to gain deeper insight into the electrolyte decomposition during cell aging. The GC-FID analyses and the evaluation of the resulting measurement data presented in this chapter were conducted by Dr. Andreas Hofmann from the “Institut für Angewandte Materialien-Werkstoffkunde” (IAM-WK). The XPS investigations, including the evaluations were realized by Lydia Gehrlein from the “Institute for Applied Materials-Energy Storage Systems” (IAM-ESS) for this chapter. The SEM images shown in this chapter were acquired by Dr. Marcus Müller from the IAM-ESS. The results presented in this chapter are described in a publication [40].

4.1 Accuracy and precision determination of quantifications by HPLC

To determine the accuracies and precisions of the quantifications, a freshly mixed, non-extracted electrolyte with a known composition consisting of 900 µl LP30+VC+LiTFSI and 500 µl DEC is quantitatively analyzed by HPLC-UV/Vis and HPLC-ESI/MS. The composition of this fresh electrolyte corresponds to the expected electrolyte composition after DEC injection in the examined, electrochemically untreated, fresh NCM111/graphite pouch cells. DEC, EC, DMC, VC, Li^+, and PF_6^- are quantified in the fresh electrolyte three times completely independent of each other on three different days resulting in three single values and one average value per quantified component. The indicated uncertainties of the average values correspond to the standard deviations of the mean calculated based on the respective, three single values per indicated average value in the following. These uncertainties are a measure for the precision (random error) of the quantifications. The real mass fractions or concentrations refer to the values calculated based on the weighed masses during mixture of the mentioned, fresh electrolyte. The indicated, average, relative deviations of the quantified mass fractions (or concentrations) from the real mass fractions (or concentrations) indicate the accuracy (systematic error) of the quantifications.

As described in section 3.6, the mass fraction of DEC in the extracted electrolyte needs to be determined for the calculation of the concentrations of EC, DMC, VC, Li^+, and PF_6^- in the original electrolyte before DEC injection. Therefore, a precise and accurate DEC quantification is desirable. For this purpose, the accuracies and the precisions of the DEC quantification by HPLC-UV/Vis and HPLC-ESI/MS are determined, first. Table 4.1 shows the average, percentage deviations of the quantified mass fraction of DEC in the fresh electrolyte from the real mass fraction of DEC. Additionally, the uncertainties of the average, percentage deviations of the quantified mass fraction of DEC in the fresh electrolyte from the real mass fraction of DEC can be seen in Table 4.1.

Table 4.1: Average, relative deviations of the quantified DEC mass fraction in the freshly mixed, non-extracted electrolyte from the real DEC mass fraction, as well as the associated uncertainties [40].

Electrolyte component	Analysis method	Average, relative deviation of quantified mass fraction from real mass fraction [%]	Uncertainty of average, relative deviation of quantified mass fraction from real mass fraction [%]
DEC	HPLC-UV/Vis	+0.9	±0.2
DEC	HPLC-ESI/MS	+1.9	±1.5

The quantification of DEC by HPLC-UV/Vis is more accurate and precise than the DEC quantification by HPLC-ESI/MS, as can be concluded from the data shown in Table 4.1. Hence, DEC is always quantified by HPLC-UV/Vis with the here applied method from now on.

In the next step, the concentrations of EC, DMC, VC, Li^+, and PF_6^- are determined in LP30+VC+LiTFSI using HPLC-UV/Vis and HPLC-ESI/MS. The calculation of these concentrations is described in section 3.6. VC can just be quantified by HPLC-UV/Vis, while Li^+ and PF_6^- can just be analyzed by HPLC-ESI/MS. In Table 4.2, the real concentrations and the average, quantified concentrations of EC, DMC, VC, Li^+, and PF_6^- in LP30+VC+LiTFSI are listed. In addition, the average, percentage deviation of the quantified concentration from the real concentration, as well as the associated uncertainty can be found in Table 4.2.

Table 4.2: The real and average, quantified concentrations in LP30+VC+LiTFSI, the average relative deviations of the quantified concentrations from the real concentrations, and the associated uncertainties [40].

Electrolyte component	Analysis method	Real concentration in LP30+VC+LiTFSI [mmol·g^{-1}]	Average, quantified concentration in LP30+VC+LiTFSI [mmol·g^{-1}]	Average, relative deviation of quantified concentration from real concentration [%]	Uncertainty of average, relative deviation of quantified concentration from real concentration [%]
EC	HPLC-UV/Vis	4.85	5.13±0.04	+5.8	±0.8
EC	HPLC-ESI/MS	4.85	5.20±0.08	+7.2	±1.5
DMC	HPLC-UV/Vis	4.74	4.74±0.02	+0.0	±0.4
DMC	HPLC-ESI/MS	4.74	4.80±0.34	+1.3	±7.1
VC	HPLC-UV/Vis	0.348	0.352±0.002	+1.1	±0.6
Li^+	HPLC-ESI/MS	0.76	0.79±0.03	+4.0	±3.8
PF_6^-	HPLC-ESI/MS	0.76	0.78±0.02	+2.6	±2.6

As can be seen in Table 4.2, HPLC-UV/Vis enable a quantification of EC and DMC with higher accuracy and precision compared to HPLC-ESI/MS. Thus, EC, DMC, and VC are always quantified by HPLC-UV/Vis with the here applied methods from now on. Li^+ and PF_6^- are always quantitatively analyzed by HPLC-ESI/MS with the here applied methods in the following. With these selected analysis methods, quantification of EC, DMC, VC, Li^+, and PF_6^- is possible with percentage deviations of the quantified concentrations from the real concentrations of <6% [40]. The associated, relative standard deviations of the mean of the quantified concentrations are <±4% [40].

The quantified concentrations of EC, VC, Li^+, and PF_6^- in Table 4.2 are higher than the real concentrations, probably due to a certain evaporation of ACN during sample preparation. The quantified DMC concentrations agree (almost) perfectly with the real DMC concentrations, supposedly because DMC also evaporates during mixing of the electrolyte and the sample preparation compensating the effect of ACN evaporation [40].

4.2 Influence of the extraction method on the electrolyte composition

To investigate the electrolyte composition in the pouch cells, the electrolyte needs to be extracted from the pouch cells. Hence, it is imperative to determine the influence of the extraction itself on the electrolyte composition. For this purpose, electrolyte is extracted by centrifugation and by the DEC extraction method from three electrochemically untreated, fresh cells each. Centrifugation is a known and approved method for electrolyte extraction from battery cells [47–54]. The quantification of the electrolyte components in the extracted electrolytes is conducted by HPLC using the selected analysis methods (see section 4.1). For both extraction methods, the analyses of the three extracted electrolytes from the three fresh cells are conducted on three different days completely independent of each other. Thus, three single values are obtained. The indicated average values are the means of these three single values in the following. The shown errors correspond to the standard deviations of the mean calculated based on the three single values per indicated average value.

In Figure 4.1, the average, quantified concentrations in the electrolytes from the fresh pouch cells are shown for both extraction methods. Additionally, the average, quantified concentrations in the freshly mixed, non-extracted electrolytes can be seen.

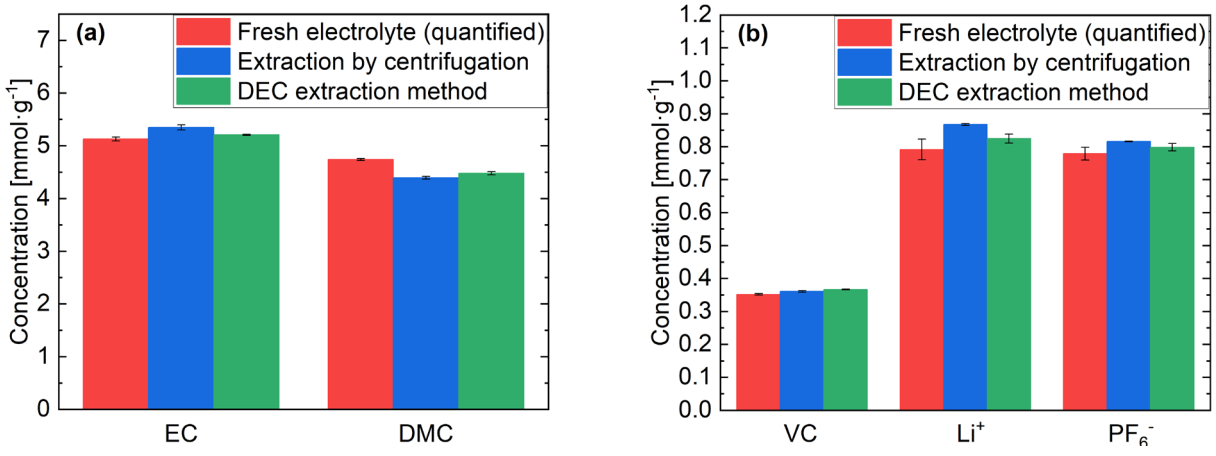

Figure 4.1: Average, quantified concentrations of EC, DMC (a), as well as VC, Li^+, and PF_6^- (b) in fresh, non-extracted electrolytes, as well as in extracted electrolytes from fresh, untreated cells using centrifugation or the DEC extraction method [40].

The data in Figure 4.1 shows that the concentrations in the electrolytes extracted by centrifugation and by the DEC extraction method are similar. The DMC concentrations in the extracted electrolytes are reproducibly below the DMC concentration in the fresh electrolyte, which might be ascribed to a certain, inevitable DMC evaporation during sealing of the cell under reduced pressure and/or during the extraction itself. In fact, DMC is by far the most volatile component in these electrolytes. Due to this DMC loss, the concentrations of the other components are accordingly higher in the extracts compared to the corresponding, quantified concentrations in the fresh electrolyte. Summarized, the DEC extraction method represents thus a reproducible and reliable extraction method like the centrifugation.

As explained in section 3.6, the DEC extraction method allows additionally the determination of the absolute amounts of substance of the electrolyte components in the cell based on the quantified concentrations in the extract and the mass of the injected DEC. To check the validity of the quantification of the absolute amounts of substance in the cell, the relative amounts of substance of EC, DMC, VC, Li^+, and PF_6^- are determined in the three fresh cells. Besides, these relative amounts of substance are also determined in the three fresh, non-extracted electrolytes. The relative amount of substance corresponds to the quantified, absolute amount of substance divided by the respective, expected amount of substance. The expected amount of substance is calculated based on the weighed masses during mixing of the electrolyte LP30+VC+LiTFSI and the weighed mass of the electrolyte filled into the cell during cell assembly. A precise description of the calculation of the absolute and relative amounts of substance in the cells can be found in section 3.6. The quantified, average, relative amounts of substance in the in the fresh, untreated cells and in the non-extracted, fresh electrolytes are shown in Figure 4.2.

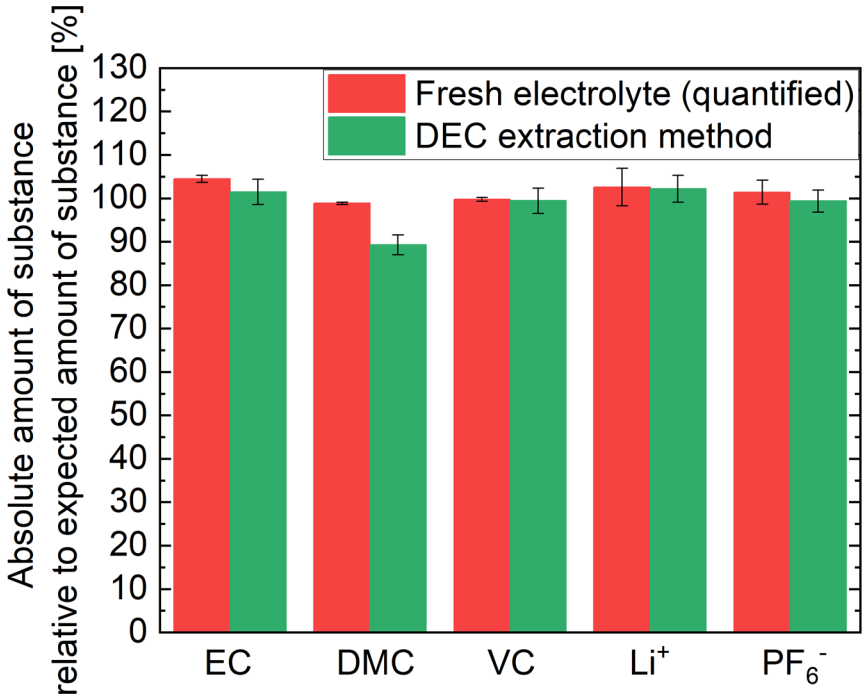

Figure 4.2: Average, relative amounts of substance of EC, DMC, VC, Li^+, and PF_6^- in the fresh, non-extracted electrolytes and in the fresh, untreated pouch cells [40].

The quantified, absolute amounts of substance are consistently close to the expected amounts of substance, as can be concluded from Figure 4.2. Just the relative amounts of substance of DMC in the fresh cells are reproducibly below the setpoint of 100%, due to the mentioned DMC loss during the sealing of the cell and/or the extraction procedure. Hence, the determination of the absolute amounts of substance in the pouch cells using the DEC extraction method is self-consistent.

4.3 Capacities and internal resistances

The electrochemical aging of the electrolyte in NCM111/graphite pouch cells initially filled with LP30+VC+LiTFSI is investigated using the DEC extraction method. These cells with an initial capacity of about 88 mAh are cycled at 2 C charge and 3 C discharge for different numbers of cycles. In Figure 4.3(a), the relative discharge capacity is plotted in dependence on the number of cycles for the investigated cells that are cycled until a remaining capacity of 80%. The relative discharge capacity is the absolute discharge capacity divided by the initial discharge capacity. Additionally, the regularly measured DC internal resistances at different SOCs are shown in dependence on the number of cycles in Figure 4.3(b) for these cells.

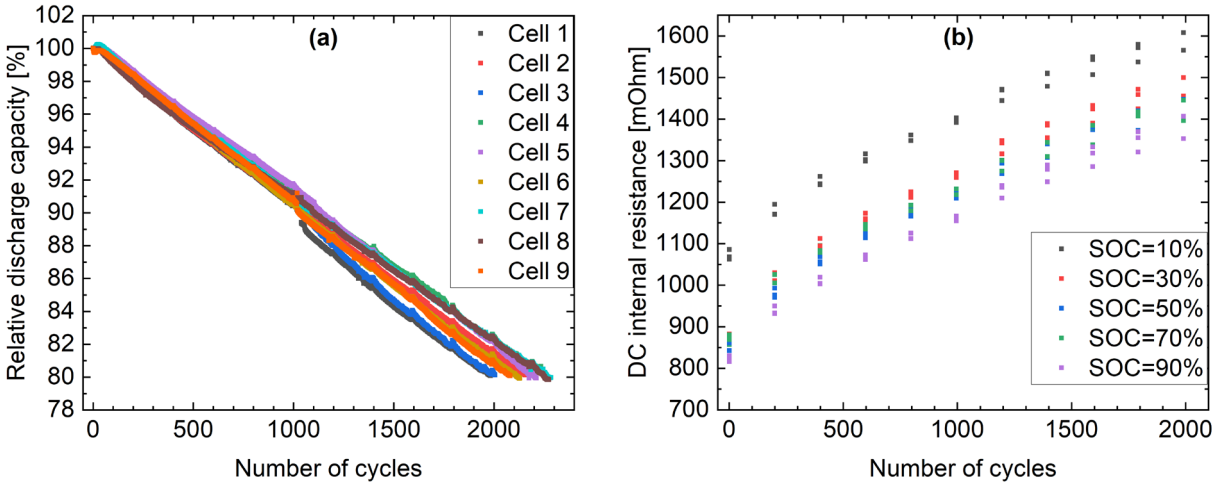

Figure 4.3: (a) Relative discharge capacity of the investigated NCM111/graphite pouch cells cycled until a remaining capacity of 80% in dependence on the number of cycles. (b) DC internal resistances of three of the NCM111/graphite pouch cells cycled until a remaining capacity of 80% at various SOCs in dependence on the number of cycles [40].

The relative discharge capacities in Figure 4.3(a) and the DC internal resistances in Figure 4.3(b) of the different cells show similar trends suggesting reproducible aging behavior of the investigated cells. Furthermore, the relative discharge capacities in Figure 4.3(a) decrease linearly with growing number of cycles indicating continuous cell aging during prolonged cycling. The DC internal resistances in Figure 4.3(b) increase continuously with the number of cycles. An increase of the DC internal resistance with the number of cycles is reported in literature especially for cells with VC-containing electrolytes [49].

4.4 Investigation of the electrochemical decompositions in the electrolyte

For the investigation of the electrochemical electrolyte decomposition in pouch cells, electrolytes are extracted from three electrochemically untreated, fresh cells, three cells after formation, three cells after 25 cycles, and three cells after about 2000 cycles (with a remaining capacity of 80%) applying the DEC extraction method. Each of these cells are NCM111/graphite pouch cells that are initially filled with the electrolyte LP30+VC+LiTFSI. The extracted electrolytes are quantitatively analyzed by HPLC with the selected analysis methods (see section 4.1). For comparison, the concentrations of EC, DMC, and VC in the original electrolyte (before DEC injection) are additionally quantified by GC-FID. The electrolytes from each of the three equally treated cells are analyzed completely independent of each other on three different days with three times complete sample preparation resulting in three single values. In the following, each indicated average value represents the mean calculated by the respective three single values. The errors of the average values are the standard deviations of the mean calculated based on the three single values per indicated average value.

In Figure 4.4, the average, quantified concentrations in the original electrolytes (before DEC injection) from the three fresh cells, the three cells each after formation, after 25 cycles, and after about 2000 cycles (with a remaining capacity of 80%) can be seen. The calculation of these concentrations is explained in section 3.6.

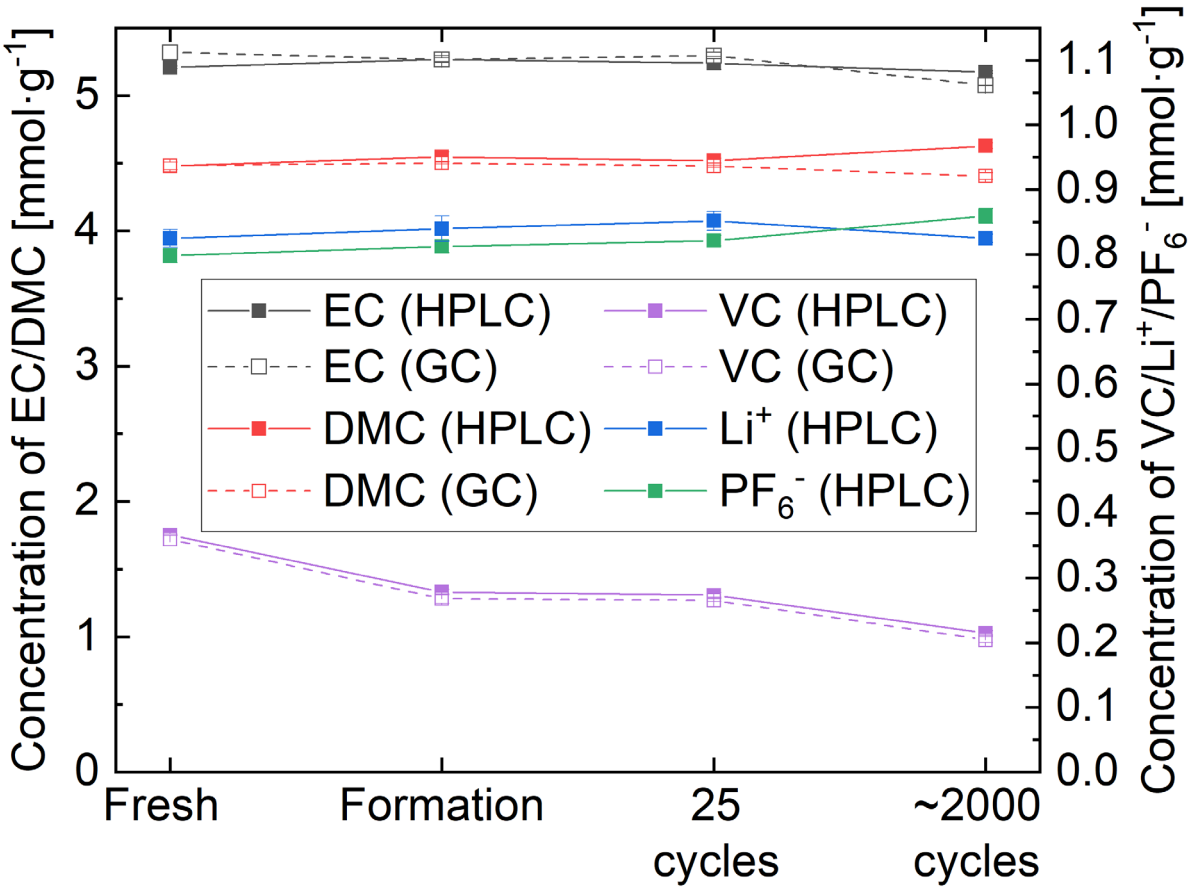

Figure 4.4: Average concentrations of EC, DMC, VC, Li^+, and PF_6^- in the electrolytes from cells at different stages of electrochemical aging. EC, DMC, and VC are quantified by HPLC-UV/Vis and GC-FID, while Li^+ and PF_6^- are quantified by HPLC-ESI/MS [40].

The concentrations in Figure 4.4 show a continuous decrease of the VC concentration, suggesting solely VC decomposition during formation and cycling. Simultaneously, the other concentrations do not change significantly. The concentrations of EC, DMC, and VC quantified by HPLC-UV/Vis are close to the corresponding concentrations quantified by GC-FID. Thus, both analysis methods enable a precise and accurate quantification of EC, DMC, and VC in battery electrolytes [40]. The error bars in Figure 4.4 are barely visible since the quantified concentrations are highly reproducible.

The average, relative amounts of substance in the three fresh cells, the three cells each after formation, after 25 cycles, and after about 2000 cycles (with a remaining capacity of 80%) are shown in Figure 4.5. The relative amount of substance is the quantified, absolute amount of substance divided by the respective initial amount of substance. The initial amount of substance is calculated based on the weighed masses during mixing of the electrolyte LP30+VC+LITFSI and the weighed mass of the

electrolyte filled into the cell during cell assembly. The calculation of the absolute and relative amounts of substance in the cells is described more precisely in section 3.6.

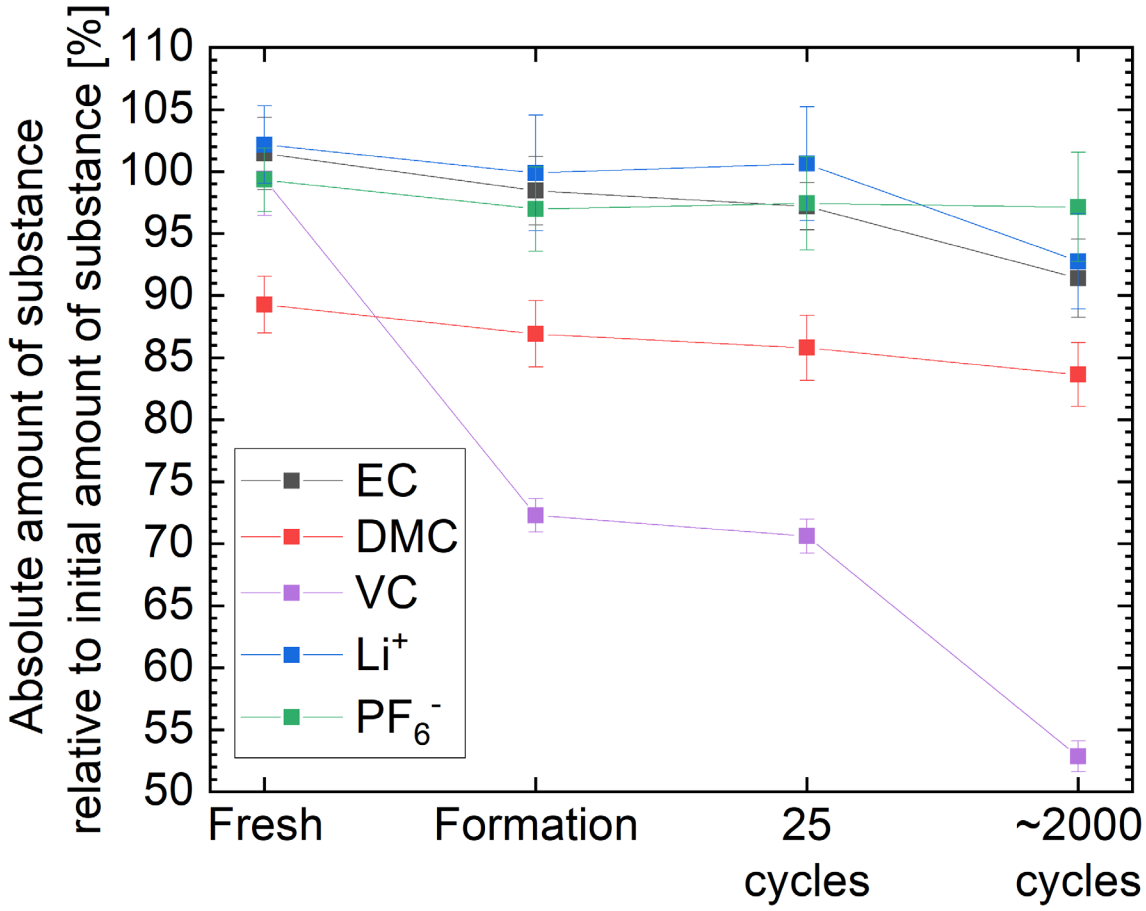

Figure 4.5: Average, relative amounts of substance of EC, DMC, VC, Li^+, and PF_6^- in cells at different aging stages determined by HPLC analyses [40].

Generally, the error bars of the relative amounts of substance in Figure 4.5 are bigger than the error bars of the concentrations in Figure 4.4, as the amounts of substance depend on the quantified concentrations with a certain error and the quantified electrolyte mass with a certain error. The data shown in Figure 4.5 also suggest a pronounced VC decomposition especially during formation, but also during long-term cycling. Furthermore, a slight, but significant decrease of the amount of substance of EC can be identified after about 2000 cycles in Figure 4.5. However, during formation only the decomposition of VC is clearly identifiable in Figure 4.5 indicating preferential VC decomposition. This observation corresponds to the expectations since VC is an SEI-forming additive, which is supposed to be electrochemically decomposed for the buildup of a SEI. A preferential reduction of VC on graphite anodes to SEI components, like poly(VC), is frequently reported in literature [25,26,34]. After formation during cycling the VC decomposition is decelerated, as can be concluded from Figure 4.5. This finding agrees with the reported suppression of further electrolyte decomposition after formation during subsequent cycling once the SEI is built by passivating the anode [26,55]. Qian et al. also detected just

slight decreases of VC content in electrolytes from pouchbag full-cells after formation during subsequent cycling [49]. Qian et al. stated that “almost no VC is further consumed” after formation during subsequent cycling [49]. In fact, it is noteworthy that more than a half of the initial VC amount is still present in the cells even after about 2000 cycles (see Figure 4.5). From this observation, it can be concluded that mass percentages of VC lower than 3 wt% in the initial electrolyte should be sufficient to ensure a high cycling stability [40].

The concentrations in Figure 4.4 and the relative amounts of substance in Figure 4.5 do not change distinctly during electrochemical aging except for the concentrations and amounts of substance of VC. To identify possible, electrochemical decompositions in the electrolytes, it is thus useful to compare the concentrations and relative amounts of substance in the fresh cells directly with the corresponding values in the cells after about 2000 cycles. The electrolytes from the electrochemically untreated, fresh cells are extracted and analyzed just a few days after the cell assembly. The indicated values for “fresh” in Figure 4.4 and Figure 4.5 refer to the electrolytes from these cells. In addition, electrolytes from three electrochemically untreated cells that are stored for about three months at room temperature are also analyzed. These stored cells are assembled on the same day as the cells cycled until a remaining capacity of 80%. The electrolytes from the electrochemically untreated, stored cells are analyzed together with the electrolytes from the cells cycled until a remaining capacity of 80%. Thereby, possible influences of storage on the electrolyte composition, such as DMC evaporation through leaks in the pouch cell or chemical decompositions, can be identified [40]. In Figure 4.6(a), the average concentrations in the electrolytes from the three electrochemically untreated, fresh cells, the three electrochemically untreated, stored cells, and the three cells after about 2000 cycles (with a remaining capacity of 80%) are shown. The average, relative amounts of substance in the three electrochemically untreated, fresh cells, the three electrochemically untreated, stored cells, and the three cells after about 2000 cycles can be seen in Figure 4.6(b).

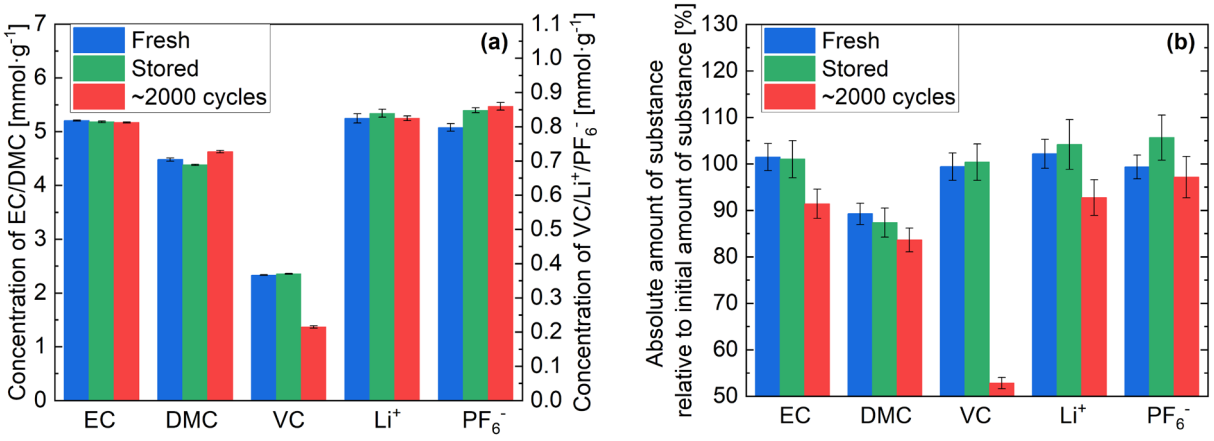

Figure 4.6: Average concentrations (a) and average, relative amounts of substance (b) in the three fresh cells, the three stored cells, and the three cells after about 2000 cycles determined by HPLC analyses [40].

The values in Figure 4.6 suggest no significant change of the electrolyte composition by simple storage of the cells, as the values of the fresh, untreated cells and the stored, untreated cells are close to each other. However, the average, relative amount of substance of EC is reduced significantly by about 10% during prolonged cycling (see Figure 4.6(b)). The average, relative amounts of substance of DMC and PF_6^- are reduced slightly, but not significantly after the 2000 cycles. Nevertheless, the significant decrease of the average, relative amount of substance of Li^+ by about 10% in the cells after about 2000 cycles (see Figure 4.6(b)) suggests a considerable salt decomposition. The concentrations in Figure 4.6(a) reveal just the electrochemical decomposition of VC.

The decomposition of EC, DMC, and the salt cannot be identified based on the concentrations since the electrolyte amount in the cells decreases during electrochemical aging. This electrolyte consumption by electrochemical aging can be observed in Figure 4.7. In Figure 4.7, the average, quantified, relative electrolyte mass in the three electrochemically untreated, fresh cells, the three cells after formation, the three cells after about 2000 cycles (with a remaining capacity of 80%), as well as the three electrochemically untreated, stored cells are depicted. The relative electrolyte mass corresponds to the absolute, quantified electrolyte mass relative to the respective initial electrolyte mass. The initial electrolyte mass is the weighed mass of the electrolyte filled into the cell during cell assembly. The calculation of the absolute, quantified electrolyte mass is specified in section 3.6.

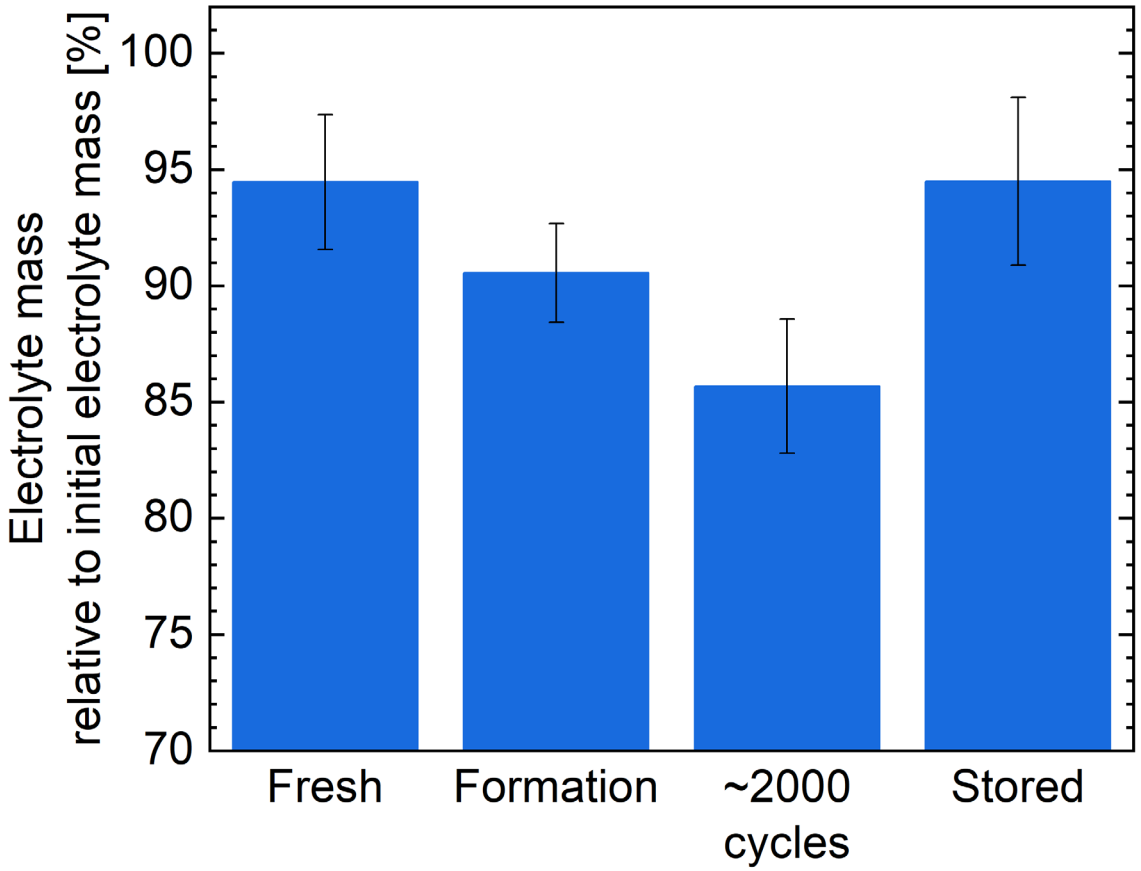

Figure 4.7: Average, relative electrolyte mass in the three electrochemically untreated, fresh cells, the three cells after formation, the three cells after about 2000 cycles, and the three electrochemically untreated, stored cells [40].

The average, relative electrolyte masses in the fresh cells and the stored cells are both similar in Figure 4.7, which confirms the already mentioned finding that the electrolyte composition is not affected by the storage of the cells. Indeed, the average, relative electrolyte masses of these cells are significantly below the setpoint of 100% because of the mentioned DMC loss during sealing of the cells and/or the extraction procedure. During formation and long-term cycling, the electrolyte mass diminishes, as can be concluded from Figure 4.7. According to this, from literature it is known that the formation and growth of surface layers on the electrodes is accompanied by electrochemical decompositions in the electrolyte leading to electrolyte consumption [25,26,33,34,55]. The observed reduction of the electrolyte amount during formation and cycling is the reason, why the consideration of the concentrations allows solely the identification of the VC decomposition. In case of VC, a high fraction of the initially present VC is consumed during formation and long-term cycling (see Figure 4.5 and Figure 4.6(b)), such that the VC decomposition can be detected based on the concentrations. In case of the other electrolyte components, much smaller fractions of the initially present amounts are decomposed during formation and long-term cycling, as can be seen in Figure 4.6(b). Hence, the average concentration of for example EC is not decreased in the cells after about 2000 cycles despite a significant reduction of the average amount of substance of EC in these cells (see Figure 4.6).

Concentrations represent quantity ratios and do not contain information about the actual absolute amounts of the electrolyte components [40]. Thus, the presented DEC extraction method and the associated determination of the absolute amounts of substance allow for the identification of decomposition reactions in battery cells that cannot be detected by the concentrations [40].

For the determination of the absolute magnitudes of the electrochemical decompositions in the cells, it is meaningful to consider the absolute consumptions of the electrolyte components. For that purpose, the difference between the quantified, absolute amount of substance in the electrochemically untreated, stored cell and the cell after about 2000 cycles each from one set of cells analyzed together is calculated resulting in three single values for each component. By these three single values, the respective, average consumption and the associated error (the standard deviation of the mean) are calculated. The calculation of these absolute, decomposed amounts of substance is described precisely in section 3.6. In Figure 4.8, the average consumptions of the electrolyte components during the formation plus the about 2000 cycles are shown.

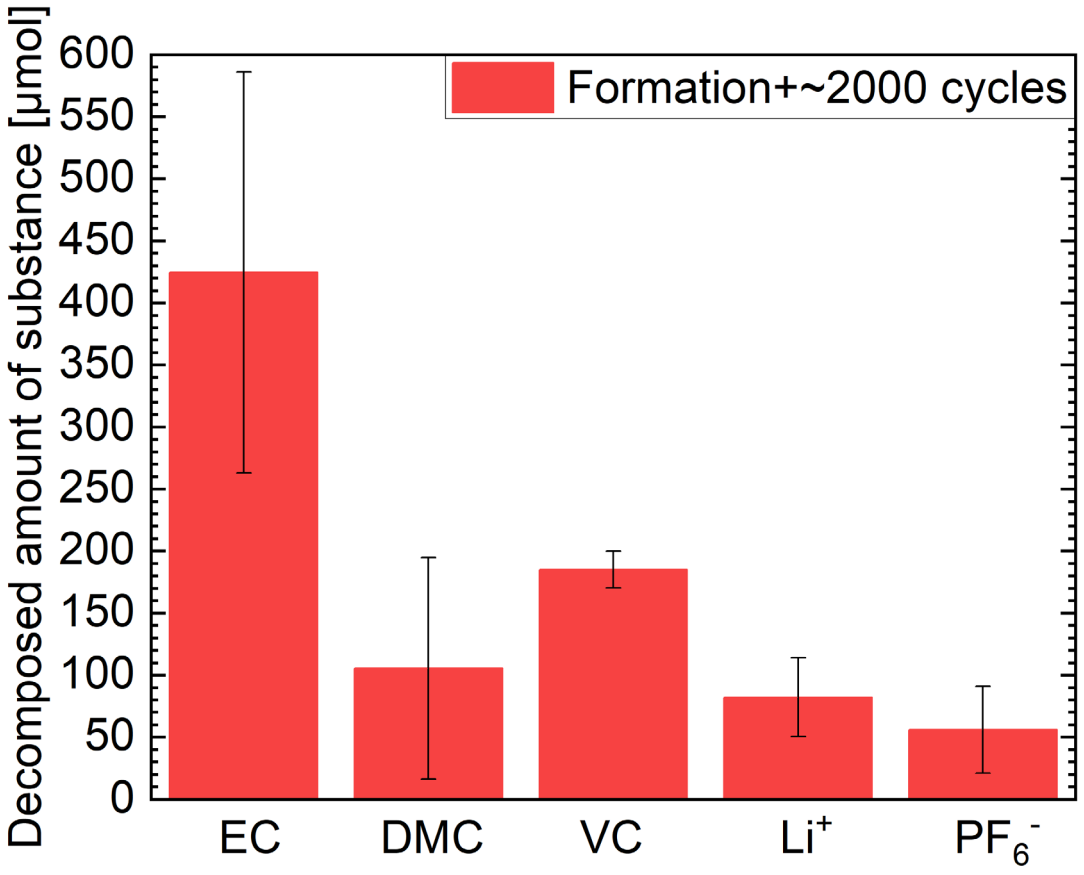

Figure 4.8: Average consumptions of EC, DMC, VC, Li^+, and PF_6^- during formation and about 2000 cycles altogether determined by HPLC analyses [40].

Figure 4.8 shows that the EC consumption during formation and long-term cycling is the highest, while the consumed amount of substance of VC is distinctly lower. This observation seems counterintuitive, as almost one half of the initial VC amount is decomposed during formation and about 2000 cycles,

whereas only about 10% of the initial EC amount is decomposed (see Figure 4.6(b)). This phenomenon can be explained by the fact that the initial VC amount is much lower than the initial EC amount in the cells. Besides, Figure 4.8 indicates just a slight DMC decomposition by formation and prolonged cycling. For lithium-ion battery cells with VC-free electrolytes, a preferential reduction of EC on graphite anodes is reported especially during the first charging associated with SEI buildup [33,35]. There might be a link between the distinct EC decomposition and the composition of the solvation sheath of Li^+. In electrolytes with a high EC concentration, like LP30+VC+LiTFSI, the solvation sheath of Li^+ is mainly composed of EC leading to a pronounced decomposition of EC on the graphite anodes to SEI components [56]. Figure 4.8 clearly shows that the presence of the SEI-forming additive VC does not suppress the decomposition of EC during prolonged cycling. To the best of our knowledge, the EC consumption during cycling in lithium-ion battery cells with VC-containing electrolyte has never been determined before [40]. Additionally, the data in Figure 4.8 suggest a moderate salt decomposition by formation and long-term cycling. $LiPF_6$ decomposes thermally and by the presence of trace water to LiF, POF_3, and HF etc. according to literature [32,57]. In this case, the salt decomposition is clearly electrochemically induced, as the amounts of substance of Li^+ and PF_6^- are diminished just in the cycled cells and not in the electrochemically untreated, stored cells (see Figure 4.6(b)) [40]. Consequently, for the first time the electrochemically induced consumption of $LiPF_6$ can be determined directly in the electrolyte of a lithium-ion battery cell, to the best of our knowledge [40].

4.5 Results from the complementary analysis methods

Complementary analysis methods, namely XPS and SEM, are applied to examine surface layers on the electrodes resulting from the observed electrolyte decompositions.

The C1s and O1s photoelectron spectra of anodes and cathodes extracted from an electrochemically untreated fresh cell, a cell after formation, as well as a cell after about 2000 cycles (with a remaining capacity of 80%) are depicted in Figure 4.9.

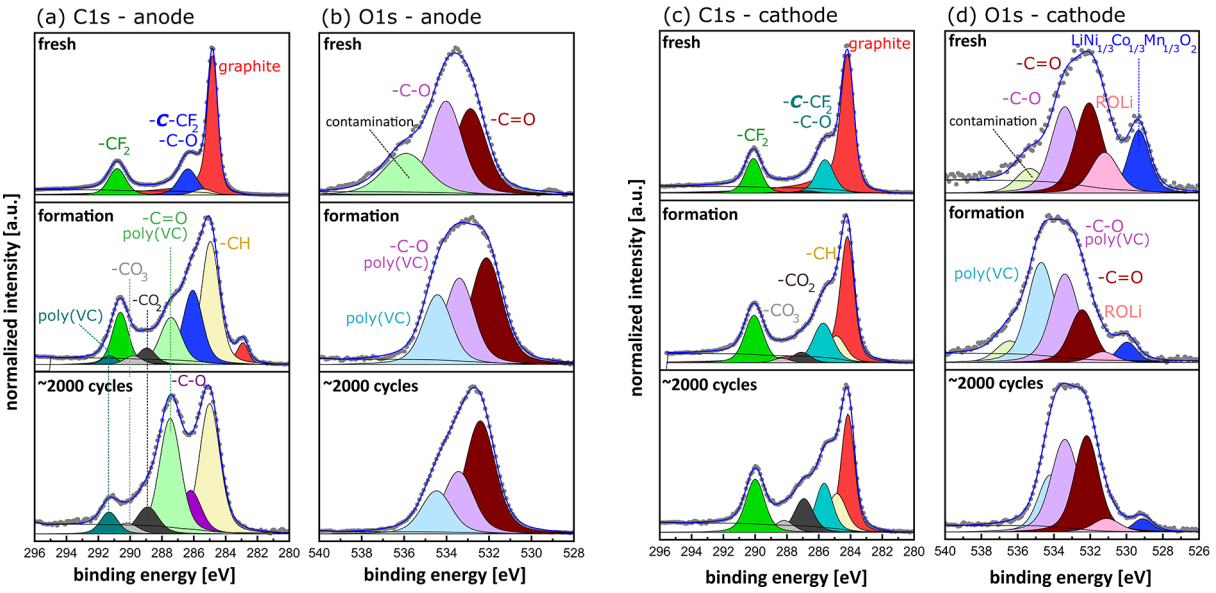

Figure 4.9: C1s photoelectron spectra from anodes (a) and cathodes (c), as well as O1s photoelectron spectra from anodes (b) and cathodes (d) before formation, after formation, and after about 2000 cycles [40].

A precise description of these XPS results can be found in the published paper about the investigations with the NCM111/graphite pouch cells [40]. In the following, only the most important findings are summarized. The C1s spectrum of the anode from the fresh cell in Figure 4.9(a) displays a red graphite peak plus two peaks in green and blue that can be assigned to the binder PVDF. After formation, the graphite peak is decreased in intensity due to the formation of the SEI layer on the graphite during formation (see Figure 4.9(a)). In addition, peaks of the VC decomposition product poly(VC) can be observed in the C1s spectrum of the anode after formation, namely the light green peak and the cyan peak [25,40]. In Figure 4.9(b), the O1s spectrum of the anode after formation also shows peaks (the purple and the light blue peak) that can be assigned to poly(VC) [25,40]. The deposition of the VC decomposition product poly(VC) on the anode surface during formation is consistent with the simultaneously observed, pronounced VC decomposition in the electrolyte [40]. In the C1s spectrum of the anode after about 2000 cycles in Figure 4.9(a), the graphite peak is disappeared suggesting a pronounced SEI growth during long-term cycling [40]. The C1s and O1s spectra of the anodes do not show any obvious changes of the SEI composition after formation during the about 2000 cycles. The F1s photoelectron spectra of the anodes (see Figure A.1 in the Appendix) reveal that the salt decomposition product LiF accumulates during electrochemical aging in the anode surface layer, so that it represents the main SEI component after the about 2000 cycles [40]. This observation agrees with the detected salt decomposition in the electrolyte. However, the detected salt decomposition in the electrolyte is just moderate after about 2000 cycles, while the XPS analyses suggest a SEI mainly composed of LiF. This discrepancy might be attributed to the fact that one PF_6^- anion could

theoretically provide up to six fluorine atoms resulting in the formation of up to six LiF. Hence, the decomposition of moderate amounts of salt could lead to the formation of high amounts of LiF.

The O1s spectra of the cathodes in Figure 4.9(d) show a continuous decrease of the blue peak that can be attributed to $LiNi_{1/3}Co_{1/3}Mn_{1/3}O_2$ (NCM111) representing the active material of the cathode [40]. Consequently, a surface layer also grows on the cathodes during formation and subsequent cycling. Indeed, this surface layer is thin even after the about 2000 cycles since the NCM111 peak is not disappeared even after prolonged cycling [40]. The C1s spectra from the cathodes in Figure 4.9(c) do not indicate remarkable changes after formation and prolonged cycling. Summarized, it can be concluded that most of the decomposition products of the electrolyte are deposited on the anode surface [40].

To examine the thick SEI formed after prolonged cycling further, SEM images are recorded of an anode extracted from a pouch cell after about 2000 cycles (with a remaining capacity of 80%). Two of these SEM images can be seen in Figure 4.10(c) and Figure 4.10(d). Figure 4.10(c) is an image from the edge of the anode (at the spot tagged by the rectangle with the green frame in Figure 4.10(b)), while Figure 4.10(d) is an image from the center of the anode (at the spot indicated by the rectangle with the red frame in Figure 4.10(b)). As can be seen in Figure 4.10(a), the cathode has smaller dimensions than the anode. Hence, electrochemical reactions hardly take place at the edge of the anode during cycling [40]. The SEM image from the edge of the anode in Figure 4.10(c) thus shows the anode almost in the pristine state [40]. By contrast, the SEM image from the center of the anode in Figure 4.10(d) displays the anode in the electrochemically aged state [40].

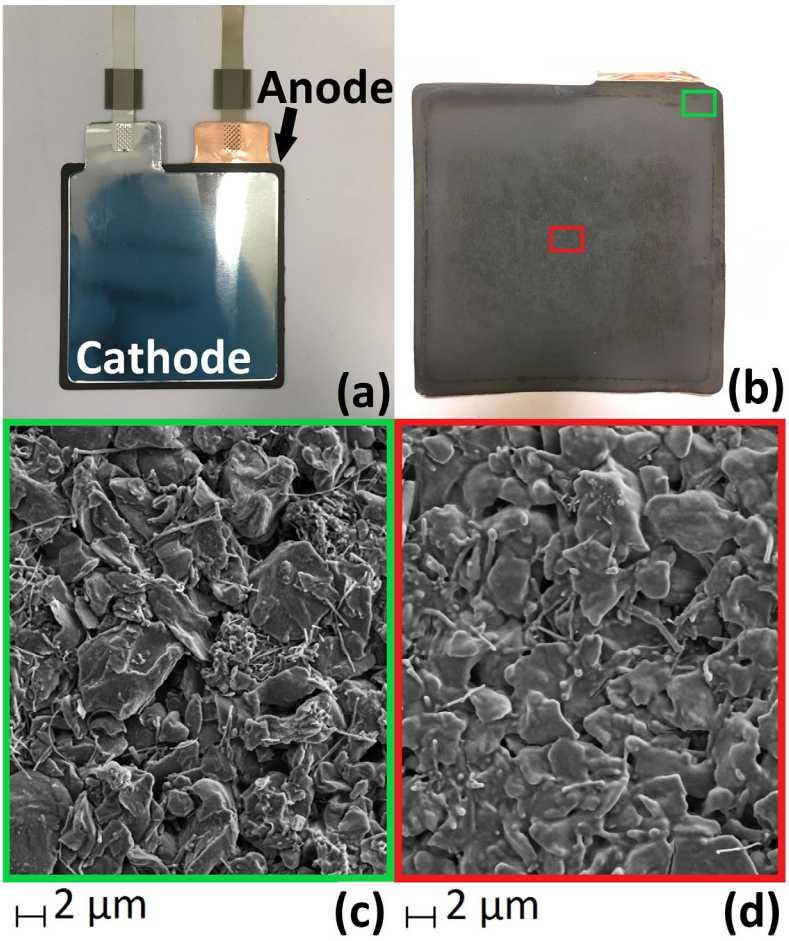

Figure 4.10: (a) Stack of electrodes in a pouch cell. (b) Image of an anode from a pouch cell. The rectangle with the green frame tags the spot, where the SEM image from the edge of the anode is recorded. The rectangle with the red frame indicates the spot, where the SEM image from the center of the anode is recorded. (c) SEM image from the edge of an anode from a cell after about 2000 cycles. (d) SEM image from the center of an anode from a cell after about 2000 cycles [40].

Comparing the image in Figure 4.10(c) with the image in Figure 4.10(d), it can be concluded that a thick SEI is formed during prolonged cycling on the electrochemically active anode surface [40]. This observation confirms the thick SEI detected by XPS on the anodes after prolonged cycling, as well as the simultaneous, pronounced electrolyte decomposition detected by HPLC.

5 Investigations with the NCM622/graphite pouch cells

The approved, newly developed extraction method and the associated determination of the absolute consumptions of the electrolyte components by HPLC analyses (see chapter 4) are used to investigate the electrochemical decomposition of the electrolyte in NCM622/graphite lithium-ion pouch cells initially filled with the electrolyte LP30+VC. The investigated electrolytes are extracted from cells at six different stages of electrochemical aging to track the electrochemical decompositions in the electrolyte precisely. To gain comprehensive insight into the mechanisms responsible for electrolyte decomposition and associated capacity loss of the cell, the complementary analysis methods GC-TCD, XPS, SEM, EDX, and ICP-OES are applied. The results from these studies are presented in this chapter. The GC-TCD analyses and the associated evaluation were conducted by Dr. Andreas Hofmann from the IAM-WK and Dr. Freya Janina Müller from the IAM-ESS. The XPS investigations for this chapter were done by Lydia Gehrlein and Dr. Julia Maibach both from the IAM-ESS. The SEM images and the measurement data from EDX for this chapter were acquired by Dr. Marcus Müller from the IAM-ESS. The data from the ICP-OES measurements presented in this chapter were acquired by Dr. Thomas Bergfeldt from the IAM-AWP. The results presented in this chapter are described in a publication [44].

5.1 Capacities and internal resistances

NCM622/graphite pouch cells are investigated in the electrochemically untreated, fresh state, after formation, after 25 cycles, after cycling until a remaining capacity of 95%, 90%, and 80%. The relative discharge capacities of the examined cells cycled until a remaining capacity of 90% and 80% are shown in dependence on the number of cycles in Figure 5.1(a). These cells are cycled at 2 C charge and 3 C discharge. The relative discharge capacity corresponds to the respective, absolute discharge capacity divided by the absolute discharge capacity of the first cycle with 2 C charge and 3 C discharge. In Figure 5.1(b), the DC internal resistances at different SOCs in dependence on the number of cycles are depicted for three of the cells cycled until a remaining capacity of 80%.

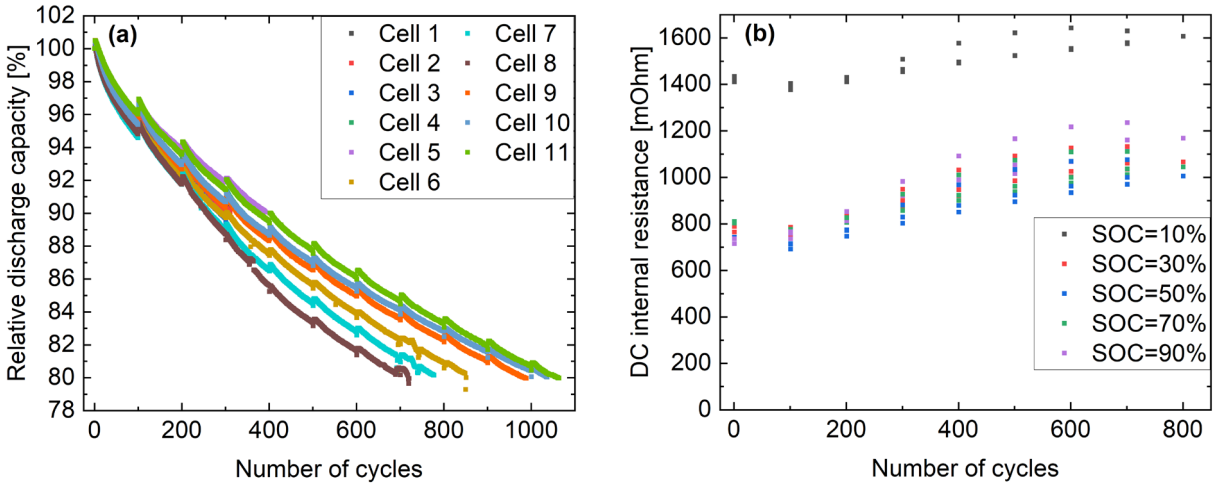

Figure 5.1: (a) Relative discharge capacities of the investigated NCM622/graphite pouch cells cycled until a remaining capacity of 90% and 80% in dependence on the number of cycles. After every 100 cycles, a slow checkup cycle with a charge and discharge rate of 0.1 C is conducted with a subsequent determination of the DC internal resistances at different SOCs. (b) DC internal resistances at various SOCs from three of the investigated NCM622/graphite pouch cells cycled until a remaining capacity of 80% in dependence on the number of cycles [44].

Figure 5.1(a) shows that the relative discharge capacities initially decrease relatively fast. With increasing number of cycles, the capacity decay is decelerated, suggesting a deceleration of cell aging during long-term cycling [44]. Furthermore, the variation of the relative discharge capacities of the cells increases with the number of cycles, as can be seen in Figure 5.1(a). Hence, the investigated cells that are cycled longer, are investigated not after a certain number of cycles, but after having reached a certain remaining capacity [44]. Thereby, it is guaranteed that the respective, investigated cells are in similar aging stages [44]. Figure 5.1(b) indicates a gradual, slow increase of the DC internal resistances with the number of cycles.

5.2 Investigation of the electrochemical decompositions in the electrolyte

For the identification of the electrochemical decomposition processes in the electrolyte during formation and cycling, the investigated electrolytes are extracted from NCM622/graphite pouch cells at several stages of electrochemical aging. The analyzed electrolytes are extracted from three electrochemically untreated cells (called “fresh”), three cells after formation, three cells after 25 cycles, plus three cells each after cycling until a remaining capacity of 95%, 90%, and 80% using the DEC extraction method. In the extracted electrolytes, DEC, EC, DMC, VC, Li^+, and PF_6^- are quantified by the selected analysis methods (see section 4.1). The electrolytes from the three cells per aging step are analyzed on three different days with three times complete sample preparation resulting in three single values for each determined average value. In this section, each indicated average value

represents the mean of the respective three single values. The associated, indicated errors correspond to the standard deviations of the mean calculated based on the respective three single values in the following.

In Figure 5.2(a), the average, quantified concentrations in the electrolytes from the three fresh cells, the three cells each after formation, after 25 cycles, after cycling until a remaining capacity of 95%, 90%, and 80% are shown. The calculation of these concentrations is specified in section 3.6. The average, relative amounts of substance in the three fresh cells, the three cells each after formation, after 25 cycles, after cycling until a remaining capacity of 95%, 90%, and 80% are depicted in Figure 5.2(b). Additionally, these average, relative amounts of substance are plotted against the number of cycles in Figure 5.2(c) to also visualize the rate of the decompositions in the electrolyte. The relative amount of substance is the quantified, absolute amount of substance relative to the respective, initial amount of substance in the cell. A description of the calculation of the relative amounts of substance can be found in section 3.6.

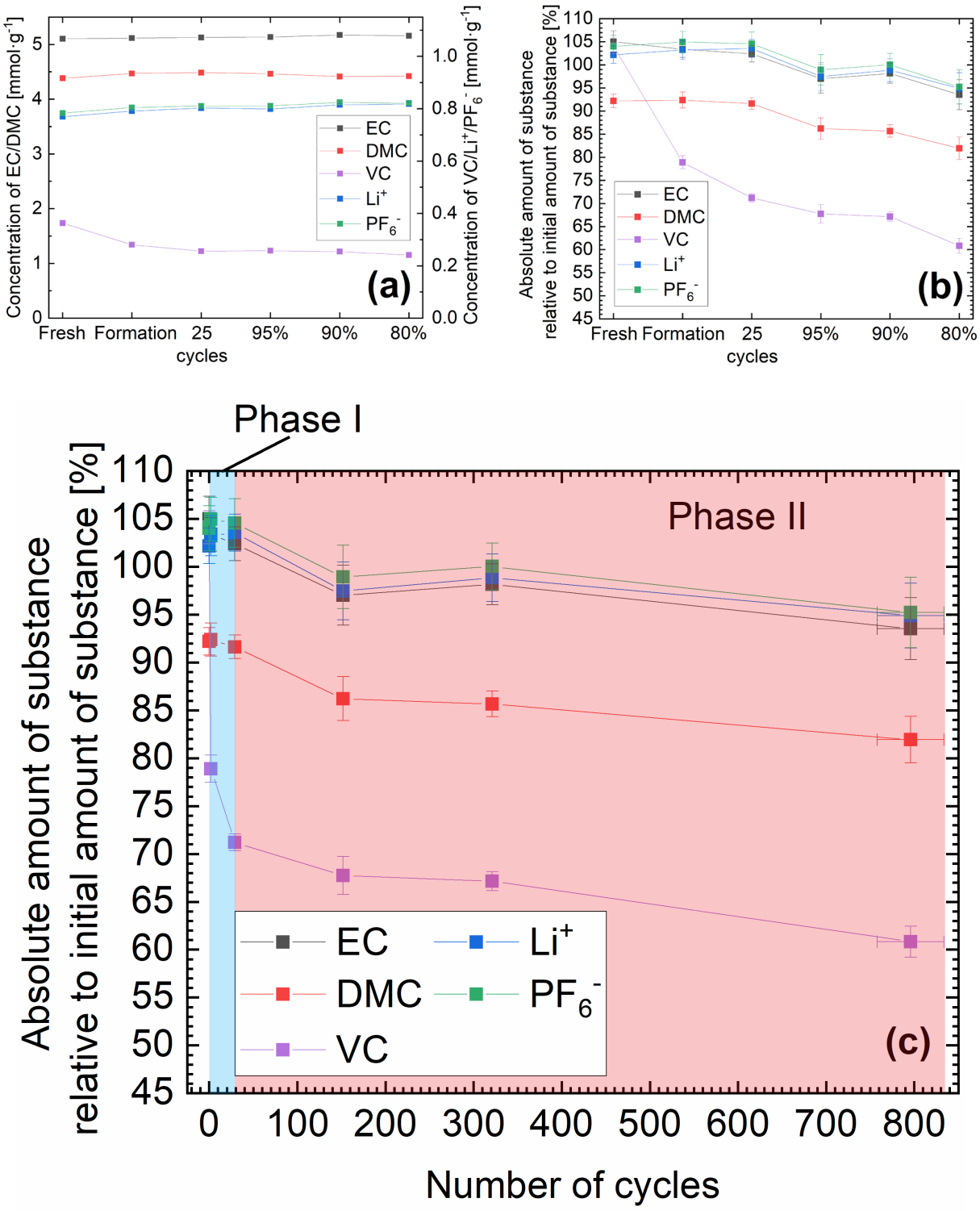

Figure 5.2: (a) Average concentrations in the investigated electrolytes from the cells in the different aging stages. (b) Average, relative amounts of substance in the investigated cells in the different aging stages. (c) Average, relative amounts of substance in the investigated cells in dependence on the number of cycles. The first phase of electrochemical aging is highlighted in blue, whereas the second phase of electrochemical aging is highlighted in red [44].

The concentrations in Figure 5.2(a) reveal solely a VC decomposition by a decreasing VC concentration basically during formation and the subsequent, first 25 cycles. The other concentrations do not show any notable changes. Again, the relative amounts of substance of DMC are reproducibly below the

expected value of 100% in the fresh cells (see Figure 5.2(b) and Figure 5.2(c)), as DMC evaporates during the electrolyte extraction and/or during the sealing of the cell under reduced pressure [40]. Considering the average, relative amounts of substance in dependence on the number of cycles in Figure 5.2(c), two phases of electrochemical aging can be identified. In phase I (during formation plus the subsequent 25 cycles) highlighted in blue in Figure 5.2(c), the VC decomposition is fast and pronounced with a VC loss of about 30% of the initially present VC [44]. Simultaneously, no decomposition of the other electrolyte components can be seen in phase I [44]. In phase II (from the 26^{th} cycle until the about 800^{th} cycle) highlighted in red in Figure 5.2(c), the VC decomposition is decelerated [44]. Only further about 10% of the initially present VC amount are lost in phase II [44]. Interestingly, also about 10% of the initially present amount of EC, DMC, Li^+, and PF_6^- in the cell are lost in phase II [44], as can be concluded from Figure 5.2(c). Hence, the electrolyte components are decomposed according to their abundance suggesting a non-preferential decomposition of all electrolyte components in phase II [44]. The differentiation of these two phases of electrochemical aging is justified further by the coulombic efficiencies of the cells [44]. In Figure 5.3, the coulombic efficiencies from the three cells cycled until a remaining capacity of 80% are plotted against the number of cycles. These cells are the three cycled cells with a remaining capacity of 80% that are used for the electrolyte analyses. Cell 6, cell 7, and cell 8 in Figure 5.3 are the same cells as cell 6, cell 7, and cell 8 in Figure 5.1(a).

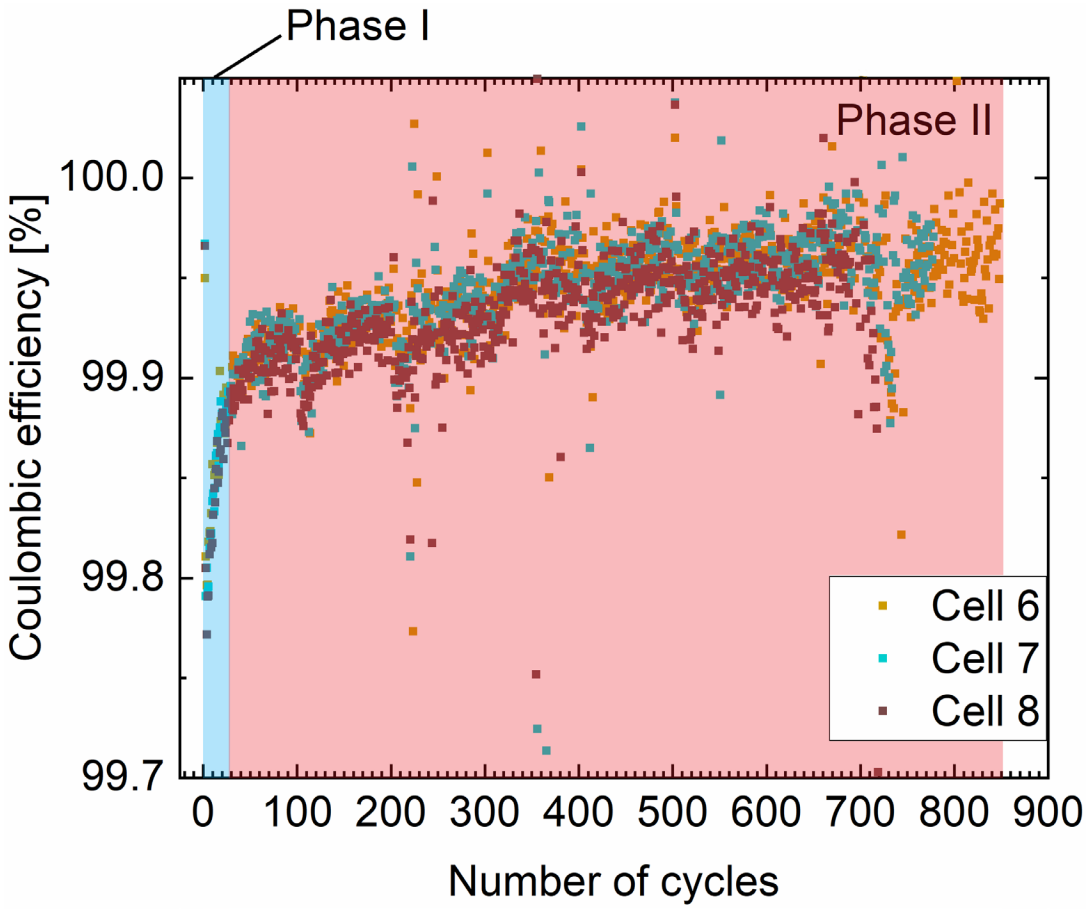

Figure 5.3: Coulombic efficiencies from three cells cycled until a remaining capacity of 80% in dependence on the number of cycles. The first phase of electrochemical aging (phase I) is highlighted in blue, and the second phase of electrochemical aging (phase II) is highlighted in red [44].

The coulombic efficiencies in Figure 5.3 are relatively low during phase I suggesting continuous SEI buildup and associated, accelerated electrolyte reduction also after formation during the subsequent, first 25 cycles [44]. In phase II during long-term cycling, the coulombic efficiencies are relatively high indicating a slow SEI growth and a deceleration of the associated electrolyte reduction [44].

To eventually identify the dominating electrochemical decompositions in the electrolyte, the absolute, decomposed amounts of substance or consumptions of the electrolyte components need to be determined. The consumptions are independent of the initial amounts of the respective electrolyte component in the cells contrary to the relative amounts of substance. Hence, the consumption indicates the absolute extent of the decomposition of an electrolyte component in the cell. The calculation of these consumptions is described in section 3.6. In Figure 5.4, the average consumptions during phase I, the average consumptions during phase II, and the average consumptions during phase I plus phase II taken together can be seen.

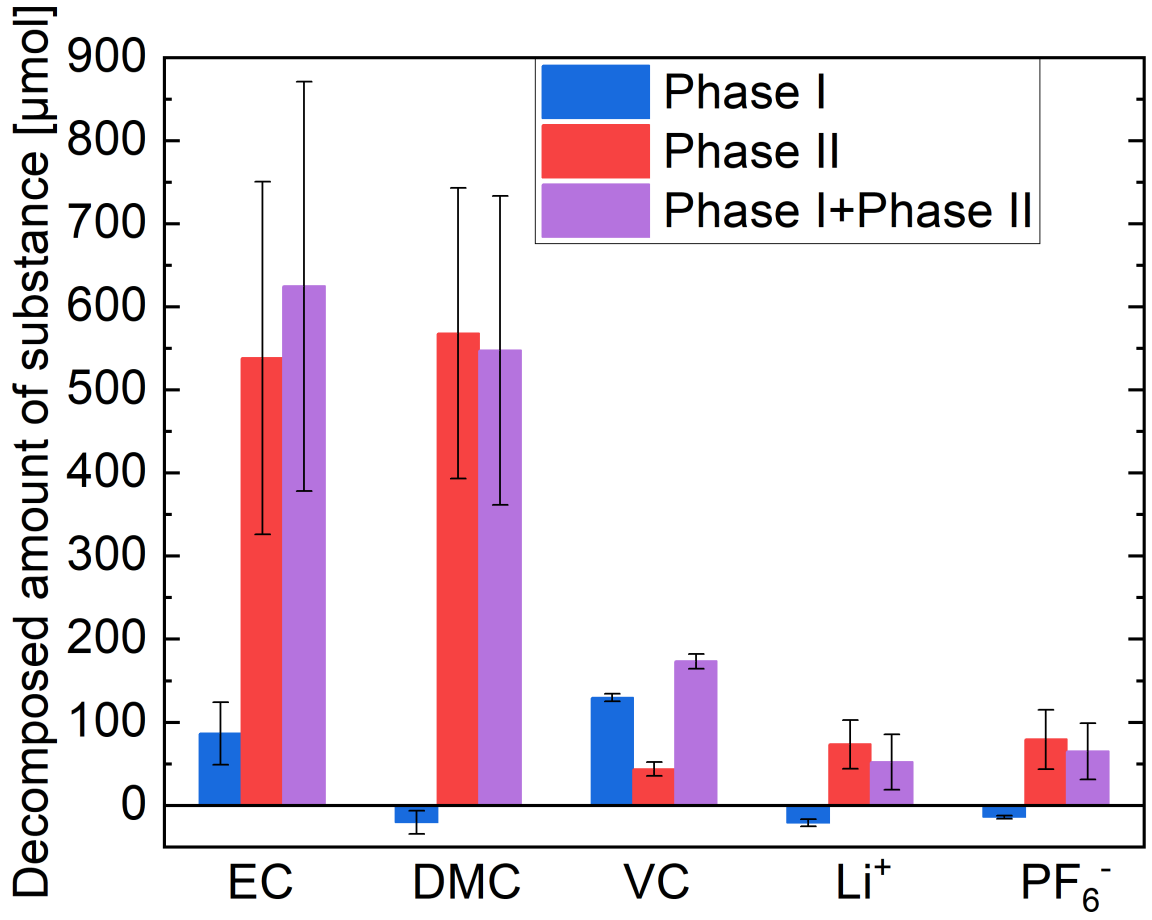

Figure 5.4: Average consumptions of EC, DMC, VC, Li^+, and PF_6^- during formation plus the subsequent 25 cycles (phase I, blue bars), between the 26th cycle and the about 800th cycle (phase II, red bars), as well as during formation plus the about 800 cycles taken together (phase I+phase II, purple bars) [44].

Figure 5.4 indicates a consumption of VC and EC each by about 100 µmol in phase I during formation and the subsequent, first 25 cycles [44]. Simultaneously, no decomposition of DMC, Li^+, and PF_6^- is observable [44]. The decomposed amounts of substance of DMC, Li^+, and PF_6^- during phase I are even slightly negative, as can be seen in Figure 5.4. This phenomenon can be explained by the fact that the electrolyte amount initially filled into the cell during cell assembly is not always exactly equal. Consequently, it might happen that the initial electrolyte mass and thereby the initial amounts of substance of DMC, Li^+, and PF_6^- are by chance slightly lower in some cells compared to other cells. If the initial electrolyte amounts in the three fresh cells are by chance slightly lower than the initial electrolyte amounts in the three cells after 25 cycles, and if DMC, Li^+, and PF_6^- are also electrochemically stable in phase I, slightly negative values for the consumed amounts of substance of these components might be obtained. In this context, it is important to know that the decomposed amount of substance during phase I corresponds to the difference between the quantified, absolute amount of substance in the fresh cell and the respective, quantified, absolute amount of substance in the cell after 25 cycles from the same set of cells. In agreement with the observed, pronounced VC consumption in Figure 5.2 and Figure 5.4, a preferential reduction of VC on graphite anodes in lithium-

ion cells is reported [25,26,34]. The VC decomposition is associated with the deposition of VC decomposition products, such as poly(VC), on the anode contributing to SEI buildup [25,26,34]. A preferential, reductive decomposition of EC on graphite anodes to SEI components in lithium-ion cells with VC-free electrolytes especially during formation is described in several publications [33,35]. Indeed, from literature it is also known that VC suppresses the reductive decomposition of the other electrolyte components on graphite anodes during first charging since it is decomposed at higher anode potentials, so that it is decomposed earlier than other electrolyte components, such as EC [34]. On the other hand, Ushirogata et al. proposed that the VC additive reacts with the EC anion radical after EC reduction, which contributes to the initial SEI formation [58]. Such a reaction of VC together with EC would explain the similar consumptions of VC and EC in phase I (see Figure 5.4) [44]. Furthermore, the distinct EC decomposition in phase I might be attributed to the preferential contribution of EC to the Li^+ solvation shell compared to DMC and VC, as reported in literature [59]. The reduction potential of the respective electrolyte component, as well as the composition of the Li^+ solvation shell both influence the preferential solvent reduction [59]. Thus, it is also possible that the pronounced EC decomposition in phase I can be ascribed to the dominance of EC in the Li^+ solvation shell, while the simultaneous, distinct VC decomposition is caused by the higher reduction potential of VC compared to EC and DMC [44,59]. The exclusive decomposition of EC and VC is not only observed during the formation, but also during the subsequent, first 25 cycles. Hence, it can be concluded that during formation and during the subsequent 25 cycles, similar electrochemical decompositions take place in the electrolyte of the cells [44].

The consumption of EC and DMC is with about 500 µmol by far the highest during phase II [44], as shown in Figure 5.4. This seems counterintuitive since about 10% of the initially present amount of each component is lost during phase II, as already mentioned. Nevertheless, it needs to be considered that the initially present amounts of EC and DMC in the cells are distinctly higher than the initial amounts of VC and $LiPF_6$ in the cells [44]. Thus, the absolute EC and DMC consumption is the highest during phase II [44]. This observation highlights the importance of the consumptions, as quantitative indicators for the decompositions in the electrolyte. Contrary to the relative amounts of substance, the consumptions are independent of the initial amounts of the respective electrolyte components in the cell. Besides, about 70 µmol of the salt are consumed during phase II [44], as indicated in Figure 5.4. In literature, a $LiPF_6$ decomposition resulting in the formation of POF_3 and LiF is described [32]. The VC loss is with about 40 µmol much slighter during phase II than during phase I, as can be concluded from Figure 5.4, which indicates a deceleration of VC decomposition during long-term cycling [44]. Summarized, the described differences in the consumptions of the components during phase I and during phase II suggest different, dominant triggers for the electrochemical electrolyte

decomposition during formation plus short-term cycling on the one hand and long-term cycling on the other hand.

This example demonstrates again the limited meaningfulness of the concentrations compared to the amounts of substance or the consumptions of the electrolyte components. The concentrations suggest an exclusive decomposition of VC, whereas the amounts of substance and the consumptions indicate a decomposition of EC, DMC, VC, and the salt [44]. The ongoing reduction of the electrolyte amount in the cells upon formation and cycling is the cause of this phenomenon [44], as already explained in section 4.4. The continuous reduction of the electrolyte amount in the cells during formation and cycling can be observed in Figure 5.5, in which the average, relative electrolyte masses of the examined cells are plotted against the number of cycles. The relative electrolyte mass is the quantified, absolute electrolyte mass divided by the weighed, initial electrolyte mass in the cell. The calculation of the quantified, absolute electrolyte mass is specified in section 3.6.

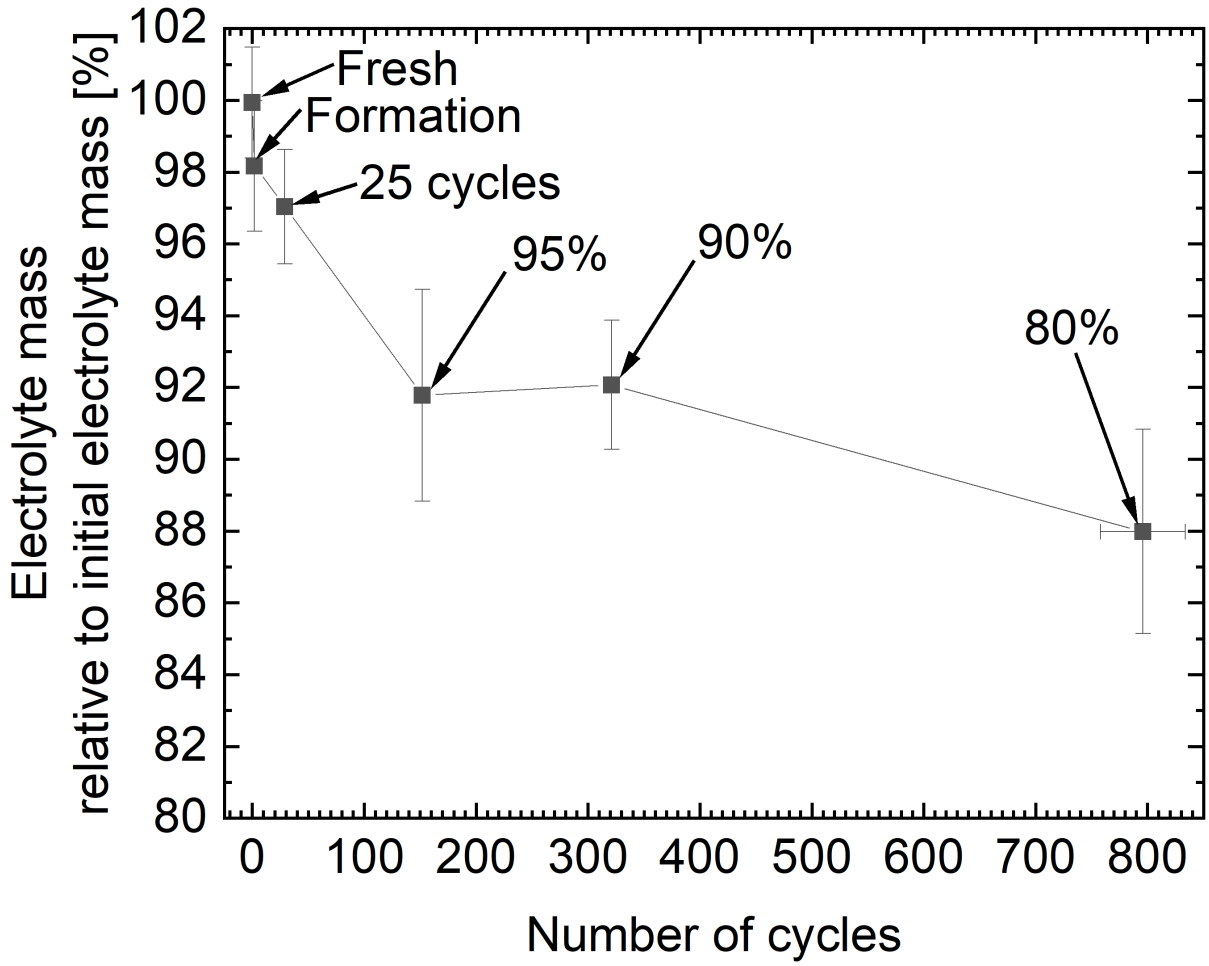

Figure 5.5: Average, relative electrolyte masses in the three fresh cell, the three cells each after formation, after 25 cycles, plus after cycling until a remaining capacity of 95%, 90%, and 80% determined by HPLC analyses plotted against the number of cycles [44].

As shown in Figure 5.5, the electrolyte consumption is fast and pronounced during formation plus the first about 150 cycles, followed by a subsequent deceleration of the electrolyte decomposition. According to literature, a continuous electrolyte consumption during formation and cycling is accompanied by the buildup and growth of surface layers on the electrodes [25,26,33,34,55]. Correspondingly, the growth of surface layers on the electrodes should be fast during the first about 150 cycles and slowed down subsequently.

5.3 Investigation of the gas evolution

The evolution of the gases ethylene and methane in the NCM622/graphite pouch cells is examined by GC-TCD to confirm the pronounced EC decomposition in phase I and the simultaneous electrochemical stability of DMC observed by the HPLC analyses (see Figure 5.4). It Is generally known that the electrochemical decomposition of DMC is indicated by methane [34,60], while the electrochemical decomposition of EC leads to the evolution of ethylene [34,61–63]. For these analyses, gas is extracted from a cell after 25 cycles containing the mixed electrolyte (LP30+VC as initial electrolyte). In addition, gas is extracted from three cells after 25 cycles (with charge and discharge at 1 C) containing different electrolytes each with just one solvent. These three cells contain either the EC electrolyte (1 M $LiPF_6$ in pure EC as initial electrolyte), the DMC electrolyte (1 M $LiPF_6$ in pure DMC as initial electrolyte), or the VC electrolyte (1 M $LiPF_6$ in pure VC as initial electrolyte). GC-TCD is used for the analyses of the extracted gases. The gases are extracted by argon injection, which is described in subsection 3.8.3. Based on the resulting chromatograms, the peak area ratios ethylene/argon (area of ethylene peak divided by area of argon peak) and methane/argon (area of methane peak divided by area of argon peak) are determined. Equal amounts of argon are injected into the cells before extraction. Consequently, these peak area ratios are measures for the evolved amounts of ethylene and methane, respectively [44]. In Figure 5.6, the determined peak area ratios are shown.

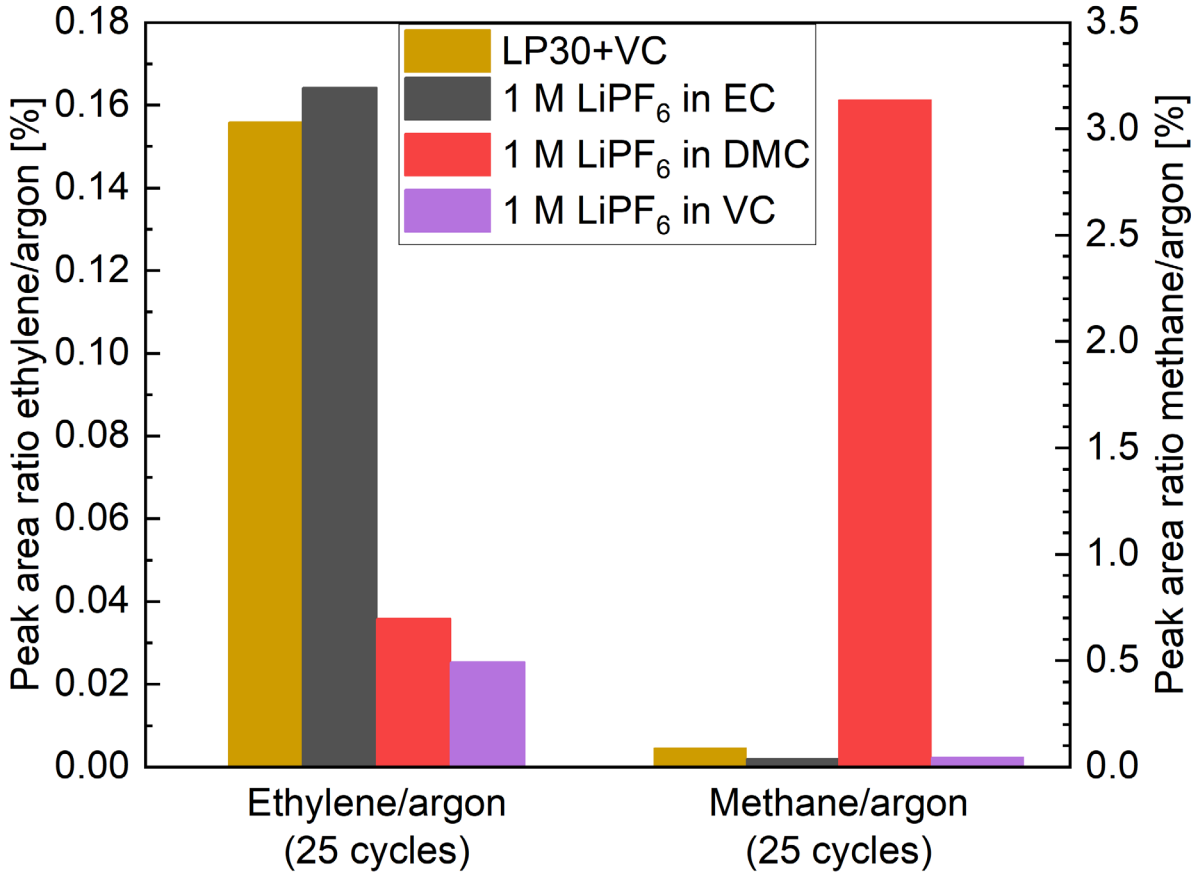

Figure 5.6: Peak area ratios ethylene/argon and methane/argon determined by GC-TCD analyses for the cells after 25 cycles containing either the mixed electrolyte (initial electrolyte: LP30+VC), the EC electrolyte (initial electrolyte: 1 M $LiPF_6$ in EC), the DMC electrolyte (initial electrolyte: 1 M $LiPF_6$ in DMC), or the VC electrolyte (initial electrolyte: 1 M $LiPF_6$ in VC) [44].

As can be seen in Figure 5.6, the peak area ratios ethylene/argon are relatively high for the cell with the mixed electrolyte and the cell with the EC electrolyte after 25 cycles. The peak area ratios ethylene/argon are relatively low for the cells with the DMC electrolyte and the VC electrolyte after 25 cycles, by contrast. These observations agree with the pronounced EC decomposition during formation and the subsequent 25 cycles in phase I shown in Figure 5.4 [44]. Solely for the cell with the DMC electrolyte, the peak area ratio methane/argon is high, as can be seen in Figure 5.6. Hence, it can be concluded that no substantial methane amounts are generated in the cell with the mixed electrolyte. As methane is an indicator for DMC decomposition, the absence of a considerable methane amount in the cell with the mixed electrolyte after 25 cycles confirms the observed, electrochemical stability of DMC during formation and the subsequent 25 cycles (see Figure 5.4) [44].

5.4 Investigation of the electrodes

To gain comprehensive insight into the mechanisms responsible for the electrolyte decomposition and the associated capacity loss, the electrodes from the NCM622/graphite pouch cells are investigated by XPS, ICP-OES, SEM, and EDX.

XPS is applied for the investigation of the surface layers on the electrodes formed by decomposition products from the electrolyte. For this purpose, anodes and cathodes from an electrochemically untreated, fresh cell, a cell after formation, after 25 cycles, plus after cycling until a remaining capacity of 80% are investigated by XPS. These cells are initially filled with LP30+VC (mixed electrolyte). To determine which SEI component originates from which carbonate in the electrolyte, investigated anodes are additionally extracted from three cells after formation containing either the DMC electrolyte (1 M $LiPF_6$ in pure DMC as initial electrolyte), the EC electrolyte (1 M $LiPF_6$ in pure EC as initial electrolyte), or the VC electrolyte (1 M $LiPF_6$ in pure VC as initial electrolyte). In Figure 5.7, the C1s and O1s photoelectron spectra of the examined anodes can be seen.

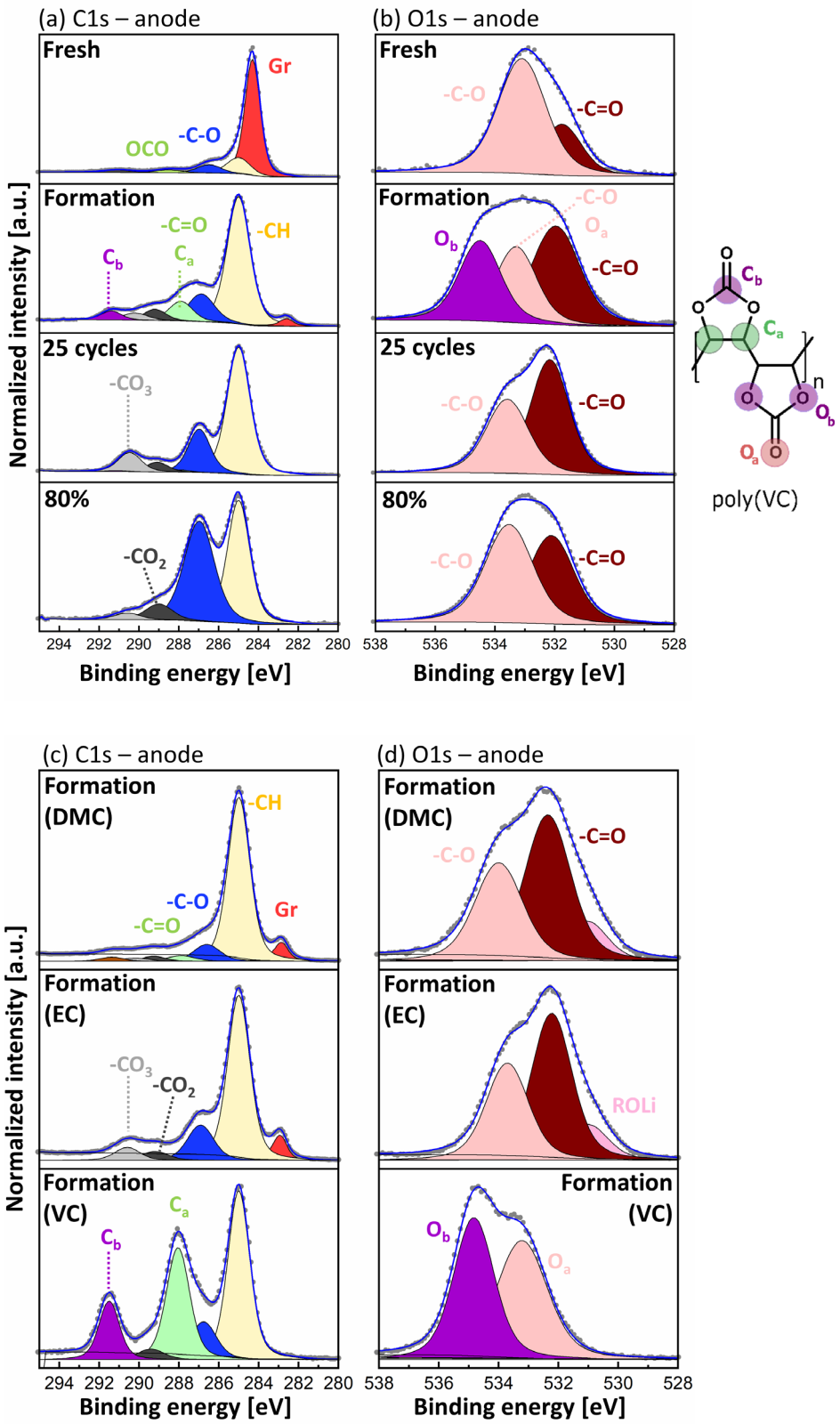

Figure 5.7: C1s spectra (a) and O1s spectra (b) of anodes from a fresh cell, a cell after formation, after 25 cycles, plus after cycling until a remaining capacity of 80%. These cells contain the regular, mixed electrolyte (initial electrolyte: LP30+VC). Besides, C1s spectra (c) and O1s spectra (d) of anodes from three cells after formation can be seen. These three cells contain either the DMC electrolyte (initial electrolyte: 1 M $LiPF_6$ in DMC), the EC electrolyte (initial electrolyte: 1 M $LiPF_6$ in EC), or the VC electrolyte (initial electrolyte: 1 M $LiPF_6$ in VC) [44].

In the following, only the most important findings from the XPS analyses are summarized. The graphite peak (red) diminishes during formation, as can be concluded from Figure 5.7(a). This reduction of the graphite peak is caused by the buildup of the SEI layer on the anode surface during formation [44]. The SEI thickness is still below 5-10 nm (the information depth of XPS) after formation since the graphite peak is not completely disappeared [44]. Only for the anodes from the cell with the mixed electrolyte and the VC electrolyte after formation, the C_b peak (291.3 eV, purple) in the C1s spectrum and the O_b peak (534.5 eV, purple) in the O1s spectrum are observable (see Figure 5.7). This is plausible since these peaks can be assigned to the VC decomposition product poly(VC) [25]. The detected poly(VC) on the anode after formation (see Figure 5.7(a) and Figure 5.7(b)) confirms the distinct VC decomposition during formation observed in the electrolyte by HPLC (see Figure 5.2) [44]. Considering the C1s spectra in Figure 5.7(c), the -CO_3 peak (290.3 eV, light grey) is visible solely in the C1s spectrum of the anode from the cell with the EC electrolyte. Thus, the -CO_3 peak can be traced back to EC decomposition products [44]. In fact, -CO_3 species might be ascribed to lithium carbonate, which represents a known component of the SEI formed in EC-containing electrolytes [44,64]. A pronounced -CO_3 peak can also be observed in the C1s spectrum of the anode from the cell after 25 cycles in Figure 5.7(a), which confirms the distinct EC decomposition during formation and the subsequent 25 cycles in the electrolyte (see Figure 5.4). Interestingly, the mentioned peaks of poly(VC) are disappeared in the C1s spectrum and the O1s spectrum from the anode after 25 cycles (see Figure 5.7(a) and Figure 5.7(b)). This observation indicates that VC is decomposed especially during formation and not during the subsequent 25 cycles. Furthermore, the graphite peak is absent in the C1s spectrum of the anode after 25 cycles (see Figure 5.7(a)) indicating a SEI thickness above 5-10 nm [44]. During long-term cycling, an accumulation of the salt decomposition product LiF in the SEI can be observed in the F1s spectra from the investigated anodes in Figure A.2 in the Appendix. According to XPS measurements, LiF represents the main SEI component after cycling until a remaining capacity of 80%. At first view, this finding does not agree completely with the only moderate salt consumption during long-term cycling observed in the electrolyte by HPLC (see Figure 5.4). As already explained in section 4.5, this phenomenon might be ascribed to the fact that one PF_6^- anion could theoretically provide up to six fluorine atoms for up to six LiF. Consequently, high amounts of LiF in the SEI might result from the decomposition of only moderate amounts of salt.

The amounts of lithium (Li), manganese (Mn), nickel (Ni), and cobalt (Co) in electrodes at different stages of electrochemical aging are determined by ICP-OES to gain suggestions about the origin of the observed decompositions in the electrolyte plus the capacity loss of the cells. The investigated cells (except the fresh cell) are discharged to 3 V and subsequently held at 3 V for four hours before the ICP-OES measurements. Thereby, it is guaranteed that each examined cell is in the completely discharged state [44], meaning all mobile lithium-ions are removed from the anodes.

First, the amounts of substance of Li in anodes and cathodes from an electrochemically untreated, fresh cell, a cell after formation, a cell each after cycling until a remaining capacity of 95%, 90%, and 80% are quantified. Based on the quantified amounts of substance of Li in the cathodes, the lost amounts of substance of Li (Li losses) of the cathodes are calculated. The Li loss of the cathodes is equivalent to the difference between the quantified amount of substance of Li in the cathodes from the fresh cell and the quantified amount of substance of Li in the cathodes from the respective, aged cell. For each cell, four anode pieces and four cathode pieces are examined resulting in four single values for each determined, average value. Besides, the loss of cycleable Li is calculated by the irreversible capacity loss using the Faraday constant. The irreversible capacity loss is the difference between the measured charge capacity of the first cycle during formation with a current of 0.1 C and the measured discharge capacity of the last cycle with a current of 0.1 C directly before the analyses of the respective cell. For this calculation, it is assumed that the capacity loss of the cell is exclusively caused by the loss of cycleable Li. In Figure 5.8, the average, quantified amounts of substance of Li in the anodes, the average, quantified Li losses of the cathodes, and the losses of cycleable Li calculated based on the irreversible capacity losses are shown. Each indicated, average value corresponds to the mean of the respective, determined four single values. The associated errors are the standard deviations of the mean calculated by the respective four single values.

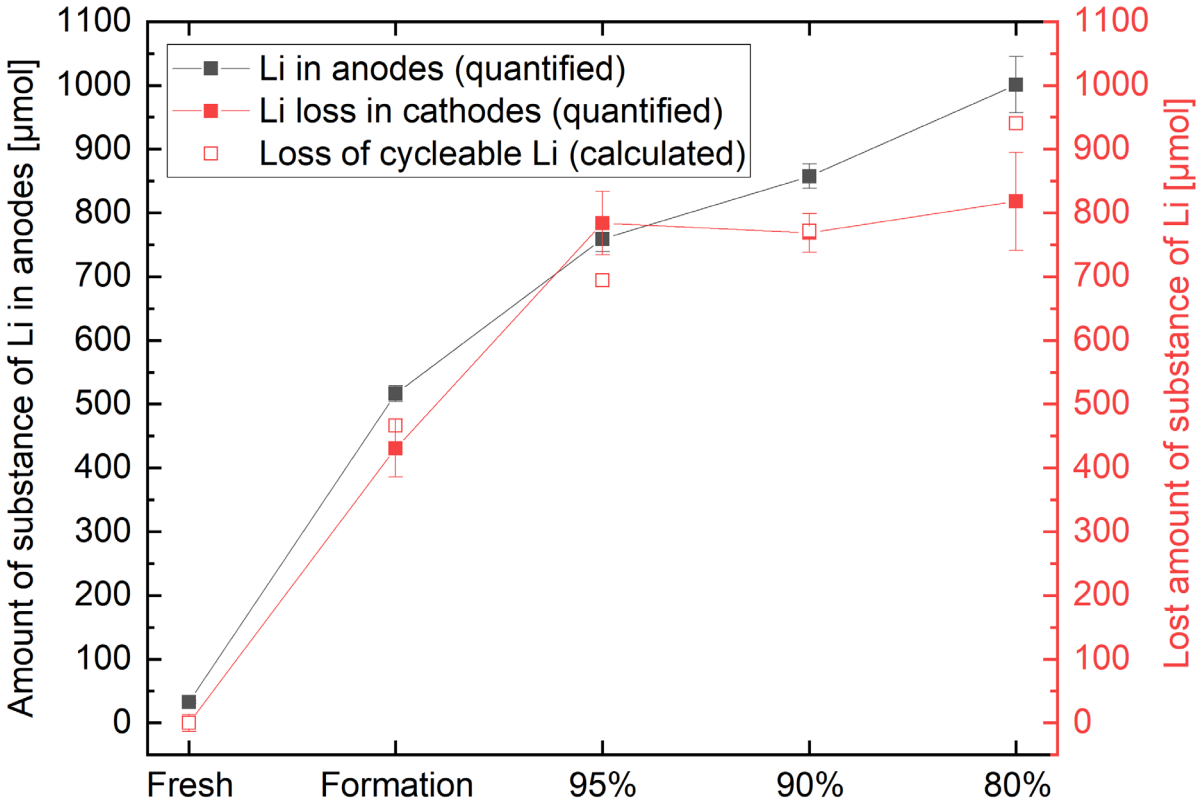

Figure 5.8: Average, quantified amounts of substance of Li in the anodes from a fresh cell, a cell after formation, plus a cell each after cycling until a remaining capacity of 95%, 90%, and 80% determined by ICP-OES. Additionally, the average, quantified Li losses of the cathodes from these cells determined by ICP-OES can be seen. The losses of cycleable Li calculated by the irreversible capacity losses are also shown for these cells [44].

As can be seen in Figure 5.8, the quantified Li losses of the cathodes are close to the calculated losses of cycleable Li. Hence, it can be concluded that the capacity losses of the cells are (almost) exclusively caused by a loss of cycleable Li. Simultaneously, the quantified Li losses of the cathodes are mainly close to the quantified amounts of substance of Li in the anodes. The Li loss of the cathodes is thus (almost) completely compensated by an irreversible bonding of Li in the anodes. Consequently, the capacity losses are mostly induced by trapping of cycleable Li in the anodes, namely in the SEI and/or in electronically isolated graphite particles, as reported in literature [44,65]. In an electrochemically untreated, fresh NCM622/graphite pouch cell, the cathodes contain about 5300 µmol Li, while the electrolyte contains about 900 µmol Li^+ [44]. Hence, the quantified Li loss of the cathodes after cycling until a remaining capacity of 80% by about 800 µmol (see Figure 5.8) corresponds to about 15 % of the initial Li amount in the cathodes [44]. For the cells after cycling until a remaining capacity of 90% and 80%, the quantified amounts of substance of Li in the anodes are slightly higher than the determined Li losses of the cathodes, as can be seen in Figure 5.8. This observation can be attributed to the deposition of additional Li on the anodes by the decomposition of $LiPF_6$ from the electrolyte [44]. This finding agrees with the moderate salt decomposition observed in the electrolyte during long-term cycling by HPLC (see Figure 5.4). As shown in Figure 5.8, 968±47 µmol additional Li is detected in the

anodes after cycling until a remaining capacity of 80% [44]. This additional Li in the anodes can originate from two sources: On the one hand, there is the “cycleable Li” that is initially present in the cathodes and contributes to the capacity of the cell [44]. On the other hand, there is the “non-cycleable Li” that is initially present in the electrolyte and does not contribute to the capacity of the cell [44]. From the 968±47 µmol additional Li detected in the anodes after cycling until a remaining capacity of 80%, 818±77 µmol is cycleable Li (equivalent to the corresponding Li loss of the cathodes shown in Figure 5.8) and 52±33 µmol is non-cycleable Li (equivalent to the Li^+ consumption during phase I plus phase II taken together shown in Figure 5.4) [44].

The amounts of substance of the transition metals Mn, Ni, and Co are additionally determined by ICP-OES in anodes in different aging stages to investigate to what extent transition metal contaminations in the SEI are responsible for the observed electrolyte decompositions and the capacity loss. Transition metals, especially Mn, from the cathode in the SEI are known to promote electrolyte decomposition and capacity loss in lithium-ion cells [36,38,66]. In Figure 5.9(a), the average, quantified amounts of substance of Mn, Ni, Co, and Li in the anodes from the fresh cell, the cell after formation, plus the cell each after cycling until a remaining capacity of 95%, 90%, and 80% are shown. In addition, these average, quantified amounts of substance are plotted against the number of cycles in Figure 5.9(b). As already mentioned, four anode pieces are analyzed for each cell resulting in four single values. Each average value shown in Figure 5.9 represents the mean calculated by the four single values. The indicated error bars are equivalent to the standard deviations of the mean calculated by the four single values.

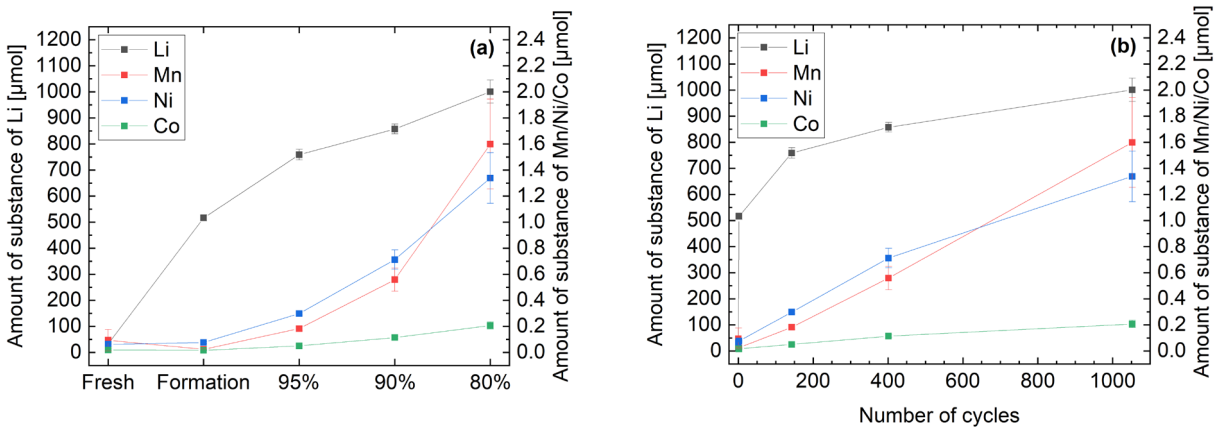

Figure 5.9: (a) Average amounts of substance of Li, Mn, Ni, and Co in anodes from a fresh cell, a cell after formation, plus a cell each after cycling until a remaining capacity of 95%, 90%, and 80% determined by ICP-OES. (b) Average amounts of substance of Li, Mn, Ni, and Co in these investigated anodes plotted against the number of cycles [44].

During formation, the irreversible bonding of Li in the anodes is fast and pronounced, as can be seen in Figure 5.9. Simultaneously, no increase of the amounts of substance of Mn, Ni, and Co in the anodes is visible during formation (see Figure 5.9(a)). Consequently, the observed Li trapping in the anodes

during formation is not induced by deposited transition metals on the anodes [44]. After formation during subsequent cycling, a linear increase of the amounts of substance of Mn, Ni, and Co in the anodes with the number of cycles can be identified in Figure 5.9(b). Besides, a preferential transfer of Mn from the cathodes to the anodes can be concluded from Figure 5.9 in accordance with the literature [36]. At first view, this conclusion does not seem completely plausible since the amounts of substance of Mn and Ni in the anodes are similar (see Figure 5.9). Indeed, it is important to note in this context that the cathodes with NCM622 as active material contain three times more Ni than Mn, which eventually justifies the mentioned conclusion [44]. As already mentioned, electrolyte decomposition and capacity loss can be accelerated by transition metals, especially Mn, in the SEI according to literature [36,38,66]. Hence, the observed accumulation of Mn, Ni, and Co in the anodes during prolonged cycling might be the crucial trigger for the massive electrolyte decompositions in phase II (see Figure 5.4) [44]. Indeed, the amounts of substance of Mn, Ni, and Co in the anodes increase linearly with the number of cycles, while the Li trapping in the anodes simultaneously slows down, as can be seen in Figure 5.9(b). This finding suggests that the Li trapping in the anodes is not directly coupled to the deposition of transition metals in the anodes [44]. By contrast, Gilbert et al. observed in $LiNi_{0.5}Co_{0.2}Mn_{0.3}O_2$ (NCM523)/graphite coin cells a direct coupling between the Li trapping in the SEI and the deposition of Mn in the SEI [36]. Gilbert et al. claimed that about 100 additional lithium-ions are trapped for every deposited manganese-ion in the SEI [36]. The data in Figure 5.9, however, suggests that for every deposited Mn atom substantially more Li atoms are additionally trapped in the anodes during cycling (about 300 additional Li atoms per Mn atom comparing the cell after formation with the cell after cycling until a remaining capacity of 80%) [44]. On the other hand, Jung et al. observed that the loss of cycleable Li and the associated capacity loss induced by transition metals in the SEI decelerate with increasing number of cycles [66]. This finding is consistent with the observed, linear increase of the transition metal amounts and the simultaneous deceleration of the irreversible bonding of Li in the anodes during cycling (see Figure 5.9(b)) [44].

To gain further information about the state of the electrodes in different stages of electrochemical aging, SEM and EDX are applied. For this purpose, electrodes from a fresh cell, a cell after formation, a cell each after cycling until a remaining capacity of 90%, and 80% are investigated by SEM and EDX. In Figure 5.10(a), SEM images from the surfaces of the investigated anodes can be seen. In addition, the distributions of the elements on the surfaces of the anodes after formation, as well as after cycling until a remaining capacity of 90%, and 80% are shown in Figure 5.10(b). These distributions of the elements on the anode surfaces are determined by EDX. In these EDX images, the color red marks high carbon concentrations in the surface layers, while the color green indicates high oxygen concentrations. Generally, a high oxygen concentration in the surface layer of an anode indicates the presence of a thick SEI consisting of the oxygen-rich decomposition products of EC, DMC, and VC [44].

A high carbon concentration in the surface layer of an anode, however, indicates graphite and thus the absence of a thick SEI [44]. In this context, it is important to note that a thin SEI is hardly observable by EDX because of a limited spatial resolution of several hundred nm [44]. Some spots in the EDX images in Figure 5.10(b) appear cyan and indicate hereby a high aluminum and oxygen concentration, which can be traced back to aluminum oxide (Al_2O_3) from the separator.

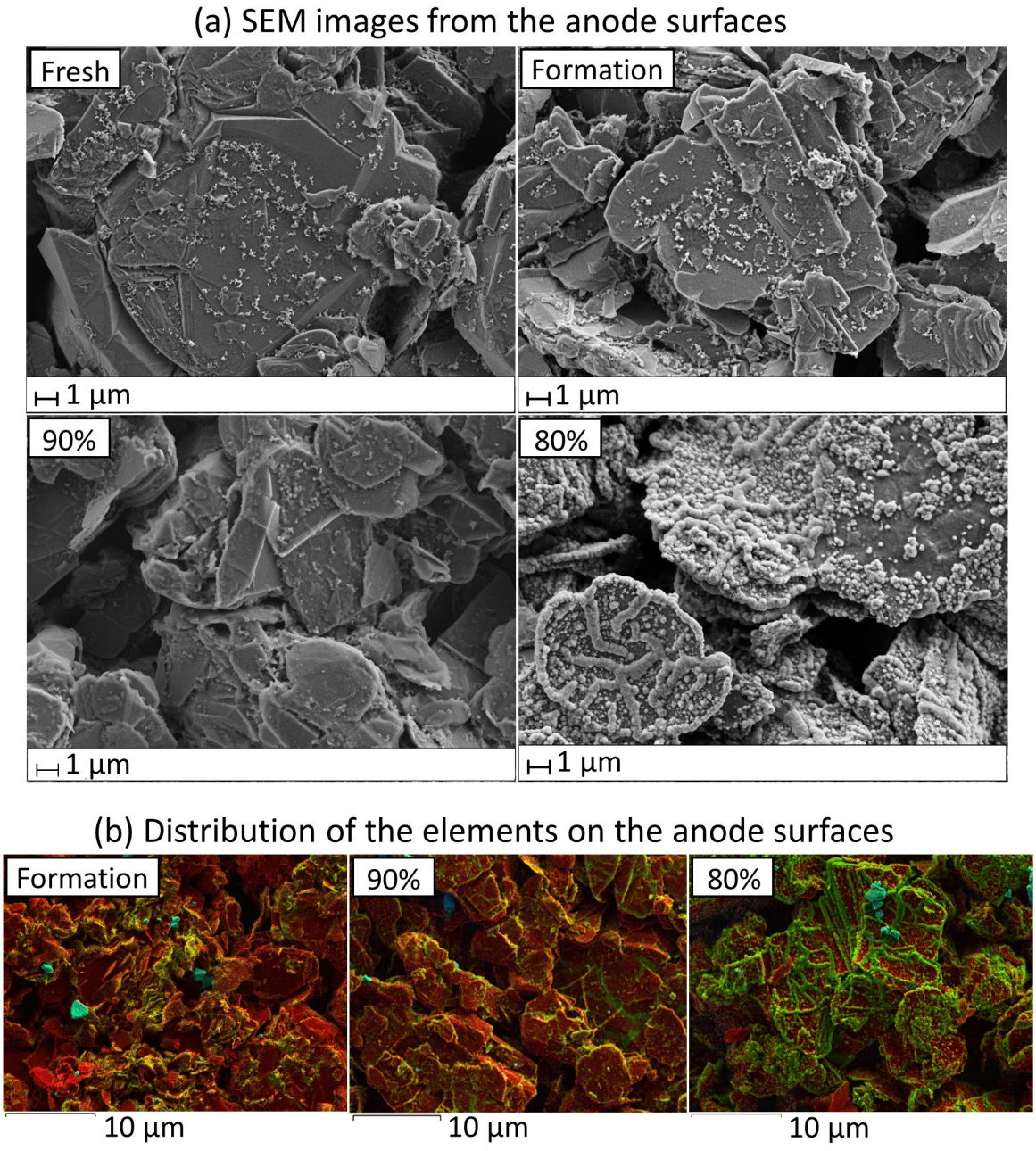

Figure 5.10: (a) SEM images from the surface of anodes from a fresh cell, a cell after formation, a cell each after cycling until a remaining capacity of 90%, and 80%. (b) Distribution of the elements on the surface of anodes from a cell after formation, a cell each after cycling until a remaining capacity of 90%, and 80% determined by EDX. High carbon concentrations are indicated by the color red, and high oxygen concentrations are indicated by the color green [44].

The big, flake-shaped particles in the images in Figure 5.10 are the graphite particles [44]. The small, dot-like particles on these graphite particles are the carbon black particles [44]. The SEM images in Figure 5.10(a) do not reveal any remarkable changes of the anode surface during formation and cycling until a remaining capacity of 90%. In the SEM image from the anode after cycling until a remaining capacity of 80%, however, spherical and tubular deposits on the basal planes of the graphite particles can be observed (see Figure 5.10(a)). In the EDX image from the anode after formation in Figure 5.10(b), the graphite particle edges appear slightly green suggesting the deposition of a relatively thin SEI especially on the graphite particle edges during formation [44]. The mentioned, spherical and tubular deposits on the graphite particles can also be identified in the EDX image from the anode after cycling until a remaining capacity of 80% in Figure 5.10(b). As these spherical and tubular deposits are green, it can be concluded that they are SEI composed of oxygen-rich decomposition products of EC, DMC, and/or VC [44]. The EDX image from the anode after cycling until a remaining capacity of 80% in Figure 5.10(b) additionally shows a thick, oxygen-rich SEI on the graphite particle edges [44]. According to the EDX images, only relatively, few, oxygen-containing SEI material is deposited on the anode after cycling until a remaining capacity of 90% compared to the anode after cycling until a remaining capacity of 80%. Indeed, beginnings of the oxygen-rich, spherical, and tubular deposits are already observable on the graphite particles after cycling until a remaining capacity of 90% [44]. Summarized, the relatively thin SEI after formation plus the massive SEI after long-term cycling detected by SEM and EDX (see Figure 5.10) match the much more pronounced electrolyte decomposition during prolonged cycling than during formation (see Figure 5.5) [44]. The SEI on the edges of the graphite particles is much thicker than the SEI on the basal planes according to literature [67–69], which is consistent with the preferential SEI formation at the graphite particle edges observed in the EDX images in Figure 5.10(b) [44]. A proposed reason for this phenomenon is that the reactivity of the carbon atoms at the edge sites of the graphite particles is higher than the reactivity of the carbon atoms in the basal planes [44,69]. The mentioned, spherical deposits on the graphite particles after prolonged cycling might be carbon black particles surrounded by thick SEI layers [44]. Carbon black particles have small particle sizes and consequent large surface areas, which is associated with enhanced capacity loss and SEI buildup [69]. The detected accumulation of transition metals in the anodes during long-term cycling (see Figure 5.9) might be responsible for the formation of the mentioned, tubular deposits on the graphite particles [44]. Solchenbach et al. proposed that Mn in the SEI induces a SEI decomposition by a reduction of lithium ethylene dicarbonate (a main SEI component) to lithium carbonate and the gas ethylene [38]. This SEI decomposition is accompanied by cracks in the SEI that are filled with electrolyte [38]. As a result, the electrolyte is reduced and the SEI grows [38]. According to this, such a SEI decomposition by Mn and a consequent electrolyte decomposition might be the cause of the observed, tubular deposits on the graphite particles after long-term cycling in Figure 5.10 [44]. Beside

the Mn contamination of the SEI, another cause of these tubular deposits might be crack formation in the graphite particles and/or the SEI induced by volume changes of the graphite during de-/lithiation [44], as known from literature [70,71]. By this crack formation new, electrochemically active surface is created, which leads to electrolyte reduction and consequent buildup of new SEI [70,71]. According to this, the tubular deposits might be traced back to SEI that is formed on graphite particles along transgranular cracks [44] like those observed by Harris et al. [72]. SEM images from the cross-sections of the fresh anode and the anode after cycling until a remaining capacity of 80% are acquired to investigate the changes of the anode structure by electrochemical aging and to identify possible crack formation in the graphite particles by electrochemical aging. Besides, also the distributions of the elements in these cross-section images are determined by EDX. In Figure 5.11(a), the cross-section images from the fresh anode and the aged anode determined by SEM and EDX are depicted. As already mentioned, green indicates spots with high oxygen concentrations and thus the presence of oxygen-rich SEI material in the EDX images [44]. Red indicates high carbon concentrations [44]. To also identify possible changes of the cathode structure by electrochemical aging, SEM images from the cross-sections of the cathodes from the fresh cell, the cell after formation, the cell each after cycling until a remaining capacity of 90%, and 80% are acquired, which can be seen in Figure 5.11(b).

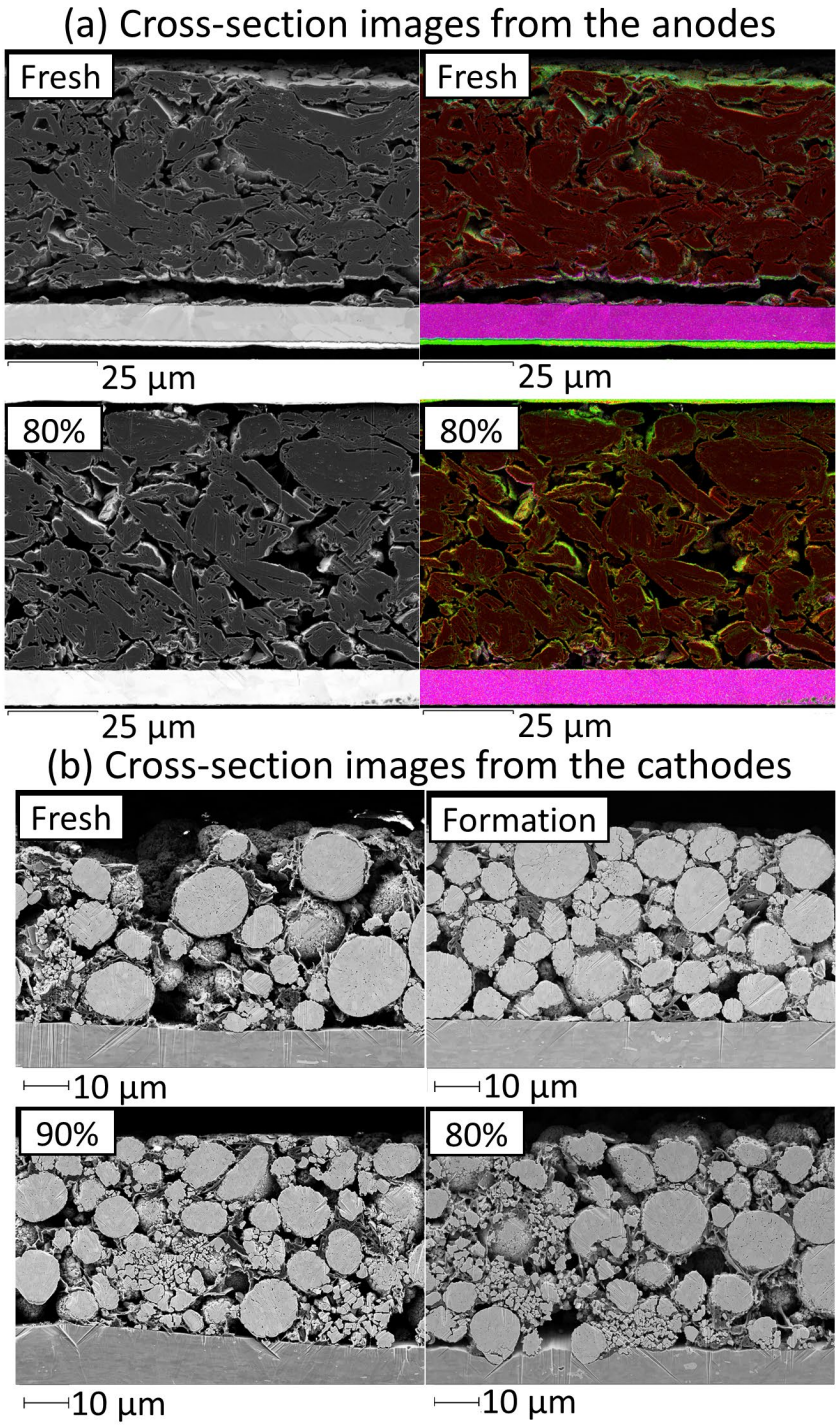

Figure 5.11: (a) Cross-section images of an anode from the fresh cell plus the cell after cycling until a remaining capacity of 80% acquired by SEM and EDX. In the EDX images, a high carbon concentration is indicated by red, and a high oxygen concentration is indicated by green. (b) Cross-section images of a cathode from the fresh cell, the cell after formation, the cell each after cycling until a remaining capacity of 90%, and 80% acquired by SEM [44].

The cross-section images from the anodes in Figure 5.11(a) reveal a thickening of the anode coating during formation and prolonged cycling induced by an enhancement of the porosity and the SEI growth [44]. As generally known, the volume ratio of the void space within materials is equivalent to the porosity [70]. “The change in porosity before and after electrochemical cycles, which results from crack

growth, can be used to quantify the degree of fracture" according to literature [70]. Hence, the observed porosity increase of the anode coating in Figure 5.11(a) suggests crack formation in the graphite particles by volume changes during formation and prolonged cycling. Another indication for possible crack formation with consequent electrolyte decomposition is the appearance of oxygen-containing SEI material also partly within the graphite particles after long-term cycling [44], as can be seen in Figure 5.11(a). In literature, an enhancement of crack formation by high charge and discharge currents because of an increased mechanical stress during de-/lithiation is reported [71]. Since the cells are cycled with a high charge and discharge current in this study, the observation of crack formation in the graphite particles during prolonged cycling seems thus reasonable [44]. Consequently, the crack formation in the graphite particles due to volume changes during de-/lithiation represents another possible trigger for the pronounced electrolyte consumption plus the capacity loss during long-term cycling, beside the mentioned transition metal contaminations in the SEI [44].

The cross-section images from the cathodes in Figure 5.11(b) indicate distinct crack formation in the spherical NCM622 secondary particles during long-term cycling. In the NCM622 secondary particles of the cathodes from the fresh cell and the cell after formation, cracks are hardly visible. In the NCM622 secondary particles of the cathodes from the cells after cycling until a remaining capacity of 90% and 80%, however, pronounced cracks are observable. Crack formation also occurs during de-/lithiation of the NCM622 particles and accelerates the dissolution of transition metals in the electrolyte [36]. The dissolved transition metals move through the electrolyte to the anode and deposit in the SEI, where they enhance electrolyte degradation and SEI growth [36,38,66]. According to this, the observed crack formation in the NCM622 particles during prolonged cycling in Figure 5.11(b) is the reason for the pronounced accumulation of transition metals in the anodes during long-term cycling (see Figure 5.9), and thus eventually also for the simultaneous, massive electrolyte consumption (see Figure 5.4), and the SEI growth (see Figure 5.10).

5.5 Proposed decomposition mechanisms

In the following, the identified decomposition mechanisms in the investigated NCM622/graphite pouch cells during formation and subsequent cycling are summarized. The investigation of the electrochemical decomposition processes in the pouch cells during formation and subsequent cycling reveal two different phases of electrochemical aging [44].

In phase I, during formation and the subsequent first 25 cycles, an exclusive decomposition of VC and EC can be observed in the electrolyte according to the HPLC analyses accompanied by a distinct capacity loss due to Li trapping in the anodes (see Figure 5.8) [44]. The consumptions of VC and EC during phase I are both about 100 µmol, while DMC and the salt are electrochemically stable (see

Figure 5.4) [44]. Considering the results from the XPS analyses in Figure 5.7 and the GC measurements in Figure 5.6, VC is reduced at the anode mostly to the SEI component poly(VC), while EC is reduced at the anode at least partly to the SEI component lithium carbonate plus the gas ethylene [44]. During formation, a relatively thin SEI consisting of the electrolyte decomposition products is deposited preferentially on the reactive graphite particle edges [44], as can be observed by EDX in Figure 5.10(b). From the relatively low coulombic efficiencies in phase I (see Figure 5.3), it can be concluded that the rate of the reductive decompositions at the anode is relatively high during phase I suggesting an ongoing SEI formation due to an incomplete anode passivation. Additionally, no accumulation of transition metals from the cathodes can be observed in the anodes during formation by ICP-OES (see Figure 5.9(a)) indicating no crucial influence of transition metal contaminations in the SEI on the electrolyte decomposition during the first cycles. Consequently, the crucial trigger for the electrolyte decomposition and the associated SEI buildup in phase I is most likely an incomplete anode passivation by a thin and unfinished SEI.

In phase II, meaning from the 26th cycle until the about 800th cycle (when a remaining capacity of 80% is reached), a non-preferential decomposition of the electrolyte components is detected by HPLC, which means that the electrolyte components are consumed according to their abundance [44], as can be concluded from Figure 5.2(c). Generally, the electrolyte consumption in phase II is much stronger, than during phase I, as shown in Figure 5.5. The consumptions of EC and DMC during phase II are the highest with both about 500 µmol, while the $LiPF_6$ consumption is only about 70 µmol (see Figure 5.4) [44]. The VC consumption during phase II is the lowest with about 40 µmol [44]. This finding is surprising since VC is a SEI-forming additive that is supposed to be decomposed for the SEI formation. $LiPF_6$ is decomposed mainly to LiF that represents an important SEI component after prolonged cycling according to the XPS results in Figure A.2. The electrolyte decompositions are accompanied by a capacity loss mostly due to Li trapping in the anodes also in phase II [44], as can be concluded from Figure 5.8. The decomposition products from the electrolyte are deposited especially on the edges of the graphite particles from the anodes like already during phase I according to the EDX analyses [44]. Simultaneously, the decomposition products from the electrolyte are additionally deposited on the basal planes of the graphite particles as SEI material in spherical and tubular deposits [44], as shown in the images acquired by SEM and EDX in Figure 5.10. The spherical deposits are SEI formed on the carbon black particles [44]. SEI cracking and resulting SEI rebuilding might be responsible for the formation of the tubular deposits [44]. The coulombic efficiency has approximately reached a saturation value at the beginning of phase II (see Figure 5.3) indicating the completion of a passivating, initial SEI. Hence, the observed electrolyte decompositions in phase II are not triggered by an unfinished SEI like in phase I. Instead, two other possible triggers for the electrolyte decompositions and the associated capacity losses are identified [44]: The contamination of the SEI with transition

metals, especially Mn, and the crack formation in the graphite particles by volume changes during de-/lithiation [44]. A linear increase of the amounts of the transition metals from the cathodes in the anodes with the number of cycles is observed by ICP-OES (see Figure 5.9(b)). The consequent Mn contamination of the SEI and the associated deterioration of the passivating property of the SEI might be the first, possible trigger for the observed, massive decompositions in the electrolyte plus the pronounced SEI growth in phase II [44]. The observed porosity increase of the anode coating during prolonged cycling (see Figure 5.11(a)) indicates crack formation in the graphite particles induced by the ongoing volume changes of the graphite during de-/lithiation. These cracks create new, electrochemically active surface leading to electrolyte reduction and buildup of new SEI material [44]. Hence, the crack formation in graphite particles by volume changes of the graphite during de-/lithiation and the associated creation of new, electrochemically active surface might be the second, possible trigger for the observed, massive decompositions in the electrolyte plus the SEI growth in phase II [44].

6 Investigations with the NCM622/silicon-graphite pouch cells

In this chapter, the results from the investigations of the NCM622/silicon-graphite pouch cells are presented. Silicon is a promising anode active material for future lithium-ion battery cells, as it offers a high, theoretical, specific capacity of about 3600 $mAh \cdot g^{-1}$ (regarding the phase $Li_{15}Si_4$ [13–15]), which is much higher than the theoretical, specific capacity of the common anode active material graphite (372 $mAh \cdot g^{-1}$ [73]). Nevertheless, the lithiation of silicon leads to a massive volume increase of up to 320%, which is associated with severe volume changes of the silicon during de-/lithiation [16]. The consequent, continuous creation of new, electrochemically active surface during cycling is accompanied by a rapid, irreversible capacity loss, continuous SEI formation, and ongoing electrolyte consumption [17]. For a commercial application of lithium-ion battery cells with silicon-containing anodes, the cycle performance needs to be systematically improved, which requires a comprehensive understanding of the electrochemical electrolyte decomposition and the associated SEI growth. The clarification of the mechanisms responsible for capacity loss in NCM622/silicon-graphite pouch cells is the objective of the studies presented in this chapter. The cathodes from the examined NCM622/silicon-graphite pouch cells are the same as those used in the NCM622/graphite pouch cells (see chapter 5). The composition of the silicon-graphite anodes is equivalent to the graphite anodes from chapter 5, except that the active material is composed of 90% graphite and 10% silicon for the silicon-graphite anodes in contrast to the graphite anodes from chapter 5, where 100% graphite is used as active material. The initial electrolytes used in the investigated NCM622/silicon-graphite pouch cells are 1 M $LiPF_6$ in FEC:DMC and 1 M $LiPF_6$ in VC:DMC, respectively (see section 3.1). The developed electrolyte extraction method, as well as the associated determination of the absolute consumptions of the electrolyte components through HPLC analyses are used for the investigation of the electrochemical electrolyte decomposition in the NCM622/silicon-graphite pouch cells. The electrolytes analyzed by HPLC are removed from pouch cells at several stages of electrochemical aging. The electrolytes, the evolved gases, and the electrodes from the NCM622/silicon-graphite pouch cells are additionally investigated at the same aging stages by complementary analysis methods, namely GC-FID, GC-TCD, XPS, SEM, EDX, and ICP-OES. The obtained results from this study are described and discussed in this chapter. In addition, the identified trigger for the capacity loss of the NCM622/silicon-

graphite pouch cells is presented in this chapter. Finally, the mechanisms for the reductive decomposition of FEC and VC are proposed based on the gained insights. The GC measurements, as well as the associated evaluation were performed by Dr. Andreas Hofmann from the IAM-WK and Dr. Freya Janina Müller from the IAM-ESS. The XPS analyses, including the associated evaluation, were carried out by Lydia Gehrlein and Dr. Julia Maibach both from the IAM-ESS. Dr. Marcus Müller from the IAM-ESS acquired the SEM images and conducted the EDX analyses for this chapter. Dr. Thomas Bergfeldt from the IAM-AWP performed the ICP-OES investigations for this chapter.

6.1 Selection of suitable electrolytes

In the first step, suitable electrolytes for the investigated NCM622/silicon-graphite pouch cells need to be found that enable an acceptable cycle performance. For this purpose, NCM622/silicon-graphite pouch cells with different FEC-containing and VC-containing electrolytes are built and cycled. The tested electrolytes contain VC or FEC since these electrolyte components are both known to improve the capacity retention of lithium-ion cells with silicon anodes during cycling [27,74]. The exact compositions of the initial electrolytes from the NCM622/silicon-graphite pouch cells used for the cycling tests are listed in Table 6.1.

Table 6.1: Compositions of the initial electrolytes from the NCM622/silicon-graphite pouch cells used for the cycling tests.

Electrolyte	Mass fraction of DMC [wt%]	Mass fraction of $LiPF_6$ [wt%]	Mass fraction of EC [wt%]	Mass fraction of VC [wt%]	Mass fraction of FEC [wt%]
LP30+3% VC	42.8±0.1	11.4±0.1	42.8±0.1	3.00±0.01	0.0
LP30+10% VC	39.7±0.1	10.6±0.1	39.7±0.1	10.0±0.1	0.0
LP30+20% VC	35.3±0.1	9.40±0.01	35.3±0.1	20.0±0.1	0.0
VC:DMC	44.0±0.1	12.0±0.1	0.0	44.0±0.1	0.0
LP30+3% FEC	42.8±0.1	11.4±0.1	42.8±0.1	0.0	3.00±0.01
LP30+10% FEC	39.7±0.1	10.6±0.1	39.7±0.1	0.0	10.0±0.1
LP30+20% FEC	35.3±0.1	9.40±0.01	35.3±0.1	0.0	20.0±0.1
FEC:DMC	44.2±0.1	11.6±0.1	0.0	0.0	44.2±0.1

The absolute and relative discharge capacities of these tested pouch cells are shown in dependence on the number of cycles in Figure 6.1. These tested pouch cells are charged at 2 C and discharged at 3 C. The relative discharge capacity is the respective, absolute discharge capacity divided by the absolute discharge capacity of the first cycle with 2 C charge and 3 C discharge.

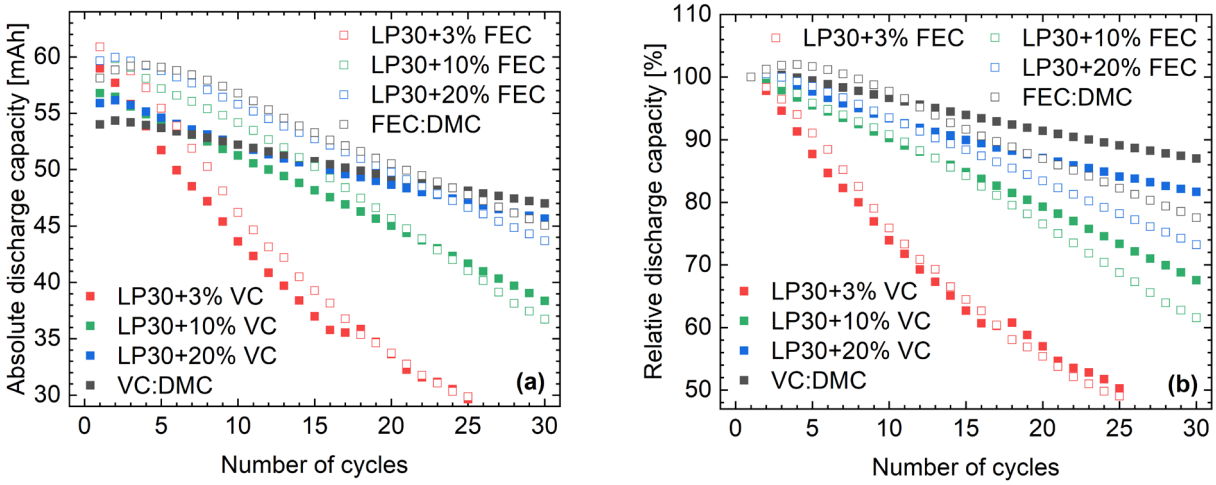

Figure 6.1: Absolute discharge capacities (a) and relative discharge capacities (b) of the tested NCM622/silicon-graphite pouch cells in dependence on the number of cycles. The initial electrolytes from these cells are LP30+3% VC, LP30+10% VC, LP30+20% VC, VC:DMC, LP30+3% FEC, LP30+10% FEC, LP30+20% FEC, and FEC:DMC.

The diagrams in Figure 6.1 indicate that the pouch cells with LP30+3 % VC and LP30+3% FEC as initial electrolytes lose capacity rapidly during cycling. These cells reach a remaining capacity of 80% already after 9 cycles, as can be seen in Figure 6.1(b). It is thus not reasonable to conduct further investigations with the NCM622/silicon-graphite pouch cells that initially contain the same electrolyte as the investigated NCM622/graphite pouch cells (see chapter 5). It is remarkable that the NCM622/silicon-graphite pouch cells with LP30+3% VC as initial electrolyte are at a remaining capacity of 80% already after 9 cycles, while the equivalent, silicon-free NCM622/graphite pouch cells with the identical, initial electrolyte reach remaining capacities of 80% only after 700-1100 cycles (see Figure 5.1(a)). The cause of the much faster capacity loss of the silicon-containing pouch cells compared to the equivalent silicon-free pouch cells could be the much higher volume change of silicon upon de-/lithiation compared to graphite. As a result, more cracks form in the SEI, so that more, new, electrochemically active surface is created, which is associated with a stronger buildup of new SEI material in the silicon-containing cell. This enhanced SEI rebuilding consumes more cycleable lithium and leads to accelerated, irreversible capacity losses of the silicon-containing cell [17]. Furthermore, the plots in Figure 6.1 show that the cycle-life of the cells improves with increasing mass fraction of VC and FEC in the initial electrolyte. It has been reported that the SEI formed by the reductive decomposition of VC and/or FEC is flexible plus stable and can adapt to the large volume changes of silicon during de-/lithation [29]. Correspondingly, a higher concentration of VC and FEC in the electrolyte might lead to a more flexible SEI due to higher fractions of decomposition products from VC and FEC in the SEI. The consequent, reduced crack formation in the SEI might be associated with a slower capacity loss during cycling. Summarized, higher concentrations of VC and FEC in the electrolyte might be accompanied by a better capacity retention of the cells with silicon-containing anodes, which might explain the observed improvement of the cycle-life with increasing concentrations of VC and FEC in

the initial electrolytes from the cells (see Figure 6.1). The absolute discharge capacities from the cells with the EC-free, initial electrolytes VC:DMC and FEC:DMC are close to the respective, absolute discharge capacities from the cells with the EC-containing, initial electrolytes LP30+20% VC and LP30+20% FEC, respectively (see Figure 6.1(a)). Hence, the better capacity retention of the cells with the VC-rich and FEC-rich, initial electrolytes is probably not induced by the simultaneously lower mass fractions of EC in these electrolytes (see Table 6.1). In addition, it is notable that the capacities decrease approximately linearly with the number of cycles and no sudden, rapid capacity losses are observable in Figure 6.1. In contrast, such sudden, rapid capacity losses during cycling are reported in literature for cells with silicon-containing anodes and FEC-containing electrolytes [17,75]. The sudden, rapid capacity drop is explained by a complete consumption of FEC in the cell [17,75]. Once FEC is fully consumed, the anode surface cannot be well passivated anymore, which leads to the mentioned, sudden capacity drop [75]. At least in case of the tested cells with LP30+3% FEC and LP30+3% VC as initial electrolytes, such a complete depletion of FEC and VC, and thus a sudden, rapid capacity loss should occur during cycling according to literature. Indeed, not only VC and FEC, but also other electrolyte components might be decomposed during cycling, especially in the pouch cells with low concentrations of VC and FEC in the initial electrolytes. Hence, no complete consumption of VC and FEC might occur during cycling even in the cells with the initial electrolytes LP30+3% FEC and LP30+3% VC, which possibly explains the absence of sudden capacity drops in the diagrams from Figure 6.1. In the cells with high concentrations of VC and FEC in the initial electrolytes, no complete depletion of VC and FEC is expected.

Beside a high cycle-life, also a high initial discharge capacity and a low internal resistance are desirable for lithium-ion battery cells. The initial discharge capacity is determined by the initial coulombic efficiency, which is the discharge capacity of the first cycle of the formation divided by the charge capacity of the first cycle of the formation. The initial coulombic efficiency indicates, how much charge is irreversibly lost during the first cycle of the formation by reduction of electrolyte components at the anode. To achieve the desired, high, initial discharge capacity, the initial coulombic efficiency should be high. Figure 6.2(a) shows the initial coulombic efficiencies from the examined NCM622/silicon-graphite pouch cells with the different, initial electrolytes. Additionally, the DC internal resistances from the same pouch cells can be seen in Figure 6.2(b). These DC internal resistances are determined at a SOC of 50% after formation.

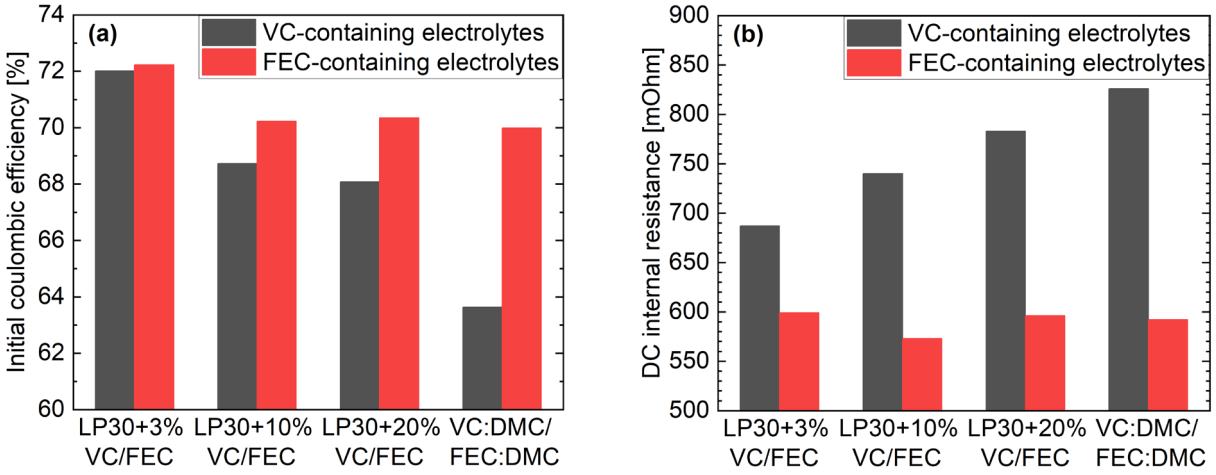

Figure 6.2: Coulombic efficiencies of the first cycle of the formation (a) and DC internal resistances (b) from NCM622/silicon-graphite pouch cells with different, initial electrolytes. The initial electrolytes from these cells are LP30+3% VC, LP30+10% VC, LP30+20% VC, VC:DMC, LP30+3% FEC, LP30+10% FEC, LP30+20% FEC, and FEC:DMC. The DC internal resistances are determined at a SOC of 50% after formation.

The data in Figure 6.2(a) shows that the initial coulombic efficiencies of the cells with the VC-containing electrolytes are lower than the initial coulombic efficiencies of the cells with the FEC-containing electrolytes. According to this, Jaumann et al. found that the initial coulombic efficiency of a silicon-carbon/lithium half-cell with VC-containing electrolyte is slightly lower than the initial coulombic efficiency of an equal cell with FEC-containing electrolyte [29]. Interestingly, the initial coulombic efficiencies of the cells with the initial electrolyte LP30+3% VC and LP30+3% FEC are still almost equal (see Figure 6.2(a)), which indicates that not the reduction of VC or FEC, but the reduction of the other electrolyte components (EC, DMC, and/or $LiPF_6$) might be dominant in these cells during the first cycle. Furthermore, the DC internal resistances of the VC-containing cells are consistently higher than the DC internal resistances of the FEC-containing cells, as can be concluded from Figure 6.2(b). According to this, Jaumann et al. reported that the film resistance of the SEI from a silicon-carbon/lithium half-cell with FEC-containing electrolyte is lower than the film resistance of the SEI from an equal cell with VC-containing electrolyte after the first cycle [29]. Interestingly, the DC internal resistances of the FEC-containing cells do not increase with increasing mass fraction of FEC in the initial electrolyte, while the DC internal resistances of the VC-containing cells increase consistently with increasing mass fraction of VC in the initial electrolyte, as can be concluded from Figure 6.2(b). The latter observation agrees with the reported increase of the internal resistance of cells with silicon-free mesophase carbon microbeads anodes with increasing VC concentration in the initial electrolyte [49]. The initial coulombic efficiency decreases and the DC internal resistance after formation increases with increasing mass fraction of VC in the initial electrolyte of the cell, as can be concluded from the diagrams in Figure 6.2. These findings suggest that higher VC concentrations in the initial electrolyte lead to a stronger electrolyte reduction during formation and thus also to a thicker SEI with a higher resistance after formation. By contrast, the initial coulombic efficiency and the DC internal resistance after formation

do not change clearly in one direction with increasing mass fraction of FEC in the initial electrolyte, as can be seen in the diagrams from Figure 6.2. These observations indicate that a higher FEC concentration in the initial electrolyte is not accompanied by an enhanced electrolyte reduction during formation and a thicker SEI with higher resistance after formation.

Summarized, the cells with the initial electrolytes VC:DMC (1 M $LiPF_6$ in VC:DMC) and FEC:DMC (1 M $LiPF_6$ in FEC:DMC) have the best capacity retention during cycling among the tested NCM622/silicon-graphite pouch cells. Hence, these two electrolytes are selected for the NCM622/silicon-graphite pouch cells used for the further investigations.

6.2 Capacities and coulombic efficiencies of the investigated cells

NCM622/silicon-graphite pouch cells are investigated in the electrochemically untreated, fresh state, after formation, after 15 cycles (at 0.5 C charge and 0.5 C discharge), after 40 cycles (at 0.5 C charge and 0.5 C discharge), and after 40 cycles (at 2 C charge and 3 C discharge). These pouch cells initially contain either the electrolyte 1 M $LiPF_6$ in VC:DMC or the electrolyte 1 M $LiPF_6$ in FEC:DMC. In the following, the cells with 1 M $LiPF_6$ in VC:DMC as initial electrolyte are called the cells with the “VC electrolyte”. The cells with 1 M $LiPF_6$ in FEC:DMC as initial electrolyte are called the cells with the “FEC electrolyte”.

The absolute discharge capacities of selected NCM622/silicon-graphite pouch cells cycled for 40 cycles at 0.5 C charge and 0.5 C discharge (0.5 C/0.5 C) are plotted against the number of cycles in Figure 6.3(a). The associated, relative discharge capacities of these cells are plotted against the number of cycles in Figure 6.3(c). This relative discharge capacity corresponds to the absolute discharge capacity of the respective cycle at 0.5 C/0.5 C divided by the absolute discharge capacity of the first cycle at 0.5 C/0.5 C after formation. The absolute discharge capacities of selected NCM622/silicon-graphite pouch cells cycled for 40 cycles at 2 C charge and 3 C discharge (2 C/3 C) are shown in dependence on the number of cycles in Figure 6.3(b). The associated, relative discharge capacities of these cells are plotted against the number of cycles in Figure 6.3(d). This relative discharge capacity is the absolute discharge capacity of the respective cycle at 2 C/3 C divided by the absolute discharge capacity of the first cycle at 2 C/3 C. In the diagrams from Figure 6.3, the black symbols depict the values of the cells with the VC electrolyte, while the red symbols represent the values of the cells with the FEC electrolyte.

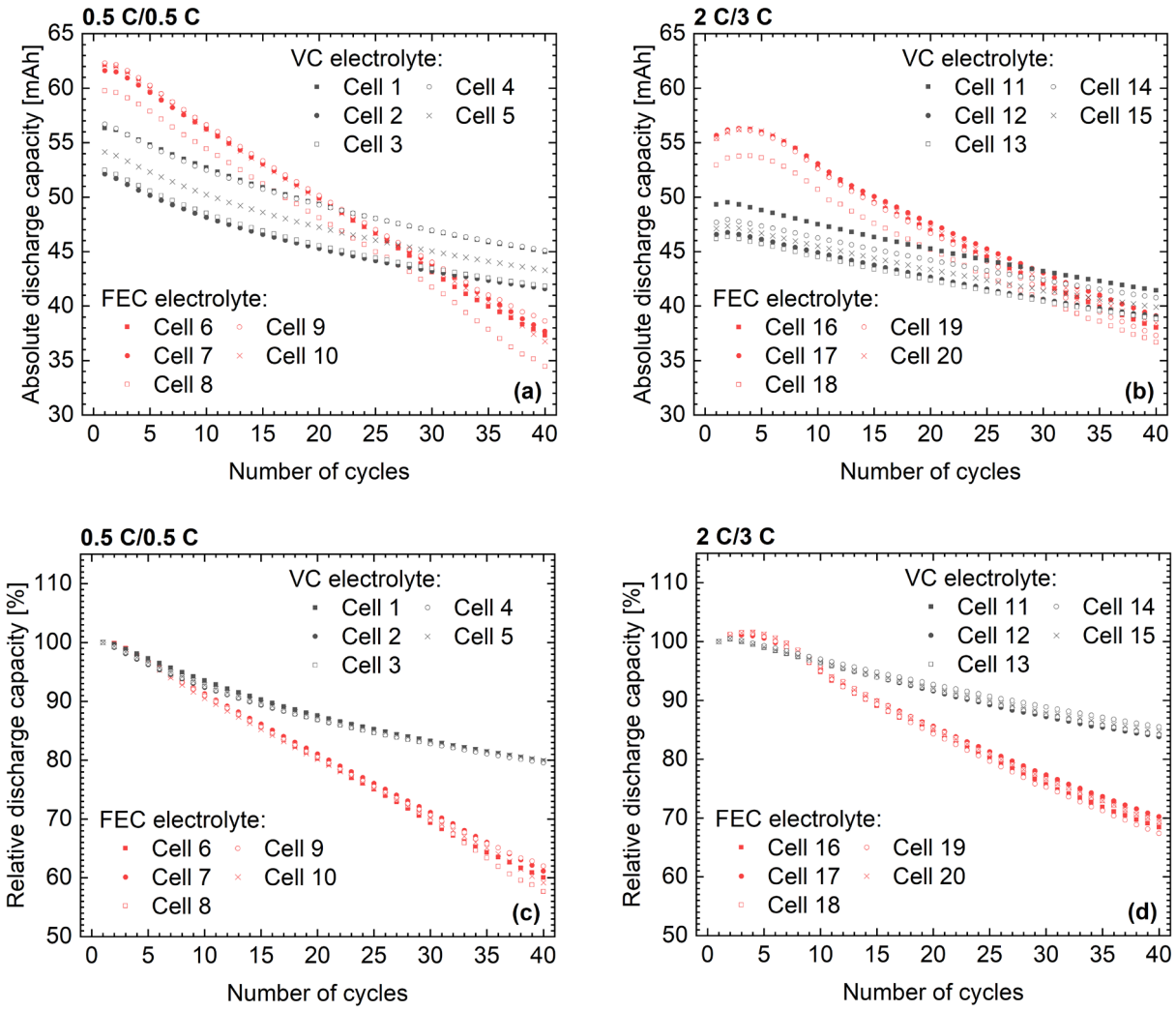

Figure 6.3: Absolute discharge capacities (a) and relative discharge capacities (c) of NCM622/silicon-graphite pouch cells cycled at 0.5 C/0.5 C in dependence on the number of cycles. Absolute discharge capacities (b) and relative discharge capacities (d) of NCM622/silicon-graphite pouch cells cycled at 2 C/3 C in dependence on the number of cycles. Black symbols represent the values of the cells with the VC electrolyte, while red symbols represent the values of the cells with the FEC electrolyte.

As can be seen in Figure 6.3(a) and Figure 6.3(b), the absolute discharge capacities of the cells with the FEC electrolyte are clearly higher than the absolute discharge capacities of the cells with the VC electrolyte during the first cycles. The coulombic efficiencies of the first cycle during formation from the cells with the VC-containing electrolytes are lower than the coulombic efficiencies of the first cycle from the cells with the FEC-containing electrolytes, as shown in Figure 6.2(a). Hence, the irreversible capacity loss of the cells with the VC electrolyte is higher than the irreversible capacity loss of the cells with the FEC electrolyte during formation. This finding explains, why the absolute discharge capacities of the cells with FEC electrolyte are higher than the absolute discharge capacities of the cells with the VC electrolyte during the first cycles (see Figure 6.3(a) and Figure 6.3(b)). Interestingly, the absolute discharge capacities of the cells with the FEC electrolyte are lower than the absolute discharge capacities of the cells with the VC electrolyte after 30-40 cycles, as can be seen in Figure 6.3(a) and

Figure 6.3(b). In addition, the data in Figure 6.3(c) and Figure 6.3(d) indicate that the discharge capacities of the cells with the FEC electrolyte decrease distinctly faster than the discharge capacities of the cells with the VC electrolyte during cycling. Accordingly, Jaumann et al. found that the capacity retention of silicon-carbon/lithium half-cells with FEC-containing electrolyte is worse than the capacity retention of equal cells with VC-containing electrolyte [29]. Additionally, the data in Figure 6.3(c) and Figure 6.3(d) suggest that the discharge capacities of the cells cycled at 2 C/3 C decrease slower than the discharge capacities of the cells cycled at 0.5 C/0.5 C. The silicon particles might be more delithiated at the minimum cell voltage of 3 V during slow cycling with 0.5 C/0.5 C than during fast cycling with 2 C/3 C. In fact, from literature it is known that the capacity fade of lithium-ion cells with silicon-containing anodes can be reduced by limiting the delithiation of silicon [76]. The maximum delithiation of the silicon and thus also the volume changes of the silicon particles are possibly higher during slow cycling with 0.5 C/0.5 C than during fast cycling with 2 C/3 C. Consequently, also the SEI buildup and thus the irreversible capacity loss is stronger during slow cycling than during fast cycling. This might explain, why the capacity retention of the cells cycled at 2 C/3 C is better than the capacity retention of the cells cycled at 0.5 C/0.5 C (see Figure 6.3(c) and Figure 6.3(d)).

In Figure 6.4(a), the coulombic efficiencies of selected NCM622/silicon-graphite pouch cells cycled for 40 cycles at 0.5 C/0.5 C are shown in dependence on the number of cycles. The coulombic efficiencies of selected NCM622/silicon-graphite pouch cells cycled for 40 cycles at 2 C/3 C are plotted against the number of cycles in Figure 6.4(b). In Figure 6.4, the coulombic efficiencies from the cells with the VC electrolyte are indicated by black symbols, whereas the coulombic efficiencies from the cells with the FEC electrolyte are indicated by red symbols.

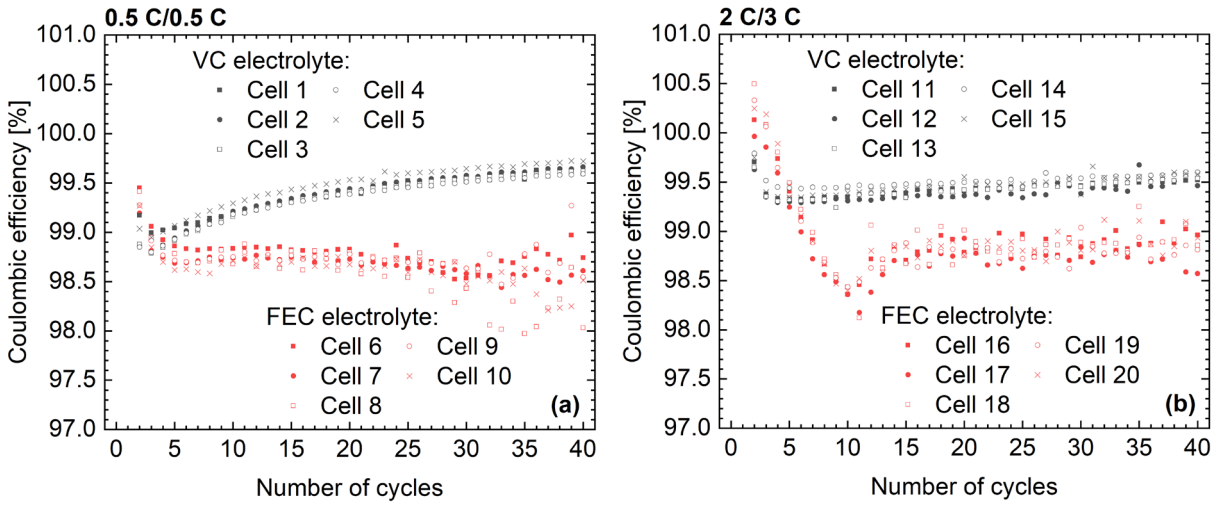

Figure 6.4: (a) Coulombic efficiencies of NCM622/silicon-graphite pouch cells cycled at 0.5 C/0.5 C in dependence on the number of cycles. (b) Coulombic efficiencies of NCM622/silicon-graphite pouch cells cycled at 2 C/3 C plotted against the number of cycles. Black symbols indicate the values of the cells with the VC electrolyte in these plots, whereas red symbols indicate the values of the cells with the FEC electrolyte.

The coulombic efficiencies from the cells with the VC electrolyte are distinctly higher than the coulombic efficiencies from the cells with the FEC electrolyte during cycling, as can be seen in the diagrams from Figure 6.4. Correspondingly, Jaumann et al. also observed that the coulombic efficiencies from silicon-carbon/lithium half-cells with VC-containing electrolyte are higher than the coulombic efficiencies from equal cells with FEC-containing electrolytes during cycling after the first two cycles [29]. Furthermore, the coulombic efficiencies of the cells with the VC electrolyte increase during cycling with 0.5 C/0.5 C (see Figure 6.4(a)). Interestingly, the coulombic efficiencies from the cells with the FEC electrolyte do not rise during cycling with 0.5 C/0.5 C (see Figure 6.4(a)). These observations suggest that the anode passivation improves in the VC-containing cells, but not in the FEC-containing cells during cycling with 0.5 C/0.5 C.

The data in Figure 6.3 and Figure 6.4 reveal the advantages, as well as the disadvantages of the electrolyte components VC and FEC in lithium-ion battery cells with silicon-containing anodes. VC enables a better capacity retention of the cells in comparison to FEC, whereas FEC allows higher absolute discharge capacities of the cells during the first cycles compared to VC. The buildup of the initial SEI in the cells with the VC electrolyte leads to massive, irreversible capacity losses during formation and thus to relatively low absolute discharge capacities during the first cycles. Indeed, the VC-derived SEI is very flexible and survives the large volume changes of silicon during cycling without crack propagation [29]. As a result, the capacity retention of corresponding cells with VC-containing electrolytes is also better than the capacity retention of equivalent cells with FEC-containing electrolytes during subsequent cycling [29]. By contrast, the buildup of the initial SEI in the cells with the FEC electrolyte results in lower, irreversible capacity losses during formation and thus in relatively high discharge capacities during the first cycles. Nevertheless, the FEC-derived SEI is less flexible and cracks during the volume changes of the silicon particles, so that the capacity retention of corresponding cells with FEC-containing electrolytes is worse than the capacity retention of equivalent cells with VC-containing electrolytes during cycling [29]. Indeed, Jaumann et al. did not state that the discharge capacities of cells with the VC-containing electrolyte were substantially lower than the discharge capacities of equal cells with the FEC-containing electrolytes during the first cycles [29].

6.3 Applied analysis methods for the investigations

Various analysis methods are applied for the investigation of the decomposition mechanisms in the NCM622/silicon-graphite pouch cells. In Table 6.2, the applied analysis techniques for the investigations of the NCM622/silicon-graphite pouch cells in the different aging stages can be seen. Additionally, the abbreviated designations for the different aging stages are indicated in Table 6.2. In the following sections, these abbreviated designations are used in figures with measurement data. All investigated NCM622/silicon-graphite pouch cells contain either the VC electrolyte or the FEC electrolyte. For each cell with the VC electrolyte that is investigated with a certain analysis method, an equivalent cell with the FEC electrolyte is examined with the same analysis method.

Table 6.2: Overview of the applied analysis methods for the investigations of the NCM622/silicon-graphite pouch cells in the different aging stages. In addition, the abbreviated designations for the different aging stages are listed. The symbol "X" means that the concerning analysis method is applied for the investigation of the cells in the concerning aging stage. The symbol "-" means that the concerning analysis method is not applied for the investigation of the cells in the concerning aging stage.

Aging stage of examined cell	Abbreviated designation	HPLC-UV/Vis/ HPLC-ESI/MS	GC-FID	GC-TCD	XPS	SEM/ EDX	ICP-OES	Cycling of coin cells
Electro-chemically untreated	Fresh	X	X	X	X	X	X	-
After formation	Formation	X	X	X	X	X	X	X
After formation plus 15 cycles at 0.5 C/0.5 C	15 cycles (0.5 C)	X	X	X	X	X	X	-
After formation plus 40 cycles at 0.5 C/0.5 C	40 cycles (0.5 C)	X	X	X	X	X	X	X
After formation plus 40 cycles at 2 C/3 C	40 cycles (2 C/3 C)	X	X	-	X	-	X	-

6.4 Investigation of the electrochemical decompositions in the electrolytes

The examined electrolytes are extracted from NCM622/silicon-graphite pouch cells at different stages of electrochemical aging to investigate the electrochemical decompositions in the electrolyte during formation and subsequent cycling. The electrolytes are extracted from cells with the VC electrolyte and from cells with the FEC electrolyte by the DEC extraction method, which is described in subsection 3.5.2. In the extracted electrolytes, DEC, DMC, and VC are quantified by HPLC-UV/Vis, while Li^+ and PF_6^- are quantified by HPLC-ESI/MS. FEC is quantified by GC-FID in the extracted electrolytes. Thus, HPLC-UV/Vis, HPLC-ESI/MS, and GC-FID are used to investigate the electrolytes from pouch cells in different aging stages that are indicated in Table 6.2. The investigated electrolytes are extracted from three equally treated cells with the VC electrolyte and three equally treated cells with the FEC electrolyte for each of these aging stages. The extracted electrolytes from the three equivalent cells are analyzed on three different days with three times complete sample preparation, so that three independent single values are determined for each average value indicated in this section. Each indicated average value is the mean of the respective three single values in this section. In this section, the associated, indicated errors are the standard deviations of the mean calculated based on the respective three single values.

The average, quantified concentrations of the components of the electrolytes from the investigated cells in the different aging stages (see Table 6.2) are shown in Figure 6.5. Figure 6.5(a) displays these concentrations for the cells with the VC electrolyte, while Figure 6.5(b) shows these concentrations for the cells with the FEC electrolyte. The calculation of the concentrations in the extracts is described in section 3.6.

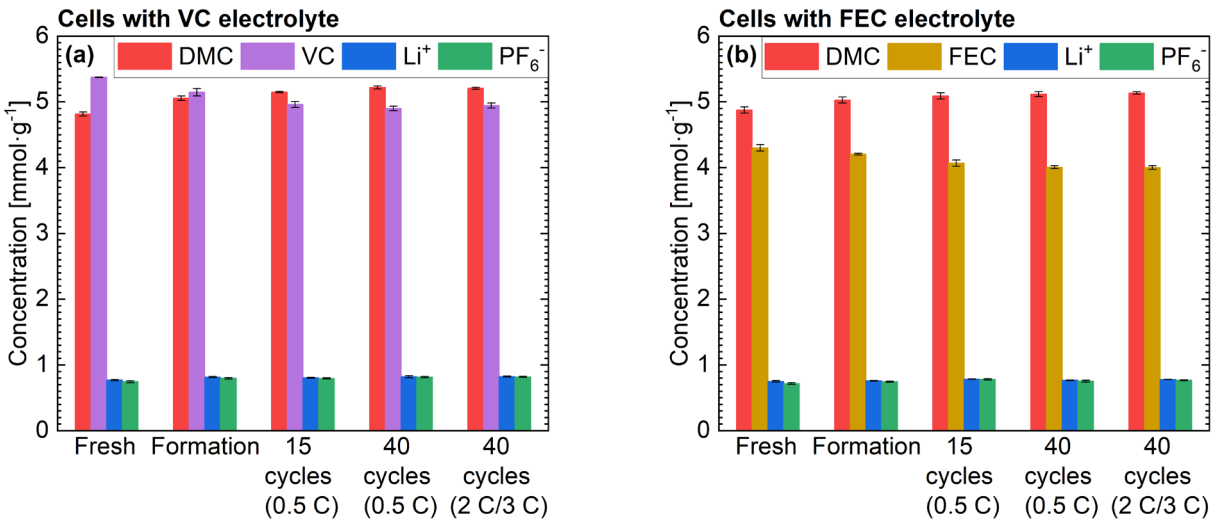

Figure 6.5: (a) Average concentrations of the components of the electrolytes from the examined cells with the VC electrolyte in the different aging stages. (b) Average concentrations of the components of the electrolytes from the examined cells with the FEC electrolyte in the different aging stages.

Figure 6.5(a) indicates an ongoing decrease of the VC concentration in the electrolytes from the cells with the VC electrolyte during formation and subsequent cycling. A continuous reduction of the FEC concentration in the electrolytes from the cells with FEC electrolyte during formation and subsequent cycling can be seen in Figure 6.5(b). By contrast, the concentrations of DMC, Li^+, and PF_6^- slightly increase during formation and subsequent cycling, as can be seen in Figure 6.5(a) and Figure 6.5(b). From these quantified concentrations, a preferential decomposition of VC in the cells with the VC electrolyte and a preferential decomposition of FEC in the cells with the FEC electrolyte can thus be concluded.

To gain more information about the electrolyte decompositions in the investigated NCM622/silicon-graphite pouch cells during formation and subsequent cycling, the absolute amounts of substance of the electrolyte components in these cells are additionally determined. Figure 6.6(a) indicates the average, relative amounts of substance of the electrolyte components in the investigated cells with the VC electrolyte. The average, relative amounts of substance in the fresh cells, the cells after formation, the cells after 15 cycles at 0.5 C/0.5 C, and the cells after 40 cycles at 0.5 C/0.5 C each with the VC electrolyte are additionally plotted against the overall number of cycles in Figure 6.6(b). The overall number of cycles includes also the two cycles during formation and in case of the cells cycled after formation additionally the checkup cycle plus the final cycle (at 0.1 C charge and 0.1 C discharge). Thus, the indicated overall numbers of cycles are two, 19, and 44 for the cells after formation, the cells after 15 cycles at 0.5 C/0.5 C, and the cells after 40 cycles at 0.5 C/0.5 C, respectively (see Figure 6.6(b)). The average, relative amounts of substance in the cells after 40 cycles at 2 C/3 C with the VC electrolyte are not shown in Figure 6.6(b). The relative amount of substance is the quantified, absolute amount of substance divided by the respective, initial amount of substance in the cell. The initial amount of

substance is determined by means of the weighed masses during mixture of the electrolyte and the weighed mass of the electrolyte filled into the cell during cell assembly. The calculation of the relative amount of substance is specified in section 3.6.

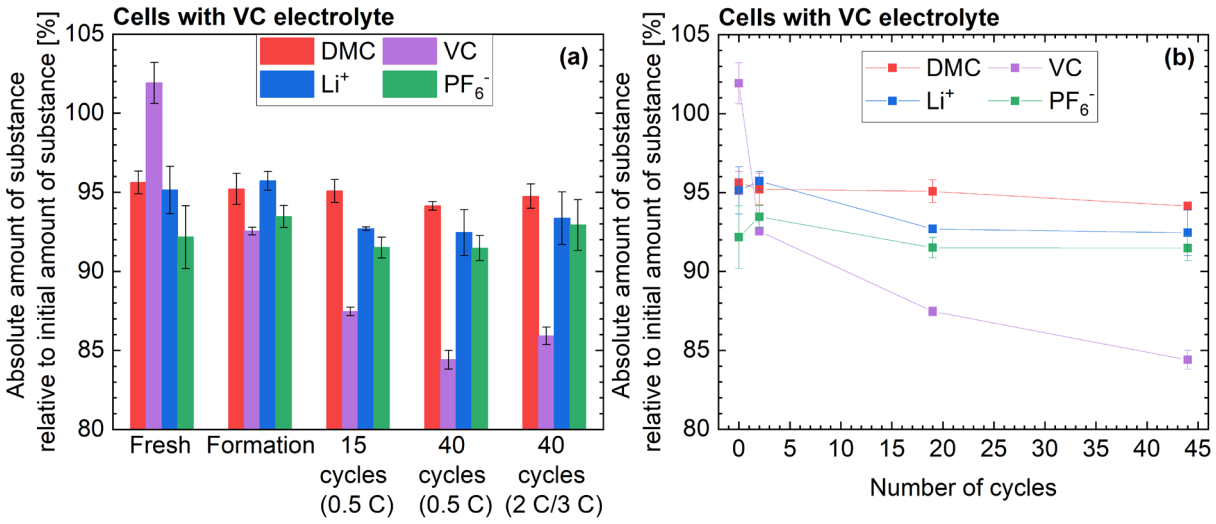

Figure 6.6: (a) Average, relative amounts of substance of the electrolyte components in the investigated cells with the VC electrolyte in the different aging stages. (b) Average, relative amounts of substance of the electrolyte components in the fresh cells, the cells after formation, the cells after 15 cycles at 0.5 C/0.5 C, and the cells after 40 cycles at 0.5 C/0.5 C each with the VC electrolyte plotted against the overall number of cycles.

The diagrams in Figure 6.6 indicate continuous VC decomposition during formation and subsequent cycling. About 9% of the initially present VC are decomposed relatively fast during formation. Further about 8% of the initially present VC are decomposed relatively slow during the subsequent 40 cycles at 0.5 C/0.5 C. Interestingly, the VC consumption during the 40 fast cycles at 2 C/3 C is slightly lower than during the 40 slow cycles at 0.5 C/0.5 C, as can be concluded from Figure 6.6(a). The relative amounts of substance of DMC in the fresh cells are distinctly below the expected value of 100% (see Figure 6.6(a) and Figure 6.6(b)) due to a certain DMC evaporation during the electrolyte extraction and/or during the sealing of the cell under reduced pressure [40]. Furthermore, the relative amounts of substance of Li^+ and PF_6^- in the fresh cells are also clearly lower than the setpoint of 100%, as can be seen in the diagrams in Figure 6.6. This observation might be explained by a certain chemical and/or thermal decomposition of $LiPF_6$ in the cells during storage. In fact, $LiPF_6$ is decomposed thermally and by reaction with trace water to LiF, POF_3, and HF among others according to literature [32,57]. Indeed, the diagrams in Figure 6.6 do not clearly reveal an electrochemical decomposition of DMC and $LiPF_6$ in the cells with the VC electrolyte during the formation and the subsequent cycling.

The average, relative amounts of substance of the electrolyte components in the cells with the FEC electrolyte can be seen in the diagrams in Figure 6.7. The data from the cells with the FEC electrolyte in Figure 6.7(a) and Figure 6.7(b) are the equivalents of the data from the cells with the VC electrolyte in Figure 6.6(a) and Figure 6.6(b).

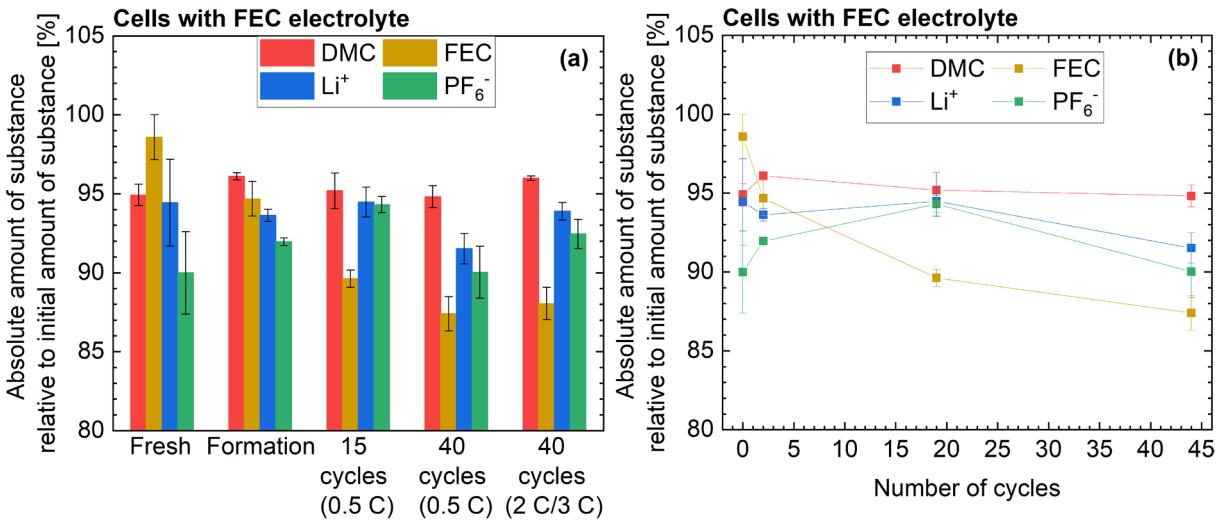

Figure 6.7: (a) Average, relative amounts of substance of the electrolyte components in the investigated cells with the FEC electrolyte in the different aging stages. (b) Average, relative amounts of substance of the electrolyte components in the fresh cells, the cells after formation, the cells after 15 cycles at 0.5 C/0.5 C, and the cells after 40 cycles at 0.5 C/0.5 C each with the FEC electrolyte plotted against the overall number of cycles.

A continuous FEC consumption during formation and subsequent cycling can be identified in the graphs from Figure 6.7. During formation, only about 4% of the initially present FEC are consumed. During the following 40 cycles at 0.5 C/0.5 C, further about 7% of the initially present FEC are decomposed. The relative amounts of substance of FEC in the cells after 40 cycles at 0.5 C/0.5 C are close to the relative amounts of substance of FEC in the cells after 40 cycles at 2 C/3 C, as can be seen in Figure 6.7(a). The relatively slight FEC consumption during formation and the relatively strong FEC consumption during the following 40 cycles suggest that the initial SEI after formation is thin, but does not inhibit further FEC decomposition very well during subsequent cycling. By contrast, the VC decomposition is relatively strong during formation and slighter during the subsequent 40 cycles in the cells with the VC electrolyte (see Figure 6.6), which indicates a thicker, initial SEI after formation, but also a better inhibition of further VC decomposition during following cycling. No clear decomposition of DMC, Li^+, and PF_6^- during formation and subsequent cycling in the cells with the FEC electrolyte can be identified based on the graphs from Figure 6.7. The relative amounts of substance of DMC, Li^+, and PF_6^- in the fresh cells with the FEC electrolyte are distinctly lower than the setpoint of 100% (see Figure 6.7), as already observed in the fresh cells with the VC electrolyte for the same reasons.

For the determination of the absolute magnitudes of the different decompositions in the electrolyte during formation and following cycling, the absolute, consumed amounts of substance or consumptions of the electrolyte components are calculated. In section 3.6, the calculation of the consumptions is described in detail. Figure 6.8 shows the calculated, average consumptions of the electrolyte components in the cells with the VC electrolyte (see Figure 6.8(a)) and in the cells with the FEC electrolyte (see Figure 6.8(b)) during formation, during the 40 cycles at 0.5 C/0.5 C, during

formation plus the 40 cycles at 0.5 C/0.5 C taken together, during the 40 cycles at 2 C/3 C, and during formation plus the 40 cycles at 2 C/3 C taken together.

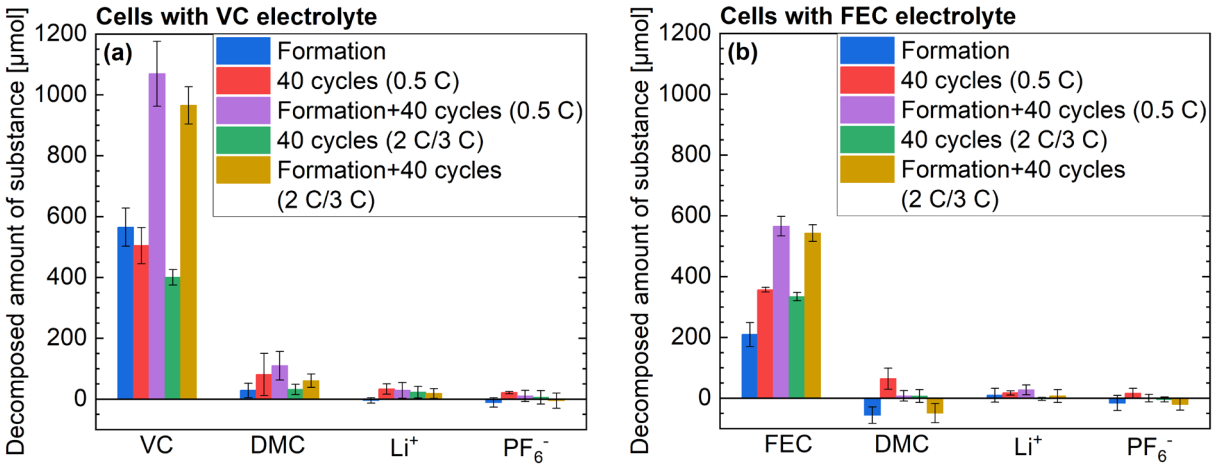

Figure 6.8: Average consumptions of the electrolyte components in the cells with the VC electrolyte (a) and in the cells with the FEC electrolyte (b) during formation, during the 40 cycles at 0.5 C/0.5 C, during formation plus the 40 cycles at 0.5 C/0.5 C taken together, during the 40 cycles at 2 C/3 C, and during formation plus the 40 cycles at 2 C/3 C taken together.

It can be concluded from Figure 6.8(a) that VC is preferentially decomposed in the cells with the VC electrolyte during formation and subsequent cycling, which agrees with the reported, preferential reduction of VC on graphite anodes in lithium-ion cells [3,25,26,34]. According to literature, the VC reduction is accompanied by the deposition of products like poly(VC) on silicon anodes and graphite anodes during formation and cycling [25,34,77]. VC has a higher reduction potential than DMC, which is associated with a preferential VC reduction at the anode [59]. Hence, VC can inhibit the DMC reduction [34], which is consistent with the high VC consumptions and the low DMC consumptions in the cells with the VC electrolyte during formation and subsequent cycling (see Figure 6.8(a)). Interestingly, VC cannot suppress completely the DMC decomposition in the cells with the VC electrolyte during formation and subsequent cycling, as can be concluded from Figure 6.8(a). This finding is remarkable since the initial electrolyte 1 M $LiPF_6$ in VC:DMC in these cells has an exceptionally high VC concentration, which should be high enough to completely suppress the electrochemical DMC decomposition. Indeed, Figure 6.8(a) shows that no significant $LiPF_6$ decomposition occurs in the cells with the VC electrolyte during formation and subsequent cycling. Furthermore, the VC consumptions are lower during the 40 fast cycles at 2 C/3 C than during the 40 slow cycles at 0.5 C/0.5 C (see Figure 6.8(a)), which might be related to the slower capacity losses of the cells cycled at 2 C/3 C compared to the cells cycled at 0.5 C/0.5 C (see Figure 6.3(c) and Figure 6.3(d)). The average VC consumption during formation plus the 40 cycles at 2 C/3 C in the NCM622/silicon-graphite pouch cells with the VC electrolyte (see Figure 6.8(a)) is distinctly higher than the average VC consumption during formation plus about 800 cycles in the NCM622/graphite pouch cells (see Figure 5.4). The NCM622/silicon-

graphite pouch cells with the VC electrolyte have reached a remaining capacity of about 80% after the 40 cycles at 2 C/3 C (see Figure 6.3(d)), whereas the NCM622/graphite pouch cells have reached a remaining capacity of 80% after about 800 cycles at 2 C/3 C (see Figure 5.1(a)). On the one hand, this difference in the VC consumption can be attributed to the higher surface of the silicon-graphite anodes compared to the graphite anodes, as the silicon-graphite anodes additionally contain silicon nanopowder with a huge surface that needs to be passivated during formation. It is known that the electrolyte decomposition increases with increasing surface area of the anode [55]. More SEI material needs to be built in the NCM622/silicon-graphite pouch cells than in the NCM622/graphite pouch cells, so that more VC is consumed during formation in the NCM622/silicon-graphite pouch cells. On the other hand, higher VC consumption in the silicon-containing cells compared to those in the silicon-free cells can be ascribed to the much higher volume changes of silicon during cycling compared to graphite [16]. The consequent, enhanced creation of new, electrochemically active surface leads to a stronger VC consumption in the NCM622/silicon-graphite pouch cells than in the NCM622/graphite pouch cells during formation and subsequent cycling. Furthermore, VC is decomposed almost exclusively during formation and subsequent cycling in the NCM622/silicon-graphite pouch cells (see Figure 6.8(a)), whereas an additional, strong decomposition of EC and DMC during formation plus long-term cycling can be observed in the NCM622/graphite pouch cells (see Figure 5.4). Consequently, almost only VC contributes to the SEI buildup in the silicon-containing cells, while mostly EC and DMC contribute to the SEI buildup in the silicon-free cells during formation and long-term cycling. This might be a third reason, why the VC consumptions during formation and the following 40 cycles at 2 C/3 C in the silicon-containing cells are much higher than the VC consumptions during formation and the following about 800 cycles at 2 C/3 C in the silicon-free cells.

FEC is exclusively decomposed during formation and during subsequent cycling in the cells with the FEC electrolyte, as can be seen in Figure 6.8(b). No significant decomposition of DMC, Li^+, and PF_6^- during formation and during subsequent cycling can be observed in the cells with the FEC electrolyte. The average DMC consumption during formation shown in Figure 6.8(b) is even slightly negative, which can be ascribed to slightly lower, initial DMC amounts in the fresh cells than in the cells after formation by chance in combination with the stability of DMC during formation. Slightly negative consumptions of electrolyte components are also observed for the NCM622/graphite pouch cells (see section 5.2). A more precise explanation for these slightly negative consumptions can be found in section 5.2. The exclusive FEC decomposition during formation and during subsequent cycling in the cells with the FEC electrolyte (see Figure 6.8(b)) is consistent with the reported, exclusive FEC decomposition in cells with silicon-containing electrodes [17]. According to literature, the reduction potential of FEC is higher than the reduction potential of DMC, which is associated with a preferential reduction of FEC [59]. The FEC

consumption is negligibly higher during the 40 fast cycles at 2 C/3 C than during the 40 slow cycles at 0.5 C/0.5 C, as can be observed in Figure 6.8(b).

The two graphs in Figure 6.8 reveal that the VC consumptions in the cells with the VC electrolyte are distinctly higher than the FEC consumptions in the cells with the FEC electrolyte during formation and subsequent cycling. Simultaneously, the absolute discharge capacities from the cells with the VC electrolyte are even higher than the absolute discharge capacities from the cells with the FEC electrolyte after 40 cycles, as can be concluded from Figure 6.3(a) and Figure 6.3(b). Hence, the irreversible capacity losses and thus also the electrolyte reduction should expectably be rather stronger in the cells with the FEC electrolyte than in the cells with the VC electrolyte during formation and the following 40 cycles. The relatively low FEC consumptions shown in Figure 6.8(b) and the relatively high VC consumptions indicated in Figure 6.8(a) contradict this assumption. The reason for the huge differences between the FEC consumptions and the VC consumptions is described in section 6.8.

The described, electrochemical decompositions in the electrolytes should be accompanied by a corresponding reduction of the overall, absolute electrolyte mass in the cells during formation and subsequent cycling, if the decomposition products are solid and/or gaseous. To estimate the consumption of the electrolyte during formation and subsequent cycling, the absolute electrolyte masses in the examined cells are calculated. In Figure 6.9(a), the average, relative electrolyte masses in the investigated cells with the VC electrolyte and the FEC electrolyte can be seen. In addition, the average, relative electrolyte masses in the fresh cells, the cells after formation, the cells after 15 cycles at 0.5 C/0.5 C, and the cells after 40 cycles at 0.5 C/0.5 C are plotted against the overall number of cycles in Figure 6.9(b). The relative electrolyte mass corresponds to the quantified, absolute electrolyte mass divided by the weighed, initial electrolyte mass in the cell. In section 3.6, the calculation of the quantified, absolute electrolyte mass is specified.

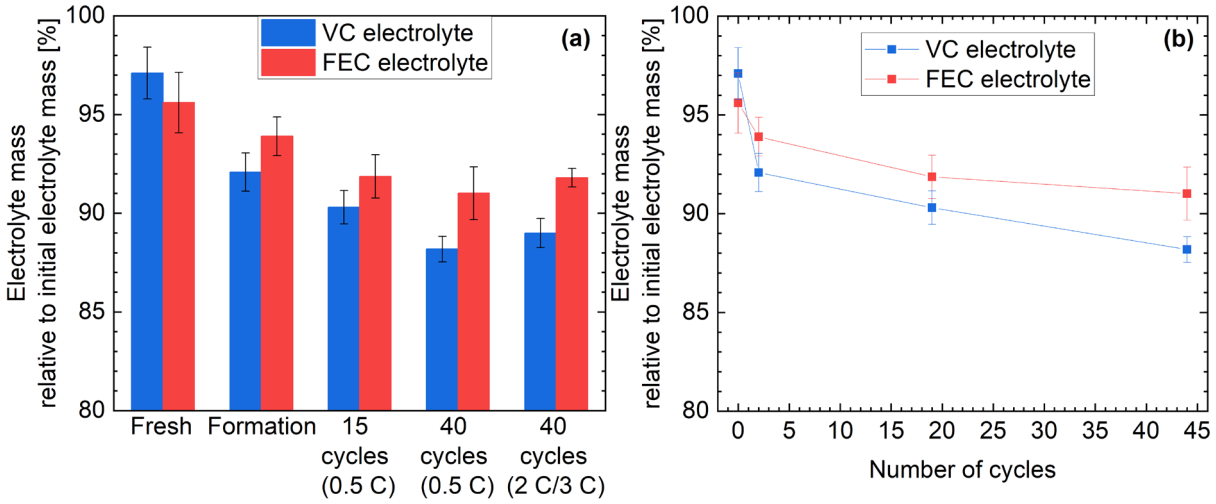

Figure 6.9: (a) Average, relative electrolyte masses in the examined cells in the different aging stages. (b) Average, relative electrolyte masses in the fresh cells, the cells after formation, the cells after 15 cycles at 0.5 C/0.5 C, and the cells after 40 cycles at 0.5 C/0.5 C plotted against the overall number of cycles. The graphs (a) and (b) show the average, relative electrolyte masses in the examined cells with the VC electrolyte and the FEC electrolyte.

The graphs in Figure 6.9 show that the average, relative electrolyte masses in the fresh cells are already below the expected value of 100% due to the DMC loss during electrolyte extraction [40]. During formation, the electrolyte decomposition is distinct in the cells with the VC electrolyte and the FEC electrolyte, as can be concluded from the graphs in Figure 6.9. Indeed, the electrolyte decomposition during formation is less pronounced in the cells with the FEC electrolyte. The relatively slight electrolyte decomposition in the cells with the FEC electrolyte and the relatively strong electrolyte decomposition in the cells with the VC electrolyte during formation (see Figure 6.9(a) and Figure 6.9(b)) can be attributed to the relatively slight FEC consumption (see Figure 6.8(b)) and the relatively strong VC consumption during formation (see Figure 6.8(a)). The electrolyte decomposition is decelerated after formation during subsequent cycling in the cells with the VC electrolyte and the FEC electrolyte, as can be seen in Figure 6.9(b). The magnitudes of the electrolyte consumptions in the cells with the VC electrolyte and the FEC electrolyte are similar after formation during subsequent cycling, as can be concluded from the graphs in Figure 6.9. Furthermore, the average, relative electrolyte masses in the cells after the 40 slow cycles at 0.5 C/0.5 C and after the 40 fast cycles at 2 C/3 C do not differ significantly from each other (see Figure 6.9(a)). Hence, the charge and discharge current do not influence substantially the magnitude of the electrolyte decomposition. It is generally known that the buildup and the growth of the SEI is associated with a corresponding electrolyte consumption during formation and subsequent cycling [17,25,26,33,34,55]. Thus, the mentioned, relatively strong electrolyte decomposition in the cells with the VC electrolyte during formation suggests the buildup of a relatively thick SEI. The mentioned, relatively slight electrolyte decomposition in the cells with the FEC electrolyte during formation indicates the formation of a relatively thin SEI. The mentioned,

similarly strong electrolyte consumptions in the cells with the VC electrolyte and the FEC electrolyte after formation during subsequent cycling indicate similar SEI growth rates in these cells.

6.5 Investigation of the gas evolution

To gain further information about the electrochemical decomposition of the electrolyte, the gases from NCM622/silicon-graphite pouch cells are analyzed by GC-TCD. GC-TCD is applied for the investigation of the evolved gases from pouch cells in different aging stages, which are indicated in Table 6.2. The analyzed gases are extracted from two equally treated cells with the VC electrolyte and two equally treated cells with the FEC electrolyte for each of these aging stages. Thus, two single values are determined for each average value indicated in this section. Each indicated average value is the mean of the respective two single values in this section. The gases are extracted from these cells by means of the gas extraction valve. This extraction method is described in subsection 3.8.4. As explained in subsection 3.8.4, this gas extraction method allows the determination of the absolute amounts of substance of the gases in the pouch cell. Figure 6.10(a) and Figure 6.10(b) display the average, absolute amounts of substance of the detected gases in the investigated cells with the VC electrolyte and the FEC electrolyte, respectively. The detected gases are hydrogen (H_2), methane (CH_4), carbon monoxide (CO), ethylene (C_2H_4), ethane (C_2H_6), and carbon dioxide (CO_2). The error bars indicated in the graphs from Figure 6.10 correspond to the standard deviations of the mean calculated based on the two determined single values.

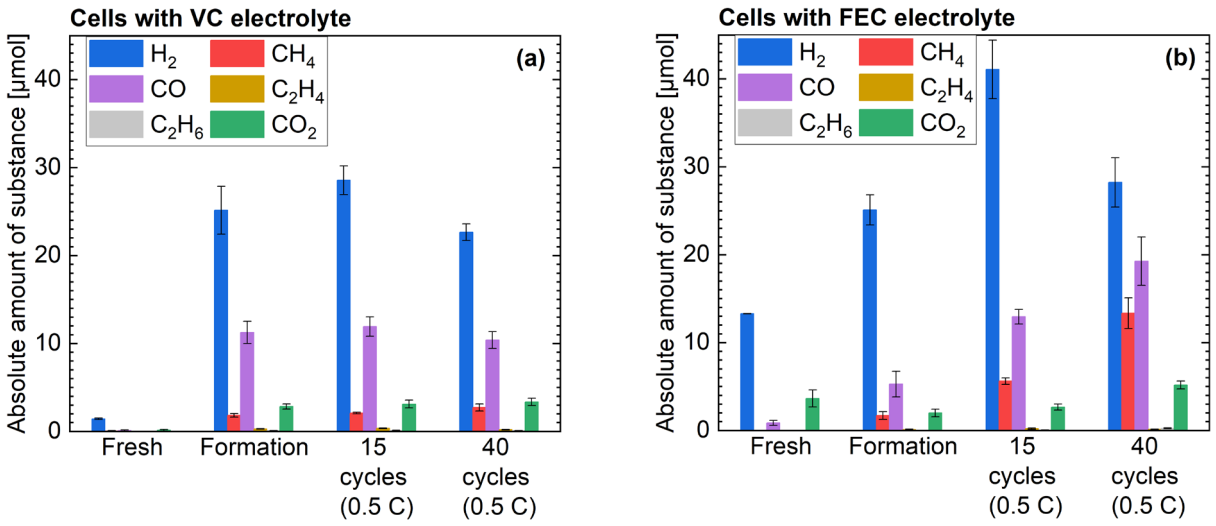

Figure 6.10: Average, absolute amounts of substance of the detected gases in the cells with the VC electrolyte (a) and in the cells with the FEC electrolyte (b). The investigated gases are extracted from cells in different aging stages.

Only minor amounts of gases are detected in the fresh cells with the VC electrolyte, as can be seen in Figure 6.10(a). A significant increase of the average amount of substance of H_2 during formation can be observed in Figure 6.10(a). H_2 is reported to be formed by the reduction of trace water at the anode

during formation [34,78,79]. However, (almost) no further H_2 is evolved after formation during subsequent cycling (see Figure 6.10(a)), which indicates that possible reduction of trace water takes place mainly during formation in the cells with the VC electrolyte. Furthermore, slight CH_4 amounts are evolved during formation and subsequent cycling in the cells with the VC electrolyte, as can be concluded from Figure 6.10(a). It is known that the evolution of CH_4 can be attributed to the reduction of DMC [34,60]. Thus, the detected, slight CH_4 evolution (see Figure 6.10(a)) matches the observed, slight DMC decomposition in the cells with the VC electrolyte during formation and following cycling (see Figure 6.8(a)). Moreover, slight amounts of CO are evolved during formation in the cells with the VC electrolyte, as can be concluded from Figure 6.10(a). Indeed, the CO amount does not further increase after formation during subsequent cycling in the cells with the VC electrolyte. From literature it is known that the evolution of CO can be attributed to the reduction of DMC and/or VC during formation [34]. The observed, slight CO evolution in the cells with the VC electrolyte (see Figure 6.10(a)) and the detected, strong VC decomposition in the cells with the VC electrolyte (see Figure 6.8(a)) indicate that the major decomposition pathway of VC does not include a CO evolution. In fact, the VC reduction mainly leads to the evolution of CO_2 during formation and subsequent cycling according to literature [34,62,80]. Interestingly, the evolved amounts of substance of CO_2 during formation (see Figure 6.10(a)) are by orders of magnitude lower than the consumed amounts of substance of VC during formation in the cells with the VC electrolyte (see Figure 6.8(a)). The average amount of substance of CO_2 in the cells with the VC electrolyte after formation is only 2.8±0.3 µmol, whereas the average, consumed amount of substance of VC during formation is about 560±60 µmol. Hence, the CO_2 formation can be traced back to a minor side reaction of the reductive decomposition of VC, as reported in literature [62]. The major decomposition pathway of VC thus does not include the evolution of CO_2 [62]. Furthermore, the data in Figure 6.10(a) suggest that no further CO_2 is formed after formation during the subsequent 40 cycles at 0.5 C/0.5 C in the cells with the VC electrolyte. This finding is remarkable, because the VC consumption after formation during the subsequent 40 cycles at 0.5 C/0.5 C is still considerable (see Figure 6.8(a)). Consequently, the pronounced VC decomposition is not accompanied by a noteworthy CO_2 evolution after formation during subsequent cycling in the cells with the VC electrolyte, which confirms the mentioned conclusion that the major decomposition pathway of VC does not include the CO_2 evolution. The amounts of C_2H_4 and C_2H_6 detected in the cells with the VC electrolyte are negligible (see Figure 6.10(a)).

The data in Figure 6.10(b) suggest that H_2 is formed during formation and following cycling in the cells with the FEC electrolyte. This electrochemically induced H_2 formation can be attributed (partly) to the reduction of trace water at the anodes, as reported in literature [34,78,79]. In addition, it is known from literature that the reductive decomposition of FEC yields H_2 among others [17,81]. According to this, the FEC decomposition (see Figure 6.8(b)) might also contribute to the H_2 evolution in the cells

with the FEC electrolyte during formation and subsequent cycling (see Figure 6.10(b)). Surprisingly, considerable amounts of H_2 are already detected in the fresh cells with the FEC electrolyte, as can be seen in Figure 6.10(b). The minor H_2 amounts in the fresh cells with the VC electrolyte (see Figure 6.10(a)) and the considerable H_2 amounts in the fresh cells with the FEC electrolyte (see Figure 6.10(b)) suggest that a chemical decomposition of FEC is responsible for a part of the detected H_2 in the cells with the FEC electrolyte. Figure 6.10(b) shows that CH_4 is formed during formation and the following 40 cycles at 0.5 C/0.5 C. As already mentioned, the DMC reduction leads to the evolution of CH_4 according to literature [34,60]. Consequently, the accumulation of CH_4 in the cells with the FEC electrolyte during formation and the subsequent 40 cycles at 0.5 C/0.5 C (see Figure 6.10(b)) indicates a certain, electrochemical DMC decomposition in these cells, which is not consistent with the observed, exclusive decomposition of FEC in the cells with the FEC electrolyte during formation plus the subsequent cycling (see Figure 6.8(b)). Indeed, it needs to be considered that the average amounts of substance of CH_4 detected in the cells with the FEC electrolyte (below 15 µmol) are negligibly low compared to the total amounts of substance of DMC in fresh cells with the FEC electrolyte (about 5500 µmol). As a result, the electrochemical DMC decomposition in the cells with the FEC electrolyte is possibly too slight to be clearly identified in the electrolyte. Moreover, a continuous increase of the average amount of substance of CO during formation and the subsequent 40 cycles at 0.5 C/0.5 C can be observed in Figure 6.10(b). In literature, the formation of CO as a result of FEC reduction is proposed based on the results from theoretical calculations [82]. Indeed, the CO amounts detected in the cells with the FEC electrolyte (see Figure 6.10(b)) are distinctly lower than the FEC consumptions in these cells (see Figure 6.8(b)). These observations indicate that the major decomposition pathway of FEC does not include a CO formation. Moreover, (almost) no C_2H_4 and C_2H_6 is detected in the cells with the FEC electrolyte, as can be seen in Figure 6.10(b). No increase of the average amounts of substance of CO_2 during formation and subsequent cycling can be seen in Figure 6.10(b). According to literature, the reduction of FEC at the anode leads to the formation of CO_2 [17,82]. Jung et al. stated that one CO_2 molecule is released for every decomposed FEC molecule in lithium-ion cells with silicon-containing anodes [17]. Consequently, the consumption of the about 550 µmol FEC during formation plus the subsequent 40 cycles at 0.5 C/0.5 C (see Figure 6.8(b)) should be associated with a simultaneous evolution of 550 µmol CO_2 in the cells with the FEC electrolyte. Indeed, the amounts of substance of CO_2 detected in the cells with the FEC electrolyte after formation plus the subsequent 40 cycles at 0.5 C/0.5 C are by orders of magnitude lower than these 550 µmol, as can be concluded from Figure 6.10(b). This discrepancy could be ascribed to a CO_2 consumption following the CO_2 formation in the cells with the FEC electrolyte during formation and subsequent cycling. It needs to be considered that Jung et al. found the release of one CO_2 molecule per consumed FEC molecule by means of On-line Electrochemical Mass Spectrometry (OEMS) measurements [17]. The used OEMS cell had a huge

volume of 9.5 ml and thus also a correspondingly large gas head space, while the silicon-containing electrode in this OEMS cell had a diameter of only 15 mm [17]. Hence, the few, evolved CO_2 could quickly diffuse away from the anode into the large gas head space. As a result, the accumulated CO_2 in the gas head space could possibly not be decomposed at the electrodes. By contrast, the investigated NCM622/silicon-graphite pouch cells in this thesis have no gas head space, so that the released CO_2 cannot quickly diffuse away from the anodes into a separated gas head space. As a result, the evolved CO_2 might be reduced after its formation instead of accumulating in the pouch cell. Petibon et al. found that the total volume of gas evolved during the first cycle in $LiCoO_2$ (LCO)/silicon-alloy-graphite pouch cells with a FEC-containing electrolyte was 0.17 ml and the average CO_2 concentration in this evolved gas was 92.1% [75]. The LCO/silicon-alloy-graphite pouch cells investigated by Petibon et al. had initial discharge capacities of about 200 mAh [75], which is admittedly higher than the initial discharge capacities from the NCM622/silicon-graphite pouch cells investigated in this study (see Figure 6.3(a)). Indeed, the initial discharge capacities of the LCO/silicon-alloy-graphite pouch cells and the NCM622/silicon-graphite pouch cells are at least of a similar order of magnitude, so that a careful comparison between these cells is reasonable. Using the ideal gas law with a temperature of 40 °C [75], a gas volume of 0.17 ml [75], and a pressure of 1 bar, the calculated, overall amount of the evolved gas in the LCO/silicon-alloy-graphite pouch cells during the first cycle is about 6.5 µmol. As the quantified, average CO_2 concentration in this evolved gas was 92.1% [75], the calculated CO_2 amount in the LCO/silicon-alloy-graphite pouch cells after the first cycle was about 6 µmol. This calculated CO_2 amount is in the same order of magnitude as the CO_2 amounts detected in the NCM622/silicon-graphite pouch cells with the FEC electrolyte (see Figure 6.10(b)). Petibon et al. used a completely different method for gas extraction and for the determination of the total volume of the evolved gas [75]. Hence, the mentioned consistency with respect to the CO_2 amounts in the LCO/silicon-alloy-graphite pouch cells and the NCM622/silicon-graphite pouch cells suggests that the unexpectedly low CO_2 amounts that are detected in the cells with the FEC electrolyte (see Figure 6.10(b)) cannot be ascribed to an incomplete CO_2 extraction from these cells specifically due to the applied gas extraction method. Instead, CO_2 is evolved in the first step, whereupon CO_2 is further decomposed in the second step. This might explain the detected, massive FEC consumption and the detected, slight CO_2 evolution in the NCM622/silicon-graphite pouch cells during formation and the subsequent 40 cycles at 0.5 C/0.5 C. In fact, a reductive decomposition of CO_2 in lithium-ion cells during formation and subsequent cycling is reported yielding SEI components, such as Li_2CO_3 [83–85].

Summarized, the results from the gas analyses reveal that none of the end products from the major decomposition pathway of VC and FEC are gaseous since the detected amounts of the evolved gases (see Figure 6.10) are by orders of magnitude lower than the consumed amounts of VC and FEC in the

investigated pouch cells (see Figure 6.8). Admittedly, the FEC reduction initially leads to the evolution of CO_2, but CO_2 is mostly further reduced resulting in additional SEI material.

6.6 Investigation of the electrode surfaces

For a further clarification of the major decomposition pathway of VC and FEC, electrodes from the NCM622/silicon-graphite pouch cells are examined by XPS, SEM, and EDX.

The surface layers on the electrodes formed by decomposition products from the electrolyte are examined using XPS. XPS is used to investigate anodes and cathodes from NCM622/silicon-graphite pouch cells in different aging stages, which are indicated in Table 6.2. For each of these aging stages, the analyzed electrodes are extracted from one cell with the VC electrolyte and one cell with the FEC electrolyte. The C1s and O1s photoelectron spectra of the anodes from the fresh cell, the cell after formation, the cell after 15 cycles at 0.5 C/0.5 C, and the cell after 40 cycles at 0.5 C/0.5 C each with the VC electrolyte are depicted in Figure 6.11(a) and Figure 6.11(c), respectively. The C1s and O1s photoelectron spectra of the anodes from the fresh cell, the cell after formation, the cell after 15 cycles at 0.5 C/0.5 C, and the cell after 40 cycles at 0.5 C/0.5 C each with the FEC electrolyte are shown in Figure 6.11(b) and Figure 6.11(d), respectively. The C1s and O1s photoelectron spectra of the anodes from the cells after 40 cycles at 2 C/3 C are not indicated in Figure 6.11.

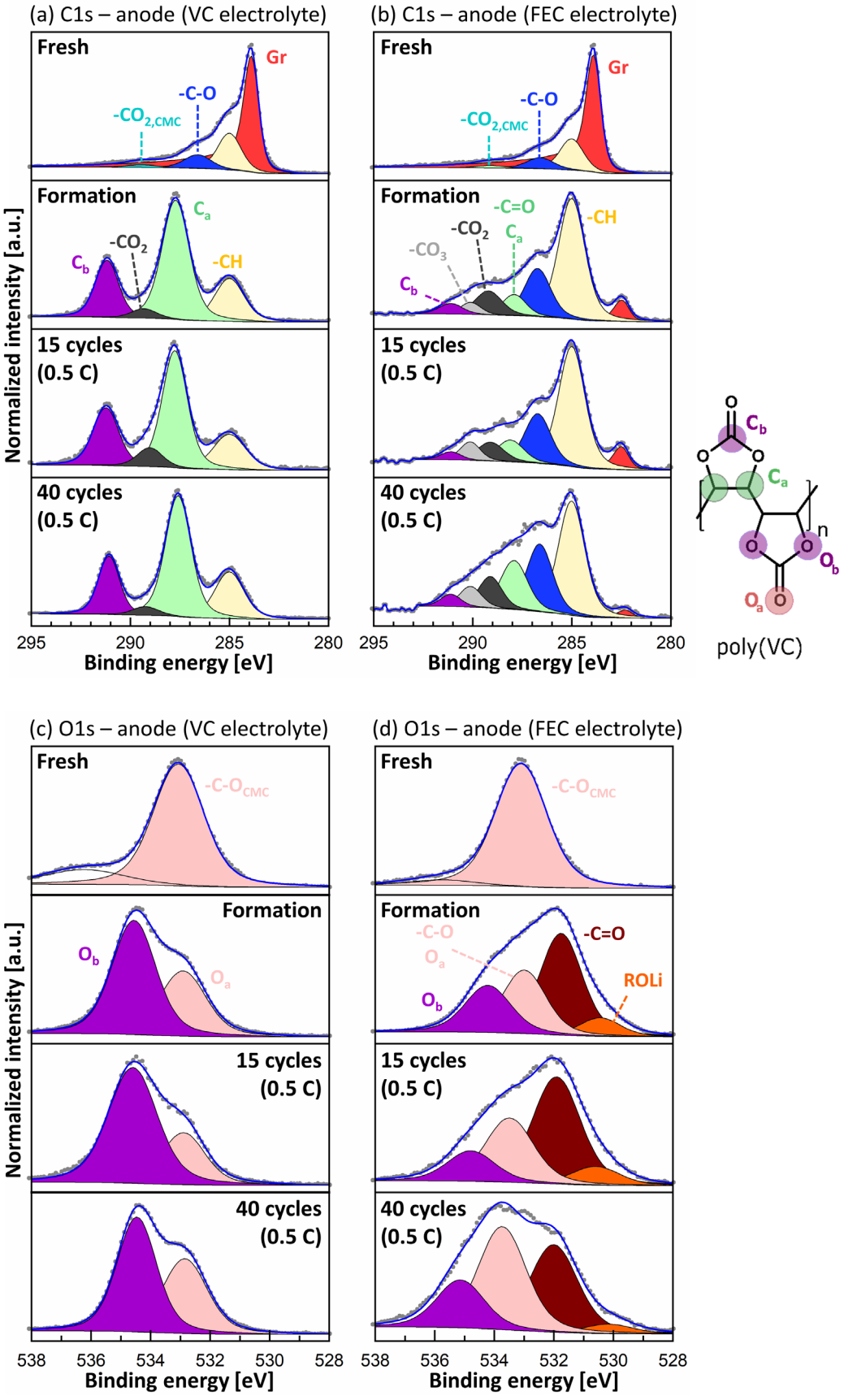

Figure 6.11: C1s spectra (a) and O1s spectra (c) of anodes from a fresh cell, a cell after formation, a cell after 15 cycles at 0.5 C/0.5 C, and a cell after 40 cycles at 0.5 C/0.5 C each with the VC electrolyte. Additionally, C1s spectra (b) and O1s spectra (d) of anodes from a fresh cell, a cell after formation, a cell after 15 cycles at 0.5 C/0.5 C, and a cell after 40 cycles at 0.5 C/0.5 C each with the FEC electrolyte are shown.

The graphite peak (red) is dominant in the C1s spectrum of the anode from the fresh cell with the VC electrolyte, as can be seen in Figure 6.11(a). Remarkably, the graphite peak is completely disappeared in the C1s spectrum of the anode from the cell with the VC electrolyte after formation (see Figure 6.11(a)). Additionally, the silicon peak (Si^0 2p3 peak at 99.51 eV) and the silicon oxide peak (SiO_2 2p3 peak at 103.69 eV) are also completely disappeared in the Si2p spectrum of the anode from the cell with the VC electrolyte after formation (see Table A.1 in the Appendix). The mentioned disappearance of the graphite peak, the silicon peak, and the silicon oxide peak indicates that the thickness of the SEI on the graphite particles and the silicon particles is greater than the information depth of XPS (5-10 nm) already after formation in the cells with the VC electrolyte. In general, the silicon oxide detected on the anodes from fresh cells can be ascribed to surface layers of silicon oxide on the silicon particles that are formed by the reaction of the silicon with the oxygen from the ambient air during storage of the anodes before the cell assembly. The C_a peak (287.7 eV, light green) plus the C_b peak (291.3 eV, purple) are pronounced in the C1s spectrum from the anode after formation in Figure 6.11(a). The O_a peak (532.9 eV, pink) and the O_b peak (534.5 eV, purple) are dominant in the O1s spectrum of the anode from the cell after formation with the VC electrolyte (see Figure 6.11(c)). The C_a peak, the C_b peak, the O_a peak, and the O_b peak are characteristic for poly(VC), which is a decomposition product of VC [25]. Additionally, Figure 6.11(a) and Figure 6.11(c) show that the C1s and O1s spectra of the anodes after 15 cycles at 0.5 C/0.5 C and after 40 cycles at 0.5 C/0.5 C do not significantly differ from the C1s and O1s spectrum of the anode after formation. The atomic percentages of the compounds detected by XPS (see Table A.1 in the Appendix) confirm that the compounds characteristic for poly(VC) (C_a, C_b, O_a, and O_b) are abundant in the SEI after formation and after subsequent cycling in the cells with the VC electrolyte. From this it can be concluded that poly(VC) represents the main component of the SEI after formation and after subsequent cycling in the cells with the VC electrolyte, which is consistent with the observed, strong VC decomposition during formation and subsequent cycling (see Figure 6.8(a)). A decomposition of VC mainly to poly(VC) is also consistent with the absence of considerable CO_2 amounts in the pouch cells with the VC electrolyte after formation and subsequent cycling (see Figure 6.10(a)) since poly(VC) contains intact carbonate moieties, so that poly(VC) must be produced without any CO_2 evolution [83]. The atomic percentages of lithium in the surface layers of the anodes from the cells with the VC electrolyte are relatively low or even negligible (see values from Li1s spectra in Table A.1 in the Appendix), which suggests a low lithium concentration in the SEI from the cells with the VC electrolyte. Furthermore, the peak of the salt decomposition product LiF (at about 685 eV) is (almost) not present in the F1s spectra of the anodes from the cells with the VC electrolyte, as can be concluded from the data in Table A.1 in the Appendix, which suggests a negligible $LiPF_6$ decomposition during formation and subsequent cycling in these cells. This finding is confirmed by the

observed, negligible consumptions of Li^+ and PF_6^- in the cells with the VC electrolyte during formation and subsequent cycling (see Figure 6.8(a)).

Figure 6.11(b) indicates that the graphite peak is also dominant in the C1s spectrum of the anode from the fresh cell with the FEC electrolyte. As can be observed in the C1s spectra of the anodes from the cells with the FEC electrolyte in Figure 6.11(b), the intensity of the graphite peak diminishes continuously during formation and subsequent cycling. The continuous growth of the SEI during formation and subsequent cycling is responsible for this reduction of the graphite peak. Interestingly, the graphite peak is not disappeared even in the C1s spectrum of the anode from the cell with the FEC electrolyte after 40 cycles at 0.5 C/0.5 C, which suggests that the thickness of the SEI on the graphite particles is always less than the information depth of XPS (5-10 nm) during formation and the subsequent 40 cycles at 0.5 C/0.5 C in these cells. As can be concluded from the data in Table A.2 in the Appendix, the silicon peak (Si^0 2p3 peak at 99.51 eV) and the silicon oxide peak (SiO_2 2p3 peak at 103.69 eV) are admittedly disappeared in the Si2p spectrum of the anode from the cell with the FEC electrolyte after formation, but the peaks of lithiated silicon (Li_xSi_y peak at about 97.4 eV) and lithiated silicon oxide (Li_xSiO_y peak at about 100.5 eV) are present in this Si2p spectrum. Lithiated silicon and lithiated silicon oxide are still detectable on the anode from the cell with the FEC electrolyte after 15 cycles at 0.5 C/0.5 C, but no longer on the anode from the cell with the FEC electrolyte after 40 cycles at 0.5 C/0.5 C (see Table A.2 in the Appendix). Hence, the thickness of the SEI on the silicon particles is only after 40 cycles at 0.5 C/0.5 C greater than the information depth of XPS (5-10 nm) in the cells with the FEC electrolyte. The mentioned, detected lithiated silicon indicates that silicon cannot be completely delithiated during the final discharge before the XPS analyses. This phenomenon might be ascribed to the accumulation of electrochemically inactive Li_xSi_y in the surface layer of the silicon particles during formation and subsequent cycling, as reported in literature [86]. The mentioned, detected lithiated silicon oxide or lithium silicate suggests that the silicon oxide cannot be (fully) delithiated during the last discharge before the XPS measurements. According to this, it is known from literature that lithium silicate remains electrochemically inactive once it is formed [67,87]. The aforementioned peaks characteristic for poly(VC), namely the C_a peak, the C_b peak, the O_a peak, and the O_b peak, are visible, but not dominant in the C1s spectra and the O1s spectra of the anodes from the cells with the FEC electrolyte, as can be observed in Figure 6.11(b) and Figure 6.11(d). These observations together with the observed, preferential decomposition of FEC (see Figure 6.8(b)) indicate that poly(VC) does not represent the main decomposition product of FEC. Instead, only a small fraction of the consumed FEC is decomposed to poly(VC) during formation and subsequent cycling. According to this, a decomposition of FEC to poly(VC) and LiF is proposed in literature [28]. Moreover, the $-CO_3$ peak (290.1 eV, light grey) is visible in the C1s spectra of the anodes from the cells with the FEC electrolyte after formation, after 15 cycles at 0.5 C/0.5 C, and after 40 cycles at 0.5 C/0.5 C (see

Figure 6.11(b)). This observation suggests a deposition of lithium carbonate in the SEI during formation and subsequent cycling in the cells with the FEC electrolyte, because the -CO_3 peak can be attributed to lithium carbonate [64]. This deposition of lithium carbonate might be induced by the reduction of the CO_2 that is evolved due to the FEC reduction. In fact, lithium carbonate represents a main product of the reductive decomposition of CO_2 in lithium-ion cells according to literature [83,88]. Hence, the deposited lithium carbonate matches the absence of considerable CO_2 amounts in the cells with the FEC electrolyte (see Figure 6.10(b)), despite the detected, massive FEC decomposition (see Figure 6.8(b)) and the consequent, massive CO_2 formation [17]. Furthermore, a pronounced -C-O peak (286.7 eV, blue) can be observed in the C1s spectra of the anodes from the cells with the FEC electrolyte after formation, after 15 cycles at 0.5 C/0.5 C, and after 40 cycles at 0.5 C/0.5 C (see Figure 6.11(b)). The -C-O peak is the dominant peak in the C1s spectrum from polyethylene oxide (PEO), as reported in literature [89]. Consequently, the mentioned, pronounced -C-O peaks in Figure 6.11(b) might suggest the deposition of PEO on the anodes during formation and subsequent cycling in the cells with the FEC electrolyte. It is reported in literature that FEC reduction leads to the formation of PEO, which forms part of the SEI [90]. Besides, the data in Table A.2 in the Appendix reveal an increase of the atomic percentages of LiF in the surface layer of the anodes from the cells with the FEC electrolyte during formation and the subsequent 40 cycles at 0.5 C/0.5 C. LiF represents a main component of the SEI in the cells with the FEC electrolyte, as can be concluded from the data in Table A.2 in the Appendix. This observation together with the observed, exclusive decomposition of FEC (see Figure 6.8(b)) suggests that FEC is largely decomposed to LiF in the cells with the FEC electrolyte during formation and subsequent cycling. In fact, the reductive decomposition of FEC in lithium-ion cells yields the SEI component LiF among others according to literature [17,27,81,91–93]. Apart from that, the atomic percentages of the phosphorus-containing compounds (Li_xPF_y, $Li_xPF_yO_z$) in the surface layers of the examined anodes do not differ substantially from each other, as can be concluded from the data in Table A.2 in the Appendix. This finding is consistent with the negligible decompositions of Li^+ and PF_6^- during formation and following cycling in the cells with the FEC electrolyte (see Figure 6.8(b)). The lithium content of the SEI in the cells with the FEC electrolyte is relatively high, as can be concluded from the data of the Li1s spectra shown in Table A.2 in the Appendix. The data in Table A.2 in the Appendix additionally indicate that the lithium of the SEI is mostly bonded in LiF and lithium carbonate in the cells with the FEC electrolyte. Interestingly, the lithium content of the SEI in the cells with the FEC electrolyte is distinctly higher than the lithium content of the SEI in the cells with the VC electrolyte (see data of the Li1s spectra shown in Table A.1 and Table A.2 in the Appendix). This observation might be ascribed to the relatively low FEC consumptions and the relatively high VC consumptions during formation and subsequent cycling (see Figure 6.8). As a result, the amount of FEC decomposition products on the anodes from the cells with the FEC electrolyte is possibly much lower than the amount

of VC decomposition products on the anodes from the cells with the VC electrolyte. Thus, the content of the lithium-free decomposition products is possibly much lower in the SEI from the cells with the FEC electrolyte than in the SEI from the cells with the VC electrolyte. Consequently, the lithium content of the SEI in the cells with the FEC electrolyte is higher than the lithium content of the SEI in the cells with the VC electrolyte. In addition, the XPS measurements indicate that the SEI thickness is mostly below 5-10 nm in the cells with the FEC electrolyte, while the SEI thickness is always above 5-10 nm in the cells with the VC electrolyte. The relatively thin SEI in the cells with the FEC electrolyte and the relatively thick SEI in the cells with the VC electrolyte might be ascribed to the relatively low FEC consumptions and the relatively high VC consumptions (see Figure 6.8). As a result, less SEI material is deposited in the cells with the FEC electrolyte than in the cells with the VC electrolyte. This might explain, why the thickness of the SEI in the cells with the FEC electrolyte is much lower than the thickness of the SEI in the cells with the VC electrolyte.

The atomic percentages of the carbon black (carbon black peak at about 285 eV) and of the cathode active material NCM622 (NCM622 peak at about 530 eV) in the surface layers of the cathodes from the cells with the VC electrolyte decrease during formation and subsequent cycling, as can be concluded from Table A.3 in the Appendix. This observation can be ascribed to the growth of a surface layer on the cathode, which is called the cathode electrolyte interface (CEI). As carbon black and NCM622 are no longer detectable on the cathode after 15 cycles at 0.5 C/0.5 C (see Table A.3 in the Appendix), the CEI thickness should be greater than the information depth of XPS (5-10 nm) already after 15 cycles at 0.5 C/0.5 C in the cells with the VC electrolyte. Hence, the CEI on the cathodes is relatively thick in case of the cells with the VC electrolyte after formation and following cycling. Interestingly, the atomic percentages of the compounds characteristic for poly(VC) (C_a, C_b, O_a, and O_b) are high in the surface layers from the cathodes after formation and subsequent cycling (see Table A.3 in the Appendix). Consequently, it can be concluded that the CEI mainly consists of poly(VC) after formation and subsequent cycling in the cells with the VC electrolyte. According to this, a deposition of poly(VC) also on the cathode surface in lithium-ion cells with VC-containing electrolyte is described in literature [25]. The deposition of poly(VC) on the cathode surface might be attributed to VC oxidation at the cathode yielding poly(VC). By contrast, the atomic percentages of carbon black and NCM622 in the surface layers of the cathodes from the cells with the FEC electrolyte decrease only slightly during formation and following cycling (see Table A.4 in the Appendix). In addition, the carbon black peak and the NCM622 peak are not disappeared even after 40 cycles at 0.5 C/0.5 C, as can be concluded from Table A.4 in the Appendix. These findings indicate that the CEI remains consistently thin in the cells with the FEC electrolyte during formation and subsequent cycling.

As can be seen in Table A.1, Table A.2, Table A.3, and Table A.4 in the Appendix, the atomic percentages of the compounds in the surface layers from the electrodes after the 40 slow cycles at 0.5 C/0.5 C and after the 40 fast cycles at 2 C/3 C are similar. Hence, the charge and discharge current does not significantly influence the composition of the SEI and the CEI in the cells with the VC electrolyte and in the cells with the FEC electrolyte. This finding suggests that the decompositions in the electrolyte are also not influenced by the charge and discharge current, which is confirmed by the similar consumptions of VC and FEC during the 40 slow cycles at 0.5 C/0.5 C and during the 40 fast cycles at 2 C/3 C (see Figure 6.8).

SEM and EDX are used to gain further information about the SEI on the anodes from the cells with the VC electrolyte and the cells with the FEC electrolyte. SEM and EDX are applied for the examination of anodes from NCM622/silicon-graphite pouch cells in different aging stages, which are indicated in Table 6.2. The investigated anodes are removed from one cell with the VC electrolyte and one cell with the FEC electrolyte for each of these aging stages.

In Figure 6.12(a), the SEM images from the surfaces of the investigated anodes from the cells with the VC electrolyte are depicted. Additionally, the distributions of the elements on the surfaces of these anodes determined by EDX can be seen in Figure 6.12(b). In the EDX images, the color red indicates a high carbon content, whereas the color green marks a high oxygen content in the surface layer of the anode. Besides, the color yellow indicates a high silicon content in the surface layer of the anode. A high oxygen content in the surface layer of the anode indicates the presence of a thick SEI consisting of the oxygen-containing decomposition products of VC and DMC. A high carbon content and a high silicon content in the surface layer of the anode indicates graphite and silicon, respectively, and thus the absence of a thick SEI. Due to a limited spatial resolution of several hundred nm, a thin SEI is barely detectable by EDX. Furthermore, a high fluorine content in the surface layer of the anode is indicated by the color cyan in the EDX images.

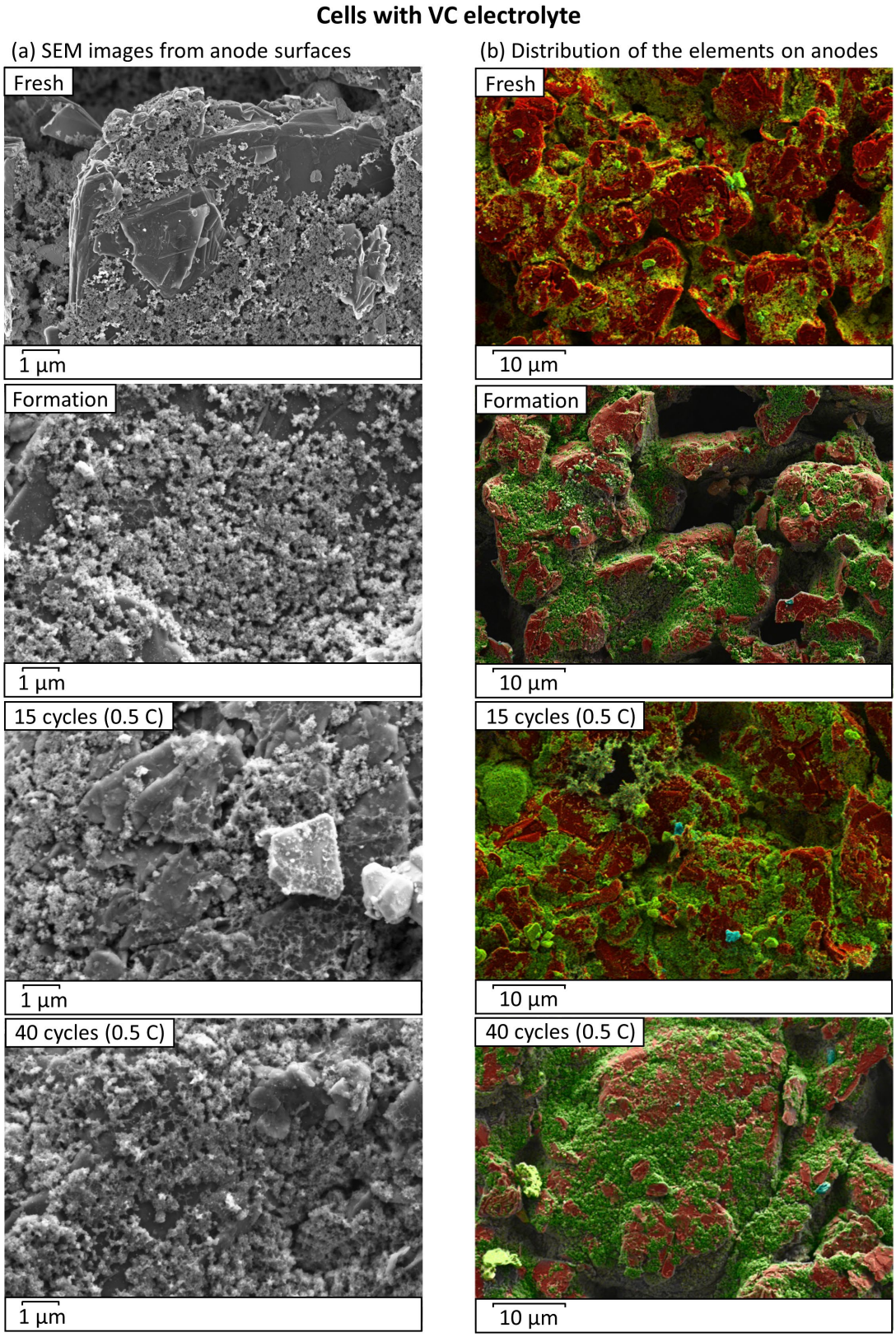

Figure 6.12: (a) SEM images from the surfaces of anodes from a fresh cell, a cell after formation, a cell after 15 cycles at 0.5 C/0.5 C, and a cell after 40 cycles at 0.5 C/0.5 C each with the VC electrolyte. (b) Distribution of the elements on the surfaces of anodes from a fresh cell, a cell after formation, a cell after 15 cycles at 0.5 C/0.5 C, and a cell after 40 cycles at 0.5 C/0.5 C each with the VC electrolyte determined by EDX. High carbon concentrations are marked by the color red, and high silicon concentrations are indicated by the color yellow. High oxygen concentrations are indicated by the color green.

The big, red, flake-shaped particles in the EDX images from Figure 6.12(b) are the graphite particles. The small, spherical particles on the surface of the anode from the fresh cell (see Figure 6.12(a) and Figure 6.12(b)) represent the silicon particles. Indeed, these silicon particles do not appear in pure yellow, but in greenish yellow in the EDX image of the anode from the fresh cell (see Figure 6.12(b)). This observation indicates that the surface of the silicon particles is oxidized by reaction of the silicon with the oxygen from the ambient air during storage of the anodes before the cell assembly. This finding confirms the aforementioned presence of surface layers of silicon oxide on the silicon particles from the fresh anodes detected by XPS. The silicon particles appear thicker in the SEM image from the anode after formation (see Figure 6.12(a)). Simultaneously, the silicon particles appear in pure green in the EDX image from the anode after formation (see Figure 6.12(b)). From this it can be concluded that a thick, oxygen-rich SEI is formed on the silicon particles during formation in the cells with the VC electrolyte. The graphite particles still appear red in the EDX image from the anode after formation in Figure 6.12(b) suggesting the absence of a thick SEI on the graphite particles after formation in the cells with the VC electrolyte. Indeed, the XPS measurements indicate that the thickness of the SEI on the graphite particles is greater than 5-10 nm after formation in the cells with the VC electrolyte, as already mentioned in this section. Hence, it can be assumed that the thickness of the SEI on the graphite particles is moderate after formation in the cells with the VC electrolyte. The SEM images and the EDX images from the anodes after 15 cycles at 0.5 C/0.5 C and after 40 cycles at 0.5 C/0.5 C do not differ significantly from the SEM image and the EDX image from the anode after formation, as can be seen in Figure 6.12. This observation indicates that the SEI no longer grows substantially after formation during subsequent cycling in the cells with the VC electrolyte. The observed, thick, oxygen-rich SEI on the silicon particles and the relatively thin SEI on the graphite particles suggest that the massive VC decomposition (see Figure 6.8(a)) and the consequent deposition of poly(VC) (see Figure 6.11(a) and Figure 6.11(c)) take place mainly at the surface of the silicon particles during formation and following cycling in the cells with the VC electrolyte.

Figure 6.13(a) shows the SEM images from the surfaces of the examined anodes from the cells with the FEC electrolyte. Figure 6.13(b) displays the distributions of the elements on the surfaces of these anodes, which are determined by EDX. The color coding in these EDX images is the same as in the EDX images in Figure 6.12(b).

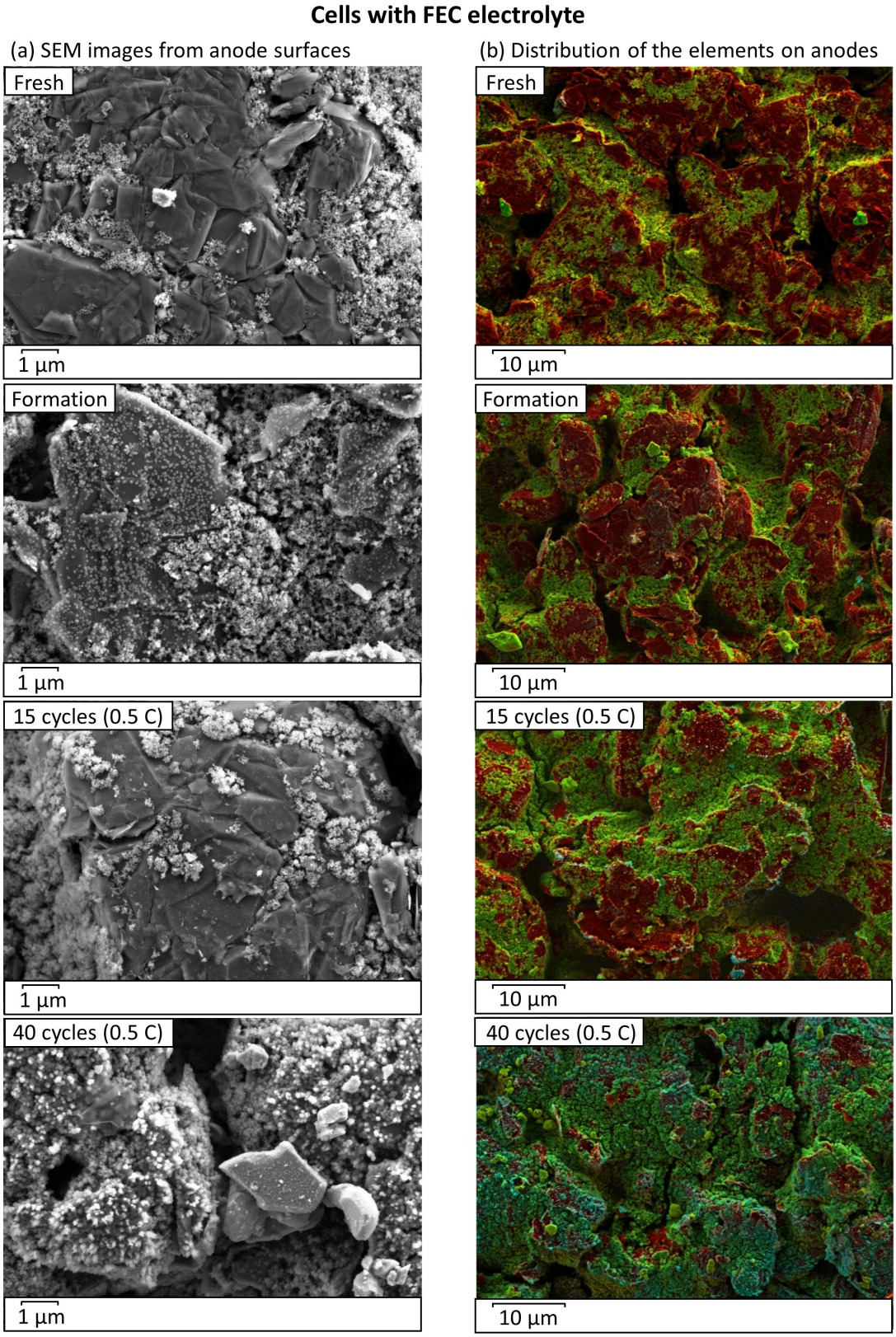

Figure 6.13: (a) SEM images from the surfaces of anodes from a fresh cell, a cell after formation, a cell after 15 cycles at 0.5 C/0.5 C, and a cell after 40 cycles at 0.5 C/0.5 C each with the FEC electrolyte. (b) Distribution of the elements on the surfaces of anodes from a fresh cell, a cell after formation, a cell after 15 cycles at 0.5 C/0.5 C, and a cell after 40 cycles at 0.5 C/0.5 C each with the FEC electrolyte determined by EDX. The color red indicates high carbon concentrations, while the color yellow marks high silicon concentrations. The color green indicates high oxygen concentrations, and the color cyan marks high fluorine concentrations.

As expected, the SEM image and the EDX image of the anode from the fresh cell with the FEC electrolyte (see Figure 6.13(a) and Figure 6.13(b)) look similar to the SEM image and the EDX image of the anode from the fresh cell with the VC electrolyte (see Figure 6.12(a) and Figure 6.12(b)). The small, spherical silicon particles also appear in greenish yellow in the EDX image from the fresh anode in Figure 6.13(b), suggesting silicon oxide in the surface layer of the silicon particles, as already explained. The spherical silicon particles on the big, flake-shaped graphite particles appear thicker in the SEM image from the anode after formation (see Figure 6.13(a)). The silicon particles appear in pure green in the EDX image of the anode after formation (see Figure 6.13(b)). These observations suggest the formation of a thick, oxygen-rich SEI on the silicon particles during formation in the cells with the FEC electrolyte. By contrast, the big, flake-shaped graphite particles appear in red in the EDX images from the fresh anode and from the anode after formation (see Figure 6.13(b)). Thus, the SEI on the graphite particles is relatively thin after formation in the cells with the FEC electrolyte. This finding confirms the low SEI thickness on the graphite particles of less than 5-10 nm in the cell with the FEC electrolyte after formation determined by XPS. The EDX images from the anodes after 15 cycles at 0.5 C/0.5 C and after 40 cycles at 0.5 C/0.5 C in Figure 6.13(b) reveal a massive SEI growth after formation during subsequent cycling in the cells with the FEC electrolyte. The thick SEI appears not only in green, but also in cyan in the EDX image of the anode from the cell with the FEC electrolyte after 40 cycles at 0.5 C/0.5 C. Consequently, the SEI is not only rich in oxygen, but also rich in fluorine after 40 cycles at 0.5 C/0.5 C in the cell with the FEC electrolyte. The high fluorine content of the SEI can be ascribed to the FEC decomposition product LiF, which represents a main component of the SEI in the cells with the FEC electrolyte according to the XPS analyses, as already explained in this section. Remarkably, the anode surface is almost completely covered by this thick SEI after 40 cycles at 0.5 C/0.5 C in the cells with the FEC electrolyte, as can be concluded from Figure 6.13(b). This thick, oxygen-rich, and fluorine-rich SEI on the silicon particles and the graphite particles indicates that the FEC decomposition (see Figure 6.8(b)) and the consequent deposition of the FEC decomposition products occur at the surfaces of the silicon particles and the graphite particles during formation and subsequent cycling in the cells with the FEC electrolyte. The thick SEI on the graphite particles after 40 cycles at 0.5 C/0.C in the cells with the FEC electrolyte observed by EDX contradicts the consistently thin SEI on the graphite particles in these cells observed by XPS. Indeed, the EDX image from the anode after 40 cycles at 0.5 C/0.5 C in Figure 6.13(b) also shows small red spots indicating a thin SEI at least at some spots on the graphite particles. A thin SEI at some spots on the graphite particles might explain, why the XPS analyses eventually indicate a thin SEI on the graphite particles even after 40 cycles at 0.5 C/0.5 C in the cells with the FEC electrolyte.

The EDX images in Figure 6.12(b) and Figure 6.13(b) indicate that the SEI growth after formation during subsequent cycling is relatively slight in the cells with the VC electrolyte and relatively strong in the

cells with the FEC electrolyte. This phenomenon might be attributed to the lower flexibility of the FEC-derived SEI compared to the VC-derived SEI, as reported in literature [29]. As a result, the FEC-derived SEI cannot accommodate as well to the volume changes of the silicon during cycling as the VC-derived SEI. Consequently, the FEC-derived SEI cracks more than the VC-derived SEI during cycling, so that the growth of the FEC-derived SEI is stronger than the growth of the VC-derived SEI during cycling. The high flexibility of the VC-derived SEI can be explained by the high content of poly(VC) in the SEI in the cells with the VC electrolyte (see Figure 6.11(a) and Figure 6.11(c)). According to this, it is known from literature that VC forms a very flexible polycarbonate layer, which resists the massive volume changes of silicon during cycling, thus preventing further SEI growth [29]. The relatively low flexibility of the FEC-derived SEI might be caused by the considerable contents of LiF and lithium carbonate in the SEI in the cells with the FEC electrolyte (see Table A.2 in the Appendix). The presence of LiF nanocrystals in the SEI decreases the flexibility of the SEI according to literature [29].

6.7 Identification of the cause of capacity loss

In this section, the triggers for the capacity losses of the NCM622/silicon-graphite pouch cells are described and discussed. In lithium-ion cells, cycleable lithium and thus capacity can be lost by SEI formation, irreversible lithium plating, active material loss, and lithium trapping in the active material [94]. Apart from that, there are parasitic reactions that consume charge, but not cycleable lithium, such as redox shuttle mechanisms or transfer of transition metals from the cathode to the anode [94]. These parasitic reactions do not contribute to the capacity losses of lithium-ion cells.

To obtain information about the cause of the capacity loss of the examined NCM622/silicon-graphite pouch cells, the amounts of lithium (Li) in electrodes at different stages of electrochemical aging are determined by ICP-OES. ICP-OES is used to analyze anodes and cathodes from NCM622/silicon-graphite pouch cells in various aging stages, which are indicated in Table 6.2. For each of these aging stages, the analyzed electrodes are removed from one cell with the VC electrolyte and one cell with the FEC electrolyte. The examined NCM622/silicon-graphite pouch cells (except for the fresh NCM622/silicon-graphite pouch cells) are discharged to 3 V and subsequently held at 3 V for four hours before the sample preparation for ICP-OES analyses. Thus, it is ensured that each investigated cell is in the completely discharged state and all mobile Li is removed from the anodes. The lost amounts of substance of Li (Li losses) of the cathodes are calculated based on the quantified amounts of substance of Li in the cathodes. The Li loss of the cathodes corresponds to the difference between the quantified amount of substance of Li in the cathodes from the fresh cell and the quantified amount of substance of Li in the cathodes from the respective, aged cell. Four anode pieces and four cathode pieces are investigated for each cell, so that four single values are determined, from which the indicated average

values are calculated. Furthermore, the loss of cycleable Li is calculated by the cumulative irreversible capacity and the Faraday constant. The cumulative irreversible capacity $Q_{irreversible}$ is given by Equation 6.1, as described in literature [17]. Q_i^{charge} corresponds to the charge capacity of the ith cycle, while $Q_i^{discharge}$ is equivalent to the discharge capacity of the ith cycle. The differences between Q_i^{charge} and $Q_i^{discharge}$ are determined for each cycle. These differences between Q_i^{charge} and $Q_i^{discharge}$ are summed up for the number of cycles (i), which are performed. Note that every single cycle is considered for the calculation of $Q_{irreversible}$, including the cycles from the formation program etc..

$$Q_{irreversible} = \sum_i \left(Q_i^{charge} - Q_i^{discharge}\right) \tag{6.1}$$

The calculated loss of cycleable Li is the cumulative irreversible capacity divided by the Faraday constant. For this calculation, it is assumed that the charge consumption is exclusively induced by a loss of cycleable Li. The average, quantified amounts of substance of Li in the anodes, the average, quantified Li losses of the cathodes, and the losses of cycleable Li calculated based on the cumulative irreversible capacities are indicated in the graphs in Figure 6.14. Each indicated, average value corresponds to the mean of the respective, determined four single values. The associated errors are the standard deviations of the mean calculated by the four single values per indicated average value.

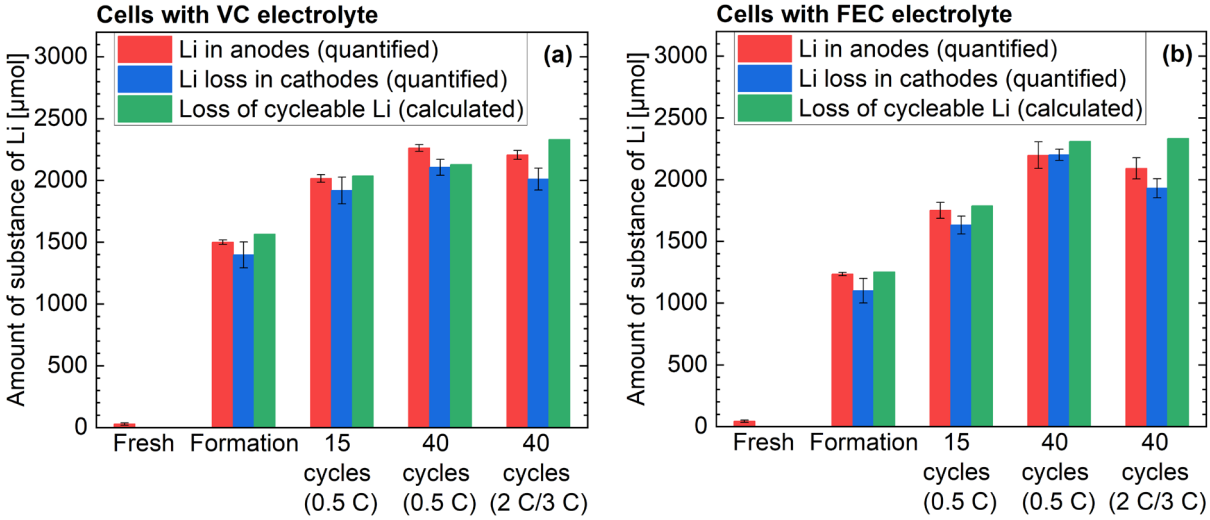

Figure 6.14: (a) Average, quantified amounts of substance of Li in the anodes from the cells with the VC electrolyte determined by ICP-OES. In addition, the average, quantified Li losses of the cathodes from these cells determined by ICP-OES, as well as the respective, calculated losses of cycleable Li are shown in (a). (b) Average, quantified amounts of substance of Li in the anodes from the cells with the FEC electrolyte determined by ICP-OES. Besides, the average, quantified Li losses of the cathodes from these cells determined by ICP-OES and the respective, calculated losses of cycleable Li are indicated in (b).

The quantified Li losses of the cathodes do not differ substantially from the calculated losses of cycleable Li, as can be seen in the graphs from Figure 6.14. Consequently, the charge consumption is (almost) exclusively induced by a loss of cycleable Li that is initially present in the cathodes. Thus, parasitic reactions that consume charge, but not cycleable Li, hardly contribute to the charge

consumptions in the cells with the VC electrolyte and the cells with the FEC electrolyte. Additionally, Figure 6.14(a) and Figure 6.14(b) indicate that the quantified Li losses of the cathodes are mostly close to the quantified amounts of substance of Li in the anodes. Hence, the Li loss of the cathodes is (almost) completely compensated by an irreversible bonding of Li in the anodes during formation and subsequent cycling in the cells with the VC electrolyte and the cells with the FEC electrolyte. The capacity losses of the examined NCM622/silicon-graphite pouch cells are thus (almost) exclusively caused by trapping of cycleable Li in the anodes. The slight amounts of substance of Li in the fresh anodes (see Figure 6.14(a) and Figure 6.14(b)) can be ascribed to slight residues from $LiPF_6$ that are not removed from the anodes during sample preparation. The anodes from the cell after formation with the VC electrolyte contain more Li than the anodes from the cell after formation with the FEC electrolyte, as can be concluded from Figure 6.14(a) and Figure 6.14(b). This observation can be explained by the lower, initial coulombic efficiencies and the consequent, higher charge consumptions during formation in the cells with the VC electrolyte (see Figure 6.2(a)). Interestingly, the amounts of substance of Li in the anodes from the cells after 40 cycles with the VC electrolyte are similar to amounts of substance of Li in the anodes from the cells after 40 cycles with the FEC electrolyte, as can be seen in Figure 6.14(a) and Figure 6.14(b). The cathodes from the electrochemically untreated, fresh cells contain about 5300 µmol Li, so that the quantified Li losses of the cathodes after 40 cycles at 0.5 C/0.5 C by about 2200 µmol (see graphs from Figure 6.14) correspond to about 42% of the initially present Li in the cathodes. The irreversible bonding of Li in the anodes can be traced back to either Li trapping in the SEI, Li trapping by irreversible Li plating, or Li trapping in the anode active material by loss of anode active material due to contact loss for example [94]. Note that the charge currents and discharge currents are relatively low at least in case of the NCM622/silicon-graphite pouch cells that are examined after formation or after the cycles at 0.5 C/0.5 C. In addition, the theoretical areal capacity of the anodes is considerably higher than the theoretical areal capacity of the cathodes to avoid lithium plating during cycling (see section 3.2). Hence, it can be assumed that irreversible lithium plating does not contribute significantly to the irreversible bonding of Li in the anodes and thus to the capacity loss in case of the investigated NCM622/silicon-graphite pouch cells.

To verify whether Li trapping in the SEI or Li trapping in the anode active material is responsible for the irreversible bonding of Li in the anodes, the areal capacities of the electrodes at different aging stages from cells with the VC electrolyte and cells with the FEC electrolyte are determined. For this purpose, NCM622/silicon-graphite pouch cells after formation and after 40 cycles at 0.5 C/0.5 C are disassembled. Subsequently, coin cell electrodes are punched out of the cathodes and anodes of these cells. Following this, coin cells are assembled with Li metal as the counter electrode and the punched electrodes from the pouch cells as working electrodes. The coin cells assembled with electrodes from the pouch cells with the VC electrolyte are filled with 1 M $LiPF_6$ in VC:DMC. The coin cells assembled

with electrodes from the pouch cells with the FEC electrolyte are filled with 1 M $LiPF_6$ in FEC:DMC. The assembled coin cells are cycled for four cycles at 0.1 C/0.1 C. Following this, the coin cells are cycled for four cycles at 0.5 C/0.5 C. In the following, “the capacity” refers to the capacity that is measured either during the delithiation of the silicon-graphite electrode or during the lithiation of the NCM622 electrode. The capacity from the second cycle at 0.1 C/0.1 C and the capacity from the second cycle at 0.5 C/0.5 C are each divided by the area of the working electrode resulting in one areal capacity at 0.1 C and one areal capacity at 0.5 C for each coin cell. Three single values of the areal capacity are determined in each case, from which the indicated, average areal capacities are calculated. Figure 6.15(a) shows the average areal capacities at 0.1 C and 0.5 C of the coin cells with the electrodes from the pouch cells with the VC electrolyte after formation and after 40 cycles at 0.5 C/0.5 C. Figure 6.15(c) displays the average areal capacities at 0.1 C and 0.5 C of the coin cells with the electrodes from the pouch cells with the FEC electrolyte after formation and after 40 cycles at 0.5 C/0.5 C. The indicated errors of the average areal capacities are the standard deviations of the mean calculated by the respective three single values. Besides, the differential capacities are shown in dependence on the voltage for the VC-containing coin cells with the silicon-graphite electrodes in Figure 6.15(b) and for the FEC-containing coin cells with the silicon-graphite electrodes in Figure 6.15(d). The differential capacities of a half-cell with a silicon-free graphite electrode are additionally shown in dependence on the voltage in Figure 6.15(b) and Figure 6.15(d) for comparison. The data shown in Figure 6.15(b) and Figure 6.15(d) are acquired during the second delithiation of the silicon-graphite electrodes at 0.1 C.

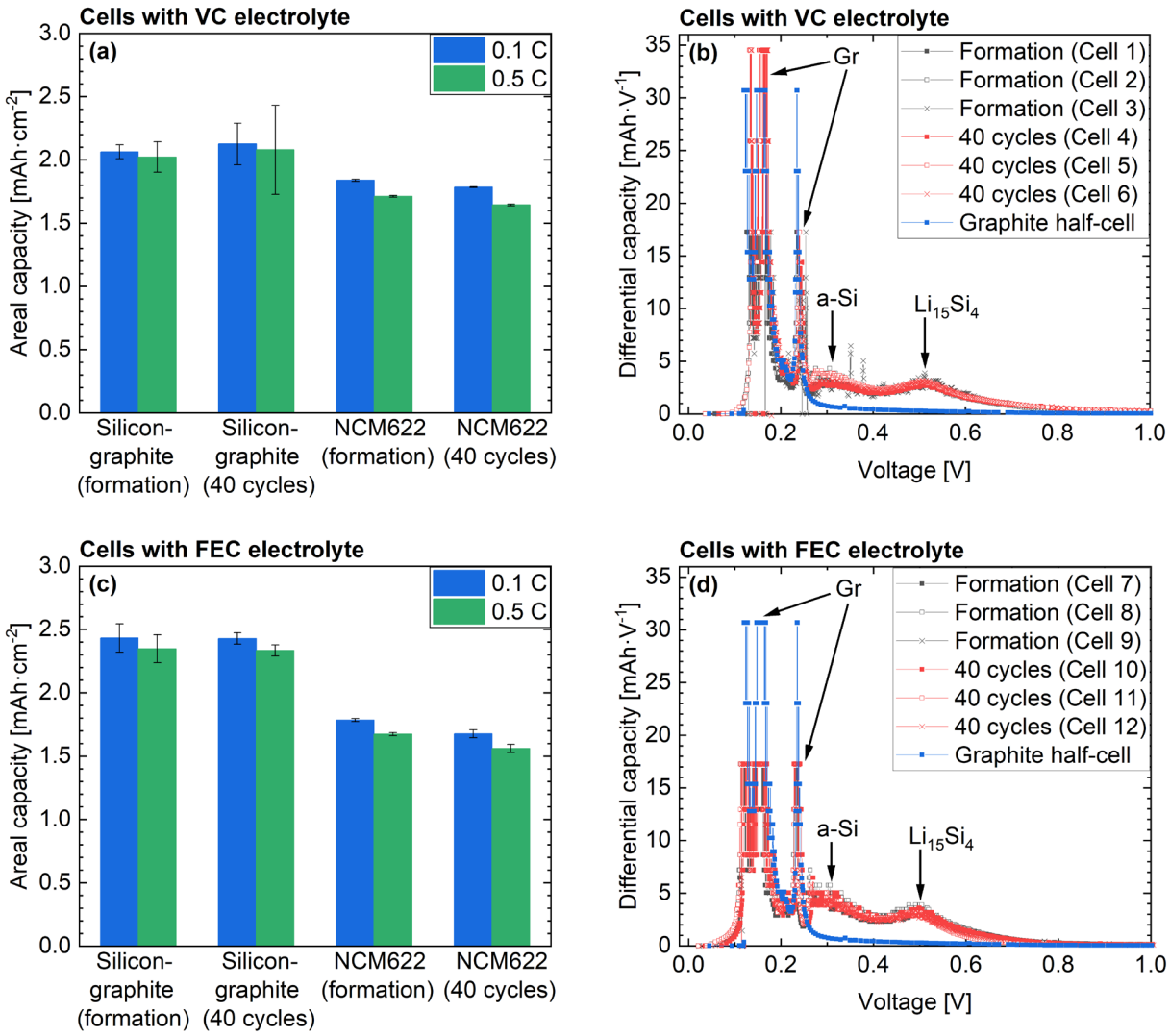

Figure 6.15: (a) Average areal capacities at 0.1 C and 0.5 C of the half-cells with the silicon-graphite electrodes and the NCM622 electrodes that are punched out of the anodes and cathodes from the NCM622/silicon-graphite pouch cells with the VC electrolyte after formation and after 40 cycles at 0.5 C/0.5 C. (b) Differential capacities of the same half-cells with the silicon-graphite electrodes as in (a) plotted against the voltage. (c) Average areal capacities at 0.1 C and 0.5 C of the half-cells with the silicon-graphite electrodes and the NCM622 electrodes that are punched out of the anodes and cathodes from the NCM622/silicon-graphite pouch cells with the FEC electrolyte after formation and after 40 cycles at 0.5 C/0.5 C. (d) Differential capacities of the same half-cells with the silicon-graphite electrodes as in (c) plotted against the voltage. The differential capacities of a half-cell with a silicon-free graphite electrode are also shown in dependence on the voltage in (b) and (d).

Using an unlimited source of Li like is in half-cells, the areal capacities of the silicon-graphite anodes from the pouch cells with the VC electrolyte and the pouch cells with the FEC electrolyte do not significantly decrease after formation during the subsequent 40 cycles at 0.5 C/0.5 C, as can be concluded from the graphs in Figure 6.15(a) and Figure 6.15(c). Consequently, the loss of anode active material and the Li trapping in the anode active material by loss of electronic contact do not significantly contribute to the capacity losses of the pouch cells with the VC electrolyte or the FEC electrolyte after formation during the following 40 cycles at 0.5 C/0.5 C. The diagrams in Figure 6.15(b) and Figure 6.15(d) show specific delithiation peaks of graphite at 0.11, 0.16, and 0.24 V vs. Li/Li^+ [95].

The identification of these peaks as delithiation peaks of graphite is plausible since the diagrams in Figure 6.15(b) and Figure 6.15(d) indicate peaks at these voltages (the Gr peaks) for each of the coin cells, including the half-cell with the silicon-free graphite electrode. In addition, two broad, small peaks at about 0.31 and 0.45 V vs. Li/Li^+ can be seen in Figure 6.15(b) and Figure 6.15(d). The former peak represents the delithiation peak of amorphous silicon-lithium alloy (a-Si peak), while the latter peak is the delithiation peak of crystalline $Li_{15}Si_4$ ($Li_{15}Si_4$ peak) [95]. The diagrams in Figure 6.15(b) and Figure 6.15(d) do not show these two peaks for the half-cell with the silicon-free graphite electrode. The differential capacity curves of the coin cells with the electrodes that are punched out of the anodes from the NCM622/silicon-graphite pouch cells are (almost) perfectly congruent, as can be seen in Figure 6.15(b) and Figure 6.15(d). Hence, neither the intensities of the delithiation peaks of graphite nor the intensities of the delithiation peaks of amorphous silicon-lithium alloy and crystalline $Li_{15}Si_4$ decrease after formation during the 40 cycles at 0.5 C/0.5 C. These observations confirm that neither the loss of electronically connected graphite, nor the loss of electronically connected silicon contribute substantially to the capacity loss of the pouch cells with the VC electrolyte or the FEC electrolyte after formation during the subsequent 40 cycles at 0.5 C/0.5 C. This finding is not expected since it is known from literature that the volume changes of the silicon during de-/lithiation lead to a loss of electrical contact and thus to a capacity loss of the cell by loss of electronically connected anode active material [96]. Indeed, it needs to be considered that the amount of active Li in full-cells, like the examined NCM622/silicon-graphite pouch cells, is limited by the cathode, so that the loss of active Li due to SEI growth translates into a capacity loss of the cell [75]. In the frequently examined half-cells, however, the loss of active Li due to SEI growth can be recovered by the (almost) infinite Li amount from the Li counter electrode, so that the loss of active Li by SEI buildup does not contribute to the capacity loss of a half-cell [75]. Consequently, the capacity losses due to loss of active Li by SEI growth are supposedly so high in the examined NCM622/silicon-graphite pouch cells during the 40 cycles at 0.5 C/0.5 C that the capacity losses due to loss of electronically connected anode active material are negligible.

The areal capacities of the NCM622 cathodes from the pouch cells with the VC electrolyte, as well as the FEC electrolyte decrease slightly after formation during the subsequent 40 cycles at 0.5 C/0.5 C, as can be concluded from the graphs in Figure 6.15(a) and Figure 6.15(c). This observation can be ascribed to a slight loss of electronically connected cathode active material, possibly because the NCM622 particles lose electrical contact due to crack formation in the NCM622 particles during de-/lithiation. Nevertheless, the areal capacities of the cathodes from the pouch cells decrease by around 5% during the 40 cycles at 0.5 C/0.5 C, so that only around 5% of the spaces for lithium-ions are lost after 40 cycles at 0.5 C/0.5 C. As already mentioned in this section, about 42% of the initially present Li from the cathodes are no longer present in the cathodes from the investigated pouch cells after the 40

cycles at 0.5 C/0.5 C. Hence, 42% of the spaces for lithium-ions remain unoccupied in the cathodes after the 40 cycles at 0.5 C/0.5 C, so that the mentioned, slight loss of spaces for lithium-ions in the cathodes likely does not lead to a capacity loss of the pouch cells. Thus, the loss of cathode active material does also not contribute substantially to the capacity loss of the examined NCM622/silicon-graphite pouch cells after formation during the following 40 cycles at 0.5 C/0.5 C. Hence, neither a loss of electronically connected anode active material, nor an effective loss of electronically connected cathode active material can be observed after formation during the subsequent 40 cycles at 0.5/0.5 C in the examined NCM622/silicon-graphite pouch cells. The cycleable Li that is additionally bonded in the anodes from the examined NCM622/silicon-graphite pouch cells after formation during the subsequent 40 cycles at 0.5 C/0.5 C is thus not bonded in lost, electronically isolated active material, but in the SEI. Simultaneously, the trapping of cycleable Li in the anodes is responsible for the capacity losses of the investigated NCM622/silicon-graphite pouch cells, as already mentioned in this section. Consequently, the trapping of cycleable Li in the SEI is the main trigger for the capacity losses of the examined NCM622/silicon-graphite pouch cells after formation during the subsequent 40 cycles at 0.5 C/0.5 C.

The measured areal capacities of the NCM622 cathodes after formation at 0.1 C (see Figure 6.15(a) and Figure 6.15(c)) are close to the theoretically calculated areal capacity of the used NCM622 cathodes (1.8 $mAh \cdot cm^{-2}$). From this it can be concluded that no cathode active material is lost during formation in the investigated NCM622/silicon-graphite pouch cells. In contrast, the measured areal capacities of the silicon-graphite anodes after formation at 0.1 C (see Figure 6.15(a) and Figure 6.15(c)) are distinctly lower than the theoretically calculated areal capacity of the used silicon-graphite anodes (3.0 $mAh \cdot cm^{-2}$). This observation can be partly attributed to the fact that the specific capacity of silicon (3579 $mAh \cdot g^{-1}$) assumed for the calculation of the theoretical areal capacity of the silicon-graphite anodes is possibly too high. In fact, this assumed, specific capacity of silicon corresponds to the specific capacity of highly lithiated $Li_{15}Si_4$ [13,15]. Indeed, the XPS and EDX analyses reveal the presence of a surface layer of silicon oxide on the silicon particles from the electrochemically untreated, fresh anodes, as described in section 6.6. According to literature, the specific capacity of silicon oxide is only 1708 $mAh \cdot g^{-1}$ [67]. As a result, the silicon oxide layer on the silicon particles from the fresh anodes might be (partly) responsible for the deviation between the measured areal capacities and the theoretically calculated areal capacity of the silicon-graphite anodes. The lithiation of silicon oxide during the first charge partly yields lithium silicate (Li_4SiO_4) that remains electrochemically inactive once it is formed [67,87]. In fact, lithium silicate is detected by XPS on the surfaces of the anodes from the cells with the FEC electrolyte after formation and after 15 cycles, as described in section 6.6. In addition, an incomplete delithiation of Li_xSi_y during delithiation might also lead partly to the mentioned deviation between the measured areal capacities and the theoretically calculated areal capacity of the

silicon-graphite anodes. As described in section 6.6, Li_xSi_y is also detected by XPS in the surface layer of the anodes from the cells with the FEC electrolyte after formation and after 15 cycles. Consequently, part of the silicon oxide and silicon might be irreversibly lithiated during the first charge of the formation in the examined NCM622/silicon-graphite pouch cells, so that a layer of lithium silicate and Li_xSi_y is formed under the SEI on the silicon particles. Lithium silicate and Li_xSi_y are possibly not detected in the surface layer of all anodes after formation and after cycling since the overlying SEI is often thicker than the information depth of XPS, as described in section 6.6. Consequently, the massive losses of cycleable Li and the consequent capacity losses of the examined NCM622/silicon-graphite pouch cells during formation might be attributed not only to Li trapping in the SEI, but also to Li trapping in lithium silicate and Li_xSi_y under the SEI.

Summarized, the capacity loss of the examined NCM622/silicon-graphite pouch cells during the first cycle of the formation program is (almost) exclusively triggered by trapping of cycleable Li in the SEI, as well as trapping of cycleable Li in irreversibly lithiated silicon and silicon oxide under the SEI. The capacity loss of the examined NCM622/silicon-graphite pouch cells after the first cycle of the formation program during the subsequent cycles at 0.5 C/0.5 C can be ascribed (almost) exclusively to the trapping of cycleable Li in the SEI.

6.8 Proposed mechanisms for electrochemical decomposition of VC and FEC

Based on the obtained results from the various analyses, mechanisms for the decomposition of VC and FEC can be proposed, which are described in this section.

First, it should be clarified whether all decomposition products of VC and FEC are actually deposited on the anodes by reductive decomposition or whether the decomposition products of VC and FEC are also deposited on the cathodes by oxidative decomposition in the examined NCM622/silicon-graphite pouch cells. In fact, the XPS measurements reveal that a CEI of electrolyte decomposition products is formed on the cathodes from the NCM622/silicon-graphite pouch cells during formation and subsequent cycling, as described in section 6.6. For this purpose, the differences between the masses of fresh electrodes and the masses of the electrodes after formation, as well as the differences between the masses of the fresh electrodes and the masses of the electrodes after 40 cycles at 0.5 C/0.5 C are calculated. These mass differences are calculated based on the weighed masses of the anodes and cathodes from the NCM622/silicon-graphite pouch cells used for the ICP-OES analyses. In the following, the increase of the anode mass during formation corresponds to the difference between the mass of the two anodes from the cell after formation with the VC electrolyte (or the FEC

electrolyte) and the mass of the two anodes from the fresh cell with the VC electrolyte (or the FEC electrolyte). Accordingly, the increase of the anode mass during formation plus the 40 cycles at 0.5 C/0.5 C is equivalent to the difference between the mass of the two anodes from the cell after 40 cycles at 0.5 C/0.5 C with the VC electrolyte (or the FEC electrolyte) and the mass of the two anodes from the fresh cell with the VC electrolyte (or the FEC electrolyte). The decrease of the cathode mass during formation is the difference between the mass of the two cathodes from the fresh cell with the VC electrolyte (or the FEC electrolyte) and the mass of the two cathodes from the cell after formation with the VC electrolyte (or the FEC electrolyte). The decrease of the cathode mass during formation plus the 40 cycles at 0.5 C/0.5 C is the difference between the mass of the two cathodes from the fresh cell with the VC electrolyte (or the FEC electrolyte) and the mass of the two cathodes from the cell after 40 cycles at 0.5 C/0.5 C with the VC electrolyte (or the FEC electrolyte). Note that the anode masses increase during formation and subsequent cycling due to the deposition of the SEI, while the cathode masses simultaneously decrease due to the loss of cycleable lithium (Li) from the cathodes that is eventually deposited at the anodes. The increases of the anode mass during formation and during formation plus the 40 cycles at 0.5 C/0.5 C are shown in Figure 6.16(a) for the cells with the VC electrolyte. Additionally, the mass of the VC consumed during formation and during formation plus the 40 cycles at 0.5 C/0.5 C taken together, as well as the mass of the Li in the anodes from the cells with the VC electrolyte after formation and after 40 cycles at 0.5 C/0.5 C can be seen in Figure 6.16(a). Figure 6.16(b) shows the decrease of the cathode mass during formation and during formation plus the 40 cycles at 0.5 C/0.5 C for the cells with the VC electrolyte, as well as the mass of the lost Li of the cathodes from the cells with the VC electrolyte after formation and after 40 cycles at 0.5 C/0.5 C. Figure 6.16(c) displays the increase of the anode mass during formation and during formation plus the 40 cycles at 0.5 C/0.5 C for the cells with the FEC electrolyte. Furthermore, the mass of the FEC decomposed during formation and during formation plus the 40 cycles at 0.5 C/0.5 C taken together, as well as the mass of Li in the anodes from the cells with the FEC electrolyte after formation and after 40 cycles at 0.5 C/0.5 C are indicated in Figure 6.16(c). The decrease of the cathode mass during formation and during formation plus the 40 cycles at 0.5 C/0.5 C for the cells with the FEC electrolyte, as well as the mass of the lost Li of the cathodes from the cells with the FEC electrolyte after formation and after 40 cycles at 0.5 C/0.5 C are shown in Figure 6.16(d). The masses of the decomposed VC and FEC, and the associated errors shown in Figure 6.16(a) and Figure 6.16(c) are calculated based on the respective, average decomposed amounts of substance of VC and FEC, and the associated errors that are indicated in Figure 6.8. The masses of Li in the anodes and the associated errors indicated in Figure 6.16(a) and Figure 6.16(c) are calculated based on the respective, average amounts of substance of Li in the anodes and the associated errors that are shown in Figure 6.14. The masses of the lost Li from the cathodes and the associated errors shown in Figure 6.16(b) and Figure 6.16(d) are calculated based

on the average, lost amounts of substance of Li from the cathodes and the associated errors, which are indicated in Figure 6.14.

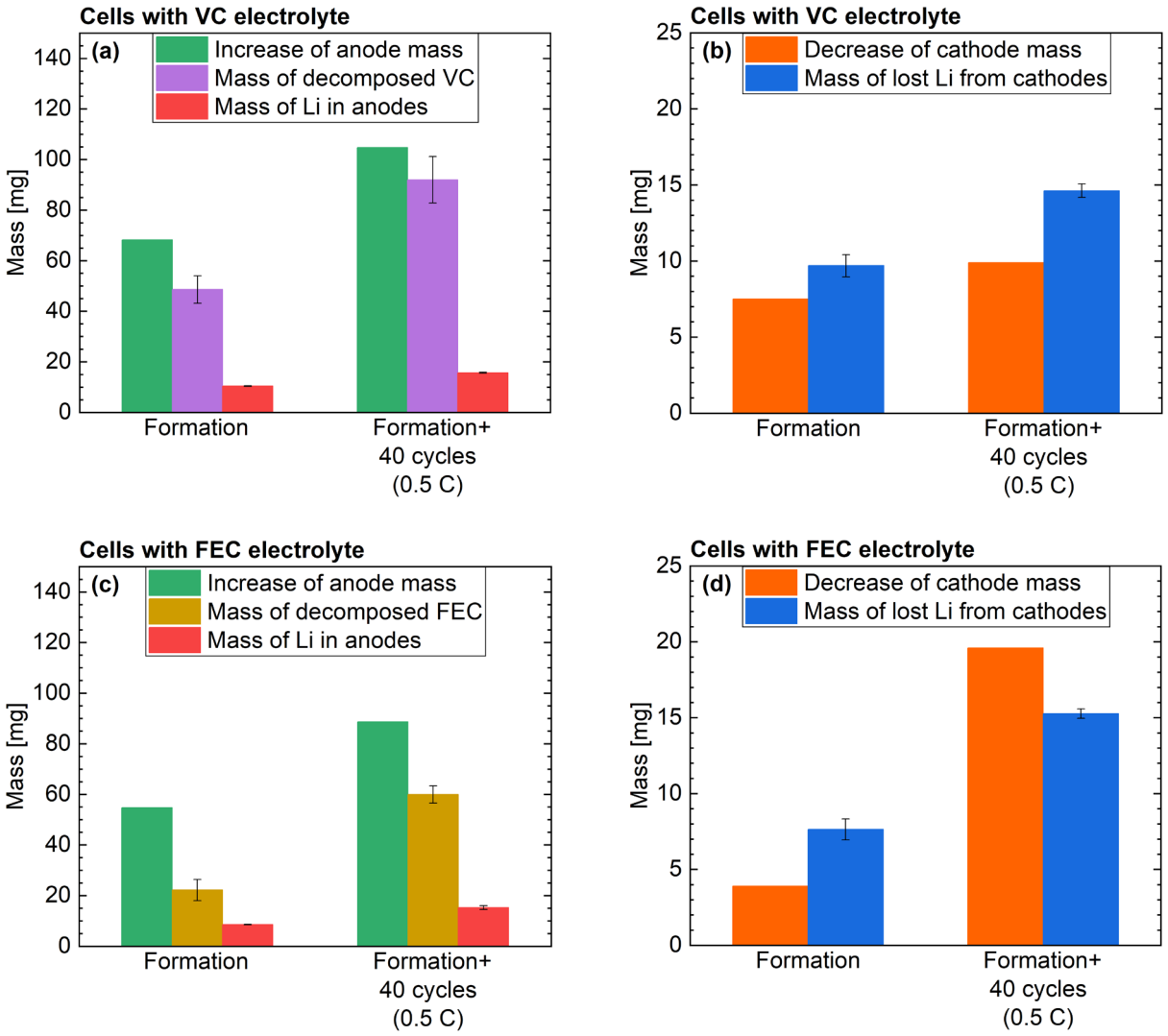

Figure 6.16: (a) Increase of the anode mass during formation and during formation plus the subsequent 40 cycles at 0.5 C/0.5 C for the cells with the VC electrolyte. Additionally, the mass of the VC decomposed during formation and during formation plus the 40 cycles at 0.5 C/0.5 C can be seen. The mass of Li in the anodes from the cells with the VC electrolyte after formation and after the 40 cycles at 0.5 C/0.5 C is also indicated. (b) Decrease of the cathode mass during formation and during formation plus the 40 cycles at 0.5 C/0.5 C for the cells with the VC electrolyte. The mass of the lost Li of the cathodes from the cells with the VC electrolyte after formation and after 40 cycles at 0.5 C/0.5 C is also displayed. (c) Increase of the anode mass during formation and during formation plus the subsequent 40 cycles at 0.5 C/0.5 C for the cells with the FEC electrolyte. Besides, the mass of the FEC consumed during formation and during formation plus the 40 cycles at 0.5 C/0.5 C is indicated. The mass of Li in the anodes from the cells with the FEC electrolyte after formation and after the 40 cycles at 0.5 C/0.5 C is also shown. (d) Decrease of the cathode mass during formation and during formation plus the 40 cycles at 0.5 C/0.5 C for the cells with the FEC electrolyte. The mass of the lost Li of the cathodes from the cells with the FEC electrolyte after formation and after 40 cycles at 0.5 C/0.5 C is also displayed.

The increases of the anode mass correspond approximately to the sums of the respective mass of the consumed VC or FEC plus the respective mass of Li in the anodes, as can be concluded from Figure 6.16(a) and Figure 6.16(c). Simultaneously, the decreases of the cathode masses are of the same order of magnitude as the respective masses of lost Li from the cathodes, as can be seen in Figure 6.16(b)

and Figure 6.16(d). From this it can be concluded that the decomposition products of VC and FEC are deposited almost exclusively on the anodes by reductive decomposition and hardly on the cathodes by oxidative decomposition. Thus, almost all end products from the decomposition of VC and FEC are solid SEI components, and also no gases, which confirms the absence of considerable gas amounts in the cells with the VC electrolyte and the cells with the FEC electrolyte (see section 6.5). It is important to repeat in this context that VC and FEC are decomposed almost exclusively in the cells with the VC electrolyte and the cells with the FEC electrolyte, respectively (see Figure 6.8). Consequently, the other electrolyte components (DMC or $LiPF_6$) do not substantially contribute to the SEI buildup and thus to the observed increases of the anode masses during formation and subsequent cycling.

An almost exclusive decomposition of VC and FEC by reduction at the anodes is observed in the cells with the VC electrolyte and the cells with the FEC electrolyte, respectively. Consequently, it is reasonable for the clarification of the mechanisms for the decomposition of VC and FEC to investigate the correlation between the charge (or "amount of substance of electrons") consumed at the anodes and the consumed amount of substance of VC and FEC. The charge consumed at the anodes during cycling is determined by the cumulative irreversible capacity, which is calculated according to Equation 6.1. The cumulative irreversible capacities of the cells used for the electrolyte analyses by HPLC and GC-FID are determined. The electrolytes from three equally treated cells are analyzed, so that three single values for the cumulative irreversible capacities are determined in each case, from which the indicated, average, cumulative irreversible capacities are calculated. The average, cumulative irreversible capacities of the three cells after formation, the three cells after 15 cycles at 0.5 C/0.5 C, and the three cells after 40 cycles at 0.5 C/0.5 C each with the VC electrolyte are plotted against the average, consumed amounts of substance of VC in these cells after formation, after the 15 cycles at 0.5 C/0.5 C, and after the 40 cycles at 0.5 C/0.5 C in Figure 6.17(a). Figure 6.17(b) shows the average, cumulative irreversible capacities of the three cells after formation, the three cells after 15 cycles at 0.5 C/0.5 C, and the three cells after 40 cycles at 0.5 C/0.5 C each with the FEC electrolyte in dependence on the average, decomposed amounts of substance of FEC in these cells after formation, after the 15 cycles at 0.5 C/0.5 C, and after the 40 cycles at 0.5 C/0.5 C. The errors of the average, cumulative irreversible capacities indicated in Figure 6.17 correspond to the standard deviations of the mean calculated based on the respective three single values. The consumed amounts of substance of VC and FEC are calculated based on the absolute amounts of substance of VC and FEC determined by HPLC-UV/Vis and GC-FID, as specified in section 3.6. The absolute amounts of substance of VC and FEC are determined in the electrolytes from three sets of cells analyzed together. One set of cells includes a fresh cell with the VC electrolyte, a fresh cell with the FEC electrolyte, a cell after formation with the VC electrolyte, a cell after formation with the FEC electrolyte, a cell after 15 cycles at 0.5 C/0.5 C with the VC electrolyte, a cell after 15 cycles at 0.5 C/0.5 C with the FEC electrolyte, a cell after 40 cycles at

0.5 C/0.5 C with the VC electrolyte, and a cell after 40 cycles at 0.5 C/0.5 C with the FEC electrolyte. For each of the three sets of cells, one single value for the consumed amounts of substance of VC and FEC after formation, after 15 cycles at 0.5 C/0.5 C, and after 40 cycles at 0.5 C/0.5 C is thus calculated. The average, consumed amounts of substance indicated in Figure 6.17 represent the means of the resulting three single values. The associated errors are the standard deviations of the mean calculated based on the respective three single values.

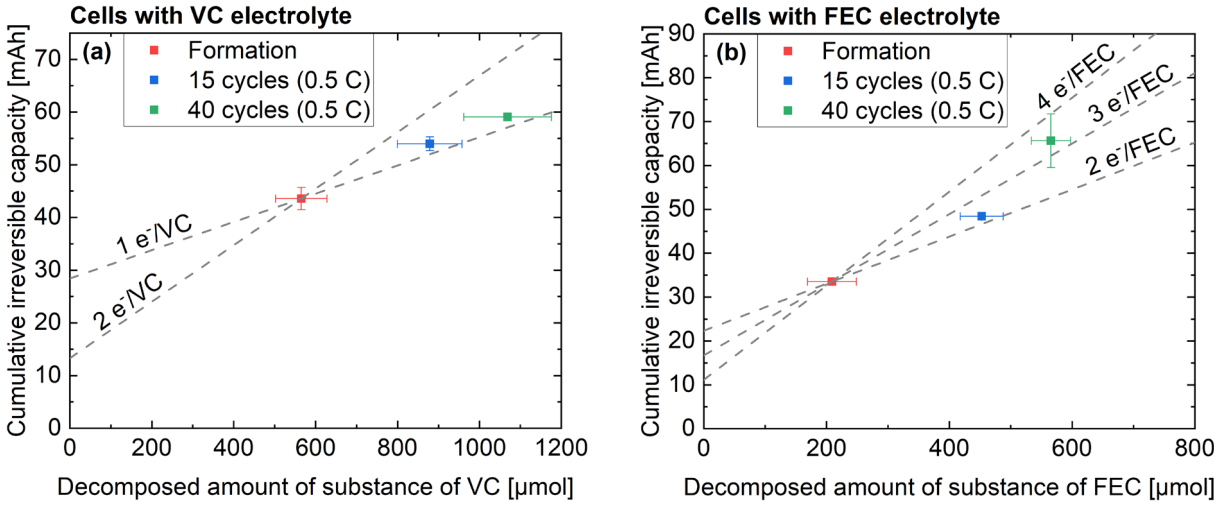

Figure 6.17: (a) Average, cumulative irreversible capacities of cells with the VC electrolyte after formation, after the 15 cycles at 0.5 C/0.5 C, and after the 40 cycles at 0.5 C/0.5 C plotted against the average, decomposed amounts of substance of VC in these cells after formation, after the 15 cycles at 0.5 C/0.5 C, and after the 40 cycles at 0.5 C/0.5 C. (b) Average, cumulative irreversible capacities of cells with the FEC electrolyte after formation, after the 15 cycles at 0.5 C/0.5 C, and after the 40 cycles at 0.5 C/0.5 C plotted against the average, decomposed amounts of substance of FEC in these cells after formation, after the 15 cycles at 0.5 C/0.5 C, and after the 40 cycles at 0.5 C/0.5 C.

The amount of substance of electrons consumed at the anodes is equivalent to the cumulative irreversible capacity (in As) divided by the Faraday constant. The number of consumed electrons per consumed VC molecule (e^-/VC value) corresponds to the quotient of the amount of substance of electrons consumed at the anodes and the consumed amount of substance of VC. The number of consumed electrons per consumed FEC molecule (e^-/FEC value) is equivalent to the amount of substance of electrons consumed at the anodes divided by the consumed amount of substance of FEC. The e^-/VC value and e^-/FEC value reveal information about the actual reactions of the reductive decomposition of VC and FEC. Based on the average cumulative irreversible capacity and the average, decomposed amount of substance of VC after 40 cycles at 0.5 C/0.5 C indicated in Figure 6.17(a), an e^-/VC value of 2.1±0.3 is calculated. From this it could be concluded that the reductive decomposition of one VC molecule consumes two electrons. An e^-/FEC value of 4.3±0.3 is calculated based on the average cumulative irreversible capacity and the average, decomposed amount of substance of FEC after 40 cycles at 0.5 C/0.5 C shown in Figure 6.17(b). This e^-/FEC value suggests a four electron reduction of FEC, which agrees with the four electron reduction proposed by Jung et al. [17]. Jung et

al. found that the reduction of one FEC molecule is associated with the consumption of four electrons in coin cells with silicon-containing anodes [17]. Thus, the reductive decomposition of FEC in coin cells is not significantly different from the reductive decomposition of FEC in much bigger pouch cells. Indeed, it needs to be considered that cycleable Li and thus also electrons are additionally consumed by the irreversible lithiation of silicon and silicon oxide during the first cycle of the formation program (see section 6.7), which is not associated with a consumption of VC or FEC. As a result, the average, cumulative irreversible capacity and the average, consumed amount of substance of VC after formation shown in Figure 6.17(a) result in a relatively high e^-/VC value of 3.0±0.5. Based on the average, cumulative irreversible capacity and the average, decomposed amount of substance of FEC after formation (see Figure 6.17(b)), a relatively high e^-/FEC value of 6.5±1.4 is calculated. Indeed, cycleable Li and thus also electrons are (almost) exclusively consumed due to the SEI growth after formation during the subsequent 40 cycles at 0.5 C/0.5 C, as described in section 6.7. Since an (almost) exclusive decomposition of VC and FEC is observed in the cells with the VC electrolyte and the FEC electrolyte, respectively (see Figure 6.8), it can be assumed that the SEI in these cells consists (almost) exclusively of cycleable Li, as well as products from the reductive decomposition of VC or FEC. Consequently, the electrons are consumed (almost) exclusively by the reductive decomposition of VC or FEC after formation during the subsequent cycling. Accordingly, it is reasonable to determine the number of consumed electrons per consumed VC molecule or FEC molecule only after formation during subsequent cycling. The dashed lines in the diagrams in Figure 6.17(a) and Figure 6.17(b) indicate the different, relevant e^-/VC ratios and e^-/FEC ratios after formation during subsequent cycling. Generally, the intersections of these dashed lines with the y-axes indicate the charges or amounts of electrons consumed by the mentioned, irreversible lithiation of silicon and silicon oxide during the first cycle of the formation program.

From Figure 6.17(a) it can be concluded that the reductive decomposition of one VC molecule is associated with the consumption of one electron. The points from the cells after 15 cycles at 0.5 C/0.5 C and after 40 cycles at 0.5 C/0.5 C lie just slightly above the dashed line that indicates the 1 e^-/VC ratio. The positions of these points slightly above the dashed line indicating the 1 e^-/VC ratio is plausible, as not only VC, but also slight amounts of DMC are decomposed in the cells with the VC electrolyte (see Figure 6.8(a)), which leads to an additional, slight electron consumption and thus to slightly higher y-values for these points. The lost amounts of substance of cycleable Li calculated based on the cumulative irreversible capacities and thus the consumed amounts of substance of electrons correspond to the quantified amounts of substance of Li in the anodes from the cells with the VC electrolyte, as can be seen in Figure 6.14(a). Consequently, one lithium-ion is deposited on the anode for every electron that is consumed at the anode in the cells with the VC electrolyte. Thus, the reductive decomposition of one VC molecule leads to the consumption of one electron and one

lithium-ion. In addition, poly(VC) represents the main component of the SEI, as described in section 6.6. Based on these findings, it is proposed that one VC molecule is reduced together with one lithium-ion by uptake of one electron at the anode yielding one monomer of a lithium-containing poly(VC). According to literature, most of the VC directly reacts to poly(VC) due to an attack by the initial VC reduction product [62,97]. However, this proposed reaction of VC to poly(VC) does not include the consumption of lithium-ions, which contradicts the mentioned observation that the decomposition of one VC molecule is associated with the consumption of one electron and one lithium-ion. Consequently, it is proposed instead that one lithium-ion is reduced together with one VC molecule from the solvation shell yielding one monomer of a lithium-containing poly(VC). The repetition of this process eventually yields a lithium-containing poly(VC) that forms the SEI in the cells with the VC electrolyte. The proposed mechanism for the reductive decomposition of VC can be seen in Figure 6.18. This mechanism for the reductive decomposition of VC is almost exclusively responsible for the capacity loss of the examined NCM622/silicon-graphite pouch cells with the VC electrolyte after formation during following cycling. It is empirically found for the first time that the reductive decomposition of one VC molecule consumes one electron and one lithium-ion in lithium-ion cells, to the best of our knowledge.

Mechanism for the reductive decomposition of VC

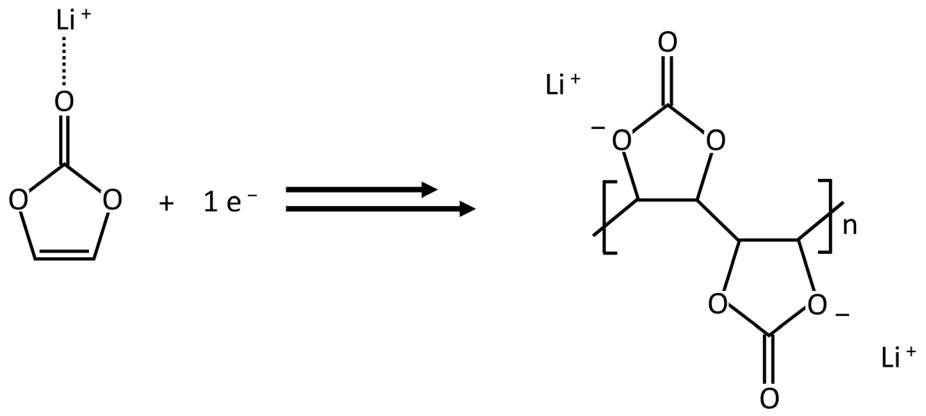

Figure 6.18: Proposed mechanism for the reductive decomposition of VC. One lithium-ion and one VC molecule from its solvation shell are reduced by uptake of one electron resulting in one monomer of lithium-containing poly(VC).

The reductive decomposition of one FEC molecule probably leads to the consumption of three electrons, as can be concluded from Figure 6.17(b). Indeed, the point from the cells after 15 cycles at 0.5 C/0.5 C is between the dashed line that indicates the 2 e^-/FEC ratio and the dashed line that indicates the 3 e^-/FEC ratio. The point from the cells after 40 cycles at 0.5 C/0.5 C is between the dashed line that indicates the 3 e^-/FEC ratio and the dashed line that indicates the 4 e^-/FEC ratio.

Consequently, a three electron reduction of FEC is the most probable possibility. The lost amounts of substance of cycleable Li calculated based on the cumulative irreversible capacities and thus the consumed amounts of substance of electrons are close to the quantified amounts of substance of Li in the anodes from the cells with the FEC electrolyte, as can be seen in Figure 6.14(b). Thus, one lithium-ion is deposited on the anode for every electron that is consumed at the anode in the cells with the FEC electrolyte. Hence, the reductive decomposition of one FEC molecule is associated with the consumption of three electrons and three lithium-ions. Besides, the SEI in the cells with the FEC electrolyte mainly consists of LiF, PEO (or a PEO-type polymer), and lithium carbonate, as described in section 6.6. In literature, it is proposed that the one electron reduction of FEC yields a FEC-radical anion, which is decomposed to LiF, CO_2, and a vinoxyl-radical [82]. In fact, Schroder et al. concluded from their experimental results that FEC reduction leads to LiF formation [98]. The formation of the vinoxyl-radical by the FEC decomposition was also detected experimentally by Shkrob et al. [99]. In addition, Jung et al. found experimentally that one CO_2 molecule is released for every reduced FEC molecule [17]. Hence, it is reasonable to assume that one FEC molecule, one lithium-ion, and one electron actually react to one LiF molecule, one CO_2 molecule, and one vinoxyl-radical. Indeed, the CO_2 evolved by the FEC reduction is apparently further reduced resulting in additional SEI material since no considerable CO_2 amounts are detected in the cells with the FEC electrolyte (see section 6.5). In addition, the data in Figure 6.16(c) reveal that all end products of the decomposition of FEC are solid SEI components and no gases, as already mentioned in this section, which confirms the CO_2 decomposition to SEI components following the CO_2 formation. In fact, Krause et al. observed that initially present CO_2 is gradually consumed during cycling in lithium-ion cells resulting in SEI buildup [84]. Additionally, Schwenke et al. found that the SEI components lithium formate, lithium oxalate, and especially lithium carbonate are formed by the CO_2 reduction in lithium-ion cells [83]. They suggested that the uptake of four electrons by three CO_2 molecules leads to the formation of two lithium carbonate molecules and one molecule of amorphous carbon in total [83]. This means that 4/3 electrons are consumed for each consumed CO_2 molecule. Nevertheless, Solchenbach et al. observed that two electrons are consumed per reduced CO_2 molecule [85]. Indeed, they explained that a fraction of the determined electron consumption might not be related to the CO_2 reduction, but to decomposition reactions of the electrolyte solvent in the examined lithium-ion cells [85]. As a result, the actual number of consumed electrons per consumed CO_2 molecule might be lower. Nevertheless, it is assumed in the following that the reduction of one CO_2 molecule leads to the consumption of two electrons. Vinoxyl-radicals can initiate polymerizations that eventually result in a highly cross-linked network [100]. Furthermore, the FEC-derived SEI consists mainly of cross-linked PEO, as reported in literature [90]. Hence, it is reasonable to assume that the vinoxyl-radicals react with each other yielding a cross-linked PEO-type polymer. Based on the results from this study and the mentioned findings from

literature, the following mechanism for the reductive decomposition of FEC is proposed: First, one FEC molecule, one lithium-ion, and one electron react with each other yielding one LiF molecule, one CO_2 molecule, and one vinoxyl-radical (consumption of the 1st electron). LiF is one end product of the FEC decomposition and represents a major SEI component. The formed CO_2 molecule, two lithium-ions, two electrons, and possibly other molecules react with each other eventually yielding the SEI component lithium formate, lithium oxalate, or lithium carbonate (consumption of the 2nd and 3rd electron). Admittedly, a precise decomposition reaction for the CO_2 reduction in lithium-ion cells cannot be proposed at this point. Plausible chemical equations for a two electron reduction of CO_2 in lithium-ion cells are also not described in literature so far, to the best of our knowledge. Indeed, it is known from literature that the reduction of one CO_2 molecule consumes two electrons in lithium-ion cells [85]. Furthermore, the CO_2 reduction yields the end products lithium formate (HCO_2Li), lithium oxalate ($Li_2C_2O_4$), and especially lithium carbonate (Li_2CO_3) [83]. The formed vinoxyl-radicals polymerize with each other without lithium-ion and electron consumption yielding another SEI component, namely a cross-linked PEO-type polymer. The proposed mechanism for the reductive decomposition of FEC is depicted in Figure 6.19. According to this, three lithium-ions and three electrons are consumed for each reduced FEC molecule in total. This mechanism for the reductive decomposition of FEC is mostly responsible for the capacity loss of the examined NCM622/silicon-graphite pouch cells with the FEC electrolyte after formation during following cycling. The cross-linked PEO-type polymer shown in Figure 6.19 is identical to parts of the FEC-derived cross-linked polymer proposed by Michan et al. [101]. Indeed, a small fraction of the decomposed FEC molecules might react each together with one lithium-ion and one electron to one LiF molecule, one hydrogen atom, and one VC molecule, as proposed in literature [100]. The formed VC molecules can subsequently react with some of the vinoxyl-radicals resulting in poly(VC) [100]. Thus, some poly(VC) units might also be integrated into the mentioned PEO-type polymer. This would explain, why slight amounts of poly(VC) are detected on the anodes from the cells with the FEC electrolyte after formation and subsequent cycling, as described in section 6.6.

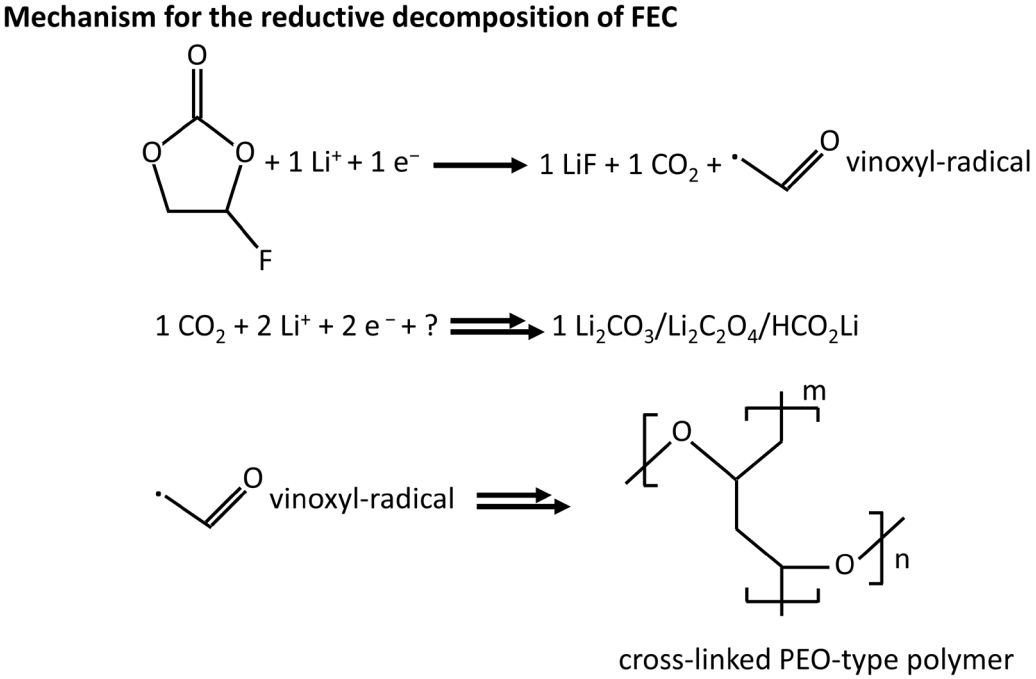

Figure 6.19: Proposed mechanism for the reductive decomposition of FEC. One FEC molecule reacts with one lithium-ion and one electron yielding one LiF molecule, one CO_2 molecule, and one vinoxyl-radical. The CO_2 molecule reacts with two lithium-ions, two electrons, and possibly other molecules to one Li_2CO_3 molecule, one $Li_2C_2O_4$ molecule, or one HCO_2Li molecule. The exact reaction of the CO_2 reduction is unknown. The formed vinoxyl-radicals polymerize yielding a cross-linked PEO-type polymer.

The proposed mechanisms for the reductive decompositions of VC and FEC shown in Figure 6.18 and Figure 6.19 are reasonable proposals, but they are not definite. Furthermore, these mechanisms represent only the proposed major decomposition pathways of VC and FEC. It can be assumed that additional, minor side reactions simultaneously take place during formation and subsequent cycling in the cells with the VC electrolyte and the FEC electrolyte.

7 Summary and Outlook

Within the scope of this thesis, a new method for electrolyte extraction from battery cells by injection of a diluent is developed that allows not only the quantification of the usually determined concentrations, but also the quantification of the absolute amounts of the electrolyte components in the cell. Based on these determined, absolute amounts, the consumed amounts of the electrolyte components during formation and/or subsequent cycling can be calculated, which indicate the absolute magnitudes of the decompositions in the electrolyte. Only based on these consumed amounts, the actual magnitude of all decompositions in the electrolyte can be determined. By contrast, the concentrations of the electrolyte components are just quantity ratios, which do not contain any information about the absolute magnitudes of the decompositions in the electrolyte. After injection of the diluent DEC, the cell is sealed and stored for 8-14 days to eventually extract the mixture of the original electrolyte and the injected DEC from the cell. The concentrations of the components of the original electrolyte and the concentration of the injected DEC are quantified in the extract by HPLC-UV/Vis, HPLC-ESI/MS, and GC-FID, respectively. Based on these concentrations and the mass of the injected DEC, the absolute amounts of the electrolyte components are determined. First, the validity of the determination of the absolute amounts is validated by extracting the electrolyte from electrochemically untreated, fresh NCM111/graphite lithium-ion pouch cells using the new extraction method and by analyzing the extracted electrolyte using HPLC-UV/Vis and HPLC-ESI/MS. Each NCM111/graphite pouch cell is initially filled with the electrolyte LP30+VC+LiTFSI. The quantified, absolute amounts of the electrolyte components in the fresh NCM111/graphite pouch cells are close to the respective setpoints calculated by the weighed masses, which confirms the validity of the determination of the absolute amounts of the electrolyte components. Subsequently, electrolytes are also extracted from NCM111/graphite lithium-ion pouch cells after formation and after different numbers of cycles to examine the electrochemical decompositions in these cells. The extracted electrolytes are quantitatively analyzed by HPLC-UV/Vis and HPLC-ESI/MS. The additionally determined concentrations of the electrolyte components indicate only a pronounced VC decomposition during formation and subsequent cycling until a remaining capacity of 80%. The consumed amounts of the electrolyte components reveal that the EC decomposition is actually dominant and the VC decomposition is distinctly weaker during formation plus cycling until a remaining capacity of 80%. Besides, the consumed amounts of the electrolyte components indicate a moderate

$LiPF_6$ decomposition and a slight DMC decomposition during formation plus cycling until a remaining capacity of 80%. This example demonstrates that the determination of the concentrations of the electrolyte components does not enable a reliable investigation of the actual decompositions in the electrolyte. Instead, the absolute amounts and the consumed amounts of the electrolyte components need to be determined to gain insight into the actual decompositions in the electrolyte from the cell during formation and subsequent cycling. Thus, the newly developed electrolyte extraction method and the associated analyses of the extracted electrolytes enable a precise investigation of the decomposition mechanisms in pouch cells.

In the next step, the newly developed electrolyte extraction method and the methods for the quantification of the electrolyte components by HPLC-UV/Vis and HPLC-ESI/MS are applied to investigate the electrochemical decompositions in NCM622/graphite lithium-ion pouch cells with custom-made electrodes during formation and subsequent cycling until a remaining capacity of 80%. The complementary analysis methods XPS, SEM, EDX, ICP-OES, and GC-TCD are used to examine the electrodes and the evolved gases from the NCM622/graphite pouch cells in the different aging stages. Each NCM622/graphite pouch cell is initially filled with the electrolyte LP30+VC. Based on the obtained results, two different phases of cell aging are identified. In phase I (during formation and the subsequent 25 cycles), only about 100 µmol EC and about 100 µmol VC are decomposed, while no decomposition of DMC and $LiPF_6$ is observed. These decompositions in the electrolyte are accompanied by the buildup of a thin SEI especially at the graphite particle edges consisting of the decomposition products of EC and VC, namely poly(VC) and lithium carbonate. The pronounced, reductive decomposition of VC can be ascribed to the higher reduction potential of VC compared to EC and DMC. The distinct, reductive decomposition of EC might be explained by the dominance of EC in the solvation shell of the lithium-ions. The relatively low coulombic efficiencies in phase I suggest that the crucial trigger for the electrolyte decompositions, the associated SEI buildup, and the capacity losses is an incomplete anode passivation by a thin and unfinished SEI. The obtained results suggest that EC, DMC, VC, and $LiPF_6$ are decomposed according to their abundance in phase II (from the 26^{th} cycle until the about 800^{th} cycle). As a result, about 500 µmol EC and about 500 µmol DMC are consumed in phase II. About 70 µmol $LiPF_6$ are consumed during phase II, while the VC consumption is unexpectedly the lowest with about 40 µmol. The SEI of decomposition products from the electrolyte is deposited on the graphite particle edges and on the basal planes of the graphite particles in spherical and tubular deposits during phase II. The spherical deposits are SEI that is preferentially deposited on the carbon black particles, while the tubular deposits might represent SEI that is rebuilt along cracks in the previous SEI. Two possible triggers for the electrolyte decompositions, the associated SEI buildup, and the capacity losses during phase II are identified: Firstly, the detected, continuous accumulation of transition metals, especially manganese, in the SEI induces accelerated electrolyte

decomposition, consequent SEI buildup, and capacity losses in phase II. Secondly, the volume changes of the graphite during de-/lithiation might lead to the creation of new, electrochemically active graphite surface, which also results in electrolyte decomposition, consequent SEI buildup, and capacity losses during phase II. This study demonstrates that the electrolyte decomposition and the resulting SEI buildup during formation and short-term cycling differ substantially from the electrolyte decomposition and the resulting SEI growth during long-term-cycling.

In the third part of the thesis, the electrochemical decompositions in NCM622/silicon-graphite lithium-ion pouch cells with custom-made electrodes during formation and the subsequent 40 cycles are examined using the developed electrolyte extraction method and the methods for the quantification of the electrolyte components by HPLC-UV/Vis, HPLC-ESI/MS, and GC-FID. The complementary analysis methods XPS, SEM, EDX, ICP-OES, and GC-TCD are applied to investigate the electrodes and the evolved gases from the NCM622/silicon-graphite pouch cells in the different aging stages. The examined NCM622/silicon-graphite pouch cells are initially filled either with the electrolyte 1 M $LiPF_6$ in VC:DMC (cells with the VC electrolyte) or with the electrolyte 1 M $LiPF_6$ in FEC:DMC (cells with the FEC electrolyte). These two electrolytes are selected for the investigations since they allow the best capacity retention during cycling among the tested VC-containing and FEC-containing electrolytes. The cycle data reveal that the cells with the VC electrolyte have better capacity retentions compared to the cells with the FEC electrolyte, while the cells with the FEC electrolyte have higher, absolute discharge capacities during the first cycles compared to the cells with the VC electrolyte. The capacity losses of the investigated NCM622/silicon-graphite pouch cells during the first cycle of the formation program are (almost) exclusively induced by trapping of cycleable lithium in the SEI and by trapping of cycleable lithium in irreversibly lithiated silicon and silicon oxide under the SEI. The capacity losses of the investigated NCM622/silicon-graphite pouch cells after the first cycle of the formation program during the following cycles at 0.5 C/0.5 C are (almost) exclusively triggered by the trapping of cycleable lithium in the SEI. VC is preferentially decomposed during formation and subsequent cycling in the cells with the VC electrolyte. Nevertheless, a slight DMC decomposition during formation and subsequent cycling in the cells with the VC electrolyte is also detected, which indicates that VC cannot suppress completely the decomposition of other electrolyte components. By contrast, a significant $LiPF_6$ decomposition during formation and following cycling in the cells with the VC electrolyte cannot be found. The reductive decomposition of one VC molecule at the anode consumes one lithium-ion and one electron. The reductive decomposition of VC eventually yields a lithium-containing poly(VC), which represents the major SEI component after formation and after subsequent cycling in the cells with the VC electrolyte. This proposed mechanism for the reductive decomposition of VC is almost exclusively responsible for the capacity loss of the examined NCM622/silicon-graphite pouch cells with the VC electrolyte after formation during following cycling (at 0.5 C/0.5 C). FEC is exclusively decomposed

during formation and following cycling in the cells with the FEC electrolyte. A significant decomposition of DMC and $LiPF_6$ during formation and following cycling in the cells with the FEC electrolyte cannot be observed. The reductive decomposition of one FEC molecule is associated with the consumption of three lithium-ions and three electrons at the anode. The following mechanisms for the reductive decomposition of FEC is proposed: First, one FEC molecule, one lithium-ion, and one electron react to one LiF molecule, one vinoxyl-radical, and one CO_2 molecule (consumption of the 1st electron). LiF represents a major SEI component after formation and after subsequent cycling in the cells with the FEC electrolyte. The formed vinoxyl-radicals react with each other to a cross-linked PEO-type polymer, which is another SEI component after formation and after subsequent cycling in the cells with the FEC electrolyte. The formed CO_2 molecule reacts together with two lithium-ions, two electrons, and possibly other molecules to the SEI component lithium formate, lithium oxalate, or lithium carbonate (consumption of the 2nd and 3rd electron). A precise mechanism for the CO_2 reduction cannot be proposed at this point. The capacity loss of the examined NCM622/silicon-graphite pouch cells with the FEC electrolyte after formation during following cycling (at 0.5 C/0.5 C) can be mainly ascribed to this proposed mechanism for the reductive decomposition of FEC. Apart from that, a minor fraction of the decomposed FEC molecules might react each together with one lithium-ion and one electron to one LiF molecule, one hydrogen atom, and one VC molecule. Following this, the formed VC molecules can react with some of the vinoxyl-radicals to poly(VC), so that some poly(VC) units might be integrated into the mentioned PEO-type polymer during formation and subsequent cycling.

Unfortunately, it is not meaningful to compare the observed decomposition processes in the NCM111/graphite pouch cells with those in the NCM622/graphite pouch cells since the compositions of the cathodes and the anodes from both pouch cell types are different from each other. The exact compositions of the commercially available electrodes from the NCM111/graphite pouch cells are not known. This is acceptable since the NCM111/graphite pouch cells are mainly used for the testing of the newly developed electrolyte extraction method and the associated determination of the absolute amounts of the electrolyte components. By contrast, the exact compositions of the custom-made electrodes from the NCM622/graphite pouch cells are known. Unfortunately, it is also not meaningful to directly compare the observed decomposition processes in the NCM622/graphite pouch cells with those in the NCM622/silicon-graphite pouch cells, as the compositions of the initial electrolytes in both pouch cell types are very different from each other. The original plan was to use the initial electrolyte of the NCM622/graphite pouch cells LP30+VC also in the investigated NCM622/silicon-graphite pouch cells, so that both pouch cell types are identical except for the silicon in the anodes (silicon-free anodes in the NCM622/graphite pouch cells vs. silicon-containing anodes in the NCM622/silicon-graphite pouch cells). Thereby, the influence of silicon in the anodes on the electrochemical decomposition processes in pouch cells should be investigated. This original plan was discarded because of the

massive capacity losses of the NCM622/silicon-graphite pouch cells with LP30+VC as initial electrolyte during cycling. Therefore, the mentioned VC electrolyte and the mentioned FEC electrolyte are eventually used in the examined NCM622/silicon-graphite pouch cells, as these electrolytes enable an optimized cycle-life.

Summarized, the presented method for the determination of consumed amounts of the electrolyte components in battery cells distinctly simplifies the clarification of the decomposition mechanisms in battery cells. A complete understanding of the decomposition processes in battery cells is crucial for a systematic optimization of the batteries. Consequently, the presented method for the determination of the consumed amounts of the electrolyte components in battery cells represents an important contribution for the battery research community. Based on the results from the analyses of the NCM622/silicon-graphite pouch cells, mechanisms for the reductive decomposition of VC and FEC can eventually be proposed. Future analyses, such as nuclear magnetic resonance spectroscopy (NMR spectroscopy) analyses, are necessary to clarify the actual structural formula of the mentioned, lithium-containing poly(VC) in the SEI. Furthermore, the precise mechanism for the reductive decomposition of CO_2 in lithium-ion cells needs to be clarified to fully determine the mechanism for the reductive decomposition of FEC in lithium-ion cells. This might be realized by injecting a defined amount of additional CO_2 into NCM622/silicon-graphite pouch cells with the initial electrolyte 1 M $LiPF_6$ in FEC:DMC through the gas extraction valve. Subsequently, the CO_2 consumptions, the consumptions of the electrolyte components, and the electron consumptions during formation and during the subsequent 40 cycles at 0.5 C/0.5 C are determined. Furthermore, it is useful to determine the composition of the SEI and the amounts of the evolved gases, such as CO, in these cells with the injected, extra CO_2 by XPS, NMR spectroscopy, and GC-TCD to identify the CO_2 decomposition products. Based on the actual number of consumed electrons per consumed CO_2 molecule and the identified CO_2 decomposition products, the mechanism for the reductive decomposition of CO_2 in lithium-ion cells might be clarified. For future investigations, it would be interesting to conduct the presented analyses of the electrolyte, the electrodes, and the evolved gases also with large-format pouch cells. In principle, the presented methods for the extraction of the electrolyte and the evolved gases can also be used for the investigation of the electrolytes and the gases from large-format pouch cells. For the extraction of the electrolyte from large-format pouch cells, the volume of the injected diluent needs to be adapted to the electrolyte volume in these cells. If the investigated cells are filled with a DEC-containing electrolyte, other diluents can be injected into the cells for electrolyte extraction. Note that the selected diluent needs to be chemically stable in the cell during storage and the diluent must not be present in the cell before injection. Thus, the presented methods represent a base for more precise investigations of the decomposition processes in battery cells, which can help

to systematically optimize battery systems. The development of optimized battery systems is one important key for a sustainable economy in the future.

References

[1] BP p.l.c., bp Statistical Review of World Energy 2022, 2022, https://www.bp.com/content/dam/bp/business-sites/en/global/corporate/pdfs/energy-economics/statistical-review/bp-stats-review-2022-full-report.pdf (Accessed 01.03.2023).

[2] N. Nitta, F. Wu, J.T. Lee, G. Yushin, Li-ion battery materials: present and future, Materials Today 18 (2015) 252–264, https://doi.org/10.1016/j.mattod.2014.10.040.

[3] L. El Ouatani, R. Dedryvère, C. Siret, P. Biensan, D. Gonbeau, Effect of Vinylene Carbonate Additive in Li-Ion Batteries: Comparison of $LiCoO_2$/C, $LiFePO_4$/C, and $LiCoO_2$/$Li_4Ti_5O_{12}$ Systems, J. Electrochem. Soc. 156 (2009) A468–A477, https://doi.org/10.1149/1.3111891.

[4] J.B. Goodenough, K.-S. Park, The Li-Ion Rechargeable Battery: A Perspective, J. Am. Chem. Soc. 135 (2013) 1167–1176, https://doi.org/10.1021/ja3091438.

[5] D. Guyomard, J.-M. Tarascon, Rocking-chair or lithium-ion rechargeable lithium batteries, Adv. Mater. 6 (1994) 408–412, https://doi.org/10.1002/adma.19940060516.

[6] J.-M. Tarascon, M. Armand, Issues and challenges facing rechargeable lithium batteries, Nature 414 (2001) 359–367, https://doi.org/10.1038/35104644.

[7] K. Ozawa, Lithium-ion rechargeable batteries with $LiCoO_2$ and carbon electrodes: the $LiCoO_2$/C system, Solid State Ionics 69 (1994) 212–221, https://doi.org/10.1016/0167-2738(94)90411-1.

[8] W. Xu, J. Wang, F. Ding, X. Chen, E. Nasybulin, Y. Zhang, J.-G. Zhang, Lithium metal anodes for rechargeable batteries, Energy Environ. Sci. 7 (2014) 513–537, https://doi.org/10.1039/C3EE40795K.

[9] R. Korthauer, Handbuch Lithium-Ionen-Batterien, Berlin, Heidelberg: Springer Vieweg (2013), https://doi.org/10.1007/978-3-642-30653-2.

[10] M. Yoshio, R.J. Brodd, A. Kozawa, Lithium-Ion Batteries, New York: Springer (2009), https://doi.org/10.1007/978-0-387-34445-4.

[11] M. Winter, J.O. Besenhard, M.E. Spahr, P. Novák, Insertion Electrode Materials for Rechargeable Lithium Batteries, Adv. Mater. 10 (1998) 725–763, https://doi.org/10.1002/(SICI)1521-4095(199807)10:10<725::AID-ADMA725>3.0.CO;2-Z.

[12] R. Wagner, N. Preschitschek, S. Passerini, J. Leker, M. Winter, Current research trends and prospects among the various materials and designs used in lithium-based batteries, J. Appl. Electrochem. 43 (2013) 481-496, https://doi.org/10.1007/s10800-013-0533-6.

[13] M.N. Obrovac, L. Christensen, Structural Changes in Silicon Anodes during Lithium Insertion/Extraction, Electrochem. Solid-State Lett. 7 (2004) A93-A96, https://doi.org/10.1149/1.1652421.

[14] M. Ashuri, Q. He, L.L. Shaw, Silicon as a potential anode material for Li-ion batteries: where size, geometry and structure matter, Nanoscale 8 (2016) 74–103, https://doi.org/10.1039/C5NR05116A.

[15] J. Xu, L. Zhang, Y. Wang, T. Chen, M. Al-Shroofy, Y.-T. Cheng, Unveiling the Critical Role of Polymeric Binders for Silicon Negative Electrodes in Lithium-Ion Full Cells, ACS Appl. Mater. Interfaces 9 (2017) 3562–3569, https://doi.org/10.1021/acsami.6b11121.

[16] W.-J. Zhang, A review of the electrochemical performance of alloy anodes for lithium-ion batteries, Journal of Power Sources 196 (2011) 13–24, https://doi.org/10.1016/j.jpowsour.2010.07.020.

[17] R. Jung, M. Metzger, D. Haering, S. Solchenbach, C. Marino, N. Tsiouvaras, C. Stinner, H.A. Gasteiger, Consumption of Fluoroethylene Carbonate (FEC) on Si-C Composite Electrodes for Li-Ion Batteries, J. Electrochem. Soc. 163 (2016) A1705–A1716, https://doi.org/10.1149/2.0951608jes.

[18] X. Wang, Y.-L. Ding, Y.-P. Deng, Z. Chen, Ni-Rich/Co-Poor Layered Cathode for Automotive Li-Ion Batteries: Promises and Challenges, Adv. Energy Mater. 10 (2020) 1-28, https://doi.org/10.1002/aenm.201903864.

[19] T.R. Jow, K. Xu, O. Borodin, M. Ue, Electrolytes for Lithium and Lithium-Ion Batteries, New York, Heidelberg, Dordrecht, London: Springer (2014), https://doi.org/10.1007/978-1-4939-0302-3.

[20] J.B. Goodenough, Y. Kim, Challenges for Rechargeable Li Batteries, Chem. Mater. 22 (2010) 587–603, https://doi.org/10.1021/cm901452z.

[21] C. Breitkopf, K. Swider-Lyons, Springer Handbook of Electrochemical Energy, Berlin, Heidelberg: Springer (2017), https://doi.org/978-3-662-46657-5.

[22] K. Xu, Nonaqueous Liquid Electrolytes for Lithium-Based Rechargeable Batteries, Chem. Rev. 104 (2004) 4303–4417, https://doi.org/10.1021/cr030203g.

[23] B. Flamme, G. Rodriguez Garcia, M. Weil, M. Haddad, P. Phansavath, V. Ratovelomanana-Vidal, A. Chagnes, Guidelines to design organic electrolytes for lithium-ion batteries: environmental impact, physicochemical and electrochemical properties, Green Chem. 19 (2017) 1828–1849, https://doi.org/10.1039/C7GC00252A.

[24] A.M. Haregewoin, A.S. Wotango, B.-J. Hwang, Electrolyte additives for lithium ion battery electrodes: progress and perspectives, Energy Environ. Sci. 9 (2016) 1955–1988, https://doi.org/10.1039/C6EE00123H.

[25] L. El Ouatani, R. Dedryvère, C. Siret, P. Biensan, S. Reynaud, P. Iratçabal, D. Gonbeau, The Effect of Vinylene Carbonate Additive on Surface Film Formation on Both Electrodes in Li-Ion Batteries, J. Electrochem. Soc. 156 (2009) A103–A113, https://doi.org/10.1149/1.3029674.

[26] D. Aurbach, K. Gamolsky, B. Markovsky, Y. Gofer, M. Schmidt, U. Heider, On the use of vinylene carbonate (VC) as an additive to electrolyte solutions for Li-ion batteries, Electrochimica Acta 47 (2002) 1423–1439, https://doi.org/10.1016/S0013-4686(01)00858-1.

[27] N.-S. Choi, K.H. Yew, K.Y. Lee, M. Sung, H. Kim, S.-S. Kim, Effect of fluoroethylene carbonate additive on interfacial properties of silicon thin-film electrode, Journal of Power Sources 161 (2006) 1254–1259, https://doi.org/10.1016/j.jpowsour.2006.05.049.

[28] V. Etacheri, O. Haik, Y. Goffer, G.A. Roberts, I.C. Stefan, R. Fasching, D. Aurbach, Effect of Fluoroethylene Carbonate (FEC) on the Performance and Surface Chemistry of Si-Nanowire Li-Ion Battery Anodes, Langmuir 28 (2012) 965–976, https://doi.org/10.1021/la203712s.

[29] T. Jaumann, J. Balach, U. Langklotz, V. Sauchuk, M. Fritsch, A. Michaelis, V. Teltevskij, D. Mikhailova, S. Oswald, M. Klose, G. Stephani, R. Hauser, J. Eckert, L. Giebeler, Lifetime vs. rate capability: Understanding the role of FEC and VC in high-energy Li-ion batteries with nano-silicon anodes, Energy Storage Materials 6 (2017) 26–35, https://doi.org/10.1016/j.ensm.2016.08.002.

[30] J. Vetter, P. Novák, M.R. Wagner, C. Veit, K.-C. Möller, J.O. Besenhard, M. Winter, M. Wohlfahrt-Mehrens, C. Vogler, A. Hammouche, Ageing mechanisms in lithium-ion batteries, Journal of Power Sources 147 (2005) 269–281, https://doi.org/10.1016/j.jpowsour.2005.01.006.

[31] E. Peled, The Electrochemical Behavior of Alkali and Alkaline Earth Metals in Nonaqueous Battery Systems—The Solid Electrolyte Interphase Model, J. Electrochem. Soc. 126 (1979) 2047–2051, https://doi.org/10.1149/1.2128859.

[32] A. Wang, S. Kadam, H. Li, S. Shi, Y. Qi, Review on modeling of the anode solid electrolyte interphase (SEI) for lithium-ion batteries, Npj Computational Materials 15 (2018) 1-26, https://doi.org/10.1038/s41524-018-0064-0.

[33] D. Aurbach, Y. Ein-Eli, B. Markovsky, A. Zaban, S. Luski, Y. Carmeli, H. Yamin, The Study of Electrolyte Solutions Based on Ethylene and Diethyl Carbonates for Rechargeable Li Batteries: II. Graphite Electrodes, J. Electrochem. Soc. 142 (1995) 2882–2890, https://doi.org/10.1149/1.2048659.

[34] H. Ota, Y. Sakata, A. Inoue, S. Yamaguchi, Analysis of Vinylene Carbonate Derived SEI Layers on Graphite Anode, J. Electrochem. Soc. 151 (2004) A1659–A1669, https://doi.org/10.1149/1.1785795.

[35] H. Yoshida, T. Fukunaga, T. Hazama, M. Terasaki, M. Mizutani, M. Yamachi, Degradation mechanism of alkyl carbonate solvents used in lithium-ion cells during initial charging, Journal of Power Sources 68 (1997) 311–315, https://doi.org/10.1016/S0378-7753(97)02635-9.

[36] J.A. Gilbert, I.A. Shkrob, D.P. Abraham, Transition Metal Dissolution, Ion Migration, Electrocatalytic Reduction and Capacity Loss in Lithium-Ion Full Cells, J. Electrochem. Soc. 164 (2017) A389–A399, https://doi.org/10.1149/2.1111702jes.

[37] C. Zhan, T. Wu, J. Lu, K. Amine, Dissolution, migration, and deposition of transition metal ions in Li-ion batteries exemplified by Mn-based cathodes – a critical review, Energy Environ. Sci. 11 (2018) 243–257, https://doi.org/10.1039/C7EE03122J.

[38] S. Solchenbach, G. Hong, A.T.S. Freiberg, R. Jung, H.A. Gasteiger, Electrolyte and SEI Decomposition Reactions of Transition Metal Ions Investigated by On-Line Electrochemical Mass Spectrometry, J. Electrochem. Soc. 165 (2018) A3304–A3312, https://doi.org/10.1149/2.0511814jes.

[39] C. Schultz, V. Kraft, M. Pyschik, S. Weber, F. Schappacher, M. Winter, S. Nowak, Separation and Quantification of Organic Electrolyte Components in Lithium-Ion Batteries via a Developed HPLC Method, J. Electrochem. Soc. 162 (2015) A629–A634, https://doi.org/10.1149/2.0401504jes.

[40] R. Stockhausen, A. Hofmann, L. Gehrlein, T. Bergfeldt, M. Müller, H. Ehrenberg, A. Smith, Quantifying Absolute Amounts of Electrolyte Components in Lithium-Ion Cells Using HPLC, J. Electrochem. Soc. 168 (2021) 080504, https://doi.org/10.1149/1945-7111/ac1894.

[41] M.H. Gey, Instrumentelle Analytik und Bioanalytik: Biosubstanzen, Trennmethoden, Strukturanalytik, Applikationen, Berlin: Springer Spektrum (2021), https://doi.org/10.1007/978-3-662-63952-8.

[42] S. Kromidas, The HPLC-MS Handbook for Practitioners, Weinheim: WILEY-VCH Verlag GmbH & Co. KGaA (2017), https://doi.org/10.1002/9783527809202.

[43] J.H. Gross, Mass Spectrometry: A Textbook, Cham: Springer (2017), https://doi.org/10.1007/978-3-319-54398-7.

[44] R. Stockhausen, L. Gehrlein, M. Müller, T. Bergfeldt, A. Hofmann, F.J. Müller, J. Maibach, H. Ehrenberg, A. Smith, Investigating the dominant decomposition mechanisms in lithium-ion battery cells responsible for capacity loss in different stages of electrochemical aging, Journal of Power Sources 543 (2022) 231842, https://doi.org/10.1016/j.jpowsour.2022.231842.

[45] A. Hofmann, A. Smith, F.J. Müller, I. Reuter, Assembly and method for supplying a gas stream, registration number: 22188274.9 (2022), patent not yet accepted (on 01.03.2023).

[46] K.L. Parry, A.G. Shard, R.D. Short, R.G. White, J.D. Whittle, A. Wright, ARXPS characterisation of plasma polymerised surface chemical gradients, Surface and Interface Anal. 38 (2006) 1497–1504, https://doi.org/10.1002/sia.2400.

[47] C. Schultz, S. Vedder, B. Streipert, M. Winter, S. Nowak, Quantitative investigation of the decomposition of organic lithium ion battery electrolytes with LC-MS/MS, RSC Adv. 7 (2017) 27853–27862, https://doi.org/10.1039/C7RA03839A.

[48] L.M. Thompson, W. Stone, A. Eldesoky, N.K. Smith, C.R.M. McFarlane, J.S. Kim, M.B. Johnson, R. Petibon, J.R. Dahn, Quantifying Changes to the Electrolyte and Negative Electrode in Aged NMC532/Graphite Lithium-Ion Cells, J. Electrochem. Soc. 165 (2018) A2732–A2740, https://doi.org/10.1149/2.0721811jes.

[49] Y. Qian, C. Schultz, P. Niehoff, T. Schwieters, S. Nowak, F.M. Schappacher, M. Winter, Investigations on the electrochemical decomposition of the electrolyte additive vinylene carbonate in Li metal half cells and lithium ion full cells, Journal of Power Sources 332 (2016) 60–71, https://doi.org/10.1016/j.jpowsour.2016.09.100.

[50] C. Schultz, S. Vedder, M. Winter, S. Nowak, Qualitative Investigation of the Decomposition of Organic Solvent Based Lithium Ion Battery Electrolytes with LC-IT-TOF-MS, Anal. Chem. 88 (2016) 11160–11168, https://doi.org/10.1021/acs.analchem.6b03379.

[51] X. Mönnighoff, P. Murmann, W. Weber, M. Winter, S. Nowak, Post-Mortem Investigations of Fluorinated Flame Retardants for Lithium Ion Battery Electrolytes by Gas Chromatography with Chemical Ionization, Electrochimica Acta 246 (2017) 1042–1051, https://doi.org/10.1016/j.electacta.2017.06.125.

[52] F. Horsthemke, V. Winkler, M. Diehl, M. Winter, S. Nowak, Concept for the Analysis of the Electrolyte Composition within the Cell Manufacturing Process: From Sealing to Sample Preparation, Energy Technol. 8 (2020) 1801081, https://doi.org/10.1002/ente.201801081.

[53] L.D. Ellis, S. Buteau, S.G. Hames, L.M. Thompson, D.S. Hall, J.R. Dahn, A New Method for Determining the Concentration of Electrolyte Components in Lithium-Ion Cells, Using Fourier Transform Infrared Spectroscopy and Machine Learning, J. Electrochem. Soc. 165 (2018) A256–A262, https://doi.org/10.1149/2.0861802jes.

[54] L. Ma, L. Ellis, S.L. Glazier, X. Ma, Q. Liu, J. Li, J.R. Dahn, $LiPO_2F_2$ as an Electrolyte Additive in $Li[Ni_{0.5}Mn_{0.3}Co_{0.2}]O_2$/Graphite Pouch Cells, J. Electrochem. Soc. 165 (2018) A891–A899, https://doi.org/10.1149/2.0381805jes.

[55] R. Fong, U. von Sacken, J.R. Dahn, Studies of Lithium Intercalation into Carbons Using Nonaqueous Electrochemical Cells, J. Electrochem. Soc. 137 (1990) 2009–2013, https://doi.org/10.1149/1.2086855.

[56] A. von Cresce, K. Xu, Preferential Solvation of Li^+ Directs Formation of Interphase on Graphitic Anode, Electrochem. Solid-State Lett. 14 (2011) A154-A156, https://doi.org/10.1149/1.3615828.

[57] U. Heider, R. Oesten, M. Jungnitz, Challenge in manufacturing electrolyte solutions for lithium and lithium ion batteries quality control and minimizing contamination level, Journal of Power Sources 81–82 (1999) 119–122, https://doi.org/10.1016/S0378-7753(99)00142-1.

[58] K. Ushirogata, K. Sodeyama, Y. Okuno, Y. Tateyama, Additive Effect on Reductive Decomposition and Binding of Carbonate-Based Solvent toward Solid Electrolyte Interphase Formation in Lithium-Ion Battery, J. Am. Chem. Soc. 135 (2013) 11967–11974, https://doi.org/10.1021/ja405079s.

[59] S.A. Delp, O. Borodin, M. Olguin, C.G. Eisner, J.L. Allen, T.R. Jow, Importance of Reduction and Oxidation Stability of High Voltage Electrolytes and Additives, Electrochimica Acta 209 (2016) 498–510, https://doi.org/10.1016/j.electacta.2016.05.100.

[60] S.K. Heiskanen, J. Kim, B.L. Lucht, Generation and Evolution of the Solid Electrolyte Interphase of Lithium-Ion Batteries, Joule 3 (2019) 2322–2333, https://doi.org/10.1016/j.joule.2019.08.018.

[61] R. Imhof, P. Novák, In Situ Investigation of the Electrochemical Reduction of Carbonate Electrolyte Solutions at Graphite Electrodes, J. Electrochem. Soc. 145 (1998) 1081–1087, https://doi.org/10.1149/1.1838420.

[62] B. Zhang, M. Metzger, S. Solchenbach, M. Payne, S. Meini, H.A. Gasteiger, A. Garsuch, B.L. Lucht, Role of 1,3-Propane Sultone and Vinylene Carbonate in Solid Electrolyte Interface Formation and Gas Generation, J. Phys. Chem. C 119 (2015) 11337–11348, https://doi.org/10.1021/acs.jpcc.5b00072.

[63] D. Aurbach, Y. Gofer, M. Ben-Zion, P. Aped, The behaviour of lithium electrodes in propylene and ethylene carbonate: the major factors that influence Li cycling efficiency, J. Electroanal. Chem. 339 (1992) 451–471, https://doi.org/10.1016/0022-0728(92)80467-I.

[64] P. Verma, P. Maire, P. Novák, A review of the features and analyses of the solid electrolyte interphase in Li-ion batteries, Electrochimica Acta 55 (2010) 6332–6341, https://doi.org/10.1016/j.electacta.2010.05.072.

[65] Y. Li, M. Bettge, B. Polzin, Y. Zhu, M. Balasubramanian, D.P. Abraham, Understanding Long-Term Cycling Performance of $Li_{1.2}Ni_{0.15}Mn_{0.55}Co_{0.1}O_2$–Graphite Lithium-Ion Cells, J. Electrochem. Soc. 160 (2013) A3006–A3019, https://doi.org/10.1149/2.002305jes.

[66] R. Jung, F. Linsenmann, R. Thomas, J. Wandt, S. Solchenbach, F. Maglia, C. Stinner, M. Tromp, H.A. Gasteiger, Nickel, Manganese, and Cobalt Dissolution from Ni-Rich NMC and Their Effects on NMC622-Graphite Cells, J. Electrochem. Soc. 166 (2019) A378–A389, https://doi.org/10.1149/2.1151902jes.

[67] J. Asenbauer, T. Eisenmann, M. Kuenzel, A. Kazzazi, Z. Chen, D. Bresser, The success story of graphite as a lithium-ion anode material – fundamentals, remaining challenges, and recent developments including silicon (oxide) composites, Sustainable Energy Fuels 4 (2020) 5387–5416, https://doi.org/10.1039/d0se00175a.

[68] D. Bar-Tow, E. Peled, L. Burstein, A Study of Highly Oriented Pyrolytic Graphite as a Model for the Graphite Anode in Li-Ion Batteries, J. Electrochem. Soc. 146 (1999) 824–832, https://doi.org/10.1149/1.1391688.

[69] E. Peled, S. Menkin, Review—SEI: Past, Present and Future, J. Electrochem. Soc. 164 (2017) A1703–A1719, https://doi.org/10.1149/2.1441707jes.

[70] P. Li, Y. Zhao, Y. Shen, S.-H. Bo, Fracture behavior in battery materials, J. Phys. Energy 2 (2020) 022002, https://doi.org/10.1088/2515-7655/ab83e1.

[71] N. Lin, Z. Jia, Z. Wang, H. Zhao, G. Ai, X. Song, Y. Bai, V. Battaglia, C. Sun, J. Qiao, K. Wu, G. Liu, Understanding the crack formation of graphite particles in cycled commercial lithium-ion batteries by focused ion beam - scanning electron microscopy, Journal of Power Sources 365 (2017) 235–239, https://doi.org/10.1016/j.jpowsour.2017.08.045.

[72] S.J. Harris, R.D. Deshpande, Y. Qi, I. Dutta, Y.-T. Cheng, Mesopores inside electrode particles can change the Li-ion transport mechanism and diffusion-induced stress, J. Mater. Res. 25 (2010) 1433–1440, https://doi.org/10.1557/JMR.2010.0183.

[73] M.T. McDowell, S.W. Lee, W.D. Nix, Y. Cui, 25th Anniversary Article: Understanding the Lithiation of Silicon and Other Alloying Anodes for Lithium-Ion Batteries, Adv. Mater. 25 (2013) 4966–4985, https://doi.org/10.1002/adma.201301795.

[74] L. Chen, K. Wang, X. Xie, J. Xie, Enhancing Electrochemical Performance of Silicon Film Anode by Vinylene Carbonate Electrolyte Additive, Electrochem. Solid-State Lett. 9 (2006) A512-A515, https://doi.org/10.1149/1.2338771.

[75] R. Petibon, V.L. Chevrier, C.P. Aiken, D.S. Hall, S.R. Hyatt, R. Shunmugasundaram, J.R. Dahn, Studies of the Capacity Fade Mechanisms of $LiCoO_2$/Si-Alloy: Graphite Cells, J. Electrochem. Soc. 163 (2016) A1146–A1156, https://doi.org/10.1149/2.0191607jes.

[76] M. Wetjen, S. Solchenbach, D. Pritzl, J. Hou, V. Tileli, H.A. Gasteiger, Morphological Changes of Silicon Nanoparticles and the Influence of Cutoff Potentials in Silicon-Graphite Electrodes, J. Electrochem. Soc. 165 (2018) A1503–A1514, https://doi.org/10.1149/2.1261807jes.

[77] S. Dalavi, P. Guduru, B.L. Lucht, Performance Enhancing Electrolyte Additives for Lithium Ion Batteries with Silicon Anodes, J. Electrochem. Soc. 159 (2012) A642–A646, https://doi.org/10.1149/2.076205jes.

[78] M. Metzger, B. Strehle, S. Solchenbach, H.A. Gasteiger, Origin of H_2 Evolution in LIBs: H_2O Reduction vs. Electrolyte Oxidation, J. Electrochem. Soc. 163 (2016) A798–A809, https://doi.org/10.1149/2.1151605jes.

[79] R. Bernhard, M. Metzger, H.A. Gasteiger, Gas Evolution at Graphite Anodes Depending on Electrolyte Water Content and SEI Quality Studied by On-Line Electrochemical Mass Spectrometry, J. Electrochem. Soc. 162 (2015) A1984–A1989, https://doi.org/10.1149/2.0191510jes.

[80] B. Strehle, S. Solchenbach, M. Metzger, K.U. Schwenke, H.A. Gasteiger, The Effect of CO_2 on Alkyl Carbonate Trans-Esterification during Formation of Graphite Electrodes in Li-Ion Batteries, J. Electrochem. Soc. 164 (2017) A2513–A2526, https://doi.org/10.1149/2.1001712jes.

[81] H. Nakai, T. Kubota, A. Kita, A. Kawashima, Investigation of the Solid Electrolyte Interphase Formed by Fluoroethylene Carbonate on Si Electrodes, J. Electrochem. Soc. 158 (2011) A798–A801, https://doi.org/10.1149/1.3589300.

[82] K. Leung, S.B. Rempe, M.E. Foster, Y. Ma, J.M. Martinez del la Hoz, N. Sai, P.B. Balbuena, Modeling Electrochemical Decomposition of Fluoroethylene Carbonate on Silicon Anode Surfaces in Lithium Ion Batteries, J. Electrochem. Soc. 161 (2014) A213–A221, https://doi.org/10.1149/2.092401jes.

[83] K.U. Schwenke, S. Solchenbach, J. Demeaux, B.L. Lucht, H.A. Gasteiger, The Impact of CO_2 Evolved from VC and FEC during Formation of Graphite Anodes in Lithium-Ion Batteries, J. Electrochem. Soc. 166 (2019) A2035–A2047, https://doi.org/10.1149/2.0821910jes.

[84] L.J. Krause, V.L. Chevrier, L.D. Jensen, T. Brandt, The Effect of Carbon Dioxide on the Cycle Life and Electrolyte Stability of Li-Ion Full Cells Containing Silicon Alloy, J. Electrochem. Soc. 164 (2017) A2527–A2533, https://doi.org/10.1149/2.1121712jes.

[85] S. Solchenbach, M. Wetjen, D. Pritzl, K.U. Schwenke, H.A. Gasteiger, Lithium Oxalate as Capacity and Cycle-Life Enhancer in LNMO/Graphite and LNMO/SiG Full Cells, J. Electrochem. Soc. 165 (2018) A512–A524, https://doi.org/10.1149/2.0611803jes.

[86] X. Zhang, S. Weng, G. Yang, Y. Li, H. Li, D. Su, L. Gu, Z. Wang, X. Wang, L. Chen, Interplay between solid-electrolyte interphase and (in)active Li_xSi in silicon anode, Cell Reports Physical Science 2 100668 (2021) 1-11, https://doi.org/10.1016/j.xcrp.2021.100668.

[87] M.A. Al-Maghrabi, J. Suzuki, R.J. Sanderson, V.L. Chevrier, R.A. Dunlap, J.R. Dahn, Combinatorial Studies of $Si_{1-x}O_x$ as a Potential Negative Electrode Material for Li-Ion Battery Applications, J. Electrochem. Soc. 160 (2013) A1587–A1593, https://doi.org/10.1149/2.115309jes.

[88] D. Aurbach, Y. Ein-Eli, O. Chusid (Youngman), Y. Carmeli, M. Babai, H. Yamin, The Correlation Between the Surface Chemistry and the Performance of Li-Carbon Intercalation Anodes for Rechargeable “Rocking-Chair” Type Batteries, J. Electrochem. Soc. 141 (1994) 603–611, https://doi.org/10.1149/1.2054777.

[89] E.K.W. Andersson, C. Sångeland, E. Berggren, F.O.L. Johansson, D. Kühn, A. Lindblad, J. Mindemark, M. Hahlin, Early-stage decomposition of solid polymer electrolytes in Li-metal batteries, J. Mater. Chem. A 9 (2021) 22462–22471, https://doi.org/10.1039/D1TA05015J.

[90] Y. Jin, N.-J.H. Kneusels, L.E. Marbella, E. Castillo-Martínez, P.C.M.M. Magusin, R.S. Weatherup, E. Jónsson, T. Liu, S. Paul, C.P. Grey, Understanding Fluoroethylene Carbonate and Vinylene Carbonate Based Electrolytes for Si Anodes in Lithium Ion Batteries with NMR Spectroscopy, J. Am. Chem. Soc. 140 (2018) 9854–9867, https://doi.org/10.1021/jacs.8b03408.

[91] C. Xu, F. Lindgren, B. Philippe, M. Gorgoi, F. Björefors, K. Edström, T. Gustafsson, Improved Performance of the Silicon Anode for Li-Ion Batteries: Understanding the Surface Modification Mechanism of Fluoroethylene Carbonate as an Effective Electrolyte Additive, Chem. Mater. 27 (2015) 2591–2599, https://doi.org/10.1021/acs.chemmater.5b00339.

[92] X. Chen, X. Li, D. Mei, J. Feng, M.Y. Hu, J. Hu, M. Engelhard, J. Zheng, W. Xu, J. Xiao, J. Liu, J.-G. Zhang, Reduction Mechanism of Fluoroethylene Carbonate for Stable Solid-Electrolyte Interphase Film on Silicon Anode, ChemSusChem 7 (2014) 549–554, https://doi.org/10.1002/cssc.201300770.

[93] M. Nie, D.P. Abraham, Y. Chen, A. Bose, B.L. Lucht, Silicon Solid Electrolyte Interphase (SEI) of Lithium Ion Battery Characterized by Microscopy and Spectroscopy, J. Phys. Chem. C 117 (2013) 13403–13412, https://doi.org/10.1021/jp404155y.

[94] F. Holtstiege, A. Wilken, M. Winter, T. Placke, Running out of lithium? A route to differentiate between capacity losses and active lithium losses in lithium-ion batteries, Phys. Chem. Chem. Phys. 19 (2017) 25905–25918, https://doi.org/10.1039/C7CP05405J.

[95] M. Wetjen, D. Pritzl, R. Jung, S. Solchenbach, R. Ghadimi, H.A. Gasteiger, Differentiating the Degradation Phenomena in Silicon-Graphite Electrodes for Lithium-Ion Batteries, J. Electrochem. Soc. 164 (2017) A2840–A2852, https://doi.org/10.1149/2.1921712jes.

[96] H. Wu, Y. Cui, Designing nanostructured Si anodes for high energy lithium ion batteries, Nano Today 7 (2012) 414–429, https://doi.org/10.1016/j.nantod.2012.08.004.

[97] F.A. Soto, Y. Ma, J.M. Martinez de la Hoz, J.M. Seminario, P.B. Balbuena, Formation and Growth Mechanisms of Solid-Electrolyte Interphase Layers in Rechargeable Batteries, Chem. Mater. 27 (2015) 7990–8000, https://doi.org/10.1021/acs.chemmater.5b03358.

[98] K. Schroder, J. Alvarado, T.A. Yersak, J. Li, N. Dudney, L.J. Webb, Y.S. Meng, K.J. Stevenson, The Effect of Fluoroethylene Carbonate as an Additive on the Solid Electrolyte Interphase on Silicon Lithium-Ion Electrodes, Chem. Mater. 27 (2015) 5531–5542, https://doi.org/10.1021/acs.chemmater.5b01627.

[99] I.A. Shkrob, J.F. Wishart, D.P. Abraham, What Makes Fluoroethylene Carbonate Different?, J. Phys. Chem. C 119 (2015) 14954–14964, https://doi.org/10.1021/acs.jpcc.5b03591.

[100] Y. Jin, N.-J.H. Kneusels, P.C.M.M. Magusin, G. Kim, E. Castillo-Martínez, L.E. Marbella, R.N. Kerber, D.J. Howe, S. Paul, T. Liu, C.P. Grey, Identifying the Structural Basis for the Increased Stability of the Solid Electrolyte Interphase Formed on Silicon with the Additive Fluoroethylene Carbonate, J. Am. Chem. Soc. 139 (2017) 14992–15004, https://doi.org/10.1021/jacs.7b06834.

[101] A.L. Michan, B.S. Parimalam, M. Leskes, R.N. Kerber, T. Yoon, C.P. Grey, B.L. Lucht, Fluoroethylene Carbonate and Vinylene Carbonate Reduction: Understanding Lithium-Ion Battery Electrolyte Additives and Solid Electrolyte Interphase Formation, Chem. Mater. 28 (2016) 8149–8159, https://doi.org/10.1021/acs.chemmater.6b02282.

A. Appendix

A.1 Appendix to section 4.5

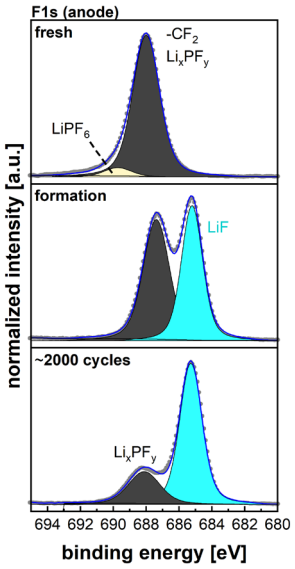

Figure A.1: F1s photoelectron spectra of an anode from a fresh cell, an anode from a cell after formation, and an anode from a cell after about 2000 cycles.

A.2 Appendix to section 5.4

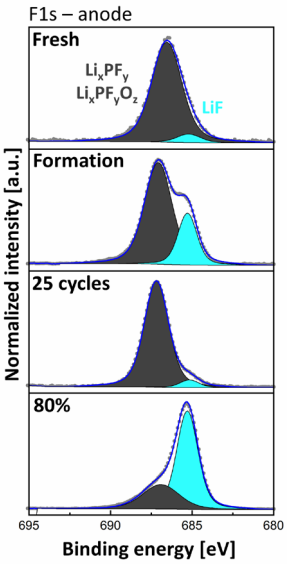

Figure A.2: F1s photoelectron spectra of anodes from a fresh cell, a cell after formation, a cell after 25 cycles, and a cell after cycling until a remaining capacity of 80%.

A.3 Appendix to section 6.6

Table A.1: Atomic percentages of different surface species on the anodes from the cells with the VC electrolyte investigated by XPS. The examined anodes are extracted from a fresh cell, a cell after formation, a cell after 15 cycles at 0.5 C/0.5 C, a cell after 40 cycles at 0.5 C/0.5 C, and a cell after 40 cycles at 2 C/3 C. "xx" indicates that the associated component is not detected on the concerning anode.

Anodes from cells with VC electrolyte		**Fresh**		**Formation**		**15 cycles (0.5 C)**		**40 cycles (0.5 C)**		**40 cycles (2 C/3 C)**	
Spectrum	Component	Binding energy at peak [eV]	Atomic percentage [%]	Binding energy at peak [eV]	Atomic percentage [%]	Binding energy at peak [eV]	Atomic percentage [%]	Binding energy at peak [eV]	Atomic percentage [%]	Binding energy at peak [eV]	Atomic percentage [%]
C1s	graphite	283.9	36.56	xx	xx	xx	xx	xx	xx	xx	xx
	-CH	285	11.88	285	9.13	285	8.68	285	9.99	285	9.12
	-C-O	286.59	5.03	xx	xx	xx	xx	xx	xx	xx	xx
	C_a	xx	xx	287.72	23.77	287.76	22.24	287.58	22.84	287.69	23.06
	$-CO_2$	xx	xx	289.32	1.74	289.01	3.6	289.24	1.64	288.82	3.04
	$-CO_3$	xx	xx	xx	xx	xx	xx	xx	xx	xx	xx
	C_b	xx	xx	291.17	9.65	291.23	11.18	291.07	9.05	291.16	10.97
F1s	LiF	xx	xx	684.81	0.72	xx	xx	xx	xx	xx	xx
	$LiPF_6/Li_xPF_yO_z$	686.79	6.73	686.78	11.4	686.87	12.6	686.6	16.5	686.77	12.8
Li1s	Li-X	xx	xx	56.08	5.97	xx	xx	56.6	3.47	xx	xx
O1s	ROLi	xx	xx	xx	xx	xx	xx	xx	xx	xx	xx
	-C=O	xx	xx	xx	xx	xx	xx	xx	xx	xx	xx
	$-C-O/O_a$	533.07	18.91	532.91	13.31	532.9	10.8	532.85	14.28	532.83	11.82
	O_b	xx	xx	534.56	22.19	534.6	27.18	534.46	19.42	534.51	25.94
Si2p	Si^0 2p3	99.51	5.11	xx	xx	xx	xx	xx	xx	xx	xx
	Li_xSi	xx	xx	xx	xx	xx	xx	xx	xx	xx	xx
	Li_xSiO_y	xx	xx	xx	xx	xx	xx	xx	xx	xx	xx
	SiO_2 2p3	103.69	4.71	xx	xx	xx	xx	xx	xx	xx	xx
P2p	Li_xPF_y	135.86	1.28	136.67	1.95	136.68	1.91	136.53	2.36	136.65	2.19
	$Li_xPF_yO_z$	132.98	0.22	132.99	0.17	132.9	0.23	132.36	0.06	xx	xx

Table A.2: Atomic percentages of different surface species on the anodes from the cells with the FEC electrolyte investigated by XPS. The examined anodes are extracted from a fresh cell, a cell after formation, a cell after 15 cycles at 0.5 C/0.5 C, a cell after 40 cycles at 0.5 C/0.5 C, and a cell after 40 cycles at 2 C/3 C. "xx" indicates that the associated component is not detected on the concerning anode.

Anodes from cells with FEC electrolyte		**Fresh**		**Formation**		**15 cycles (0.5 C)**		**40 cycles (0.5 C)**		**40 cycles (2 C/3 C)**	
Spectrum	Component	Binding energy at peak [eV]	Atomic percentage [%]	Binding energy at peak [eV]	Atomic percentage [%]	Binding energy at peak [eV]	Atomic percentage [%]	Binding energy at peak [eV]	Atomic percentage [%]	Binding energy at peak [eV]	Atomic percentage [%]
C1s	graphite	284.2	48.65	282.47	2.46	282.5	2.5	282.31	0.64	282.35	1.01
	-CH	285	5.47	285	18.02	285	16.12	285.01	11.74	285	10.16
	-C-O	286.32	6.1	286.72	7.08	286.71	6.6	286.61	6.89	286.68	6.42
	C_a/-C=O	xx	xx	287.9	2.79	288.1	2.99	287.91	5.15	287.9	4.4
	$-CO_2$	xx	xx	289.2	3.61	289.1	2.55	289.11	2.85	289.1	2.47
	$-CO_3$	xx	xx	290.1	1.36	290.12	1.89	290.11	1.76	290.1	1.94
	C_b	xx	xx	291.1	1.4	291.1	0.83	291.11	0.96	291.1	0.82
F1s	LiF	xx	xx	685.07	6.21	685.38	8.96	685.54	8.48	685.34	7.68
	$LiPF_6/Li_xPF_yO_z$	686.6	4.29	686.52	7.43	686.91	7.72	686.85	10.77	686.97	11.22
Li1s	Li-X	xx	xx	55.67	19.69	56.92	24.34	56.05	22.74	56.28	22.86
O1s	ROLi	xx	xx	530.44	1.92	530.59	2.09	530.16	0.94	530	0.43
	-C=O	xx	xx	531.76	10.89	531.91	12.04	532	8.66	532	9.18
	$-C-O/O_a$	532.92	19.07	533	6.98	533.49	7.21	533.73	10.2	533.9	9.99
	O_b	xx	xx	534.22	5.51	534.79	3.43	535.14	4.75	535.41	4.36
Si2p	Si^0 2p3	99.37	5.56	xx	xx	xx	xx	xx	xx	xx	xx
	Li_xSi	xx	xx	97.35	0.64	97.37	0.79	xx	xx	xx	xx
	Li_xSiO_y	xx	xx	100.58	0.38	100.48	0.57	xx	xx	xx	xx
	SiO_2 2p3	103.54	5.11	102.58	0.29	103.15	0.28	xx	xx	xx	xx
P2p	Li_xPF_y	135.82	1.19	136.55	1.1	136.54	0.89	136.75	1.29	136.51	0.96
	$Li_xPF_yO_z$	133.03	0.21	133.53	0.56	133.54	0.6	132.61	0.39	133.7	0.39

Table A.3: Atomic percentages of different surface species on the cathodes from the cells with the VC electrolyte investigated by XPS. The examined cathodes are extracted from a fresh cell, a cell after formation, a cell after 15 cycles at 0.5 C/0.5 C, a cell after 40 cycles at 0.5 C/0.5 C, and a cell after 40 cycles at 2 C/3 C. "xx" indicates that the associated component is not detected on the concerning cathode.

Cathodes from cells with VC electrolyte		**Fresh**		**Formation**		**15 cycles (0.5 C)**		**40 cycles (0.5 C)**		**40 cycles (2 C/3 C)**	
Spectrum	Component	Binding energy at peak [eV]	Atomic percentage [%]	Binding energy at peak [eV]	Atomic percentage [%]	Binding energy at peak [eV]	Atomic percentage [%]	Binding energy at peak [eV]	Atomic percentage [%]	Binding energy at peak [eV]	Atomic percentage [%]
C1s	Carbon black	284.3	20.61	283.98	6.24	xx	xx	xx	xx	xx	xx
	-CH	285	2.27	285	5.23	285	7.46	285	5.53	285	13.76
	-CH-CF_2-	285.82	16.61	xx	xx	xx	xx	xx	xx	xx	xx
	C_a	287.78	1.84	287.25	17.35	287.69	17.97	287.86	18.5	287.9	15.86
	-CO_2	xx	xx	288.95	3.71	289.15	4.14	289.79	1.54	289.2	1.29
	-CO_3	xx	xx	xx	xx	xx	xx	xx	xx	xx	xx
	-CF_2	290.31	12.82	xx	xx	xx	xx	xx	xx	xx	xx
	C_b	xx	xx	290.65	8.81	291.22	9.32	291.3	9.27	291.39	7.95
F1s	LiF	684.6	1.02	xx	xx	xx	xx	xx	xx	685.67	3
	$LiPF_6$/ $Li_xPF_yO_z$	696.46	0.04	686.34	17.41	686.82	15.79	686.8	14.21	686.86	15.99
	-CF_2	687.36	34.35	xx	xx	xx	xx	689.57	6.4	xx	xx
Li1s	Li-X	xx	xx	55.55	9.04	56.03	12.24	57.56	12.56	56.62	15.15
O1s	NCM622	529.22	3.48	528.85	0.3	xx	xx	xx	xx	xx	xx
	ROLi	531.44	4.32	xx	xx	xx	xx	xx	xx	xx	xx
	-C=O	xx	xx	xx	xx	xx	xx	xx	xx	xx	xx
	-C-O/O_a	533.42	1.77	532.54	9.52	533.03	9.11	533.05	7.23	533.14	8.61
	O_b	xx	xx	534.22	20.32	534.7	21.61	534.75	19	534.77	15.72
P2p	Li_xPF_y	134.84	0.86	136.29	2.06	136.77	2.36	136.94	2.2	136.91	2.66

Table A.4: Atomic percentages of different surface species on the cathodes from the cells with the FEC electrolyte investigated by XPS. The examined cathodes are extracted from a fresh cell, a cell after formation, a cell after 15 cycles at 0.5 C/0.5 C, a cell after 40 cycles at 0.5 C/0.5 C, and a cell after 40 cycles at 2 C/3 C. "xx" indicates that the associated component is not detected on the concerning cathode.

Cathodes from cells with FEC electrolyte		**Fresh**		**Formation**		**15 cycles (0.5 C)**		**40 cycles (0.5 C)**		**40 cycles (2 C/3 C)**	
Spectrum	Component	Binding energy at peak [eV]	Atomic percentage [%]	Binding energy at peak [eV]	Atomic percentage [%]	Binding energy at peak [eV]	Atomic percentage [%]	Binding energy at peak [eV]	Atomic percentage [%]	Binding energy at peak [eV]	Atomic percentage [%]
C1s	Carbon black	284.35	21.27	285.34	16.6	285.34	15.39	285.34	11.25	285.32	15.45
	-CH	285.05	0.39	xx	xx	xx	xx	xx	xx	xx	xx
	-CH-CF_2-	285.78	16.77	286.44	16.73	286.44	18.25	286.44	20.5	286.44	19.2
	C_a	287.61	1.91	288.43	2.37	288.47	3.13	288.41	4.93	288.44	2.96
	-CO_2	xx	xx	xx	xx	xx	xx	xx	xx	xx	xx
	-CO_3	xx	xx	xx	xx	xx	xx	xx	xx	xx	xx
	-CF_2	290.31	13.02	290.89	13.99	290.89	13.58	290.85	13.2	290.87	13.67
	C_b	xx	xx	xx	xx	xx	xx	xx	xx	xx	xx
F1s	LiF	684.55	2.16	685.49	2.5	685.57	2.69	685.6	3.32	685.54	3.3
	$LiPF_6$/ $Li_xPF_yO_z$	xx	xx	xx	xx	xx	xx	xx	xx	xx	xx
	-CF_2	687.36	34.4	687.89	32.6	687.85	31.02	687.78	30.87	687.83	32.73
Li1s	Li-X	xx	xx	xx	xx	xx	xx	xx	xx	xx	xx
O1s	NCM622	529.23	2.99	530.13	1.95	530.2	2.3	530.19	1.91	530.23	2.78
	ROLi	531.33	4.4	xx	xx	xx	xx	xx	xx	xx	xx
	-C=O	xx	xx	xx	xx	xx	xx	xx	xx	xx	xx
	-C-O/O_a	533.29	1.6	532.78	6.87	532.77	5.02	532.94	6.21	532.68	4.49
	O_b	xx	xx	535.68	3.89	534.42	5.25	534.4	6.49	534.42	4.4
P2p	Li_xPF_y	134.69	1.05	137.25	1.09	137.14	1.24	136.99	1.31	136.45	1.02

Own publications

R. Stockhausen, A. Hofmann, L. Gehrlein, T. Bergfeldt, M. Müller, H. Ehrenberg, A. Smith, Quantifying Absolute Amounts of Electrolyte Components in Lithium-Ion Cells Using HPLC, J. Electrochem. Soc. 168 (2021) 080504, https://doi.org/10.1149/1945-7111/ac1894.

R. Stockhausen, L. Gehrlein, M. Müller, T. Bergfeldt, A. Hofmann, F.J. Müller, J. Maibach, H. Ehrenberg, A. Smith, Investigating the dominant decomposition mechanisms in lithium-ion battery cells responsible for capacity loss in different stages of electrochemical aging, Journal of Power Sources 543 (2022) 231842, https://doi.org/10.1016/j.jpowsour.2022.231842.

R. Stockhausen, L. Gehrlein, M. Müller, T. Bergfeldt, A. Hofmann, F.J. Müller, J. Maibach, K. Pesta, J. Klemens, H. Ehrenberg, A. Smith, Investigating the reductive decomposition of FEC and VC in lithium-ion pouch cells with silicon-graphite composite anodes, manuscript in preparation.

Conference posters

R. Stockhausen, A. Smith, H. Ehrenberg, Quantifying Absolute Amounts of Electrolyte Components in Lithium-Ion Cells Using HPLC, 241st ECS Meeting, Vancouver, Canada.

Acknowledgment

First of all, I want to thank my supervisors Prof. Dr. Michael J. Hoffmann and Prof. Dr. Helmut Ehrenberg for their support, for their advice, and for giving me the opportunity to do a PhD. In addition, I would also like to express my deep gratitude to Dr. Anna Smith for her guidance and support during this work. Our discussions were particularly helpful to me and resulted in several, new ideas for the present thesis. Additionally, I owe a lot of gratitude to Dr. Andreas Hofmann for his helpful support and for conducting GC investigations for the present thesis. Your profound knowledge about cell chemistry helped me a lot.

I especially want to thank Dr. Marcus Müller for performing the large number of SEM and EDX analyses, including the acquisition of the time-consuming cross-section images. Furthermore, I would like to give thanks to Lydia Gehrlein and Dr. Julia Maibach for realizing and evaluating all the XPS analyses. In addition, my thanks go to Dr. Thomas Bergfeldt for carrying out the ICP-OES measurements. I want to thank Dr. Freya Janina Müller for conducting GC examinations and for the advice regarding the HPLC. Besides, I would like to thank Dr. Ronald Gordon Grajales, Katarzyna Pesta, and Julian Klemens for the complicated production of the silicon-graphite anode tapes. Moreover, I also owe gratitude to Sven Leuthner for his support in the cell assembly and for the production of various electrode tapes.

Eventually, I would like to express my gratitude to my parents and my sister for their moral support and their understanding. I would not have gotten this far without you. A special thanks goes to my girlfriend Nicole for her support, her patience, and her confidence in me.